KU LEUVEN

University of Cologne

The Quantum Anomalous Hall Effect in Magnetically Doped Topological Insulators

A Study of the Current-Induced Breakdown

12 May 2023

Gertjan Lippertz

Supervisors:
Prof. Dr. Yoichi Ando
Prof. Dr. Lino M. C. Pereira
Prof. Dr. Margriet Van Bael

Dissertation presented in partial fulfillment of the requirements for the degree of Doctor of Science (PhD): Physics, and Doktor der Naturwissenschaften (Dr. rer. nat.)

Faculties:
KU Leuven, Faculty of Science
University of Cologne, Faculty of Mathematics and Natural Science

The Quantum Anomalous Hall Effect in Magnetically Doped Topological Insulators

A Study of the Current-Induced Breakdown

Gertjan LIPPERTZ

Examination committee:
Prof. Dr. Thomas E. Cocolios, chair
Prof. Dr. Yoichi Ando, supervisor
Prof. Dr. Lino M. C. Pereira, supervisor
Prof. Dr. Margriet Van Bael, co-supervisor
Prof. Dr. Erwann Bocquillon
Prof. Dr. Michel Houssa
Prof. Dr. Chris Van Haesendonck
Prof. Dr. André Vantomme
Prof. Dr. Badih A. Assaf
(University of Notre Dame)

Dissertation presented in partial fulfillment of the requirements for the degree of Doctor of Science (PhD): Physics, and Doktor der Naturwissenschaften (Dr. rer. nat.)

12 May 2023

Uitgegeven in eigen beheer, Gertjan Lippertz, Celestijnenlaan 200D box 2414, B-3001 Leuven (Belgium)

Preface

> *I awoke this morning with devout thanksgiving for my friends, the old and the new.*
>
> Ralph Waldo Emerson

This thesis describes the joint PhD project between the KU Leuven and the University of Cologne, on the breakdown of the quantum anomalous Hall effect (QAHE) in magnetically doped topological insulator thin films. The research was conducted at both universities under the supervision of Prof. Lino Pereira (Quantum Solid State Physics, KU Leuven, Belgium) and Prof. Yoichi Ando (Topological Matter Laboratory Cologne, University of Cologne, Germany).

The research presented in this thesis received funding from the European Research Council (ERC) under the European Union's Horizon 2020 research and innovation program (Grant Agreement No. 741121) and was also funded by the Deutsche Forschungsgemeinschaft (DFG, German Research Foundation) under Germany's Excellence Strategy - Cluster of Excellence Matter and Light for Quantum Computing (ML4Q) EXC 2004/1 - 390534769, as well as under CRC 1238 - 277146847 (Subprojects A04). Moreover, I personally received support in the form of a PhD scholarship from the KU Leuven BOF and Research Foundation–Flanders (FWO, Belgium), file No. 27531 and No. 52751.

With the formalities out of the way, I would like to thank all the people who have contributed to this thesis and my PhD life in general. First and foremost, I would like to thank Prof. Lino Pereira and Prof. Yoichi Ando for welcoming me in their respective laboratories and for their guidance throughout the years of my PhD studies.

The first years of my PhD I spent in Leuven; here I would like to thank my colleagues and friends: Eva Anton, Valérie Augustyns, Harsh Bana, Sergey Basov, Manisha Bisht, Jolien Debehets, Pía Homm Jara, Vincent Joly, Vera Lazenka, Tiago de Lemos Lima, Pin-Cheng Lin, Asteriona Maria Netsou, Sérgio Miranda, Bas Opperdoes, Daniel Pérez, Nuno Santos, Koen van Stiphout, Renan Villarreal, and Yingying Wang. In particular, I am grateful to James McNulty for his friendship and guidance during the initial period of my PhD. Furthermore, this section would not be complete without thanking Ivan Mađarević for the many conversations and jokes during the long hours we spent sputtering and annealing the InSb wafers for the α-Sn project. I would like to thank Ulrich Wahl and Angelo Costa for the fun and interesting night shifts we had at the ISOLDE facility at CERN. Lastly, I am grateful to Vincent Joly, Natália Mello, and Thiago Monteiro for the board game nights, exciting conversations, and friendship throughout the years.

After my initial period at the KU Leuven, my research project turned into a joint PhD with the University of Cologne, and I took residence under the shadow of the mighty Dom. Here too, I met many talented people which I am lucky to call my friends: Lionel Andersen, Sweta Bagchi, Mengmeng Bai, Richard Bounds, Jens Brede, Oliver Breuning, Linh Dang, Christian Dickel, Cornelius Dietrich, Dingxun Fan, Junya Feng, Rafael Fister, Adrian Greichgauer, Luc Janssen, Jonas Krause, Felix Münning, Ella Nikodem, Matthias Rößler, Jakob Schluck, Elmore Vaal, Zhiwei Wang, Yongjian Wang, Fan Yang, and Nicolas Zapata. I would like to thank Henry Legg for being our *theorist-on-call*, always happy to discuss our experiments, and for the fun times we had at conferences. I am particularly grateful to Alexey Taskin; working alongside of you for all these years, I have learned so much. Thank you for your patience, guidance and friendship. Moreover, I want to thank Andrea Bliesener and Roozbeh Yazdanpanah with whom I worked very closely in the lab as well; thank you for the nice working environment and the great times in- and outside of work. Lastly, I would like to thank Dennis Hardt, Yaren Itak, Aprem Joy, and Veena V. S. for the nice evenings in Cologne and their friendship.

I am grateful to my parents Roger Lippertz and Christiane Simons, my brother Edwin Lippertz, my uncle Philip Simons, and my grandparents Jo Lippertz (†), Riny Franssen, Eugène Simons (†) and Astrid Peerboom, for their continued support and encouragement throughout the years. I am also grateful to my family in India, Udayakumar Chonat, Nandini Kottarappatt, and Arathy Uday for being so welcoming. Most of all, I want to thank my partner in life, as well as in science, Anjana Uday for her love, support and kindness since that fateful day she walked through the doors of the II. Physikalisches Institut.

Gertjan Lippertz

Abstract

The quantum Hall effect, in which the transverse conductance of a two-dimensional (2D) electron gas in an applied magnetic field becomes quantized to multiples of e^2/h, has fascinated physicists for over forty years. In the last decade, the quantum-Hall research field has expanded with the discovery of 2D topological insulators (i.e. the quantum spin Hall effect in 2007) and magnetic topological insulators (i.e. the quantum anomalous Hall effect in 2013). The later effect, typically abbreviated as 'QAHE', is of particular technological interest, as its quantization can be observed in macroscopic devices and does not require the application of an external magnetic field. Hence, the QAHE is expected to supplant conventional quantum Hall systems in many applications, e.g. as the resistance standard for the international system of units (SI).

The hallmark of the QAHE is its dissipationless chiral 1D state running along the edge of the quasi-2D magnetic-topological-insulator thin film, resulting in a vanishing longitudinal resistance and quantized Hall resistance equal to h/e^2. However, when reducing the device dimensions or increasing the current density, an abrupt breakdown of the dissipationless state occurs with a relatively small critical current, limiting the applications of the QAHE. In this thesis, the mechanism of this breakdown is studied in multi-terminal devices and the electric field created between opposing chiral edge states is identified as the driving force. It is well-known that Coulomb disorder plays a strong role in compensated topological-insulator crystals as a consequence of the random distribution of the charged donor and acceptor impurities. In regions with large uncompensated charge, metallic n- or p-type 'puddles' are formed. In this thesis, the electric-field-driven percolation of such 2D charge puddles in the gapped surface states of the quantum-anomalous-Hall-insulator (QAHI) thin films is proposed as the most likely cause of the breakdown of the QAHE. Namely, the hopping transport between the 2D charge puddles causes an electrical short between the opposing chiral edge states across the width of the sample, which leads to a loss of edge potential. This results in a nonzero longitudinal resistance and a Hall resistance smaller than h/e^2.

Although generally it is desirable to avoid breakdown of the QAHE, the chiral nature of the edge states gives rise to rectification (nonreciprocal) effects in the longitudinal resistance when the ideal QAHI-state is lost with increasing probe current, or by tuning the chemical potential away from the charge-neutrality-point into the 2D valence or conduction band. In this thesis, the nonreciprocal charge transport in QAHIs is studied over a large parameter space of different temperatures, applied magnetic fields, electrostatic gate-potentials, and probe currents. Two distinct regimes are identified. At high currents and/or temperatures where Coulomb disorder only plays a minor role, the current-voltage relation follows the well-known quadratic current-dependence of nonreciprocal systems. However, at ultra-low temperatures (< 100 mK) when the current amplitude is decreased to only slightly exceed the critical current for breakdown, the description of the nonreciprocal charge transport becomes more complex. In this regime, the finite nonreciprocal response when the chemical potential lies inside the exchange gap is argued to be determined by the majority 2D charge puddles (either n- or p-type) resulting from an imperfect charge compensation. The largest rectification ($\sim$20%) is found in this regime close to breakdown, which has remained unexplored so far.

Since electrostatic gating is an efficient way to switch between the ideal and broken-down QAHI-states, the system constitutes a unique 'quantum circuit element' offering both dissipationless transport and rectification, as well as a quantized transverse resistance of h/e^2. The thesis advances the understanding of the current-induced breakdown of the QAHE in magnetically doped topological insulators, and its findings are relevant to the fundamental research in QAHI systems, as well as its potential applications.

Beknopte Samenvatting

Het kwantum-Hall-effect, waarbij de transversale geleidbaarheid van een tweedimensionaal (2D) elektronengas in een magnetisch veld wordt gekwantiseerd tot veelvouden van e^2/h, fascineert natuurkundigen al meer dan veertig jaar. In het afgelopen decennium is het kwantum-Hall-onderzoeksveld uitgebreid met de ontdekking van 2D topologische isolatoren (i.e. het kwantum-spin-Hall-effect in 2007) en magnetische topologische isolatoren (i.e. het kwantum-afwijkende-Hall-effect in 2013). Dit laatste effect, meestal afgekort als 'QAHE' verwijzend naar zijn Engelse naam, is van bijzonder technologisch belang, omdat de kwantisering kan worden waargenomen in macroscopische monsters en daarvoor geen extern magnetisch veld vereist is. Daarom wordt verwacht dat het QAHE conventionele kwantum-Hall-systemen in veel toepassingen zal vervangen, b.v. als weerstandsnorm voor het internationale systeem van eenheden (SI).

Het kenmerk van het QAHE is de dissipatieloze chirale 1D-toestand die zich op de rand van de quasi-2D magnetische-topologische-isolator dunne laag bevindt. Deze chirale randtoestand zorgt dat de longitudinale weerstand verdwijnt en de Hall-weerstand gekwantiseerd wordt tot h/e^2. Bij het verkleinen van de monsterafmetingen of het vergroten van de stroomdichtheid treedt echter een abrupte ineenstorting van het dissipatieloze transport op voor een relatief kleine kritische stroom, wat de mogelijke toepassingen van het QAHE inperkt. In dit proefschrift wordt het mechanisme van deze ineenstorting bestudeerd in monsters met meerdere meetterminals en wordt het elektrische veld dat wordt gecreëerd tussen tegengestelde chirale randtoestanden geïdentificeerd als de drijvende kracht. Het is bekend dat Coulomb-stoornis een sterke rol speelt in gecompenseerde topologische isolatoren als gevolg van de willekeurige verdeling van de geladen donor- en acceptoronzuiverheden. In gebieden met grote ongecompenseerde lading worden metalen n- of p-type 'ladingsplassen' ('charge puddles' in het Engels) gevormd. In dit proefschrift wordt de percolatie van dergelijke 2D-ladingsplassen in de geopende oppervlaktetoestanden van de kwantum-afwijkende-Hall-(QAH)

isolator aangewezen als de meest waarschijnlijke oorzaak van de ineenstorting van het QAHE. Het hoppende elektronentransport tussen de 2D-ladingsplassen veroorzaakt namelijk een elektrische kortsluiting tussen de tegenoverliggende chirale randtoestanden over de breedte van het monster. Dit leidt tot een verlies van randpotentieel, wat resulteert in een longitudinale weerstand die niet langer nul is en een Hall-weerstand kleiner dan h/e^2.

Hoewel het over het algemeen wenselijk is om de ineenstorting van het QAHE te voorkomen, geeft de chirale aard van de randtoestanden aanleiding tot rectificatie (niet-reciproke) effecten in de longitudinale weerstand wanneer de ideale QAH-toestand verloren gaat met toenemende stroomdichtheid, of door de chemische potentiaal van het ladingsneutraliteitspunt weg te sturen tot in de 2D-valentie- of geleidingsband. In dit proefschrift wordt het niet-reciproke ladingstransport in QAH-isolatoren bestudeerd over een grote parameterruimte van verschillende temperaturen, externe magnetische velden, elektrostatische poortpotentialen en stroomdichtheden. Er worden twee verschillende regimes waargenomen. Bij hoge stromen en/of temperaturen waar de Coulomb-stoornis slechts een ondergeschikte rol speelt, volgt de stroom-spanningsrelatie de bekende kwadratische stroomafhankelijkheid van niet-reciproke systemen. De beschrijving van het niet-reciproke ladingstransport wordt daarentegen echter complex wanneer bij ultra-lage temperaturen (< 100 mK) de stroomamplitude wordt verkleind tot slechts een paar nanoampère boven de kritieke stroom voor de ineenstorting. In dit regime wordt de niet-reciproke respons wanneer de chemische potentiaal in de geopende oppervlaktetoestanden ligt, toegeschreven aan de 2D-ladingsplassen (n- of p-type) die in de meerderheid zijn, als gevolg van een onvolledige ladingscompensatie. De grootste rectificatie ($\sim$20%) wordt waargenomen in dit regime dicht bij het instortingspunt, dat tot nu toe nog niet onderzocht werd.

Aangezien een elektrostatische poort een efficiënte manier is om tussen de ideale en ineengestorte QAH-toestand te schakelen, vormt het QAH-systeem een uniek 'kwantum-circuitelement' dat zowel dissipatieloos transport als rectificatie biedt, evenals een gekwantiseerde Hall-weerstand van h/e^2. Het proefschrift vordert het begrip van de stroomgeïnduceerde ineenstorting van het QAHE in magnetisch gedoteerde topologische isolatoren, en de bevindingen zijn relevant voor het verder fundamenteel onderzoek in QAH-systemen, evenals de mogelijke toepassingen ervan.

List of Abbreviations

2DEG Two-dimentional electron gas. 1, 3

AAAS American Association for the Advancement of Science. 14, 16, 18, 27

AC Alternating current. xviii, 9, 39, 52, 53, 55–59, 70–73, 79, 80, 82, 95, 99, 104, 108, 132, 145

AFM Atomic force microscopy. xxi, 39, 40, 46, 47

AH Anomalous Hall. 39, 46, 104

ALD Atomic layer deposition. 46, 51

ANE Anomalous Nernst effect. 115

APT Atom probe tomography. 42

ARPES Angle-resolved photoemission spectroscopy. xxi, 17–19

BCB Bulk conduction band. 18, 25, 65

BCS Bardeen-Cooper-Schrieffer (theory). 52

BdG Bogoliubov-de Gennes (Hamiltonian). 33, 34, 125

BEP Beam-equivalent-pressure. 43, 45, 46, 58

BHZ Bernevig-Hughes-Zhang (model). 13, 26, 28

BSEH Bootstrap electron heating. xi, 6, 9, 86, 118

BST $(Bi_xSb_{1-x})_2Te_3$. 121

BVB Bulk valence band. 18, 20, 25, 65

BZ Brillouin zone. 14–16

CNP Charge-neutrality-point. 81–84, 97, 99–101, 106, 108, 110, 113, 115, 122, 152

DC Direct current. xviii, 7, 40, 52, 55, 58, 62, 69–71, 82, 83, 95–97, 99, 101, 104, 108, 109, 145, 146

DFG Deutsche Forschungsgemeinschaft. i

DI Deionized (water). 49, 51

DNQ Diazonaphthoquinone sulfonic acid esters (DNQ sulphonates). 49

DP Dirac point. 20

EBL Electron-beam lithography. 51

EDX Energy-dispersive X-ray spectroscopy. 46

ERC European Research Council. i

FM Ferromagnetic. 7, 25, 31, 32

FMI Ferromagnetic insulator. 122, 123

FQAHE Fractional quantum anomalous Hall effect. 123

FWO Research Foundation–Flanders. i

MBE Molecular beam epitaxy. xvii, xxi, 39–43, 45–47, 58

MCA Magnetochiral anisotropy. xi, 94, 104, 157, 158

MDPI Multidisciplinary Digital Publishing Institute. 41

ML4Q Cluster of Excellence 'Matter and Light for Quantum Computing'. i

MOSFET Metal-oxide-semiconductor field-effect transistor. 2

NI Normal insulator. 34, 35

NMP N-methyl-2-pyrrolidone. 50, 51

NSC Normal superconductor. 35

PBN Pyrolytic boron nitride. 44

PMMA Polymethyl methacrylate. 51

PPMS Physical property measurement system. 39, 40

PSD Phase-sensitive detector. 56, 57

QAH Quantum anomalous Hall. v, vi, xi, xiii, xiv, xvii, xviii, xxi, xxii, 7–9, 11, 24, 28, 30–37, 41, 42, 46, 47, 59, 61–64, 66, 68, 70, 72–74, 76, 78, 80–92, 94, 95, 97, 108, 113–119, 121–123, 129, 140, 147

QAHE Quantum anomalous Hall effect. i, iii–vi, xv, xviii, xxi, xxii, 6–9, 25, 28, 29, 31, 32, 37, 39, 41, 46, 52, 61–66, 69–71, 73, 74, 76, 77, 79, 81–94, 108, 109, 114, 117–119, 121–123, 129–131, 133, 142, 144, 146, 147

QAHI Quantum anomalous Hall insulator. iii, iv, xi, xii, xiv, xxi–xxiii, 11, 12, 25, 27, 30–34, 36, 37, 56, 64, 65, 67, 73, 76, 84–95, 99, 101, 104, 113, 116–119, 121, 123, 125, 133, 139, 157, 159

QH Quantum Hall. 3

QHE (Integer) quantum Hall effect. xiii, xxi, 1–6, 8, 9, 83, 86, 87, 89, 119

QL Quintiple layer. 40–42, 46

QMS Quadrupole mass spectrometer. 43

QPT Quantum phase transition. 32

QSH Quantum spin Hall. xiv, 13, 15, 16, 28

QSHE Quantum spin Hall effect. xxi, 13, 16, 28, 29, 37, 139

QSHI Quantum spin Hall insulator. 12, 16, 28, 29, 31, 37

qubit Quantum-bit. 8, 119

QUILLS Quasi-elastic inter-Landau-level scattering. 4, 9

QW Quantum well. xxi, 13–17, 31

RHEED Reflection high-energy electron diffraction. 43

RKKY Ruderman-Kittel-Kasuya-Yosida. 31

rms Root-mean-square. xxii, 46, 55, 57, 70, 72, 73, 79, 100

SC Superconductor/superconducting. xxi, 8, 34–37, 94, 159

SI International system of units. iii, v, xxi, 2, 3, 8, 119

SNCSC Springer Nature Customer Service Center GmbH. 18, 20, 22, 33, 54, 96

SOC Spin-orbit coupling. 27, 32, 37

SQUID Superconducting quantum interference device. 33, 63, 87

SSB Surface-state band. 18

STEM Scanning transmission electron microscopy. 42

STM Scanning tunneling microscopy. 23, 119

TI Topological insulator. xxi, 6–8, 11, 12, 17, 19–25, 28, 31, 32, 35, 37, 51, 74, 83–85, 87, 89, 91, 114, 119, 122, 123

TMAH Tetramethylammonium hydroxide. 48–51

Transene D Transene Aluminum Etchant type-D. 51, 59

TRS Time-reversal symmetry. 7, 12, 13, 16, 17, 23, 25, 85, 94, 157

TSC Topological superconductor. 34–37

TSS Topological surface state. 18, 25, 65

UHV Ultra-high-vacuum. 40, 43, 51

UMR Unidirectional magnetoresistance. 115

USR Unoccupied surface resonance. 18

VdW Van-der-Waals. 41, 123

VdWE Van-der-Waals Epitaxy. 41

VRH Variable-range hopping. 23, 91

XRD X-ray diffraction. xxi, 39, 40, 42, 46, 47

XRR X-ray reflectometry. 39

List of Symbols

α, β, γ	Scattering probabilities in the Landauer-Büttiker model
Δ	Pairing gap function of the superconductor
$\Delta\nu_{\mathrm{Cs}}$	Caesium hyperfine frequency = 9192631770 Hz
Δ_{a}	Thermal activation energy
$\dot{n}$	Flow rate
$\dot{Q}$	Cooling power
$\epsilon(T)$	Energy of the system at temperature T in the BSEH model
ϵ_{m}	Lattice mismatch between the film and substrate
γ	Rectification coefficient for the magnetochiral anisotropy (MCA)
$\hat{M}$	Magnetization index, distinguishing the out-of-plane upward ($\hat{M} = +1$) and downward ($\hat{M} = -1$) direction
$\hbar$	Reduced Planck constant = $1.054571817 \times 10^{-34}$ Js
λ	Exchange gap in the QAH Hamiltonian ($\lambda = gM$), due to Zeeman splitting
$\hat{\mathbf{d}}$	Unit vector representing a Hamiltonian
$\mathcal{C}$	Chern number
$\mathcal{P}$	Polarity of the nonreciprocal response in a QAHI
μ	Chemical potential
$\mu_0 H$	Magnetic field, with $\mu_0 = 4\pi \times 10^{-7}$ H/m the vacuum permeability
ω	Measurement frequency

ω_c	Cyclotron frequency
ω_l	Internal lock-in oscillator frequency
ω_r	Frequency reference
ω_s	Sample frequency
ρ_xx	Longitudinal sheet resistance
ρ_yx	Transverse sheet resistance
σ_i	Pauli matrices
σ_xx	Longitudinal conductance
σ_xy	Transverse conductance
τ	Relaxation time
θ_l	Internal lock-in oscillator phase
θ_s	Sample phase
$\tilde{\gamma}$	Rectification coefficient for a QAHI at high currents
$\varepsilon(k)$	Term of a Hamiltonian
ε, κ	Relative permittivity (dielectric constant) of the material
ε_0	Vacuum permittivity $= 8.8541878128 \times 10^{-12}$ F/m
$a_\mathrm{f}, a_\mathrm{s}$	In-plane lattice constants of the film and substrate, respectively
B	Applied magnetic field, or a material constant in a Hamiltonian
c	Speed of light in vacuum $= 299792458$ m/s
$c_\mathrm{L/R}$	Edge index, distinguishing left ($c_\mathrm{L} = +1$) and right ($c_\mathrm{R} = -1$)
d, D	Layer thickness
d_def	Average defect separation
$d_\mathrm{i}(k)$	Terms of a Hamiltonian ($i = 1, 2, 3$)
e	Elementary charge $= 1.602176634 \times 10^{-19}$ C
E_BD	Critical Hall electric field
E_B	Bottom of the bulk conduction band

E_{C}	Bottom of the bulk conduction band
E_{c}	Critical Hall electric field
E_{def}	Coulomb interaction between neighboring defects
E_{D}	Dirac point
E_{e}	Electron percolation level
E_{F}	Fermi level
E_{g}	Bulk band gap
E_{h}	Hole percolation level
E_{V}	Top of the bulk valence band
E_{yx}	Transverse electric field
g	Effective g-factor in the QAH Hamiltonian
h	Planck constant $= 6.62607015 \times 10^{-34}$ Js
$H(k)$	Hamiltonian
$H(T)$	Enthalpy
H_{c}	Coercive field
H_{r}	Remnant magnetization
I	Current
i	Filling factor of the QHE, or the imaginary unit ($i^2 = -1$)
I_0	Peak-current amplitude
$I_{\mathrm{AC}}(t)$	Alternating current
I_{c}	Critical current
I_{DC}	Direct current
I_{i}	Current flowing through the ith contact into the sample
I_{rms}	Root-mean-square current amplitude
j	Current density
j_{c}	Critical current density

K	Degree of charge compensation
k_B	Boltzmann constant $= 1.380649 \times 10^{-23}$ J/K
K_cd	Luminous efficacy of a defined visible radiation (yellow-green, 540×10^{12} Hz) $= 683$ lm/W
k_i	Wave vectors of the lattice ($i = x, y, z$)
L	Hall-bar voltage-contact spacing
l_B	Magnetic length
M	Dirac-mass term in the QSH Hamiltonian, Exchange field in the QAH Hamiltonian, or the magnetization of the QAHI
m^*	Effective mass
m_0	Hybridization gap in the QAH Hamiltonian
m_e	Electron mass $= 9.1093837015 \times 10^{-31}$ kg
m_k	Mass term in the QAH Hamiltonian, stemming from tunneling between the top and bottom surface states
N_A	Avogadro number $= 6.02214076 \times 10^{23}$ mol^{-1}
N_A^-	Acceptor defect concentration
N_def	Defect concentration
N_D^+	Donor defect concentration
$n_\mathrm{p/n}$	2D charge carrier index, distinguishing p-type ($n_\mathrm{p} = +1$) and n-type ($n_\mathrm{n} = -1$)
R	Resistance, or the radius of a sphere
R^NL	Nonlocal resistance
R_0	Ohmic resistance of a QAHI at high currents
R_1	Nonreciprocal resistance of a QAHI at high currents
R_H	Hall resistance
r_i	Escape distance for the electric field lines in a TI ($i = \mathrm{TI}$) or trivial insulator ($i = 0$)
R_p	Characteristic length scale of puddle formation

R_{xx} Longitudinal resistance

R_{yx} Transverse resistance

T Temperature, or the averaging time of a lock-in

t Time

T_0 Activation temperature

T_C Curie temperature

T_{el} Electron temperature

T_{Ex} Temperature of the last heat exchanger

T_{ji} Transmission probability from the ith to the jth contact

T_L Lattice temperature

T_{MC} Temperature of the mixing chamber

T_{QAHE} Zero-field quantization temperature of the QAHE

V Voltage

v_F Fermi velocity

V_{Gate} Gate voltage

V_i Potential of the ith contact

$V_{L/R}$ Voltage drop on the left/right edge of the Hall-bar at high currents

V_l Internal lock-in oscillator peak-voltage

$V_{PSD+low\text{-}pass}$ Filtered phase-sensitive detector output

V_{PSD} Phase-sensitive detector output

V_{rms} Root-mean-square voltage amplitude

V_s Sample peak-voltage

V_x Longitudinal voltage

V_y Transverse voltage

W Hall-bar or contact width

W_{Hb} Hall-bar width

$X^{2\omega}$	'In-phase' lock-in output at the second harmonic 2ω
X^{ω}	'In-phase' lock-in output at the first harmonic ω
$Y^{2\omega}$	'Quadrature' lock-in output at the second harmonic 2ω
Y^{ω}	'Quadrature' lock-in output at the first harmonic ω

Contents

List of Figures

Chapter 1

Introduction

> *Even truth needs to be clad in new garments if it is to appeal to a new age.*
>
> Georg C. Lichtenberg

In 1879, the American physicist Edwin Hall discovered the Hall effect while working on his doctoral thesis. He found that when an electric current flows through a conductor and a magnetic field is applied perpendicular to the current direction, a potential difference (the 'Hall voltage') is created between the opposite sides of the conductor, perpendicular to both the applied current and magnetic field [57, 58].

A century later, in 1980, the German physicist Klaus von Klitzing discovered the integer quantum Hall effect (QHE). By studying the Hall resistance of a two-dimentional electron gas (2DEG) as a function of gate voltage at 1.5 K in a magnetic field of 18 T [182], he found that when the Fermi level is tuned to lie between Landau levels (where the longitudinal resistance vanishes), the Hall resistance is given by

$$R_{\mathrm{H}} = \frac{h}{ie^2}, \qquad i = 1, 2, 3, \ldots \tag{1.1}$$

where h is the Planck constant, e the elementary charge, and i the filling factor. A historic review by von Klitzing about his unexpected discovery of the QHE and his early measurement results can be found in Ref. [180]. Figures 1.1(a-b)

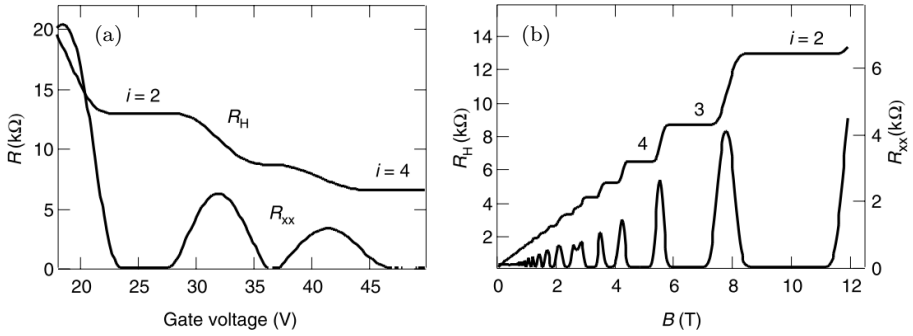

Figure 1.1: The integer quantum Hall effect (QHE), measured at a temperature of 0.3 K. The longitudinal and Hall resistance, R_{xx} and R_H respectively, are shown as a function of (a) the gate voltage for a Si-MOSFET in 13.8 T, and (b) the applied magnetic field B for a GaAs/$Al_x$$Ga_{1-x}$As heterostructure. When the Fermi level lies between two Landau levels (where R_{xx} vanishes), R_H is quantized to $h/(ie^2)$. Figures (a) and (b) are reprinted from Ref. [73]. © IOP Publishing. Reproduced with permission. All rights reserved.

show more recent measurements of the longitudinal and Hall resistance, R_{xx} and R_H respectively, for a Si-MOSFET as a function of the gate voltage, and a GaAs/$Al_x$$Ga_{1-x}$As heterostructure as a function of the applied magnetic field [73]. The precise quantization of the Hall resistance shows that the electronic resistance can be defined in terms of fundamental constants, even in disordered samples [181].

In 2018, in Versailles (France), 60 countries made the unanimous vote to revise the international system of units (SI) to be based on seven fundamental constants of nature, see Fig. 1.2(a). The idea being that if the numerical values of the fundamental constants $\{h, c, \Delta\nu_{\rm Cs}, e, k_{\rm B}, N_{\rm A}, K_{\rm cd}\}$ are defined, the properties of entities expressed in the seven basic units {kg, m, s, A, K, mol, cd} can be evermore accurately measured. Hence, defining the fundamental constants alleviates the need to update their numerical values with every technological improvement in metrological accuracy. While the new definition of the ampere does not imply any particular experiment for its practical realization, it is the combination of the quantum Hall and Josephson effect (acting as the resistance and voltage standard, respectively), which yields the smallest uncertainty [43], see Fig. 1.2(b). Note that single electron transport offers an elegant direct realization of the ampere; however, its implementation still has technical limitations and often yields larger relative uncertainties [43].

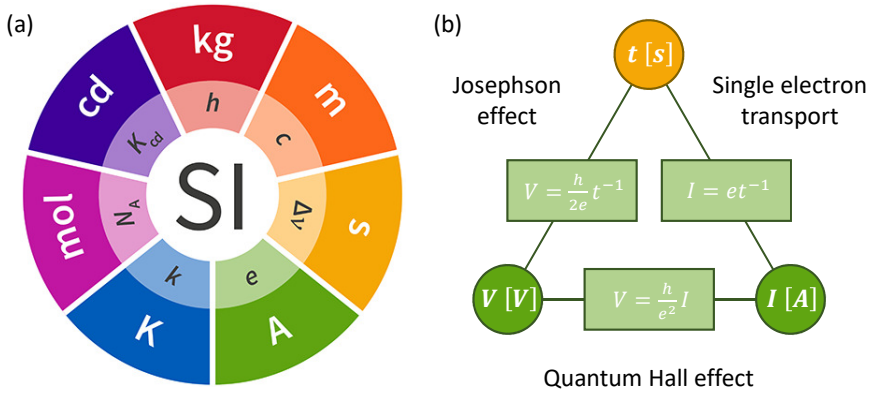

Figure 1.2: (a) The international SI logo, showing the seven basic units and the fundamental constants they are based on. (b) The metrological triangle relating the three quantum electrical effects via Ohm's law. Figure (a) is reprinted with permission from Ref. [43], while Fig. (b) is based on Ref. [73].

The potential advancements in metrology were apparent immediately after the discovery of the QHE [182], sparking intense investigations to determine the physical limits of the effect [127]. A sudden breakdown of the near dissipationless state of the QHE was observed if the applied current exceeded a certain limit. Figure 1.3 shows that at this critical current, the system becomes unstable with the longitudinal resistance R_{xx} increasing abruptly by several orders of magnitude. Moreover, the value of the critical current decreases linearly as the magnetic field B moves away from the center of the QH plateau, as shown in Fig. 1.4(a) for $i = 2$. If the critical Hall field $E_c = (I_c/W)R_H$ at the plateau center, on the other hand, is plotted for different values of B (and i), a $B^{3/2}$-dependence for E_c is found, as shown in Fig. 1.4(b). This B-dependence of E_c holds true for semiconductors [46, 74, 81] as well as for graphene [2], indicating it is an universal property of the breakdown of the QHE, independent of the details of the 2DEG system.

Various mechanisms have been proposed to explain the breakdown phenomenon (see Ref. [127] for a comprehensive review), most of which rely on inter-Landau-level transitions of electrons in the highest occupied Landau level into the lowest unoccupied level due to the large Hall field. In this context, the natural scale for E_c is the Zener field

$$E_Z \approx \hbar\omega_c/el_B\sqrt{i}, \tag{1.2}$$

where $\omega_c = eB/m^*$ is the cyclotron frequency, $l_B = \sqrt{\hbar/eB}$ the magnetic length, and m^* the effective mass [45, 199]. Generally, such an inter-Landau-

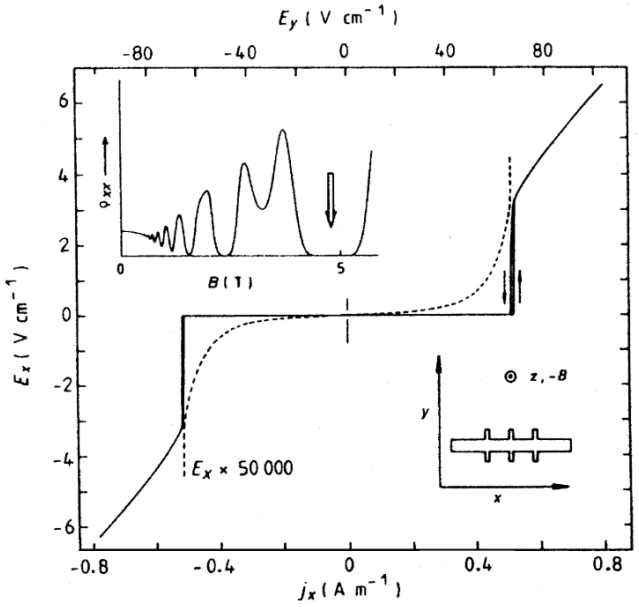

Figure 1.3: The current-induced breakdown of the QHE in a GaAs/Al_xGa_{1-x}As heterostructure. The current-voltage characteristic is plotted as the longitudinal electric field E_x versus the current density j_x. The data were recorded at 1.4 K, at filling factor $i = 2$ for an applied magnetic field of 4.7 T, as shown in the upper inset. The dotted curve shows a magnification of the pre-breakdown region by a factor of 5×10^4. The lower inset shows the sample geometry. This figure is reprinted from Ref. [46]. © IOP Publishing. Reproduced with permission. All rights reserved.

level tunneling process would be subject to a large momentum mismatch [44]. However, this problem can be circumvented assuming impurity-assisted or phonon-mediated quasi-elastic inter-Landau-level scattering (QUILLS) [33, 45]. Notice that Eq. 1.2 yields the experimentally observed $B^{3/2}$-dependence shown in Fig. 1.4(b), but fails to correctly reproduce the dependence on the filling factor i. Moreover, if Eq. 1.2 is used to calculate the critical current density for the GaAs/Al_xGa_{1-x}As device shown in Fig. 1.3, one obtains $j_c \approx 36$ A/m (with $m^* = 0.07m_e$, where m_e is the electron mass), which is approximately two orders of magnitude too large when compared with the experimental value.

In general, the QUILLS model yields values for the critical field E_c which are much larger than those observed experimentally. As a result, the leading explanation for breakdown shifted to a thermal instability caused by the

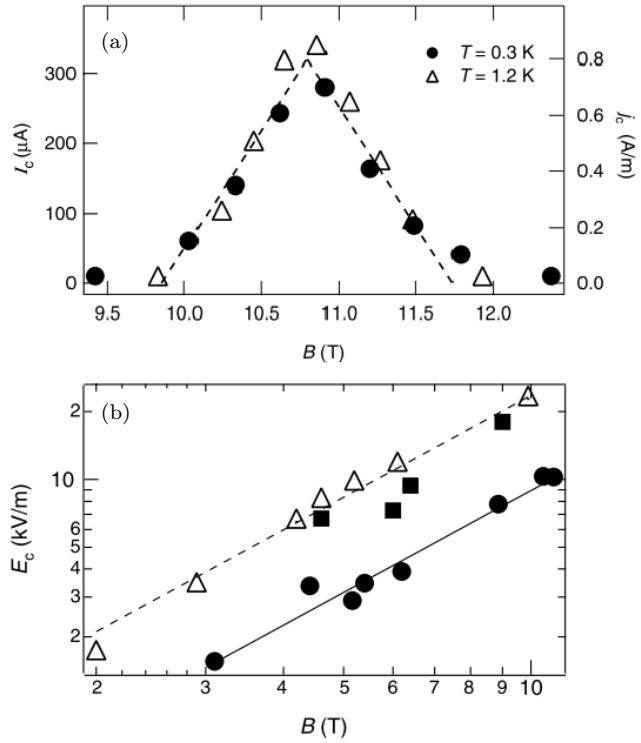

Figure 1.4: The magnetic-field dependence of the breakdown of the QHE. (a) Critical current $I_c = j_c W$ (with a sample width of $W = 400$ μm) as a function of the magnetic field B for filling factor $i = 2$. The dashed line is a guide to the eye. (b) Critical Hall field E_c at the plateau center as a function of the magnetic field B. Data on Hall-bar devices reported by different authors: • $W = 400$ μm for filling factor $i = 2, 4$ [74], ■ $W = 380$ μm for $i = 2$ [46], and △ $W = 400$ μm for $i = 2, 4$ [81]. The lines on the log-log plot have a slope of 3/2. Note that the apparent $B^{3/2}$-dependence does not depend on the filling factor i. Figures (a) and (b) are reprinted from Ref. [73].

imbalance between the energy gained by electrons in an electric field and the phonon relaxation [91]. This thermal instability is thought to eventually lead to an avalanche-type electron–hole pair multiplication, giving rise to a jump in the electron temperature of the QHE system [90] (a more detailed discussion is given in chapter 4). In this 'bootstrap electron heating' (BSEH) model the critical electric field is given by

$$E_{\mathrm{BSEH}} = \sqrt{\frac{2\hbar}{m^*\tau}}B, \tag{1.3}$$

where τ is the relaxation time over which the energy of the hot electrons is released to the lattice [90]. Notice that Eq. 1.3 is independent of the filling factor i. Moreover, Komiyama and Kawaguchi [90] argued that

$$1/\tau \approx B/(1\ \mathrm{T}) \times (1\ \mathrm{ns})^{-1}, \tag{1.4}$$

which would reproduce the observed $B^{3/2}$-dependence shown in Fig. 1.4(b). Using this approximation, the critical current density for the GaAs/Al_xGa_{1-x}As device shown in Fig. 1.3 becomes $j_c \approx 0.40$ A/m, which is surprisingly close to the experimental value.

The BSEH model, in general, gives good agreement with the experimentally observed breakdown values. Moreover, when comparing the critical current densities for the best performing GaAs devices (∼1 A/m [73, 141]) with graphene (∼10 A/m [2, 9]), graphene's better breakdown characteristics can be explained by its much shorter energy relaxation time τ consistent with the BSEH model [2, 9]. Nevertheless, a complete understanding of the breakdown phenomenon of the QHE is still missing, and the debate on the breakdown mechanism seems far from settled [2, 9, 55, 73, 90, 91, 127, 141, 198, 199], even after four decades of research into the QHE!

Having introduced the breakdown of the QHE, let us now turn to the subject of this thesis, i.e. the *breakdown of the quantum anomalous Hall effect* (QAHE). The hallmark of the QAHE is the dissipationless longitudinal transport accompanied by a quantized Hall resistance of h/e^2. This is similar to the QHE at filling factor $i = 1$ (cf. Eq. 1.1), although the underlying physics is very different [210], as will be explained in chapter 2. Moreover, the QAHE does not require the application of an external magnetic field, unlike the QHE.

In 2013, the QAHE was achieved in thin films of the topological insulator (TI) material $(Bi_xSb_{1-x})_2Te_3$ doped with the transition-metal ion Cr [30]. Soon after, full quantization was achieved in V-doped thin films in 2015 [32]. Interestingly, the QAHE was recently also realized in the intrinsic magnetic TI $MnBi_2Te_4$ [42], in $MnBi_2Te_4/Bi_2Te_3$ superlattices [41], as well as in twisted bilayer graphene [164] and $MoTe_2/WSe_2$ moiré heterobilayers [107]. This thesis focuses on

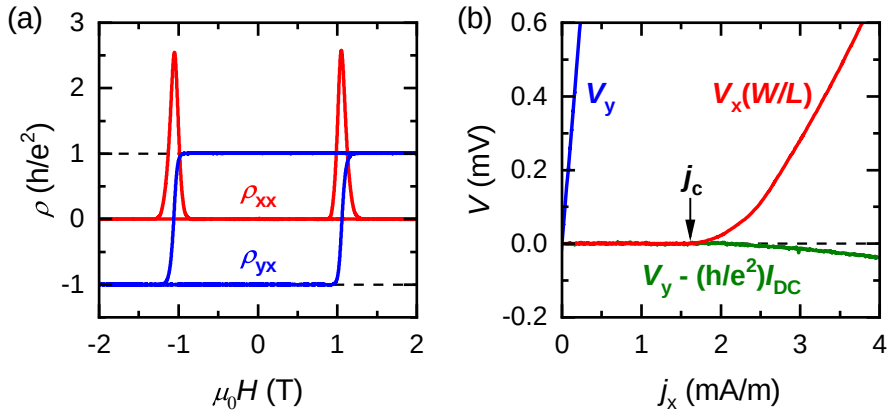

Figure 1.5: The quantum anomalous Hall effect (QAHE), measured in Hall-bar device A ($W = 100$ μm) at 10 mK. (a) The magnetic-field dependence of the longitudinal sheet and Hall resistance, ρ_{xx} and ρ_{yx}, respectively. The DC probe-current was 80 nA, which is less than the critical current for breakdown. (b) I-V characteristic at 0 T (after training the sample at +2 T to align all the magnetic domains), showing the current-induced breakdown of the QAHE. Above a current density of $\sim$1.6 mA/m, the longitudinal voltage V_x and the transverse voltage V_y show deviations from the ideal QAHE. Notice that V_x was normalized by the Hall-bar width W and voltage-contact spacing L for a fair comparison. The dashed lines in (a) and (b) are a guide to the eye.

the prototypical and most established QAH material, which relies on the substitutional doping of a TI with Cr or V. At low temperature ($\lesssim$ 20 K), spontaneous magnetization in these systems gives rise to a ferromagnetic (FM) ground state with an out-of-plane easy-axis [210]. The broken time-reversal symmetry (TRS) together with the non-trivial band topology of the system gives rise to a chiral dissipationless edge state, and consequently the quantization of the Hall resistance. Figure 1.5(a) shows the longitudinal sheet and Hall resistance, ρ_{xx} and ρ_{yx} respectively, as a function of the magnetic field for a V-doped $(Bi_xSb_{1-x})_2Te_3$ thin film grown as part of this thesis. ρ_{xx} is zero for all values of the magnetic field with the exception of a peak at the coercive field H_c, where the QAHE is lost over a narrow field range upon magnetization reversal. Similarly, ρ_{yx} shows a square hysteresis loop with a plateau transition between $+h/e^2$ and $-h/e^2$ at $\pm H_c$. Figure 1.5(b) shows the corresponding I-V characteristic for the QAH film. Above a current density of $\sim$1.6 mA/m, both the longitudinal voltage V_x and the transverse voltage V_y show deviations from

the ideal QAHE. The loss of the zero-resistance state marks the critical current density j_c for the breakdown of the QAHE. The breakdown mechanism, as well as the limitations it imposes on QAH systems, are the subject of this thesis and will be addressed in chapters 4 and 5.

The quantized Hall response of the QAHE could potentially replace the QHE as the reference standard of resistance [43]. The QHE requires very low temperatures, as well as the application of a high magnetic field. The latter is not needed for the realization of the QAHE, as the sample's remanent magnetization ensures the quantization at zero-applied magnetic field. This opens up the possibility to integrate the QAHE and Josephson effect into one low-temperature set-up, creating a quantum current generator in line with the new SI definition of the ampere [26, 43], see Fig. 1.2. The precise quantization of the QAHE has already been verified down to an error of about 10^{-6} in uniformly doped TI thin films [17, 50, 54], and down to 10^{-8} in magnetic heterostructures [132, 133]. However, the QHE is currently still unparalleled with an error of about 10^{-10} [40, 73], which is the consequence of the 2–3 order of magnitude lower current densities the QAHE can sustain before breakdown [Fig. 1.5(b)], as compared to the QHE [Fig. 1.3].

The QAHE is not only interesting because of its potential merits to the field of metrology; it also offers a promising platform for novel quantum phenomena [24], such as chiral topological superconductivity [145, 189]. When a QAH sample is proximitized by an s-wave superconductor (SC), the sample's edges are predicted to host chiral Majorana fermion modes [145]. A more detailed discussion will be given in chapter 2. Majorana fermions, which were proposed by the Italian physicist Ettore Majorana in 1937 [119], are spin-1/2 particles with the peculiar property of being their own antiparticle. If so-called Majorana zero modes, a 0D realization of these Majorana fermions, could be realized in a QAH-SC heterostructure [1, 13, 59], their non-Abelian braiding properties could potentially lead to the realization of topological qubits, paving the way to fault-tolerant quantum computation [85, 162].

The research objectives of this thesis are to identify the experimental parameters influencing the critical current density j_c for the breakdown of the QAHE, as well as to evaluate the consequences of breakdown for different measurement set-ups and geometries. Based on the dependencies of j_c on these parameters the most likely breakdown mechanism will be postulated for the QAHE.

The content of this thesis is structured into several chapters: Chapter 2 provides the reader with a concise theoretical background on (magnetic) topological insulators and the intriguing physics expected to occur in QAH-SC heterostructures, while chapter 3 gives an overview of the most important experimental techniques used in this thesis. In chapter 4, magneto-transport

measurements in multi-terminal Hall-bar devices are addressed in both local and nonlocal measurement geometries to gain insights into the current-induced breakdown mechanism of the QAHE. The detailed nonlocal transport data allow not only the dismissal of additional dissipative edge states contributing to the charge transport, but also the identification of the transverse electric field E_{yx} as the driving force for the breakdown. Moreover, electric-field-driven percolation of 2D charge puddles is proposed as the most likely cause of the abrupt onset of dissipation at the critical current density j_c, contrary to BSEH or QUILLS believed to cause the breakdown of the QHE. In chapter 5, the broken-down QAH state is investigated further by studying the second Fourier (or 'second harmonic') component of the AC resistance. The interplay between the 1D chiral edge state and the 2D surface state is shown to give rise to a nonreciprocal (diode-like) contribution to the measured longitudinal resistance. Moreover, the nonreciprocal response is studied for the first time near the current-induced breakdown point, deepening the understanding of the nonreciprocity in the QAHI system. Lastly, open research questions and a summary of the most important results of the thesis are given in chapter 6, while a brief outlook for QAH material systems is given in chapter 7.

Chapter 2

Theoretical Background

> *One shouldn't work on semiconductors, that is a filthy mess; who knows if they really exist!*
>
> Wolfgang Pauli

The Nobel prize in physics for 2016 was awarded to David J. Thouless, F. Duncan M. Haldane, and J. Michael Kosterlitz "for theoretical discoveries of topological phase transitions and topological phases of matter". Their seminal work ultimately lead to the discovery of topological insulators (TIs), which form the building blocks for the quantum anomalous Hall insulator (QAHI), covered in this chapter. The role of Coulomb disorder in compensated (magnetic) TI thin films will be addressed. It will be shown that Pauli's words hold true for these 'topological semiconductors' as well, where the long-range nature of the Coulomb interaction gives rise to the formation of electron and hole puddles in both their 2D and 3D band structures. Perhaps these issues will be overcome just as they were for semiconductors, opening up the possibility of another technological revolution. Lastly, the intriguing physics of a QAH heterostructure proximitized by an s-wave superconductor will be briefly discussed.

2.1 Topological Insulators

The continuum Dirac Hamiltonian in $2+1$ dimensions, the corresponding tight-binding lattice model, and the evaluation of the Chern number will be introduced in the context of the time-reversal invariant 2D topological insulator, i.e. the quantum spin Hall insulator (QSHI). It will become apparent that in essence a QSHI consists of two time-reversal copies of a QAHI, which will be useful when discussing the model Hamiltonian for magnetically doped topological insulators in section 2.2. The 3D topological insulators will be briefly discussed as well, before moving on to address the effect of Coulomb disorder in compensated TI crystals and thin films.

2.1.1 2D Topological Insulators

As a consequence of the nontrivial topology of the band structure of 2D-TIs, the insulating band gap has to close at the interface with an ordinary insulator (including the vacuum) [3], see Fig. 2.1. This gives rise to two counter-propagating, spin-polarized edge states, which lie inside the bulk band gap [16, 146]. These helical edge states form Kramers' pairs and time-reversal symmetry (TRS) is preserved in the system. As a result, the Hall conductance is zero. Moreover, the absence of elastic backscattering of the helical edge states gives rise to dissipationless edge transport (at least for distances smaller than

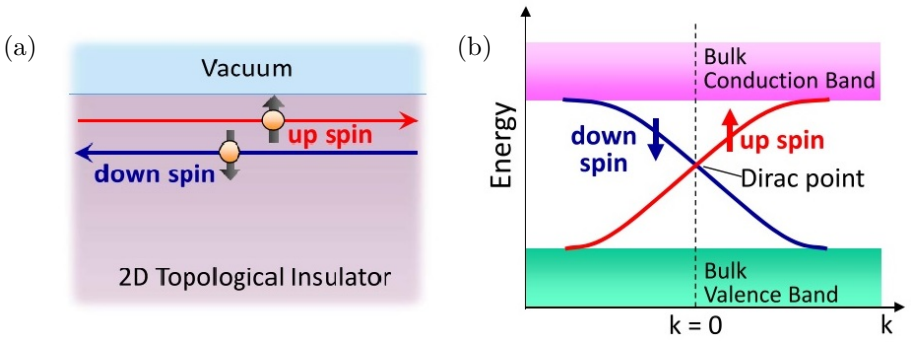

Figure 2.1: Illustration of the helical edge states of a 2D topological insulator in real space (a), and reciprocal space (b). The spin degeneracy is lifted for the energy dispersion of the edge state forming a 1D Dirac cone at the Γ-point. Figures (a) and (b) are reprinted with permission from Ref. [3]. © (2013) The Physical Society of Japan.

the inelastic mean-free-path) [93]. These transport phenomena are collectively known as the quantum spin Hall effect (QSHE), and were proposed to occur in graphene [80], as well as in semiconductors [15, 16, 38, 146]. Unfortunately, the gap opened by the spin-orbit interaction in graphene was shown to be of the order $\sim$1 μeV [122, 200], making the experimental observation of the QSHE in graphene unrealistic. However, Bernevig *et al.* predicted that the QSHE can be achieved in CdTe-HgTe-CdTe quantum wells (QWs) [15], which lead to its experimental realization in 2007 by König *et al.* [93].

The bulk energy bands of HgTe and CdTe (Γ_6 and Γ_8), as well as the subbands (E1 and H1), near the Γ-point are shown in Fig. 2.2. Note that the E1 subband is formed from the linear combination of $|\Gamma_6, m_j = \pm\frac{1}{2}\rangle$ and $|\Gamma_8, m_j = \pm\frac{1}{2}\rangle$ states, whereas the H1 subband is formed from $|\Gamma_8, m_j = \pm\frac{3}{2}\rangle$ states (see Ref. [15] for details). As shown in Fig. 2.2, CdTe has a normal band order with $\Gamma_6 > \Gamma_8$, whereas HgTe has an inverted band order with $\Gamma_6 < \Gamma_8$. For $d < d_c$, the QW is in the 'normal' regime, where the CdTe band order is predominant (E1 > H1). For $d > d_c$, on the other hand, the HgTe layer is thick and the QW is in the 'inverted' regime (E1 < H1). Hence, as the thickness of the HgTe QW is increased, the E1 and H1 subbands must cross at the critical thickness d_c, which turns out to be $\sim$6.3 nm [93].

The low-energy effective Hamiltonian near the Γ-point [15], where the band crossing between the subbands E1 and H1 occurs, is given by

$$H = \begin{bmatrix} H(k) & 0 \\ 0 & H^*(-k) \end{bmatrix}$$

$$H(k) = \varepsilon(k) + \sum_i d_i(k)\sigma_i \tag{2.1}$$

with the basis of $|\text{E1}\uparrow\rangle$, $|\text{H1}\uparrow\rangle$, $|\text{E1}\downarrow\rangle$, and $|\text{H1}\downarrow\rangle$, where $\uparrow$ and $\downarrow$ represent the spin up and down states, respectively. Here, σ_i are the Pauli matrices for spin, and

$$d_1 + id_2 = A(k_x + ik_y) \equiv Ak_+, \tag{2.2}$$

$$d_3 = M - B(k_x^2 + k_y^2), \tag{2.3}$$

$$\varepsilon(k) = C - D(k_x^2 + k_y^2), \tag{2.4}$$

where A, B, C, and D are material specific constants [15], with B being negative in HgTe QWs [93]. This model is called the Bernevig-Hughes-Zhang (BHZ) model, and shows that the QSH phase in HgTe QWs can be described by two copies, $H(k)$ and $H^*(-k)$, of the $(2+1)$-dimensional Dirac Hamiltonian (plus an $\varepsilon(k)$-term), where the form of $H^*(-k)$ is determined by TRS [15].

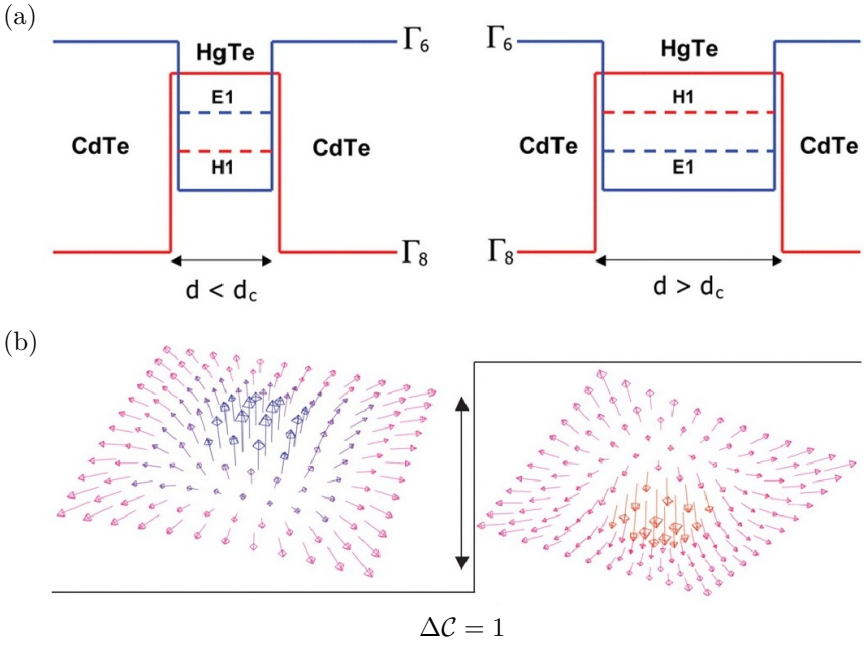

Figure 2.2: (a) Band diagram near the Γ-point for a CdTe-HgTe-CdTe heterostructure. The HgTe QW is in the normal regime $E1 > H1$ for $d < d_c$ and in the inverted regime $E1 < H1$ for $d > d_c$. (b) Schematic of the Meron configurations of the vector $\hat{\mathbf{d}} = \mathbf{d}(k)/|\mathbf{d}(k)|$ near the Γ-point. The change in Meron number $\Delta\mathcal{C}$ for the E1 and H1 subband crossing at d_c is exactly equal to 1. Figures (a) and (b) are taken from Ref. [15]. Reprinted with permission from AAAS.

At the critical thickness d_c, where the E1 and H1 subbands cross, the mass M in Eq. 2.3 changes sign between the two sides of the transition [15]. It is instructive to discuss the effect of the sign change of M on $H(k)$. When $H(k)$ is expressed in terms of the vector $\mathbf{d}(k) = [d_1(k), d_2(k), d_3(k)]^T$, the Chern number [144, 147] can be defined as

$$\mathcal{C} = \frac{1}{4\pi} \iint \hat{\mathbf{d}} \cdot \left(\frac{\partial \hat{\mathbf{d}}}{\partial k_x} \times \frac{\partial \hat{\mathbf{d}}}{\partial k_y} \right) dk_x dk_y. \tag{2.5}$$

where $\hat{\mathbf{d}} = \mathbf{d}(k)/|\mathbf{d}(k)|$, and the integral is taken over the first Brillouin zone (BZ). Note that the low-energy effective Hamiltonian describes only the band structure near the Γ-point; and is not on a lattice ($k_x, k_y \to \infty$). While it is *not* possible to determine the Chern number of the full system by analyzing only a

small part of the band structure in the BZ, it *is* possible to calculate the change in Chern number upon closing and reopening the gap by focusing only on the vicinity of the point where the transition happens [14]. Let us first consider the simple case of the continuum Dirac Hamiltonian $\mathbf{d}(k) = [Ak_x, Ak_y, M]^T$ up to linear[1] terms in k. Integrating Eq. 2.5 to infinity, yields the well-know result [14]:

$$\mathcal{C} = \frac{1}{2}\,\mathrm{sign}(M). \tag{2.6}$$

The unit vector $\hat{\mathbf{d}} = \mathbf{d}(k)/|\mathbf{d}(k)|$ with $\mathbf{d}(k) = [Ak_x, Ak_y, M]$ is shown as a function of k in Fig. 2.2(b) for $M > 0$ and $M < 0$. The $\hat{\mathbf{d}}$ vector has a Meron configuration (i.e. half of a Skyrmion) with $\hat{\mathbf{d}}$ pointing up or down at the origin ($d_3 = \pm M$), and with $\hat{\mathbf{d}}$ pointing in-plane and away from the origin for large values of k [14]. Hence, closing and reopening the gap, which corresponds to the sign-inversion of M, gives rise to a change in the Chern number by $\Delta\mathcal{C} = 1$. This means that the band crossing between the subbands E1 and H1 with increasing QW-thickness is a topological phase transition (see Fig. 2.2). However, by solely examining the continuum Dirac Hamiltonian, it is not possible to identify which regime, normal ($d < d_c$) or inverted ($d > d_c$), corresponds to the topologically nontrivial phase.

The Chern number is only an integer if the base manifold (the BZ) is compact, whereas for the continuum Dirac Hamiltonian the momentum runs over a noncompact manifold (i.e. the infinite Euclidean plane) [14]. Hence, in order to obtain a precise determination of the Chern number for the QSH system, it is instructive to consider a simple tight-binding model for the E1 and H1 subbands:

$$d_1 + id_2 = A\left[\sin(k_x) + i\sin(k_y)\right], \tag{2.7}$$

$$d_3 = -2B\left[2 - \frac{M}{2B} - \cos(k_x) - \cos(k_y)\right], \tag{2.8}$$

$$\varepsilon(k) = C - 2D\left[2 - \cos(k_x) - \cos(k_y)\right]. \tag{2.9}$$

This is identical[2] to the continuum Dirac Hamiltonian in Eqs. 2.2–2.4 when expanded around the Γ-point [14, 15]. The tight-binding model is fully gapped except for certain values of M at high-symmetry points in the BZ. Namely,

[1] In order to get the result shown in Eq. 2.6 the quadratic term $B(k_x^2 + k_y^2)$ of d_3 was not included. This quadratic term should be thought of as a correction near the Γ-point ($k = 0$), and hence would leads to an erroneous Chern number if integrated to infinity.

[2] Notice that the quadratic term $B(k_x^2 + k_y^2)$ of d_3 follows naturally from the Taylor expansion of the cosine near $k = 0$ in the tight-binding model (Eq. 2.8).

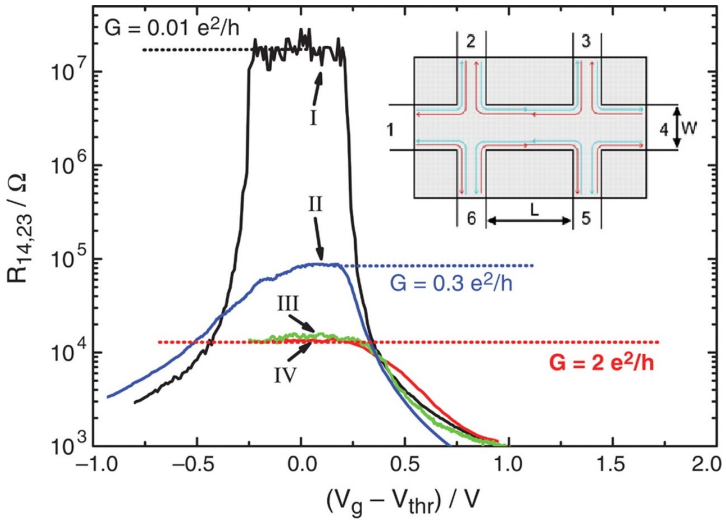

Figure 2.3: The first observation of the quantum spin Hall effect (QSHE). The four-terminal longitudinal resistance $R_{14,23} \equiv V_{23}/I_{14}$, measured at $T = 30$ mK in $B = 0$ T, is shown for several HgTe QW devices, in the normal ($d = 5.5$ nm, device I) and inverted regime ($d = 7.3$ nm, devices II, III, and IV) as a function of the normalized gate voltage ($V_g - V_{\mathrm{thr}}$), where V_{thr} corresponds to the voltage for which $R_{14,23}$ is largest. The inset shows the schematic of the gated Hall-bar device. The contacts are labeled 1 to 6, and the gray shaded region indicates the top-gate electrode. The red and blue arrows represent the counter-propagating, spin-polarized edge channels of the QSHI. The Hall-bar sizes are 20.0×13.3 μm^2 for devices I and II, 1.0×1.0 μm^2 for device III, and 1.0×0.5 μm^2 for device IV. This figure is taken from Ref. [93]. Reprinted with permission from AAAS.

the $(0,0)$ point becomes gapless at $M/2B = 0$, the $(0,\pi)$ and $(\pi,0)$ points become gapless at $M/2B = 2$, whereas the (π,π) point becomes gapless at $M/2B = 4$ (see Ref. [14] for details). Integrating this lattice model over the BZ yields: $\mathcal{C} = 0$ for $M/2B < 0$ and $\mathcal{C} = 1$ for $0 < M/2B < 2$, which are the experimentally relevant conditions with $M/2B = 2.02 \times 10^{-4}$ for the inverted regime at $d = 7$ nm, and $M/2B < 0$ for the normal regime [15]. Hence, the inverted band structure for $d > d_c \approx 6.3$ nm is the topologically nontrivial regime supporting the QSHE.

Until now, only the upper 2×2 block $H(k)$ of the low-energy effective Hamiltonian (Eq. 2.1) was considered. TRS dictates that $\mathcal{C}(H) = -\mathcal{C}(H^*)$; hence, the total Chern number of the system vanishes and so too does the Hall conductance $\sigma_{xy} = \mathcal{C}e^2/h$. However, in the QSH phase the charge current

flows through two counter-propagating 1D edge states [Fig. 2.1(a)], and their quantized $h/(2e^2)$ signature can be measured in two- and four-terminal transport measurements. Here, it is important to point out that each metal contact leads to the equilibration of the two helical edge channels with opposite spin, since the metal contacts themselves are not spin sensitive [93]. As a result, there will be a quantized voltage drop $h/(2e^2)I$, not only at the source and drain contacts, but at each metal contact.

Figure 2.3 shows the four-terminal longitudinal resistance $R_{14,23}$ as a function of the gate voltage for several QW devices. Here, the first index denotes the current probes (1–4), while the second index denotes the voltage probes (2–3). The Fermi level could be scanned through the bulk band gap for all QW devices, as evidenced by the low-resistance regions at large positive (n-type) and negative (p-type) gate voltages. Device I is in the normal regime with $d = 5.5$ nm ($< d_c \approx 6.3$ nm), whereas devices II, III, and IV have the inverted band structure with $d = 7.3$ nm. Inside the bulk gap, the conductance (denoted by 'G' in Fig. 2.3) is close to zero for device I, while for device III and IV it is very close to the quantized value $2e^2/h$ expected for two helical edge channels. Notice that the conductance of device III and IV does not scale with the width of the Hall-bar, which is consistent with the current flowing predominately through the 1D edge channels. For the large device II, the conductance is no longer quantized $G = 0.3e^2/h$, which indicates the inelastic mean-free-path l_{in} is in the range $1\ \mu\text{m} < l_{\text{in}} < 20\ \mu\text{m}$ at the measurement temperature of 30 mK.

2.1.2 3D Topological Insulators

The concept of a 2D-TI can be readily expanded to three dimensions, where the bulk-boundary correspondence leads to 2D surface states at the interface of the 3D-TI and an ordinary insulator [3], see Fig. 2.4(a). For time-reversal invariant 3D-TIs, the nontrivial band topology is protected by TRS and the spin degeneracy is lifted, giving rise to a 2D Dirac cone with helical spin polarization, as shown in Fig. 2.4(b). The 2D surface states can be described by the effective Hamiltonian

$$H(k) = v_F(k_y\sigma_x - k_x\sigma_y), \tag{2.10}$$

where v_F is the Fermi velocity and σ_i are again the Pauli matrices for spin [144, 147]. As seen from Eq. 2.10, the spin is locked perpendicular to the momentum. Moreover, this helical spin polarization prohibits elastic backscattering between the states at k and $-k$, as long as TRS is not broken. Figure 2.5(a-b) show the electronic band structure of the 3D-TI Bi_2Se_3 measured by angle-resolved photoemission spectroscopy (ARPES) [36]. The 2D surface state of Bi_2Se_3 shows an almost ideal Dirac cone with only slight convex hexagonal warping near

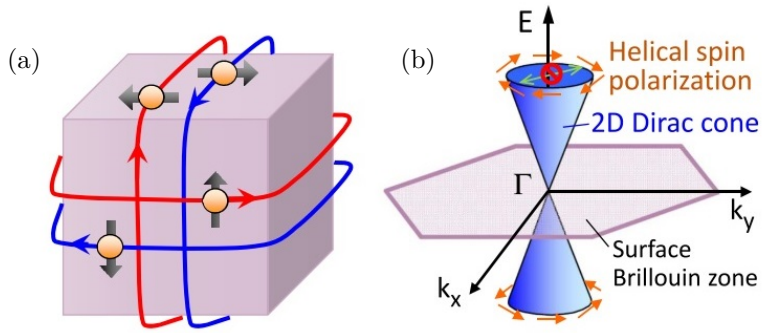

Figure 2.4: Illustration of the helical surface states of a 3D topological insulator in real space (a), and reciprocal space (b). The spin degeneracy is lifted for the energy dispersion of the surface state forming a 2D Dirac cone at the Γ-point. Figures (a) and (b) are reprinted with permission from Ref. [3]. © (2013) The Physical Society of Japan.

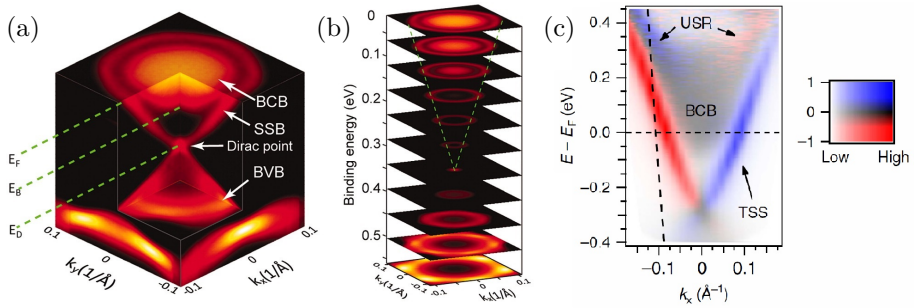

Figure 2.5: Electronic band structure of Bi_2Se_3 measured by ARPES. (a) The 2D surface-state band (SSB) forms a Dirac cone at the Γ-point, whereas the bulk conduction band (BCB) and bulk valence band (BVB) are well separated. The position of the Fermi level (E_F), the bottom of the BCB (E_B), and the Dirac point (E_D) are indicated. (b) The corresponding constant-energy contours of the band structure showing the SSB evolution to a hexagonal shape near E_B. (c) The spin-resolved pump-probe ARPES spectrum along the Γ-K direction, showing the spin texture of the topological surface state (TSS). The spectrum is plotted with a 2D color-scale, with the horizontal axis corresponding to the intensity and the vertical axis corresponding to the spin polarization along the k_y-axis. The spectrum also shows an unoccupied surface resonance (USR) with a helical spin texture opposite to that of the TSS. Figures (a-b) are taken from Ref. [36]. Reprinted with permission from AAAS. Figure (c) is taken from Ref. [78], and reproduced with permission from SNCSC.

the bulk conduction band. Figure 2.5(c) shows the spin-resolved pump-probe ARPES spectrum for the surface state of Bi_2Se_3 along the Γ-K direction [78]. The helical spin polarization is clearly visible with states at k_x and $-k_x$ showing a spin polarization along k_y and $-k_y$, respectively.

An in-depth discussion of all the properties of 3D (and 2D) TIs, as well as the Z_2 topological classification, falls outside the scope of this thesis, and the reader is directed to Refs. [3, 14, 144, 147, 196] for a comprehensive review of the topic. Before moving to the next section, it is interesting to remark that ever since the early experimental works on TIs [66, 67, 93, 131, 160, 172], the field of TI materials has grown exponentially. While a topological band structure was initially thought to be a peculiar exception to the rule, Bernevig *et al.* have demonstrated in recent years that 52.65% of all known nonmagnetic materials are topological at the Fermi level, whereas 87.99% contain at least one topological band in their band structure [23, 177, 179]. Of course only very few materials will show such a clean topological phase as for instance Bi_2Se_3 in Fig. 2.5. The inverted band gaps can be very small, or the topological surface states could be masked by a large number of trivial surface or bulk bands at the Fermi level. The (re)discovered 'topologically derived surface states' in Au and other noble metals [195] are a good example of this omnipresence of topological bands in nature. In summary, it is fair to say that band topology constitutes a new paradigm in condensed matter physics, which will inspire researchers for years to come.

2.1.3 Charge Compensation & Puddles

Until now, the band structures of 2D and 3D TIs were addressed without paying much attention to the position of the Fermi level E_F. Returning to the surface states of Bi_2Se_3 shown in Fig. 2.5, one can see that E_F lies deep in the bulk conduction band. This is certainly beneficial for ARPES which probes the occupied electronic states, and hence will resolve the 2D Dirac cone of Bi_2Se_3 across the full bulk band gap (without the need for surface doping or pump-probe techniques). However, the bulk bands will dominate the electrical conductivity in magneto-transport measurements masking the contribution of the 2D surface states, unless E_F lies inside the bulk band gap. In fact, the binary chalcogenide TI materials – Bi_2Se_3, Bi_2Te_3, and Sb_2Te_3 – always show a large bulk conductivivity due to charge carriers stemming from naturally occurring crystalline defects.

In order to tune E_F into the bulk band gap, and hence obtain 'bulk-insulating' TIs, a band engineering approach relying on the ternary compound $(Bi_xSb_{1-x})_2Te_3$ was proposed [92, 213]. Since Bi_2Te_3 and Sb_2Te_3 have the

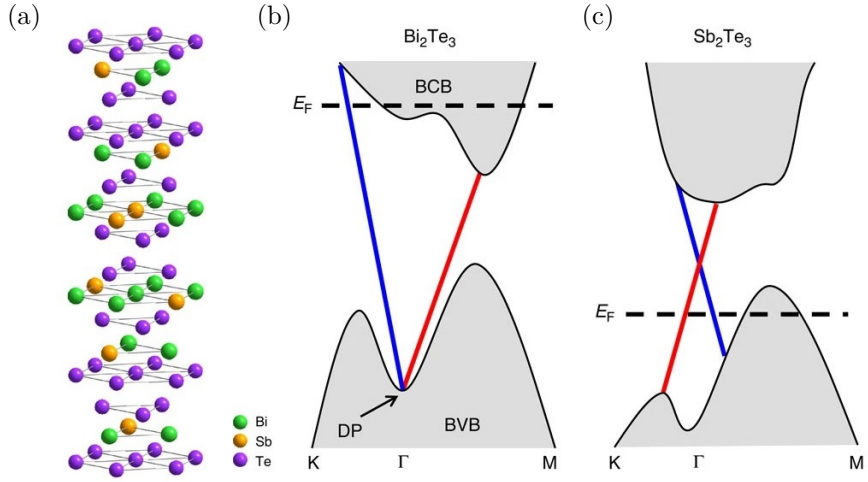

Figure 2.6: (a) The tetradymite crystal structure of the topological insulator $(Bi_xSb_{1-x})_2Te_3$. The Bi and Sb atoms occupy random cation positions. (b-c) The schematic band structure of pure Bi_2Te_3 (b) and Sb_2Te_3 (c). The helical surface states are represented by red and blue lines. For pure Bi_2Te_3 the Dirac point (DP) is buried in the bulk valence band (BVB), whereas for Sb_2Te_3 the DP lies within the bulk band gap. Hence, by fine-tuning the Bi/Sb composition ratio in $(Bi_xSb_{1-x})_2Te_3$ charge compensation can be achieved, while simultaneously moving the Dirac point position into the bulk band gap. Figures (a-c) are taken from Ref. [213], and reproduced with permission from SNCSC.

same crystal structure with close lattice constants [211], the ternary compound $(Bi_xSb_{1-x})_2Te_3$ is stable over the full composition range x [92, 213]. Figure 2.6(a) shows the crystal structure of $(Bi_xSb_{1-x})_2Te_3$ with Bi and Sb randomly occupying the cation positions, while Figs. 2.6(b-c) show the schematic band structures of pure Bi_2Te_3 and Sb_2Te_3. For Bi_2Te_3, E_F lies in the bulk conduction band due to the n-type bulk carriers induced by Te vacancies [213]. For Sb_2Te_3, on the other hand, the p-type bulk carriers induced by Sb–Te anti-site defects cause E_F to lie in the bulk valence band [213]. Moreover, for Bi_2Te_3 the Dirac point is buried in the bulk valence band, whereas for Sb_2Te_3 it lies within the band gap. As shown in Ref. [213] for thin films and in Ref. [92] for bulk crystals and flakes, one can simultaneously achieve charge compensation and tune the Dirac point position by changing the Bi/Sb composition ratio. In principle, this band engineering approach via isostructural (and isovalent) alloying can be extended to ternary compounds, e.g. $(Bi_xSb_{1-x})_2(Te_ySe_{1-y})_3$ [152, 161]. However, care needs to be taken to avoid a topological phase transition to the trivial phase, e.g. pure Sb_2Se_3 is topologically trivial [211].

The problem of the high concentration of n-type (Donor, N_D^+) and p-type (Acceptor, N_A^-) crystalline defects in $(Bi_xSb_{1-x})_2Te_3$ might seem solved now. Namely, the degree of charge compensation $K = N_A^-/N_D^+$ can be tuned to $K = 1$ (i.e. 'perfect compensation') by simply varying the Bi/Sb composition ratio. For $K = 1$, E_F lies in the middle of the bulk band gap and the most insulating state for the TI is realized [169]. However, it is important to consider the effect of the random spatial distribution of the charged impurities on both the bulk and surface properties of 3D-TIs.

For perfect compensation ($K = 1$), the donors give their electrons to the acceptors, resulting in positively charged empty donors and negatively charged occupied acceptors [20]. As a result, the average concentration of electrons in the bulk ($n = N_D^+ - N_A^-$) vanishes, and the random spatial fluctuations of N_A^- and N_D^+, i.e. the spatial charge fluctuations, are poorly screened due to the limited amount of free charge carriers [169]. In a volume of size R^3, these random fluctuations lead to an uncompensated charge[3] of $\sim e\sqrt{N_{\text{def}}R^3}$ with $N_{\text{def}} = N_A^- = N_D^+$ for $K = 1$, and a Coulomb potential of $\sim e^2\sqrt{N_{\text{def}}R^3}/(4\pi\varepsilon_0\varepsilon R)$, where ε is the dielectric constant [20]. Hence, the fluctuations in the Coulomb potential grow as $\sim\sqrt{R}$, and will bend the conduction and valence band edges. The potential fluctuations will, in some regions, reach an amplitude of $E_g/2$ (i.e. half the bulk band gap), causing the band edges to cross E_F. This results in the creation of electron and hole puddles [see Fig. 2.7(a)], which in turn nonlinearly screen the random potential [169]. The characteristic length scale for this process is given by

$$R_p = \left(\frac{E_g}{E_{\text{def}}}\right)^2 \frac{d_{\text{def}}}{8\pi}, \tag{2.11}$$

where $d_{\text{def}} = N_{\text{def}}^{-\frac{1}{3}}$ is the average defect separation and E_{def} is the Coulomb interaction between neighboring defects [20, 167]. Assuming $E_g = 0.3$ eV, $N_{\text{def}} = 10^{20}$ cm^{-3}, and $\varepsilon = 200$ [20], the characteristic length scale becomes $R_p \approx 690$ nm. The distance R_p is related to the average puddle size, as shown in Fig. 2.7(a), and is much larger than $d_{\text{def}} \approx 2.2$ nm, meaning we are dealing with a long-range potential.

At relatively high temperatures T, the resistivity ρ of 3D-TI crystals is dominated by the thermal activation of bulk carriers:

$$\rho = \rho_0 \exp\left(\frac{\Delta_a}{k_B T}\right), \tag{2.12}$$

[3]The uncompensated charge makes a random walk in one-dimension over the integer numbers $\mathbb{Z}$. Hence, the expected 'translation distance' after x steps is of the order of $\sqrt{x}$.

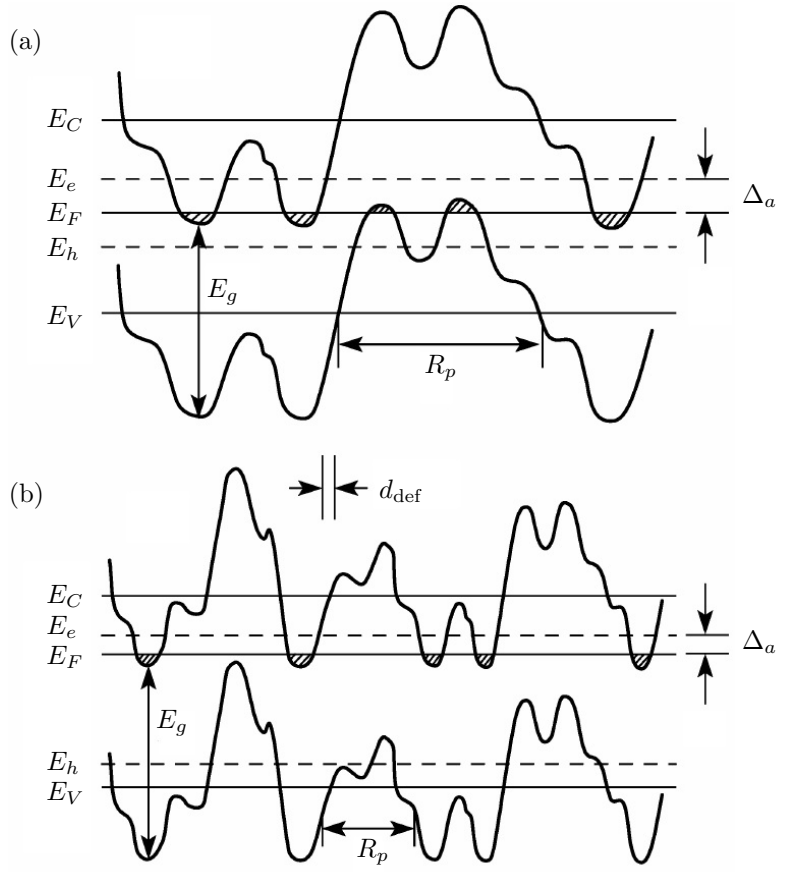

Figure 2.7: Schematic of the 3D real-space band structure of a completely compensated ($K = 1$) TI crystal (a), and a strongly compensated ($1 - K \ll 1$) TI crystal (b). The Fermi level E_F, as well as the unperturbed conduction band bottom E_C and valence band top E_V, are represented by the solid straight lines. The meandering lines, on the other hand, represent the deformed band edges in the presence of the long-range Coulomb potential, resulting from the random spatial fluctuations of the charged impurities. The electron and hole percolation levels, E_e and E_h, are shown by the dashed lines. The shaded regions indicate the electron and hole charge puddles. The size of the characteristic length scale R_p, average defect separation d_{def}, bulk band gap E_g, and activation energy Δ_a are shown by the arrows. Figures (a) and (b) are taken from Ref. [169], and reproduced with permission from SNCSC.

where Δ_a is the activation energy, and k_B is the Boltzmann constant. Naively, one would expect $\Delta_a = E_g/2$. However, as shown in Fig. 2.7(a), Δ_a is significantly smaller than $E_g/2$. In fact, Skinner *et al.* predicted $\Delta_a \approx 0.15E_g$ for $K = 1$ [167], which is consistent with the small activation energies measured in transport experiments [152]. These small activation energies can be understood as the electrons and holes inside the puddles being thermally excited to their corresponding percolation levels (E_e and E_h in Fig. 2.7) in the conduction and valence band, rather than electrons from the valence band being thermally excited to the conduction band [169]. In other words, the thermal energy $k_\mathrm{B}T$ causes electrons to hop between the nearest-neighbor sides at the Fermi level, i.e. between neighboring puddles.

Figure 2.7(b) shows a schematic of the 3D band structure of an n-type TI crystal close to perfect compensation ($1 - K \ll 1$). As $1 - K$ increases, the average concentration of electrons $n = N_D^+ - N_A^-$ ($\ll N_D^+$) increases as well, resulting in better screening of the Coulomb potential. The Fermi level E_F will move towards higher energy, causing the hole puddles to shrink and eventually disappear, but the electron puddles remain [169]. Moreover, as E_F increases, the activation energy Δ_a will decrease. Chen *et al.* predicted that $\Delta_a \approx 0.3(E_C - E_F)$ for n-type crystals and $\Delta_a \approx 0.3(E_F - E_V)$ for p-type crystals close to perfect compensation ($1 - K \ll 1$) [35].

At sufficiently low temperatures, the electrons and holes can hop or tunnel directly between the puddles, and the activated transport gives way to a variable-range-hopping (VRH) temperature dependence of the resistance [169]. This crossover was also observed experimentally [152], giving further evidence of the puddle physics in TI crystals. Moreover, by comparing the optical and electrical conductivity, Borgwardt *et al.* clearly demonstrated the presence of 3D puddles in the bulk-insulating TI crystal $BiSbTeSe_2$ at low temperatures, as well as their disappearance ('evaporation') with increasing temperature [20].

It is important to comment on the effect of Coulomb disorder on the surface potential as well. Close to the surface of the TI crystal, the Coulomb potential is strongly screened by the metallic surface states. As a result, the amplitude of the potential fluctuations might not reach $E_g/2$, suppressing the formation of 3D charge puddles near the surface [19, 168]. However, the screening by the metallic surface states is achieved by the redistribution of the Dirac-like charge carriers, which results in fluctuations of the surface potential (i.e. E_F versus the Dirac-point position). Scanning tunneling microscopy (STM) experiments revealed surface potential fluctuations of ∼8–14 meV in compensated $BiSbTeSe_2$ crystals over a characteristic length scale of 40–50 nm [86]. Since the surface states are gapless (as long as TRS is preserved), any finite variation of the surface potential will lead to the creation of 2D electron and hole puddles on the TI surface.

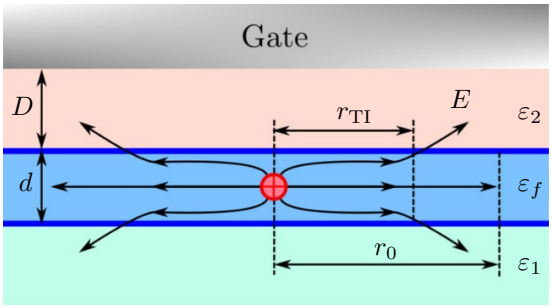

Figure 2.8: Schematic of the electric field lines emanating from a positively charged impurity inside a TI thin film with thickness d and dielectric constant ε_f. If $\varepsilon_f \gg (\varepsilon_1 + \varepsilon_2)/2$, the electric field E channels through the high-ε film for a distance r_{TI} before escaping into the low-ε environment. For comparison, $r_0 \approx \frac{\varepsilon_f}{\varepsilon_1+\varepsilon_2} d$ indicates the larger distance electric field lines would travel before escaping a topologically trivial film, due to the absence of the screening provided by the metallic surface states. Reprinted figure with permission from Ref. [69].

Lastly, one might naively expect that the Coulomb disorder plaguing TI crystals, disappears when working with TI thin films instead. Indeed, the defect concentration for a film with thickness d would be small ($N_{\mathrm{def}}d$). Moreover, for sufficiently thin films the potential fluctuations in the bulk are screened simultaneously by the metallic surface states on the top and bottom surfaces. However, Huang *et al.* recently showed that due to the large dielectric constant of TI materials relative to the low-dielectric environments of typical device architectures (see Fig. 2.8), the electric field lines emanating from charged defects are trapped inside the TI film for a distance r_{TI} before escaping outside [69]. As a result, the fluctuations of the Coulomb potential decay slowly in space, leading to significant fluctuations of the surface potential even for small defect concentrations $N_{\mathrm{def}}d$ [69]. For thicknesses as small as several nanometers, Huang *et al.* predicted surface fluctuations of tens of meV, which are values comparable to those found on the surfaces of TI crystals [69].

2.2 Magnetic Topological Insulators

In this section, the role of an out-of-plane magnetic field or magnetization on the 2D surface states of a TI thin film will be discussed, and the realization of the QAH phase in a magnetically doped TI in the presence of significant charge and magnetic disorder will be addressed.

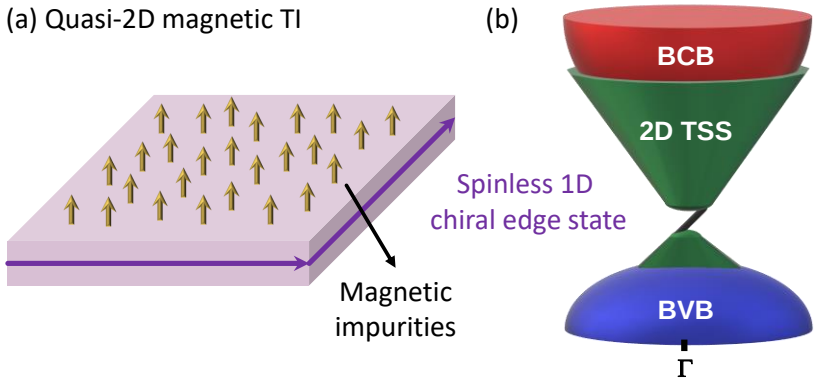

Figure 2.9: Illustration of a quantum anomalous Hall insulator (QAHI). (a) A thin slab of a magnetic TI can be considered as a quasi-2D material as the 3D bulk conduction band (BCB) and bulk valence band (BVB) are well separated in energy, and the topological surface states (TSS) on the size surfaces gap out due to the confinement effect (see section 4.9 for details). The spontaneous magnetization of the magnetic impurities, represented by the yellow arrows, break time-reversal symmetry (TRS) on the top and bottom surface. (b) Illustration of the energy spectrum of a QAHI. The 2D TSS on top and bottom surface are gapped due to broken TRS, but this exchange gap closes at the sample's edges where the chiral edge state connects the upper and lower branches.

2.2.1 The Quantum Anomalous Hall Effect

The QAHE is realized in thin films of magnetically doped TIs, where the combined effect of broken TRS on the top and bottom surface gives rise to a spinless chiral 1D edge state, see Fig. 2.9. To understand the underlying physics, it is instructive to discuss the low-energy effective Hamiltonian describing the TI system and include an exchange field M along the z-axis to represent the ferromagnetic (FM) ordering of the magnetic dopants. Note that in a 3D-TI Eq. 2.10 describes the topological surface state on the top surface, which can be rewritten as

$$H_{\text{Top}} = v_F(k_y\sigma_x - k_x\sigma_y) = \begin{bmatrix} 0 & iv_Fk_- \\ -iv_Fk_+ & 0 \end{bmatrix}, \tag{2.13}$$

using $k_\pm = k_x \pm ik_y$. Similarly, the bottom surface hosts a surface state described by

$$H_{\text{Bottom}} = -v_F(k_y\sigma_x - k_x\sigma_y) = \begin{bmatrix} 0 & -iv_Fk_- \\ iv_Fk_+ & 0 \end{bmatrix}, \tag{2.14}$$

where the minus sign ensures the spatial inversion-symmetry relation between the top and bottom surface. The 3D bulk conduction and valence band [Fig. 2.9(b)] are well separated and not considered in this low-energy model. Now, the 4×4 effective Hamiltonian for the 2D system [188, 210], can be written as

$$H_{\mathrm{SS}} + H_{\mathrm{Zeeman}} = \begin{bmatrix} 0 & iv_F k_- & m_k^* & 0 \\ -iv_F k_+ & 0 & 0 & m_k^* \\ m_k & 0 & 0 & -iv_F k_- \\ 0 & m_k & iv_F k_+ & 0 \end{bmatrix} + \begin{bmatrix} gM & 0 & 0 & 0 \\ 0 & -gM & 0 & 0 \\ 0 & 0 & gM & 0 \\ 0 & 0 & 0 & -gM \end{bmatrix}, \tag{2.15}$$

with the basis $|t\uparrow\rangle$, $|t\downarrow\rangle$, $|b\uparrow\rangle$, and $|b\downarrow\rangle$, where t, b denotes the surface states on the top and bottom surfaces, while $\uparrow$, $\downarrow$ represents the spin up and down states, respectively. Note that tunneling between the top and bottom surface states is allowed via the mass term m_k, which can be expanded up to second order[4] as $m_k = m_0 + B(k_x^2 + k_y^2)$. H_{Zeeman} describes the Zeeman splitting due to the exchange field $\pm gM$, where g is the effective g-factor.

It is convenient to rewrite the Hamiltonian (Eq. 2.15) in terms of the symmetric and antisymmetric combinations of the surface states on the top and bottom surfaces [188, 210], i.e. $|\pm\uparrow\rangle = (|t\uparrow\rangle \pm |b\uparrow\rangle)/\sqrt{2}$ and $|\pm\downarrow\rangle = (|t\downarrow\rangle \pm |b\downarrow\rangle)/\sqrt{2}$, which yields

$$\begin{aligned} \tilde{H}_{\mathrm{SS}} + \tilde{H}_{\mathrm{Zeeman}} &= \begin{bmatrix} m_k + gM & iv_F k_- & 0 & 0 \\ -iv_F k_+ & -m_k - gM & 0 & 0 \\ 0 & 0 & m_k - gM & -iv_F k_+ \\ 0 & 0 & iv_F k_- & -m_k + gM \end{bmatrix} \\ &= \begin{bmatrix} h_k + gM\sigma_z & 0 \\ 0 & h_k^* - gM\sigma_z \end{bmatrix} \\ &= \begin{bmatrix} \tilde{H}_+(k) & 0 \\ 0 & \tilde{H}_-(k) \end{bmatrix}, \end{aligned} \tag{2.16}$$

with the new basis $|+\uparrow\rangle$, $|-\downarrow\rangle$, $|+\downarrow\rangle$, and $|-\uparrow\rangle$. The expression can be written more concisely using $h_k = m_k\sigma_z + v_F(k_y\sigma_x - k_x\sigma_y)$.

[4] Notice that the mass term m_k differs slightly from the mass term in the BHZ model (Eq. 2.3) which has a minus sign in front of B.

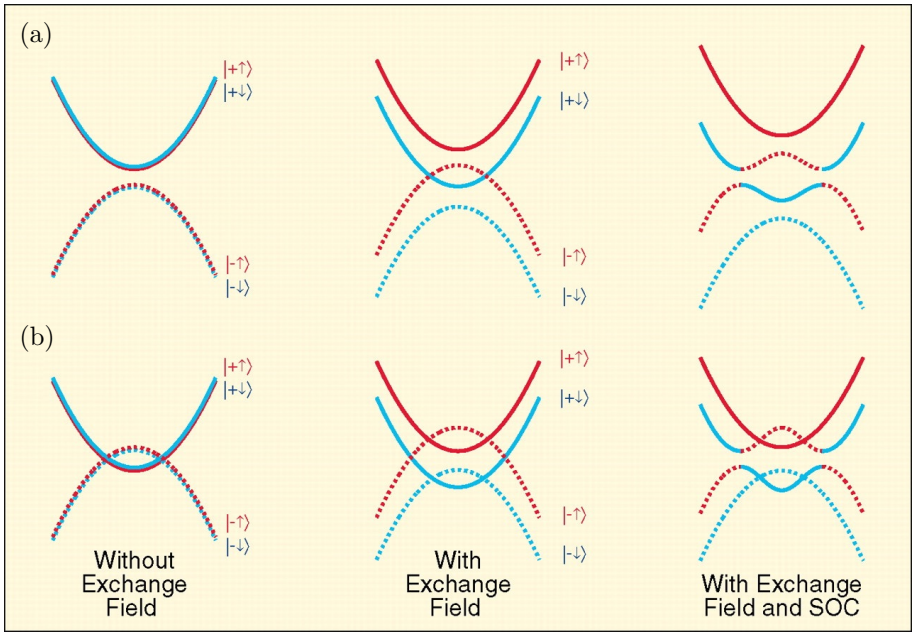

Figure 2.10: Band diagram for a QAHI, showing the evolution of the subbands with increasing exchange field. The solid (dashed) lines denote the subbands with even (odd) parity at the Γ-point, while the red (blue) color denotes the spin up (down) electrons. (a) The initial subbands are not inverted ($m_0 B > 0$). A strong enough exchange field causes one pair of subbands (red dashed and blue solid line) to invert. (b) The initial subbands are already inverted ($m_0 B < 0$). The exchange field lifts the band inversion in one pair of subbands (red solid and blue dashed line) and increases the band inversion in the other pair (red dashed and blue solid line). Lastly, the degeneracy at the band crossings is lifted by turning on the spin-orbit coupling (SOC) interaction, giving rise to an insulating state with a topologically nontrivial band structure characterized by a finite Chern number. This figure is taken from Ref. [210]. Reprinted with permission from AAAS.

Notice that Eq. 2.16 is similar to the BHZ model discussed in section 2.1.1. Namely, the system will be in the QSH phase if $m_0 B < 0$ [210]. However, whether the system is initially in the topologically nontrivial phase or not, a strong enough exchange field $gM\sigma_z$ will change the Chern number of one of the two blocks of the effective Hamiltonian realizing the QAH phase [210], as shown in Fig. 2.10.

Suppose the four-band system is initially in the topologically trivial phase [$m_0 B > 0$, Fig. 2.10(a)], the exchange field will push the two subbands of the upper block $\tilde{H}_+(k)$ farther apart, while inducing a band inversion between the two subbands of the lower block $\tilde{H}_-(k)$. If the system, on the other hand, is initially in the QSH phase [$m_0 B < 0$, Fig. 2.10(b)], the band structure of both blocks are inverted. In this case, the exchange field will undo the band inversion between the two subbands of the upper block $\tilde{H}_+(k)$, while further increasing the band inversion of the lower block $\tilde{H}_-(k)$. Hence, in both cases the upper (lower) block acquires a (non)trivial band structure. Obviously, the situation is reversed for the opposite magnetization direction.

Here, it is prudent to point out the importance of the fact that the realization of the QAH phase is *independent* of the underlying topology of the 2D system (QSHI or trivial). Namely, Liu *et al.* showed that the crossover regime from a 3D-TI to 2D-TI (with QSHE) occurs in an oscillatory fashion as a function of the layer thickness, alternating between topologically trivial and nontrivial 2D phases [114]. On the other hand, the growth of thin films of Cr/V-doped $(Bi_xSb_{1-x})_2Te_3$, the prototypical QAH material system, is always accompanied by considerable roughness [cf. Fig. 3.5(b)]. Hence, if the underlying topology of the 2D system would have been important, the realization of an uniform QAH phase throughout the whole thin film of Cr/V-doped $(Bi_xSb_{1-x})_2Te_3$ might have been impossible. Details on the growth of QAH thin films will be given in chapter 3.

Next, let us rewrite the Hamiltonian in Eq. 2.16 in term of the Pauli matrices:

$$\tilde{H}_\pm = v_F(k_y\sigma_x \mp k_x\sigma_y) + (m_k \pm gM)\sigma_z = \sum_i d_{\pm,i}(k)\sigma_i. \tag{2.17}$$

However, in order to get a better understanding of the topology of $\tilde{H}_\pm$, and to show that the Chern number of the blocks can indeed change for sufficiently large exchange fields, it is better to consider the corresponding tight-binding model for the QAHE [146]:

$$d_{\pm,1} + id_{\pm,2} = v_F\left[\sin(k_y) \mp i\sin(k_x)\right], \tag{2.18}$$

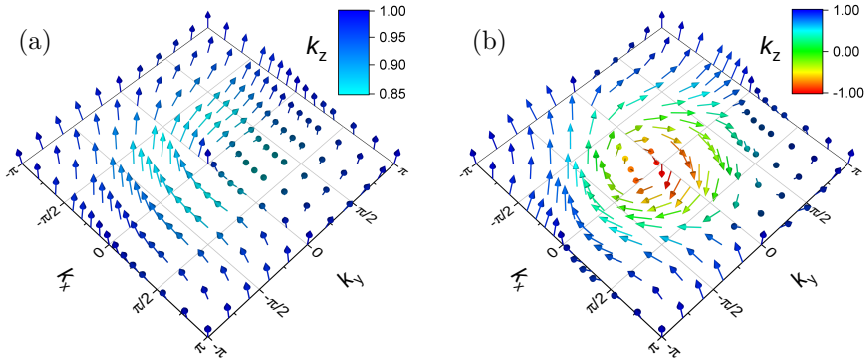

Figure 2.11: The configuration of $\hat{\mathbf{d}}_+ = \mathbf{d}_+/|\mathbf{d}_+|$ in the first Brillouin zone with $v_F = 1$, $|m_0 + gM| = 1$, and $B = 0.5$. The vector $\hat{\mathbf{d}}_+$ acquires a trivial (zero) winding number for $m_0 + gM > 0$ (a), whereas a Bloch-type Skyrmion configuration is obtained for $m_0 + gM < 0$ (b). The color scale shows the amplitude along the k_z-direction.

$$d_{\pm,3} = 2B\left[2 + \frac{m_0 \pm gM}{2B} - \cos(k_x) - \cos(k_y)\right]. \tag{2.19}$$

Notice that this tight-binding model for $\tilde{H}_\pm$ is identical to the tight-binding model of the QSHI (Eqs. 2.7–2.8) up to a rotation.[5] In the following we will take $B > 0$. Figure 2.11 shows the configuration of $\hat{\mathbf{d}}_+ = \mathbf{d}_+/|\mathbf{d}_+|$ in the first Brillouin zone. It is immediately clear from the figure, that for $m_0 + gM > 0$ the winding number is trivial [Fig. 2.11(a)], while for $m_0 + gM < 0$ the vector $\hat{\mathbf{d}}_+$ has a Skyrmion configuration [Fig. 2.11(b)].

Using Eq. 2.5, the Chern number of $\tilde{H}_\pm(k)$ is found to be either ∓ 1 or 0, depending on whether the Dirac mass is inverted ($m_0 \pm gM < 0$) or not ($m_0 \pm gM > 0$) at the Γ-point [188]. The total Chern number of the system[6]

[5] Notice that Eqs. 2.18–2.19 for the QAHE give rise to a Bloch-type Skyrmion configuration (see Fig. 2.11), whereas Eqs. 2.7–2.8 for the QSHE define a Néel-type Skyrmion configuration.

[6] In principle, the total Chern number in Eq. 2.20 for the tight-binding model (Eqs. 2.18–2.19) has an upper-limit given by the gap closure at the $(0, \pi)$ and $(\pi, 0)$ points for $(m_0 \pm gM)/2B = -2$. However, Wang *et al.* showed that higher energy bands need to be considered for large exchange fields [186].

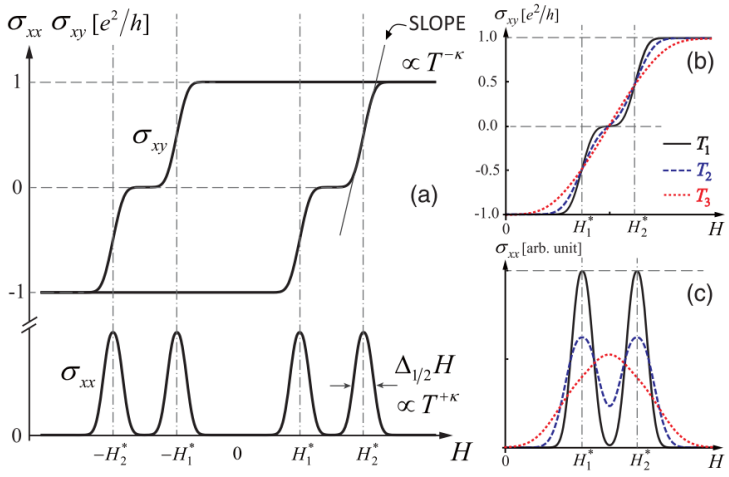

Figure 2.12: Magnetic-field dependence of σ_{xy} and σ_{xx}. (a) Sketch of σ_{xy} and σ_{xx} as a function of the applied magnetic field H. The hysteresis loop of σ_{xy} shows a zero-conductance-plateau, while σ_{xx} shows two peaks around the coercive field. (b) Temperature dependence of the zero-conductance-plateau $\sigma_{xy} = 0$ with $T_1 < T_2 < T_3$. (c) The corresponding curves for σ_{xx}. Reprinted figure with permission from Ref. [188]. © Copyright (2014) by the American Physical Society.

can than be summarized as

$$\mathcal{C} = \begin{cases} gM/|gM|, & \text{for } |gM| > |m_0| \\ 0, & \text{for } |gM| < |m_0| \end{cases}. \tag{2.20}$$

Hence, the Hall conductance $\sigma_{xy} = \mathcal{C}e^2/h$ is quantized and depends only on the magnetization direction as long as the exchange field gM is large enough to change the band ordering of $\tilde{H}_{\pm}(k)$. Note that the Chern number changes by 1 at $gM = \pm m_0$, which can give rise to a pronounced zero-conductance-plateau in σ_{xy} at the coercive field H_c for thin QAH films with a sizable hybridization gap m_0 [82, 95], see Fig. 2.12. However, the QAHI films used in this thesis are rather thick (∼8 nm), and hence did not show such a zero-conductance-plateau.

A Chern number of $\mathcal{C} = \pm 1$ implies the existence of a 1D chiral gapless edge state at the boundary of the QAHI and an ordinary insulator (including the vacuum), see Fig. 2.9(b). Let us focus on $\tilde{H}_{-}(k)$ which is topological for $gM > m_0$, and assume the edge of the QAHI is perpendicular to the y-direction. The localized wave-function of the chiral edge state along the y-direction can then be found

by solving the eigenvalue equation:

$$[(m_0 - B\partial_y^2 - gM)\sigma_z - iv_F\sigma_x\partial_y]\psi(y) = 0, \tag{2.21}$$

which yields:

$$\psi(y) = C\left(e^{-\lambda_+ y} - e^{-\lambda_- y}\right)(i|+\downarrow\rangle + |-\uparrow\rangle), \tag{2.22}$$

$$\lambda_\pm = \frac{v_F \pm \sqrt{v_F^2 + 4B(m_0 - gM)}}{2B}, \tag{2.23}$$

where C is a normalization factor [214]. Notice that the wave-function $\psi(y)$ of the chiral edge mode consists of an equal superposition of $|+\downarrow\rangle$ and $|-\uparrow\rangle$, and hence is *spinless*. Surprisingly, this means that the chiral edge state of the QAH phase in a magnetic 3D-TI has no spin polarization. Only when the inversion symmetry between the top and bottom surfaces is broken, does the edge state obtain a small spin polarization along the in-plane y-direction [214].

Lastly, since the QSHI consists of two spin-polarized, time-reversal copies of the QAHI,[7] it begs the question: "Why has the QAHE not been realized in magnetically doped HgTe QWs?". The QAH phase has indeed been proposed for $Hg_{1-x}Mn_xTe$ QWs [112]. Experimentally, however, Mn doping leads to paramagnetism,[8] rather than ferromagnetism. That being said, Shamim *et al.* showed that applying an out-of-plane magnetic field of only ∼50–85 mT to $Hg_{1-x}Mn_xTe$ QWs with the inverted band order can induce an $i = -1$ quantum Hall plateau (cf. Eq. 1.1 with i the filling factor) in the transverse resistance, depending on the position of the Fermi level [165]. The underlying physics, however, is very different from the QAHE.[9]

2.2.2 Magnetic Disorder, Charge Compensation, and 2D Puddles

The QAHE can be realized by substitutional doping of the topological insulator $(Bi_xSb_{1-x})_2Te_3$ with the transition metal ions Cr or V, which leads to a insulating FM ground state with an out-of-plane easy-axis [30, 32]. The nature of the FM interaction between the dopants is still not well understood. The Ruderman-Kittel-Kasuya-Yosida (RKKY) interaction can be ruled out when the Fermi

[7] Unlike the spinless QAH phase in a magnetic 3D-TI (Eq. 2.22), the two time-reversal blocks $H(k)$ and $H^*(-k)$ in Eq. 2.1 each describe a spin-polarized QAHI [112].

[8] Some $Hg_{1-x}Mn_xTe$ crystals also displayed a transition to a (frustrated) antiferromagnet at low temperature [129].

[9] Note that the initial claim on arXiv of the realization of the "Quantum anomalous Hall effect in Mn doped HgTe quantum wells" was never published [27].

level lies inside the exchange gap due to the negligible amount of free carriers [79]. Initially, the sizable spin susceptibility in the insulating state, stemming from Van Vleck paramagnetism, was proposed to facilitate the FM ordering of the magnetic dopants [106, 210, 212]. More recent studies, on the other hand, point to a Zener-type *pd*-exchange interaction mediated by the Sb/Te $5p$ states [173, 178, 206, 207]. In addition to the uncertainty about the exchange interaction [170], the magnetic order in a macroscopic QAH system might also be rather complicated, with reports of superparamagnetism [53, 98, 99]. In particular, Lachman *et al.* demonstrated that instead of long-range ferromagnetic order, a superparamagnetic phase forms in Cr-doped $(Bi_xSb_{1-x})_2Te_3$ thin films as a consequence of the inhomogeneous spatial distribution of the magnetic impurities, resulting in weakly interacting magnetic domains of a few tens of nm in size [98, 99], see Fig. 2.13.

Such an inhomogeneous spatial distribution of the magnetic impurities will induce strong local fluctuations in the size of the exchange gap. Nevertheless, the band engineering approach relaying on fine-tuning the Bi/Sb composition ratio (see section 2.1.3) has proven very successful in tuning the Fermi level into the exchange gap of Cr/V-doped $(Bi_xSb_{1-x})_2Te_3$ thin films. Indeed, the high degree of charge compensation has lead to the precise quantization of the transverse resistance to within an error of about 10^{-8} [133], and a longitudinal sheet resistance as low as 1–2 mΩ [50, 133]. One might expect an even better charge compensation for magnetically doped $(Bi_xSb_{1-x})_2(Te_ySe_{1-y})_3$ thin films. However, adding Se atoms is not straightforward as demonstrated by Zhang *et al.*, who observed a quantum phase-transition (QPT) from a magnetic TI to a paramagnetic trivial insulator for $Bi_{1.78}Cr_{0.22}(Se_xTe_{1-x})_3$ when increasing the Se content above $x \gtrsim 0.63$ [212]. The observed QPT is caused by the loss of SOC strength due to the combined effect of substituting Bi with Cr and Te with Se [77], whereas the loss of the FM state was explained by the Van Vleck mechanism [210]. Hence, the V/Cr-doped $(Bi_xSb_{1-x})_2(Te_ySe_{1-y})_3$ system has a rich topological and magnetic phase diagram as a function of its chemical composition.

As discussed in section 2.1.3, the random spatial distribution of the charged donors and acceptors, leads to 3D charge puddles in TI crystals, as well as 2D charge puddles on the surface of TI crystals and thin films. In QAHI films, the tendency to form 2D puddles would be strong, because little surface carriers are available to screen the Coulomb potential, since E_F lies inside the 2D surface gap [Fig. 2.9(b)]. Hence, screening can only occur nonlinearly through the formation of 2D electron and hole puddles [169]. In chapter 4, the consequences of 2D charge puddles on the QAHE will be discussed, and the electric-field-driven percolation of these puddles will be put forward as the most likely cause of the current-induced breakdown of the QAHE.

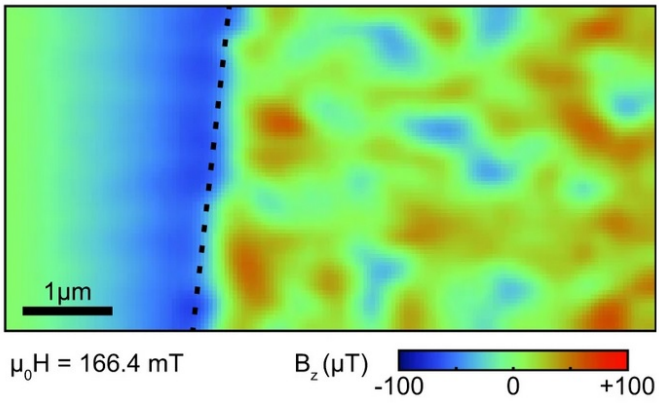

Figure 2.13: Scanning SQUID image of the out-of-plane magnetic field B_z above the sample surface of a Cr-modulation-doped $(Bi_xSb_{1-x})_2Te_3$ thin film. The measurement of B_z was performed over an area of 8×4 μm^2 at 300 mK in an applied field of 166.4 mT, which is slightly higher than the coercive field ($\mu_0 H_C = 137$ mT). The dotted line indicates the edge of the sample. The red and blue colored regions, with positive and negative values of B_z respectively, are interpreted as weakly coupled superparamagnetic domains. This figure is taken from Ref. [98], and reproduced with permission from SNCSC.

2.3 Topological Superconductivity in QAH Hybrid Structures

Let us end the chapter by briefly addressing the intriguing physics of a QAHI proximitized by an s-wave superconductor. Using Eq. 2.15 (with $H_0 = H_{\rm SS} + H_{\rm Zeeman}$), the Bogoliubov-de Gennes (BdG) Hamiltonian [189] becomes

$$\mathcal{H}_{\rm BdG} = \frac{1}{2}\sum_k \Psi_k^\dagger H_{\rm BdG} \Psi_k, \tag{2.24}$$

$$H_{\rm BdG} = \begin{bmatrix} H_0(k) - \mu & \Delta_k \\ \Delta_k^\dagger & -H_0^*(-k) + \mu \end{bmatrix}, \tag{2.25}$$

$$\Delta_k = \begin{bmatrix} i\Delta_1\sigma_y & 0 \\ 0 & i\Delta_2\sigma_y \end{bmatrix}, \tag{2.26}$$

where $\Psi_k = [(c^t_{k\uparrow}, c^t_{k\downarrow}, c^b_{k\uparrow}, c^b_{k\downarrow}), (c^{t\dagger}_{-k\uparrow}, c^{t\dagger}_{-k\downarrow}, c^{b\dagger}_{-k\uparrow}, c^{b\dagger}_{-k\downarrow})]^T$. Here, μ denotes the chemical potential, while Δ_1 and Δ_2 are the pairing gap functions for the top and bottom surface state, respectively.

For the special case of $\Delta_1 = -\Delta_2 \equiv \Delta$ and $\mu = 0$, H_{BdG} can be block-diagonalized (see appendix A for details), yielding:

$$\tilde{H}_{\mathrm{BdG}} = \begin{bmatrix} \tilde{H}_1(k) & 0 \\ 0 & \tilde{H}_2(k) \end{bmatrix}, \tag{2.27}$$

where

$$\tilde{H}_1(k) = \begin{bmatrix} m_k + gM + \Delta & iv_F k_- & 0 & 0 \\ -iv_F k_+ & -m_k - gM - \Delta & 0 & 0 \\ 0 & 0 & -m_k - gM + \Delta & -iv_F k_+ \\ 0 & 0 & iv_F k_- & m_k + gM - \Delta \end{bmatrix},$$

$$\tilde{H}_2(k) = \begin{bmatrix} m_k - gM - \Delta & -iv_F k_+ & 0 & 0 \\ iv_F k_- & -m_k + gM + \Delta & 0 & 0 \\ 0 & 0 & -m_k + gM - \Delta & iv_F k_- \\ 0 & 0 & -iv_F k_+ & m_k - gM + \Delta \end{bmatrix}.$$

The BdG Hamiltonian $\tilde{H}_{\mathrm{BdG}}(k)$ decouples into two models, $\tilde{H}_1(k)$ and $\tilde{H}_2(k)$, with opposite chirality [189]; while each model describes two copies of a spinless $p_x \pm ip_y$ superconductor [51, 150, 189]. Moreover, notice the similarity between $\tilde{H}_1(k)$, $\tilde{H}_2(k)$ and $\tilde{H}_{\mathrm{SS}} + \tilde{H}_{\mathrm{Zeeman}}$ (Eq. 2.16). Hence, the Chern number (Eq. 2.5) of $\tilde{H}_1(k)$ and $\tilde{H}_2(k)$ depends only on the sign of the mass term at the Γ-point:

$$\mathcal{N}_1 = \begin{cases} -2, & \text{for } |\Delta| < -m_0 - gM \\ -1, & \text{for } |\Delta| > |m_0 + gM| \\ 0, & \text{for } |\Delta| < m_0 + gM \end{cases}, \tag{2.28}$$

$$\mathcal{N}_2 = \begin{cases} 2, & \text{for } |\Delta| < -m_0 + gM \\ 1, & \text{for } |\Delta| > |m_0 - gM| \\ 0, & \text{for } |\Delta| < m_0 - gM \end{cases}, \tag{2.29}$$

and the total Chern number of the system is $\mathcal{N} = \mathcal{N}_1 + \mathcal{N}_2$ [189].

Figure 2.14 shows the phase diagram of the QAHI-SC system with $\Delta_1 = -\Delta_2 \equiv \Delta$ and $\mu = 0$; the phase boundaries are defined by the straight lines: $\Delta \pm m_0 \pm gM = 0$. For $\Delta = 0$, the critical points at $gM = \pm|m_0|$ separate the QAH phase with $\mathcal{C} = \pm 1$ from the normal insulator (NI) with $\mathcal{C} = 0$.[10] For $\Delta > 0$, on the other hand, the QAH phase is driven into the $\mathcal{N} = \pm 2$ topological superconductor (TSC) phase, while a $\mathcal{N} = \pm 1$ TSC phase emerges

[10] Remember, that this topological phase transition from the QAH phase with $\mathcal{C} = \pm 1$ to the NI phase with $\mathcal{C} = 0$ gives rise to the zero-conductance-plateau in σ_{xy} at the coercive field H_c, see Fig. 2.12.

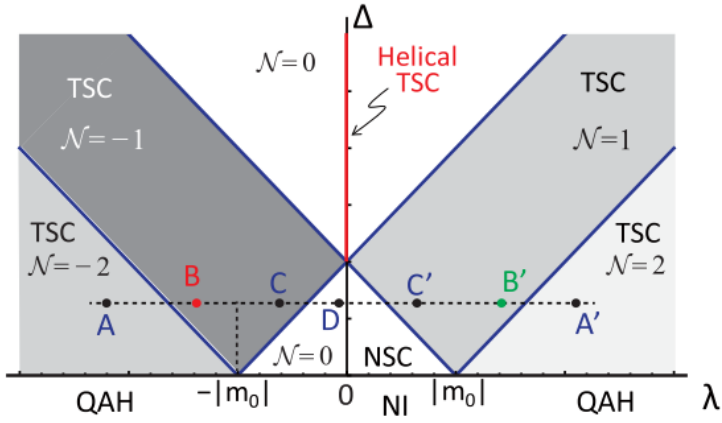

Figure 2.14: Phase diagram of the QAH-SC hybrid system for the special case of $\Delta = \Delta_1 = -\Delta_2$ and $\mu = 0$. The diagram shows the SC gap Δ versus the exchange field $\lambda = gM$. The phase boundaries are determined by the condition: $\Delta \pm m_0 \pm gM = 0$. Note that Δ and λ are in units of $|m_0|$. Reprinted figure with permission from Ref. [189]. © Copyright (2015) by the American Physical Society.

in the regions near the QAH-NI transition. Moreover, for $\Delta_1\Delta_2 < 0$ with zero exchange field $gM = 0$, a helical TSC phase emerges with helical Majorana edge states (see Ref. [189] for details), as depicted by the red line in Fig. 2.14. Note that the phase diagram shown in Fig. 2.14 is qualitatively similar to the phase diagram derived by Qi *et al.* in Ref. [145]. However, the authors only considered a single spin-momentum-locked 2D surface state, which means that the dependence on the hybridization gap m_0 is missing. Moreover, it should be noted that the effect of an exchange field on the proximitized surface state of a TI was already commented on in the seminal work by Fu and Kane [51].

Until now, we have focused on the special case of $\Delta = \Delta_1 = -\Delta_2$ (and $\mu = 0$), whereas this scenario might not be easily achieved in an experimental set-up. Wang *et al.* calculated the phase diagram for general values of Δ_1 and Δ_2, and for finite μ [189]. If the symmetry between the top and bottom surface states is preserved, i.e. $\Delta = \Delta_1 = \Delta_2$, the Chern number can only change by ± 2 between the $\mathcal{N} = \pm 2$ TSC phase and the $\mathcal{N} = 0$ normal superconductor (NSC) phase, as shown in Fig. 2.15(b). On the other hand, if Δ_2 is made to decrease, the $\mathcal{N} = \pm 1$ TSC phase emerges and becomes the widest for $\Delta_2 = 0$ [Fig. 2.15(a)], i.e. only the top surface is proximitized [189]. Figures 2.15(c-d) show two cases with finite doping $\mu \neq 0$, where the SC proximity effect will be enhanced by the increased density of states at the Fermi level [145]. Comparing Fig. 2.15(a) to

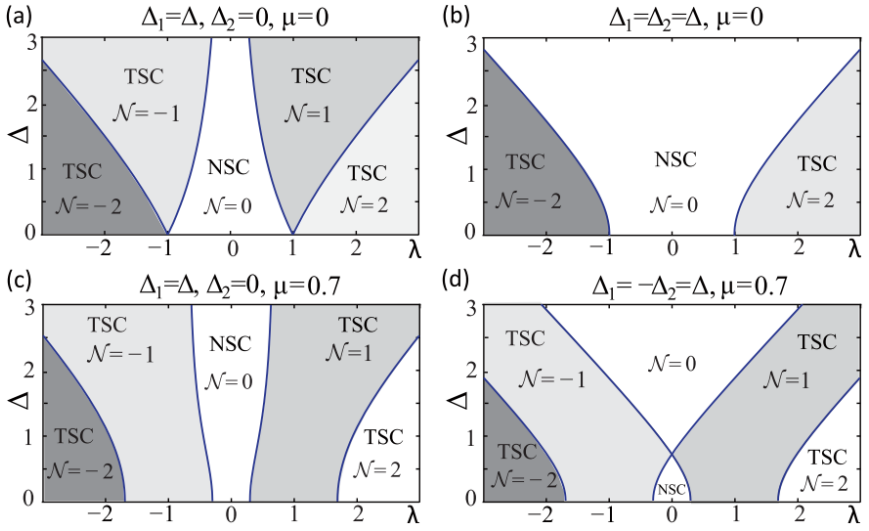

Figure 2.15: Phase diagram of the QAH-SC hybrid system, as a function of the SC gap Δ and the exchange field $\lambda = gM$ for: (a) $\Delta_1 = \Delta$, $\Delta_2 = 0$, and $\mu = 0$. (b) $\Delta_1 = \Delta_2 = \Delta$ and $\mu = 0$. (c) $\Delta_1 = \Delta$, $\Delta_2 = 0$, and $\mu = 0.7$. (d) $\Delta_1 = -\Delta_2 = \Delta$ and $\mu = 0.7$. Note that Δ_1, Δ_2, μ and λ are in units of $|m_0|$. Reprinted figure with permission from Ref. [189]. © Copyright (2015) by the American Physical Society.

2.15(c), and Fig. 2.14 to 2.15(d), it is clear that the phase space of the $\mathcal{N} = \pm 1$ TSC state near the region of $\Delta = 0$ is larger for the case of finite doping $\mu \neq 0$.

Using a simple low-energy effective Hamiltonian, it was shown that a QAHI in proximity to an s-wave SC realizes the chiral TSC phase with Chern numbers $\mathcal{N} = \pm 1$, or ± 2. The $\mathcal{N} = 1$ TSC phase is of particular interest, as it is expected to host a Majorana zero mode in the vortex core [51, 150]. Moreover, TSCs with Chern number $\mathcal{N}$ have $\mathcal{N}$ topologically-protected gapless chiral Majorana edge modes, which can be thought of as a superconducting analogue of the quantum (anomalous) Hall edge states [51, 145, 189]. While definitive proof of the realization of a TSC phase in QAH-SC heterostructures is still lacking, several experiments have aimed at studying the SC proximity effect at QAH-SC interfaces [84, 166]. It should be noted that He *et al.* claimed to have observed the Chern-number transitions $\mathcal{N} = -2 \leftrightarrow -1 \leftrightarrow 0 \leftrightarrow 1 \leftrightarrow 2$ [cf. A–A' in Fig. 2.14] in the hysteresis loop of the two-terminal conductance when the external magnetic field is swept [63]. Half-integer quantized conductance plateaus $e^2/(2h)$ were observed near the magnetization reversals, which were claimed to correspond to the $\mathcal{N} = \pm 1$ TSC states [63]. However, the data came

under immediate scrutiny [12, 68, 75]. Moreover, Kayyalha *et al.* showed that the observation of $e^2/(2h)$ is consistent with a trivial electrical short caused by the superconducting Nb strips used in the experiments [84]. The publication by He *et al.* [63] was ultimately retracted under suspicion of scientific misconduct.

Recently, intriguing new experiments have been proposed relying on the creation and fusion of edge vortices (π-phase domain walls) at Josephson junctions in a TSC to braid Majorana zero modes [1, 13, 59]. The proposed experiments are highly innovative and well-suited to the QAH-SC platform. Unfortunately, as will be discussed in chapter 4, the current-induced breakdown of the QAHE becomes worse for reduced device dimensions, which means special care will have to be taken to avoid or mitigate breakdown in mesoscopic QAH devices.

2.4 Summary

In this chapter, it was shown that the low-energy effective Hamiltonians describing the QSHE, QAHE, and the proximity effect in QAH-SC heterostructures can be block-diagonalized into $(2+1)$-dimensional Dirac Hamiltonians, using clever basis transformations. Consequently, the topological phase transitions for these systems are fully captured by the sign-change of the Dirac mass.

Moreover, it is important to reiterate that:

(i) the QAHE can be realized in narrow-gap semiconductors with sizable SOC (described by Eq. 2.16) for a large enough Zeeman field, irrespective of whether the initial system is topological or trivial;

(ii) while the QSHI can be thought of as two time-reversal copies of a QAHI, the QAH edge state in a magnetic 3D-TI is rather special due to the lack of a (sizable) spin polarization;

(iii) in charge-compensated magnetically-doped $(Bi_xSb_{1-x})_2Te_3$ thin films, the inhomogeneous spatial distribution of the magnetic dopants (V or Cr) will lead to spatial fluctuations of the exchange gap size, whereas the random distribution of the charged donor and acceptor crystalline defects will result in the formation of 2D charge puddles as the Fermi level E_F locally crosses the 2D band edges of the exchange gap;

(iv) even for thick QAH films, where an s-wave SC proximitizes only the top surface of the film (i.e. $\Delta_1 = \Delta$ and $\Delta_2 = 0$ in Eqs. 2.24–2.26), the $\mathcal{N} = \pm 1$ TSC phase is still predicted to emerge over a large region of the phase diagram.

Chapter 3

Experimental Techniques

> *Never underestimate the joy people derive from hearing something they already know.*
>
> Enrico Fermi

For the research performed in this PhD thesis, thin films of V-doped $(Bi_xSb_{1-x})_2Te_3$ were grown on InP(111)A substrates using the molecular beam epitaxy (MBE) technique. The crystal quality and morphology were verified using X-ray diffraction (XRD) and atomic force microscopy (AFM). The thicknesses of the thin films were extracted by fitting the Kiessig fringes measured in X-ray reflectometry (XRR) or around film peaks in the XRD spectra.

After the structural characterization verified the quality of the V-doped $(Bi_xSb_{1-x})_2Te_3$ thin films, the charge-carrier concentration, mobility, and Curie temperature were determined by magneto-transport in a physical property measurement system (PPMS) by cooling the sample down to 2 K. Only the samples with an anomalous Hall (AH) amplitude $\geqslant 18$ kΩ at 2 K, together with a downturn in the longitudinal resistance, were selected for the study of the QAHE in this thesis.

The selected high-quality films were patterned into multi-terminal Hall-bar devices using conventional clean-room techniques. The breakdown of the QAHE and the nonreciprocal charge transport, in chapters 4 and 5 respectively, were investigated by magneto-transport experiments carried out using standard AC

lock-in and DC methods at a base temperature of ∼10 mK in a dry dilution refrigerator equipped with an 8 T superconducting magnet.

Below a brief description of the MBE growth, device fabrication, and ultra-low-temperature magneto-transport measurements is given. Representative AFM, XRD, and PPMS measurements of the V-doped $(Bi_xSb_{1-x})_2Te_3$ thin films are included in this chapter, as well as a list of the devices.

3.1 Molecular Beam Epitaxy

MBE is a versatile thin film growth technique, where thermally generated molecular or atomic beams are deposited on a heated substrate in an ultra-high-vacuum (UHV) environment. Of crucial importance are the choice of growth substrate, substrate temperature and deposition rate.

3.1.1 Choice of Growth Substrate

As the name implies the aim of MBE is the epitaxial growth of a single-crystal thin film on top of a single-crystal substrate. In order to achieve this the crystal structure, lattice constant, and surface orientation of the substrate have to be carefully chosen to match the crystal lattice of the thin film to be grown. The lattice mismatch between the film and substrate is defined as

$$\epsilon_m = \frac{a_f - a_s}{a_s}, \tag{3.1}$$

where a_f and a_s are the in-plane lattice constants of the film and substrate [65], respectively. A distinction has to be made between homoepitaxy, where the substrate and film are the same material ($\epsilon_m = 0$), and heteroepitaxy, where the elemental composition and/or crystal structure of the film are different. If the atomic arrangement of the film and substrate crystal structures at the interface do not match well or ϵ_m is simply too large, the film and substrate are incommensurate. This means the film-substrate interface will contain a large numbers of defects, and the grown film may be textured[1] or polycrystalline, rather than monocrystalline.

The crystal structure of the ternary compound $(Bi_xSb_{1-x})_2Te_3$ was already shown in Fig. 2.6(a). This tetradymite structure has rhombohedral symmetry and the space group is $R\bar{3}m$ [29, 52]. The crystal structure consists of stacked covalently-bonded quintiple layers (QLs) of (Te1)–(Bi/Sb)–(Te2)–(Bi/Sb)–(Te1), with

[1] The alignment between the substrate and film has a single fixed axis [149].

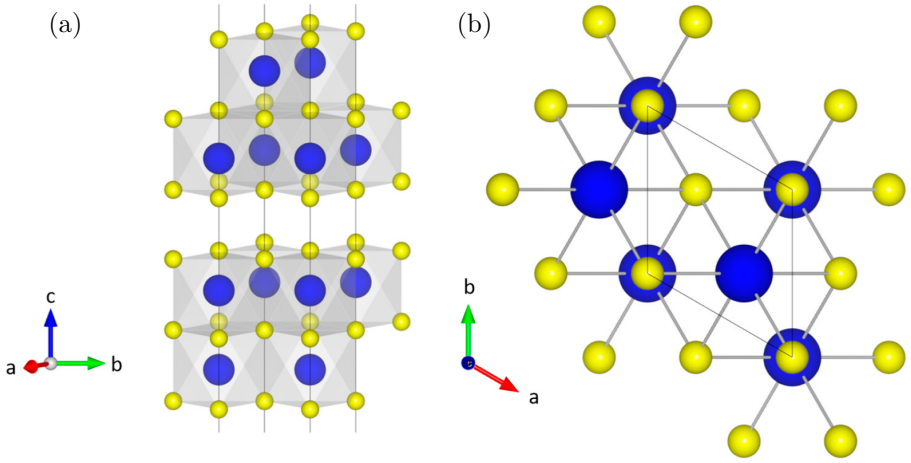

Figure 3.1: The tetradymite crystal structure of the ternary compound $(Bi_xSb_{1-x})_2Te_3$, along the c-axis showing two QLs and the VdW gap (a), and in the a–b plane showing the hexagonal symmetry (b). The cations (Bi, Sb) are shown in blue, while the anions (Te) are shown in yellow. This figure is taken from Ref. [52], and reproduced with permission from MDPI.

neighboring QLs being held together by Van-der-Waals (VdW) bonds [29, 52], see Fig. 3.1. Due to these weak VdW bonds, an epilayer of $(Bi_xSb_{1-x})_2Te_3$ immediately starts growing with its own lattice constant, forming only weak VdW bonds with the growth substrate. Hence, strain relaxation at the film-substrate interface via the nucleation of dislocations does not occur [149], and the lattice matching condition is drastically relaxed for this kind of MBE growth, called 'Van-der-Waals Epitaxy' (VdWE) [87, 88, 89], allowing the growth of highly lattice-mismatched systems with only a small amount of defects.

In this thesis, the hexagonal (111)A surface of zincblend InP was chosen as the growth substrate, after insightful discussions with Y. Tokura, M. Kawasaki, and R. Yoshimi from RIKEN, Japan. InP(111)A is a proven substrate for the realization of the QAHE [83, 125, 132]. It matches the hexagonal (001) Te-terminated surface of the QL of $(Bi_xSb_{1-x})_2Te_3$ with a lattice mismatch of $\epsilon_m \approx +4.9\%$ (Eq. 3.1). Other candidate substrates are $Al_2O_3(001)$ ($\epsilon_m \approx -8.5\%$), $SrTiO_3(111)$ ($\epsilon_m \approx -21.2\%$), Si(111) ($\epsilon_m \approx +13.4\%$), and GaAs(111) ($\epsilon_m \approx +8.9\%$). While high-quality thin films of $(Bi_xSb_{1-x})_2Te_3$ are regularly grown on c-plane Al_2O_3 in our research group [18], we were unable to reach full quantization of R_{yx} when V or Cr dopants were added. $SrTiO_3$ is also a proven substrate for the growth of QAH thin films [30, 32, 215], and has the

added benefit that it can serve as a high-κ dielectric, allowing for back-gating of the grown thin films. However, scanning transmission electron microscopy (STEM) and XRD studies have shown that the large lattice mismatch with $SrTiO_3$ leads to a poor crystal quality of the first QLs of $(Bi_xSb_{1-x})_2Te_3$ grown on top of $SrTiO_3$ [139, 153, 154]. While QAH films were successfully grown on top of Si(111) [49, 54, 193], XRD studies showed that the crystal quality of $(Bi_xSb_{1-x})_2Te_3$ thin films grown on Si(111) substrates is inferior when compared to the other growth substrates [138, 154]. Moreover, atom probe tomography (APT) revealed Sb accumulation at the film-substrate interface, which potentially dopes the surface of the Si substrate, since Sb is a well-known n-type dopant in Si [100]. Lastly, it should be noted that GaAs(111)B substrates yield excellent QAH films as well [50, 63, 94, 95]. Moreover, STEM images of Cr-doped $(Bi_xSb_{1-x})_2Te_3$ thin films on InP(111)A [153] and GaAs(111)B [94] showed atomically sharp and well-ordered interfaces.

For a comprehensive overview of the epitaxial relationship of MBE-grown V/Cr-doped $(Bi_xSb_{1-x})_2Te_3$ thin films on various substrates, the reader is directed to Refs. [153, 154], and the references therein.

3.1.2 MBE Growth

The main MBE system used in this work, the Octoplus 400 from Dr. Eberl MBE-Komponenten GmbH, is shown in Figs. 3.2 and 3.3. The set-up consists of the main chamber, the buffer chamber, and the load-lock chamber. The chambers are isolated from each other by gate valves. The main chamber, where the MBE growth takes place, is pumped by a cryo and ion getter pump to a base pressure of about 5×10^{-11} mbar. The buffer chamber is pumped by an ion getter pump yielding a base pressure of about 5×10^{-10} mbar. The annealing station in the buffer chamber is used to clean the growth substrates prior to introducing them into the MBE chamber. The load-lock chamber is only pumped by a turbo-molecular pump and is regularly vented with N_2 to introduce or take out samples. While the load-lock ensures that a good base pressure can be maintained in the system, the sample cleaning in the buffer chamber allows for a time-efficient operation of the MBE system.

The materials to be deposited on the growth substrates are loaded in their elementally pure form into separate crucibles. In this work, Bi and Te were evaporated by Joule heating from a 'Knudsen effusion cell', see inset of Fig. 3.3. Sb, on the other hand, was evaporated from a cracker source, in which the large Sb_x molecules evaporating from the heated crucible are dissociated by a thermal cracker stage to form a molecular beam containing mainly Sb_2. An electron-beam evaporator was used for the magnetic dopant V due to its very

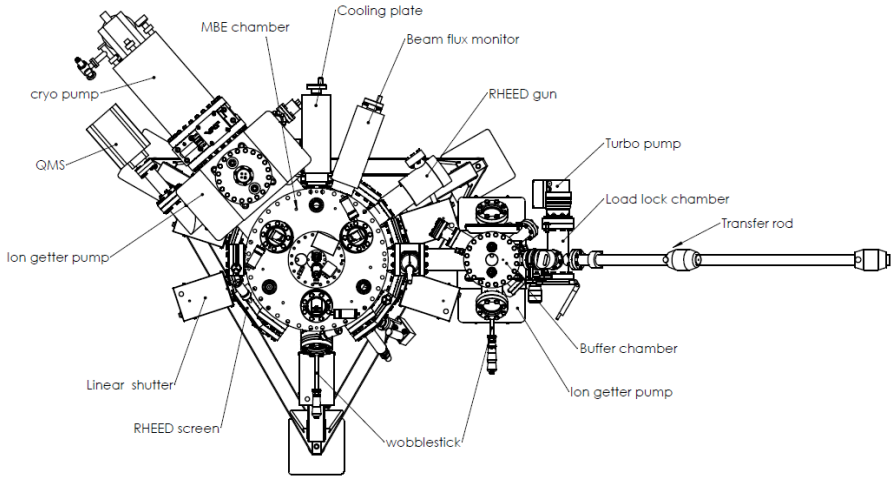

Figure 3.2: Technical drawing of the molecular beam-epitaxy-vacuum chamber (top view). The set-up consists of the MBE main chamber, the buffer chamber, and the load-lock chamber. Each chamber has its own dedicated pumps as indicated in the figure. The transfer rods and wobblesticks are used to manipulate the samples inside the UHV environment. The quadrupole mass spectrometer (QMS) monitors the residual gas molecules in the MBE chamber. The reflection high-energy electron diffraction (RHEED) set-up is a powerful tool that allows to in-situ study the growth process. Figure courtesy of Dr. Eberl MBE-Komponenten GmbH.

high melting point of 1910°C. All the evaporators are mounted at the bottom of the MBE chamber as shown in Fig. 3.3, and their molecular beams are focused at the growth substrate. Figure 3.4 shows an illustration of the MBE deposition process. The cells containing the source materials are heated to produce the molecular beams, while shutters in front of the cells and substrate are used to regulate which species are arriving on the surface of the growth substrate. The amount of evaporated material is determined by the beam-equivalent-pressure (BEP) which is measured by placing an ion gauge (i.e. the beam flux monitor in Fig. 3.2) in front of the substrate position in the direct path of the molecular beams. In the UHV environment the mean-free-path of the gas molecules, as well as in the molecular beams themselves, is several orders of magnitude greater than the source-to-sample distance [65]. Hence, no gas phase reactions occur and the species impinge on the substrate unreacted which is a requisite for MBE growth as will be explained below.

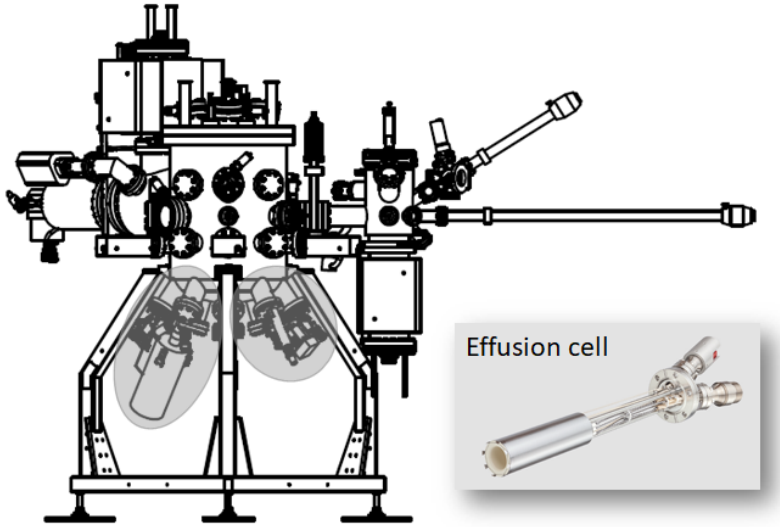

Figure 3.3: Technical drawing of the molecular-beam-epitaxy vacuum chamber (side view). The grey shaded areas indicate the positions of the evaporators. The inset shows a picture of a Knudsen effusion cell. The top of the white PBN crucible, in which the source material is mounted, can be seen in the picture. The source material is evaporated by Joule heating of the crucible, using a Ta coiled heating element. The power supply and thermocouple cables are lead through the bottom flange and connected externally. Figures courtesy of Dr. Eberl MBE-Komponenten GmbH.

A key parameter in MBE growth is the choice of the substrate temperature. If chosen too high all arriving species will desorb and no deposition will take place, while a too low substrate temperature will result in a poor surface mobility and rapid incorporation of the arriving species into the grown film. This will lead to an amorphous or polycrystalline growth, rather than the desired epitaxial single-crystal film. Hence, a compromise between the deposition rate and growth temperature has to be found. For multi-element crystals, a limiting and abundant species is identified [65]. In the example of Bi_2Te_3 in Fig. 3.4, Bi due to its higher melting point will act as the limiting species, while the easier to evaporate Te will be supplied in excess. The substrate temperature is chosen in such a way that if only one of the elements were evaporated, the Bi atoms would stick to the substrate, while the Te atoms would be fully re-evaporated. However, if Bi and Te are deposited together, the impinging Bi atoms will bind to the abundantly available Te, and form the desired Bi_2Te_3

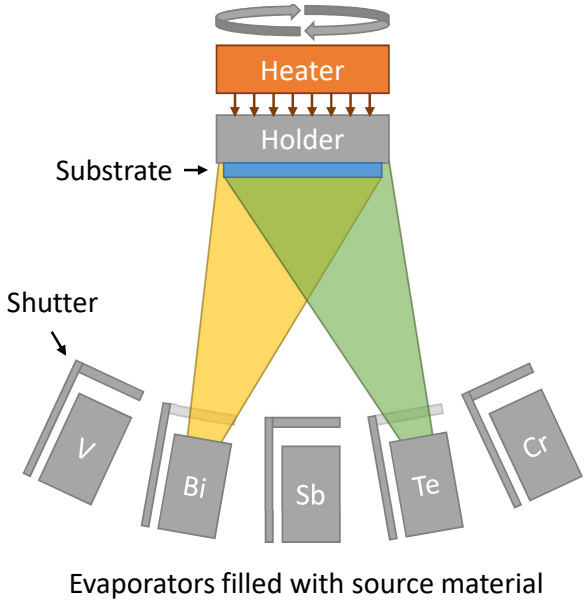

Figure 3.4: Illustration of the molecular-beam-epitaxy growth process. The evaporators are filled with elementally pure source material and heated to produce molecular beams. When the shutter of a particular evaporator is opened, the molecular beam of said material reaches the substrate; e.g. Bi and Te in the figure. The substrate is rotated to yield a uniform distribution of the arriving species and heated to promote surface diffusion. The crystal structure of the substrate acts as the nucleation site for crystal growth of the thin film; in this case Bi_2Te_3.

crystal structure. Since the substrate temperature is too high to deposit pure Te, the stoichiometric growth of Bi_2Te_3 is ensured.

In this work, the InP(111)A substrates were annealed at 550°C in the buffer chamber to thermally desorb the surface oxide layer. After transferring the InP substrates into the MBE chamber, they were kept at 190°C while V, Bi, Sb, Te were co-evaporated for 40 min to produce uniform films with a thickness of ∼8 nm. The Bi, Sb, and Te cell temperatures were 440°C, 444.4°C, and 278°C, respectively. Te was supplied in excess, while Bi and Sb acted as the limiting species. The BEP ratio of Bi+Sb:Te was 1:20. The V electron-beam source was operated with an acceleration voltage of 6 kV and an electron-beam current of 72 mA. The V-flux was too small to be measured with the beam flux monitor, and did not influence the growth rate significantly.

As explained in chapter 2 (section 2.1.3), the chemical potential is determined by the Bi:Sb ratio $x/(1-x)$ of the $(Bi_xSb_{1-x})_2Te_3$ crystal. A BEP ratio for Bi:Sb of 1:4 was found to yield the most insulating behavior at low temperature; this corresponds to an x-value of $\sim$0.3 as determined by energy-dispersive X-ray (EDX) spectroscopy. A detailed discussion of the growth parameters falls outside the scope of this thesis; the reader is directed to the PhD dissertation of A. Bliesener [18].

3.2 Basic Characterization & Sample Screening

Immediately after taking the thin films out of the load-lock of the MBE system ($\lesssim$ 3 min), they were covered with a 3-nm Al_2O_3 capping layer using atomic layer deposition (ALD) to protect the films from degradation in air. Subsequently, the films were characterized by AFM and XRD. Figure 3.5(b) shows an AFM image representative for the QAH films grown in this work. Small, but well-pronounced $\sim$1 nm high terraces are observed, corresponding to 1 QL steps in the film thickness. The film is continuous with a rms-roughness of $\sim$0.7 nm over a scan area of 1×1 μm^2.

Figure 3.5(a) shows an XRD spectrum for a thick V-doped $(Bi_xSb_{1-x})_2Te_3$ film grown by MBE under similar conditions as the QAH films. Only the $(00\underline{3n})$ reflections[2] of $(Bi_xSb_{1-x})_2Te_3$ are observed, indicating the epitaxial growth of the hexagonal (001) crystal surface of V-doped $(Bi_xSb_{1-x})_2Te_3$ on top of the hexagonal (111) surface of the zincblende InP substrate.

Figure 3.6(a) shows the temperature dependence of the sheet resistance of a high-quality V-doped $(Bi_xSb_{1-x})_2Te_3$ thin film from room temperature down to 2 K. The sample was field-cooled in 2.5 mT. At the Curie temperature $T_C \approx 20$ K the transverse resistance ρ_{yx} becomes nonzero and starts to increase towards h/e^2, while the longitudinal sheet resistance ρ_{xx} starts to vanish. Figure 3.6(b) shows the magnetic-field dependence of ρ_{yx} at 2 K. The 2D bulk states of QAH film are n-type, as can be seen from the negative slope of the ordinary Hall effect.

Only continues epitaxial thin films of V-doped $(Bi_xSb_{1-x})_2Te_3$ with an AH amplitude $\geqslant 18$ kΩ at 2 K and a downturn in the longitudinal resistance below T_C were selected for the study of the QAHE in this thesis.

[2]Note that in literature it is customary to use the hexagonal indexing scheme, where the $(00n)$ reflections are along the (111) direction of the rhombohedral unit cell [153].

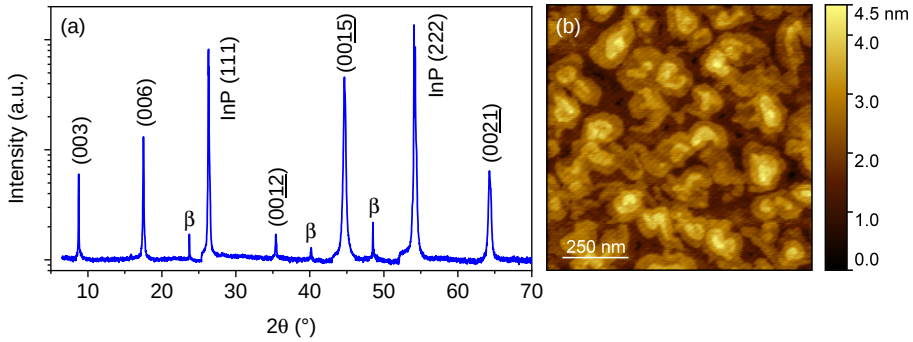

Figure 3.5: Structural characterization of the MBE grown films. (a) Cu K-α XRD spectrum (with Ni filter) of a thick V-doped $(Bi_xSb_{1-x})_2Te_3$ film (deposition time ∼20 hours). The raw XRD spectrum was divided by a smooth background. (b) AFM image of a QAH thin film (thickness ∼8 nm).

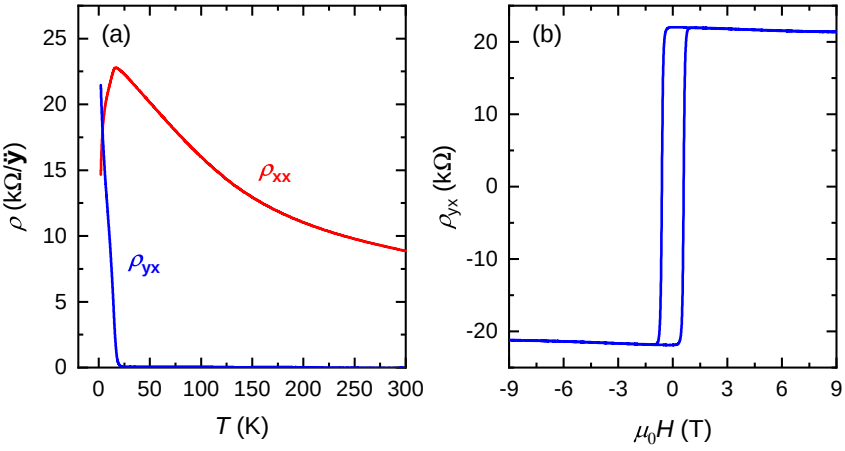

Figure 3.6: (a) Temperature dependence of the longitudinal sheet resistance ρ_{xx} and transverse resistance ρ_{yx} of Hall-bar device C (see table 3.1 for details). The sample was field-cooled in 2.5 mT. (b) Magnetic-field dependence of the transverse resistance ρ_{yx} at 2 K. The negative slope of the ordinary Hall effect shows the n-type character of the 2D bulk of the V-doped $(Bi_xSb_{1-x})_2Te_3$ thin film.

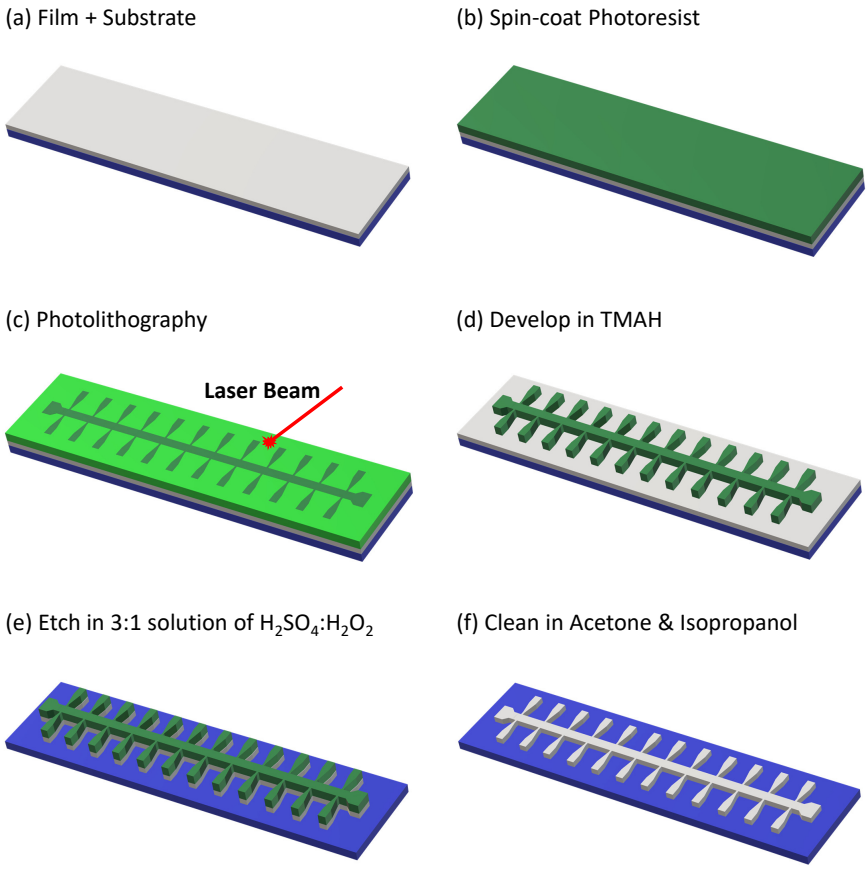

Figure 3.7: Schematic of the microfabrication steps for an etched Hall-bar structure. (a) The V-doped $(Bi_xSb_{1-x})_2Te_3$ thin film (white) on top of the InP substrate (blue). (b) Positive photoresist (green) is spin-coated on the sample. (c) Photolithography of the Hall-bar structure. (d) After developing in TMAH, the exposed regions of the photoresist are dissolved. (e) After etching the film in H_2SO_4:H_2O_2, the regions not covered by the photoresist are removed. (f) The etched Hall-bar structure after cleaning off the photoresist.

3.3 Device Fabrication

After the screening process, the high-quality V-doped $(Bi_xSb_{1-x})_2Te_3$ thin films were patterned into multi-terminal Hall-bar devices, using conventional clean-room techniques. Below a brief description of the fabrication details is given, as well as a list of all the Hall-bar devices used in this thesis.

3.3.1 Microfabrication

Most Hall-bar devices in this thesis relied on two photolithography steps. In the first step, the Hall-bar structure were etched into the V-doped $(Bi_xSb_{1-x})_2Te_3$ thin film, as shown in Figs. 3.7(a-f). In the second step, the contact arms of the Hall-bar were metalized by sputtering 5 nm Pt + 45 nm Au, and performing a lift-off process, as shown in Figs. 3.8(a-f).

First, a layer of positive photoresist (AZ 1505 from MicroChemicals) was spin-coated on the sample at 4500 rpm. The photoresist was baked at 100°C for 1 min, after which the sample was loaded into the lithography machine (Heidelberg μPG 101), see Figs. 3.7(a-b). Here, the Hall-bar design was written into the photoresist layer by a 10 mW laser beam operating at 35%, see Fig. 3.7(c). After the 'exposure', the sample was post-baked at 120°C for 30 s.

The AZ 1505 photoresist used in this work consists of a polymerized phenolic resin (Novolak) and photosensitive Diazonaphthoquinone sulfonic acid esters (DNQ sulphonates). The DNQ sulphonates reduce the alkaline solubility of the pure phenolic resin by one or two orders of magnitude [121]. However, when exposed to the appropriate wavelengths, the DNQ sulphonates are converted into carboxylic acids, which leads to a three to four orders of magnitude increase of the alkaline solubility of the pure phenolic resin [121]. Hence, the exposed parts of the photoresist layer, shown in light green in Fig. 3.7(c), could be selectively removed by 'developing' the photoresist layer in an aqueous alkaline solution, while the unexposed areas of the photoresist remained on the sample, protecting the film from being etched in the alkaline solution. In this work, a Tetramethylammonium hydroxide (TMAH) solution (AZ 326 from MicroChemicals) was used for the development (20 s) of the lithographic pattern, see Fig. 3.7(d). The sample was subsequently rinsed in deionized (DI) water for 30 s. It is important to point out that the TMAH solution, not only removes the exposed photoresist, but also attacks the 4-nm-thick Al_2O_3 capping layer, as well as the V-doped $(Bi_xSb_{1-x})_2Te_3$ film underneath.

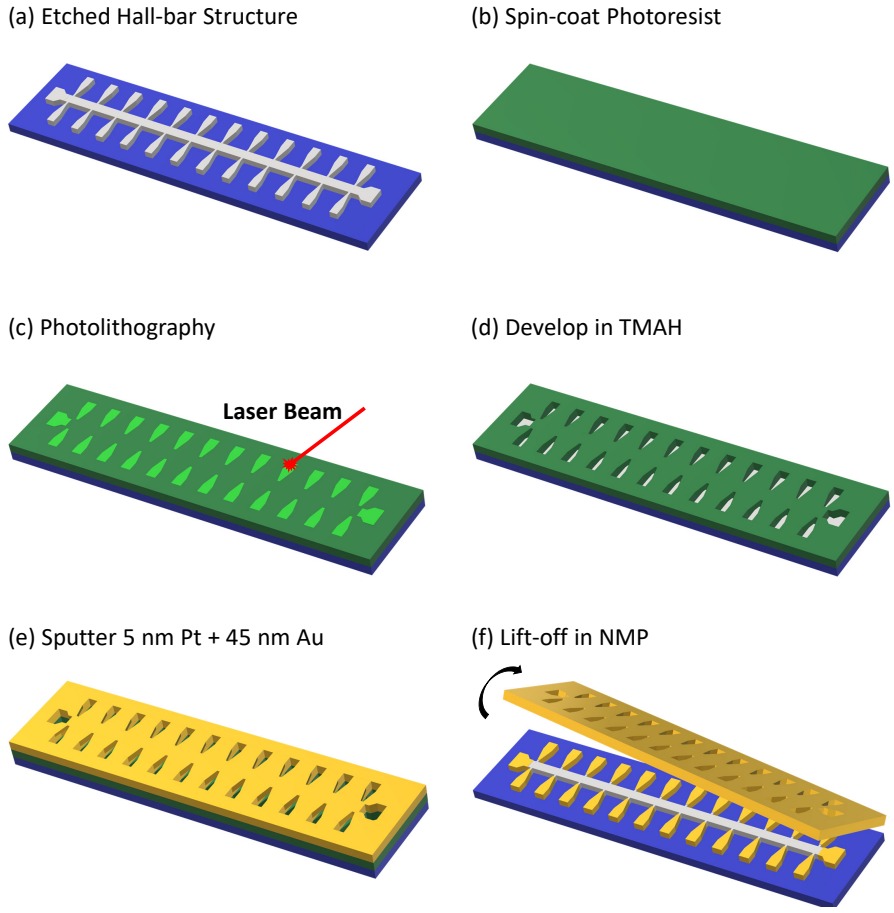

Figure 3.8: Schematic of the microfabrication steps for the metalization of the contacts. (a) The etched Hall-bar structure in the V-doped $(Bi_xSb_{1-x})_2Te_3$ thin film (white) on top of the InP substrate (blue). (b) Positive photoresist (green) is spin-coated on the sample. (c) Photolithography of the contact pads. (d) After developing in TMAH, the exposed regions of the photoresist are dissolved. (e) A metal layer consisting of 5 nm Pt + 45 nm Au is sputter-deposited on top of the sample. (f) Lift-off process in NMP. The photoresist is dissolved, removing the Pt/Au layer everywhere except in the contact regions.

Next, the (remainder of the) V-doped $(Bi_xSb_{1-x})_2Te_3$ film not protected by the photoresist, was etched in an 'inverted piranha' solution[3] consisting of 1 part of concentrated sulfuric acid (1 mol/L) and 3 parts of 35 wt.% hydrogen peroxide solution, see Fig. 3.7(e). The sample was subsequently rinsed in DI water for 1 min, and the photoresist was cleaned off in acetone (5 min) and isopropanol (1 min). The etched Hall-bar structure (white) on top of the InP substrate (blue) is shown in Fig. 3.7(f).

Before the second photolithography step, 30 nm of Al_2O_3 was deposited by ALD at 80°C, which will protect the contact areas of the Hall-bar during the developing step in the TMAH solution. Next, the positive photoresist was spin-coated on the sample, and the metal contacts were written by the photolithography tool, as shown in Figs. 3.8(a-c). Afterwards, the pattern was developed in the TMAH solution for 20 s, which is a too short time to completely etch through the 30-nm-thick Al_2O_3 layer. The remainder of the thick Al_2O_3 layer was etched in Transene Aluminum Etchant type-D (Transene D) at 50°C for 1 min. The sample was subsequently rinsed in DI water for 30 s. Note that Transene D was found to show excellent selectivity towards Al metal and Al_2O_3, and TI thin films were not noticeably affected even after being submerged for 45 min at 50°C.

The film was quickly transferred to our (MANTIS) UHV sputtering chamber, to reduce the V-doped $(Bi_xSb_{1-x})_2Te_3$ surface in the contact areas being exposed to air. Here, a 5-nm Pt sticking layer, followed by 45 nm of Au were deposited on top of the sample covering the photoresist as well as the exposed Hall-bar contact areas, see Fig. 3.8(e). Next, the sample was submerged in N-methyl-2-pyrrolidone (NMP) for 45 min. NMP is an excellent solvent and completely dissolved the photoresist layer underneath the Pt/Au layer. Next, the Pt/Au layer was 'lifted-off' by mild agitation, and only the Pt/Au in the contact regions directly contacting the V-doped $(Bi_xSb_{1-x})_2Te_3$ film remained, see Fig. 3.8(f). A picture of a 26-terminal Hall-bar device is shown in Fig. 3.9.

Lastly, for some Hall-bar devices a third lithography step was performed to define a Pt/Au gate electrode on top of the thick Al_2O_3 layer (in this case 45 nm was deposited instead of 30 nm) above the center of the Hall-bar. Here, the electron-beam-lithography (EBL) machine had to be used, not for its much higher resolution, but because the EBL resist, Polymethyl methacrylate (PMMA), is developed in an isopropanol–DI water solution. If instead photolithography were used the quality of the Al_2O_3 gate dielectric would have strongly deteriorated due to direct contact with the TMAH developer.

[3] A typical piranha solution consists of a 3:1 mixture of H_2SO_4:H_2O_2.

3.3.2 List of Devices

The data of thirteen Hall-bar devices are shown in this thesis. Devices A, B, and C are 26-terminal Hall-bar devices, as shown in Fig. 3.9. Devices D, E, F1, F2, G1, G2, H, I, J, and K are regular 6-terminal Hall-bar devices; a picture of device D is included in Fig. B.1 of the appendix. Devices A and B were fabricated on the same V-doped $(Bi_xSb_{1-x})_2Te_3$-InP wafer, as well as devices F1, F2, G1, G2, H, and I. The other devices were fabricated on separate wafers. A top-gate electrode was fabricated on devices F1, F2, G1, G2, H, I, J, and K. Sadly, the gate dielectric was leaking for devices F2, G2, and I, which made the devices not gate tune-able. However, all devices (A–I) showed a clean QAHE without the need for gating; their details are listed in table 3.1. Unless stated otherwise, data for devices F1, G1, H, J, and K are presented at zero gate voltage.

3.4 Ultra-low-temperature Magneto-transport

Heike Kamerlingh Onnes was the first person to liquefy helium on 10 July 1908, which led to his 1913 Nobel Prize in Physics "for his investigations on the properties of matter at low temperatures which led, inter alia, to the production of liquid helium". While his studies at a temperature of ∼1.5 K were an extraordinary feat of engineering at the time, currently mK-temperatures are readily available for magneto-transport experiments. For this thesis, a dry dilution refrigerator (Oxford Instruments Triton 200), equipped with an 8 T superconducting magnet, was used at a base temperature of ∼10–65 mK. Below a brief description of dilution refrigeration is given, as well as a discussion of the AC and DC measurement techniques employed in this thesis.

3.4.1 Dilution Refrigeration

Dilution refrigeration is based on the enthalpy of mixing of ^{3}He and ^{4}He. Figure 3.10(a) shows the phase diagram of the ^{3}He/^{4}He mixture. ^{4}He is a spin-zero boson, while ^{3}He is a spin-1/2 fermion. Pure ^{4}He undergoes a transition from a normal liquid phase to a superfluid at 2.17 K [4]. For pure ^{3}He, on the other hand, the superfluid transition occurs around 2.7 mK [4] (not shown in Fig. 3.10(a)), and the underlying physics is much more complicated.[4]

[4] In ^{3}He spin fluctuations lead to an attractive pairing potential between ^{3}He atoms, akin to the formation of 'Cooper pairs' in the Bardeen-Cooper-Schrieffer (BCS) theory of superconductivity [4]. The exchange interaction in ^{3}He is ferromagnetic, which results in spin-triplet, p-wave pairing and a rich superfluid phase diagram at ultra-low temperatures [4].

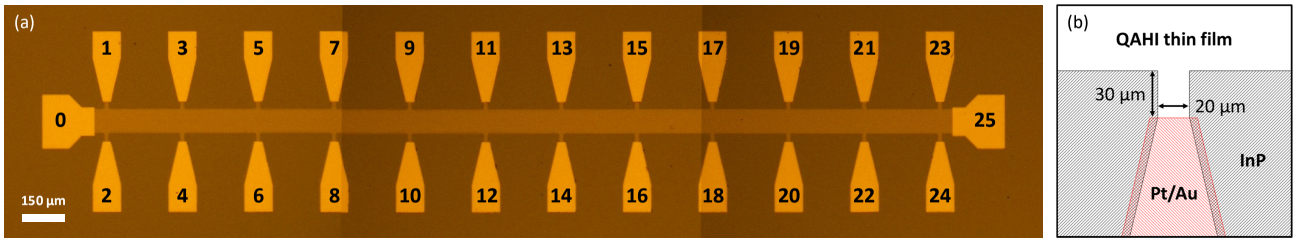

Figure 3.9: (a) Picture of the 26-terminal Hall-bar device A (width 100 μm, contact separation 300 μm). Three photographs are merged, as the device was too long for the microscope camera frame. (b) Schematic of the 20-μm-wide contacts.

Device	Terminals	Hall-bar		Contact		I_c across W_{Hb} [nA]
		Contact separation [μm]	Width [μm]	Length [μm]	Width [μm]	
A, B	26	300	100	30	20	$\sim$ 160
C	26	300	100	30	20	$\sim$ 85*
D	6	350	100	50	50	$\sim$ 85*
E	6	200	100	0	20	$\sim$ 125
F1, F2	6	350	100	30	30	$\sim$ 55–95
G1, G2	6	350	150	40	40	$\sim$ 100–145
H	6	350	200	50	50	$\sim$ 160
I	6	350	250	60	60	$\sim$ 240
J	6	200	100	0	20	$\sim$ 50
K	6	200	100	0	20	$\sim$ 30

Table 3.1: Hall-bar device characteristics. The I_c values shown in the last column are the breakdown current for the full width of the Hall-bar device W_{Hb} for $V_{Gate} = 0$ V. *Devices C and D were measured with the AC lock-in technique; their I_c values are expressed in peak-current amplitudes. The film thickness is $\sim$8 nm for all devices.

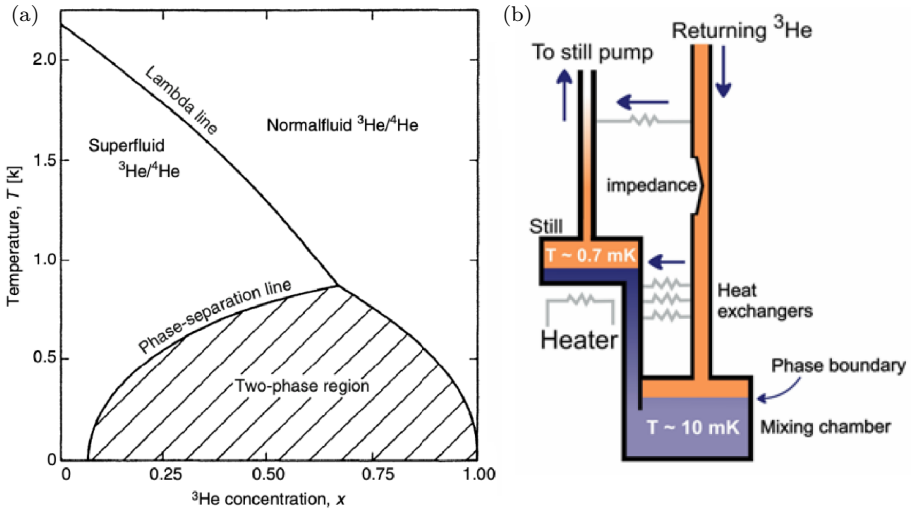

Figure 3.10: (a) Phase diagram of the ^{3}He/^{4}He mixture, and (b) schematic of a dilution refrigerator. Below 867 mK, the ^{3}He/^{4}He mixture phase separates into two liquid phases with the ^{3}He-rich (or 'concentrated') phase shown in orange floating on top of the heavier ^{4}He-rich phase (the 'dilute' phase) shown in dark blue. Figure (a) is taken from Ref. [140], and reproduced with permission from SNCSC. Figure (b) is taken from Ref. [10], courtesy of Oxford Instruments plc.

When the ^{3}He/^{4}He mixture is cooled below 867 mK, it phase separates into two liquid phases with the ^{3}He-rich (or 'concentrated') phase floating on top of the heavier ^{4}He-rich phase (the 'dilute' phase) [10]. At ultra-low temperatures, the concentrated phase is nearly pure ^{3}He, whereas the solubility of ^{3}He in the dilute phase remains finite (~6.4%) down to 0 K. Figure 3.10(b) shows a schematic of a 'dry' dilution refrigerator. The sample to be measured is mounted in thermal contact to the 'mixing chamber'. The orange regions represent the nearly pure ^{3}He phase, while the dark blue regions are the dilute phase.

A distiller ('still') pulls the dilute phase from below the phase boundary in the mixing chamber, and using a heater distills the ^{3}He from the ^{4}He due to the difference in vapor pressures. As the ^{3}He vapor is pumped away from the still reservoir, the ^{3}He concentration of the dilute phase in the still will decrease. The difference in ^{3}He concentration between the still and the mixing chamber results in an osmotic pressure gradient along the connecting tube, which causes ^{3}He to diffuse from the mixing chamber to the still [10]. Next, the ^{3}He vapor from the still passes through a room temperature gas handling system and compressor which sends pressurized ^{3}He back into the return line. The returning

^{3}He passes through a heat exchanger with the ^{3}He vapor leaving the still. The high pressure ($\sim$0.5–2.5 bar) is maintained up to the impedance, after which the Joule-Thompson expansion liquefies the ^{3}He [10]. Next, the ^{3}He liquid passes through several more types of heat exchangers, which further precools the ^{3}He before reaching the mixing chamber. Here, the ^{3}He crosses the phase boundary into the dilute phase to replenish the ^{3}He which is continuously diffusing away towards the still, and the ^{3}He concentration is kept constant at $\sim$6.4%.

The associated cooling power $\dot{Q}$ is determined by the enthalpy difference $\Delta H(T)$ between ^{3}He in diluted ^{4}He and pure liquid ^{3}He multiplied by the ^{3}He flow rate $\dot{n}$: $\dot{Q} = \dot{n}\Delta H(T)$ [10]. The ^{3}He atoms in liquid ^{4}He behave as a Fermi gas. As a result, the enthalpy of ^{3}He in ^{4}He is higher than for pure liquid ^{3}He [10].[5] The cooling power [10] can be described by:

$$\dot{Q} = \dot{n}(95T_{\mathrm{MC}}^2 - 11T_{\mathrm{Ex}}^2), \tag{3.2}$$

where T_{MC} and T_{Ex} are the temperature of the mixing chamber and the last heat exchanger, respectively. Note that T_{Ex} has to be included in Eq. 3.2, because the ^{3}He entering the mixing chamber is always slightly warmer than the ^{3}He leaving to the still due to non-ideal heat exchangers, which reduces the maximum achievable cooling power.

Lastly, it is important to point out that evaporative cooling is limited by the exponential dependence of the vapor pressure on the temperature [10]. The solubility of ^{3}He in ^{4}He, on the other hand, is nearly temperature independent at ultra-low temperatures [Fig. 3.10(a)]. For the dilution process, the lowest achievable temperature is instead limited by the T^2-dependence of the enthalpy [10]. This is the key advantage of dilution refrigeration over evaporative cooling.

3.4.2 AC and DC Measurement Techniques

The DC data presented in chapters 4 and 5 were measured using standard DC techniques with Keithley 2182A nanovoltmeters and a Keithley 2450 current source, whereas the AC data were measured using standard AC lock-in techniques with a low frequency (3–7 Hz) using NF Corporation LI5640 and LI5645 lock-in amplifiers. For the AC technique, the peak current amplitude at which the measured voltage/resistance started to deviate from the dissipationless state gave a good measure of the breakdown current I_{c}; note that the peak current value is $\sqrt{2}$ times larger than the root-mean-square (rms) current value.

To avoid confusion in chapters 4 and 5, it is instructive to briefly explain noise filtering and Fourier components for the AC lock-in technique.

[5] This is analogous to the cooling power stemming from the enthalpy difference between ^{3}He gas and ^{3}He liquid in an evaporation refrigerator.

Noise Filtering

In order to perform a lock-in measurement, a frequency reference ω_r is needed. Typically, the sample in the experiment is excited at a fixed frequency and the lock-in detects the sample's response at this reference frequency. In what is known as a 'phase-locked-loop', the lock-in tracks the external reference frequency ω_r and equates the frequency ω_l of its internal oscillator to it [171]. This allows the lock-in to generate a sine wave with $\omega_l = \omega_r$ and a fixed phase shift of θ_l with respect to the reference. Let's assume $\theta_l = 0$ for simplicity.

A generic response of the sample can be written as $V_s \sin(\omega_s t + \theta_s)$. The lock-in amplifies this signal and multiplies it by the lock-in reference $V_l \sin(\omega_r t)$ using a phase-sensitive detector (PSD) or multiplier [171], yielding:

$$\begin{aligned} V_{\text{PSD}} &= V_s V_l \sin(\omega_s t + \theta_s) \sin(\omega_r t) \\ &= \frac{1}{2} V_s V_l \cos\left((\omega_s - \omega_r)t + \theta_s\right) + \frac{1}{2} V_s V_l \cos\left((\omega_s + \omega_r)t + \theta_s\right) \end{aligned} \tag{3.3}$$

Hence, the PSD output is the sum of two AC signals, one at the difference frequency $(\omega_s - \omega_r)$ and the other at the sum frequency $(\omega_s + \omega_r)$. The PSD output is subsequently passed through a low-pass filter which removes both AC signals [171], unless $\omega_s = \omega_r$ $(= \omega)$:

$$V_{\text{PSD+low-pass}} = \frac{1}{2} V_s V_l \cos(\theta_s). \tag{3.4}$$

Hence, all noise signals with $\omega_s \neq \omega_r$ are filtered out, and the 'in-phase' response at the selected reference frequency ω_r is recorded (more details below).

The First & Second-Fourier Components

In chapter 5, it will be shown that the four-terminal I-V characteristic of a QAHI (at high currents and/or temperatures) follows the relation:

$$V_{L/R} = R_0 I (1 + \tilde{\gamma} c_{L/R} n_{p/n} \hat{M} I), \tag{3.5}$$

where $V_{L/R}$ is the voltage drop measured along the left/right edge, I the excitation current, R_0 the Ohmic resistance term, $\tilde{\gamma}$ the rectification coefficient, $c_{L/R}$ the measured sample edge ($c_L = +1$ and $c_R = -1$ for the left and right edge, respectively), $n_{p/n}$ the 2D charge-carrier type ($n_p = +1$ and $n_n = -1$ for a p- and n-type 2D bulk, respectively), and $\hat{M}$ the magnetization direction ($\hat{M} = +1$ and $\hat{M} = -1$ for an upward and downward, out-of-plane magnetization, respectively) [201].

In the experiments an AC excitation current is applied to the sample and the voltage response is recorded using a lock-in amplifier as a PSD. The AC excitation current is a sine wave:

$$I_{\mathrm{AC}} = I_0 \sin(\omega t), \tag{3.6}$$

with the excitation amplitude $I_0 (= \sqrt{2} I_{\mathrm{rms}})$, frequency ω, and time t. Inserting Eq. 3.6 into Eq. 3.5 gives the sample's voltage response to the excitation current I_{AC}:

$$\begin{aligned} V_{L/R} &= R_0 I_{\mathrm{AC}} + R_1 I_{\mathrm{AC}}^2, \\ &= R_0 I_0 \sin(\omega t) + R_1 I_0^2 \sin^2(\omega t), \\ &= R_0 I_0 \sin(\omega t) + R_1 I_0^2 \left(\frac{1 + \sin(2\omega t - \pi/2)}{2} \right), \end{aligned} \tag{3.7}$$

where $R_1 = \tilde{\gamma} R_0 c_{L/R} n_{p/n} \hat{M}$. Notice that Eq. 3.7 yields a term $\sim \sin(2\omega t - \pi/2)$. Hence, the I_{AC}^2-term in Eq. 3.5 generates a 'second-harmonic' response at twice the excitation frequency.

The lock-in amplifier in our experiments is phase-locked to the frequency of the excitation current I_{AC}. For the first-harmonic measurement, the phase-sensitive detection of the lock-in converts the signal into an 'in-phase' X- and 'quadrature' Y-component by multiplying the signal by $\sin(\omega t)$ and $\cos(\omega t)$, respectively, and performing a low-pass integration:

$$X^{\omega} = \frac{2}{T\sqrt{2}} \int_0^T V_{L/R}(t) \sin(\omega t) dt \approx R_0 I_{\mathrm{rms}}, \tag{3.8}$$

$$Y^{\omega} = \frac{2}{T\sqrt{2}} \int_0^T V_{L/R}(t) \cos(\omega t) dt \approx 0, \tag{3.9}$$

where the averaging time T is large compared to the signal period. The first-harmonic voltage is in-phase and determined by the Ohmic resistance R_0, as expected. Notice the $\sqrt{2}$ in the denominator of Eqs. 3.8-3.9, which ensures the X- and Y-components are expressed in rms-voltages as is the convention for most lock-in amplifiers.

Since a lock-in amplifier multiplies the input signal with a pure sine and cosine wave, it actually measures the Fourier components of the signal at the reference frequency ω. Similarly to Eqs. 3.8-3.9, the Fourier components of the second harmonic at 2ω can be measured by multiplying the input signal by $\sin(2\omega t)$ and $\cos(2\omega t)$.

The low-pass integration than yields:

$$X^{2\omega} = \frac{\sqrt{2}}{T}\int_0^T V_{L/R}(t)\sin(2\omega t)dt \approx 0, \tag{3.10}$$

$$Y^{2\omega} = \frac{\sqrt{2}}{T}\int_0^T V_{L/R}(t)\cos(2\omega t)dt \approx -\frac{1}{\sqrt{2}}R_1 I_{\mathrm{rms}}^2. \tag{3.11}$$

Hence, the second-harmonic voltage only shows up in the Y-component and depends on $R_1 = \tilde{\gamma}R_0 c_{L/R} n_{p/n}\hat{M}$, the nonreciprocal resistance.

It is useful to derive the relation between the nonreciprocal resistance observed in DC and AC measurements. Equation 3.5 can be used to directly describe the DC voltage drop along the right and left edge of the sample. Switching between forward and reverse current flow, while keeping the polarity $\mathcal{P} \equiv c_{L/R} n_{p/n}\hat{M}$ the same, yields a DC resistance difference of

$$\Delta R_{\mathrm{DC}} = 2\tilde{\gamma}R_0 I_{\mathrm{DC}}. \tag{3.12}$$

For the second-harmonic voltage $Y^{2\omega}$, on the other hand, the Ohmic contribution is already removed via the integration in Eq. 3.11. Hence, the relation between the AC and DC nonreciprocal response is simply:

$$\Delta R_{\mathrm{DC}} = -2\sqrt{2}R^{2\omega}. \tag{3.13}$$

Moreover, in chapter 5 it will sometimes be instructive to compare the resistance difference between the right and left edges for the same 2D charge-carrier type $n_{p/n}$, magnetization $\hat{M}$, and current direction. In this case, the second-harmonic resistance difference is simply $\Delta R^{2\omega} = 2R^{2\omega}$, and

$$\Delta R_{\mathrm{DC}} = -\sqrt{2}\Delta R^{2\omega}. \tag{3.14}$$

Note that Eq. 3.14 also holds when comparing the difference in resistance between the opposite magnetization directions, for the same edge and current direction. In this case $\hat{M}$, rather than $c_{L/R}$, causes the sign change.

3.5 Summary

In this chapter, the MBE growth of V-doped $(Bi_xSb_{1-x})_2Te_3$ thin films was discussed. The stoichiometric composition was ensured by supplying an overpressure of Te and choosing the substrate temperature above the sticking temperature of Te, whereas by tuning the Bi:Sb BEP ratio near perfect charge compensation was achieved. Moreover, it was argued that GaAs(111)B and

InP(111)A are the best growth substrates. In the next chapter, it will be shown that QAH films grown on these substrates also yield the highest breakdown currents.

With regards to the device fabrication process, it is important to emphasize that the successful fabrication of Ohmic metal contacts relied on the excellent selectivity of the etchant Transene D. Namely, Transene D completely removed the protective Al_2O_3 capping layer, while leaving the $\sim$8 nm QAH film unaffected.

Lastly, the principles of dilution refrigeration and magneto-transport were discussed. It was shown that an I^2-contribution to the I-V relation gives rise to a second-harmonic component of the AC resistance, which will be important for chapter 5.

Chapter 4

The QAH Breakdown Mechanism

> *Crystals are like people, it is the defects in them which tend to make them interesting!*
>
> Colin Humphreys

In this chapter, the current-induced breakdown of the QAHE will be studied in both local and nonlocal measurement geometries. A toy-model describing the breakdown process will be presented, and the transverse electric field will be identified as the driving force for breakdown. Lastly, different possible breakdown mechanisms for the QAHE will be discussed.

4.1 Breakdown of the QAHE

To elucidate the breakdown mechanism of the QAHE it is beneficial to study the magneto-transport in multi-terminal Hall-bar devices.[1] Figure 4.1(a) shows a schematic of a 26-terminal Hall-bar device[2] with the current flowing from contact

[1] In appendix B, it is shown that regular 6-terminal Hall-bar device are not well-suited for nonlocal transport measurements.

[2] A microscope picture of such a device is shown in Fig. 3.9 of chapter 3.

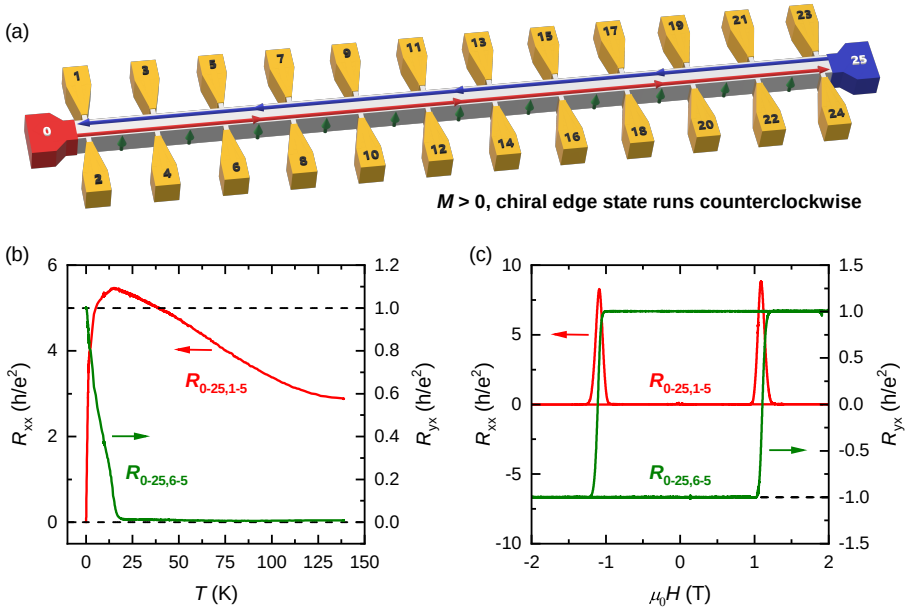

Figure 4.1: Regular Hall-bar configuration for the 26-terminal Hall-bar device B. (a) Schematic of the potential distribution in the chiral edge state for $M > 0$; red (blue) color signifies the source (drain) potential when current flows from contact 0 to 25. The arrow heads signify the direction of the current flow. Note that the chirality of the edge state inverts for $M < 0$. (b) Temperature dependence of the longitudinal and transverse resistance, $R_{0\text{-}25,1\text{-}5}$ and $R_{0\text{-}25,6\text{-}5}$, respectively. The curves were measured from 140 K to 40 mK, with a DC current of 50 nA. (c) Magnetic-field dependence of $R_{0\text{-}25,1\text{-}5}$ and $R_{0\text{-}25,6\text{-}5}$ measured at 40 mK with a DC current of 30 nA, showing an ideal QAHE. The dashed lines in (a) and (b) are guides to the eye.

0 to 25; namely, a voltage is applied to contact 0 and contact 25 is grounded. For an upward, out-of-plane magnetization ($M > 0$), the bottom edge of the Hall-bar (colored red) is at the source potential, while the top edge (colored blue) is at the drain potential, as a consequence of the dissipationless transport in the QAH phase. Figure 4.1(b) shows the temperature dependence of the QAHE from 140 K to 40 mK. The four-terminal resistance $R_{0\text{-}25,6\text{-}5}$ corresponds to the transverse resistance; here, the first index denotes the current probes (0–25), while the second index denotes the voltage probes (6–5). Similarly, $R_{0\text{-}25,1\text{-}5}$ corresponds to the longitudinal resistance measured between contact 1 and 5. $R_{0\text{-}25,6\text{-}5}$ remains zero till the Curie temperature[3] ($T_C \approx 18$ K), after which it quickly increases with decreasing temperature becoming equal to the von Klitzing constant h/e^2 at 40 mK. Starting from 140 K, $R_{0\text{-}25,6\text{-}5}$ increases with decreasing temperature, showing an insulating temperature dependence until ∼18 K; here the 2D (and 3D) bulk states dominate the charge transport. Below ∼18 K, $R_{0\text{-}25,6\text{-}5}$ quickly drops to zero, as the chiral edge becomes the dominant transport channel.

Figure 4.1(c) shows the corresponding magnetic-field dependence of $R_{0\text{-}25,1\text{-}5}$ and $R_{0\text{-}25,6\text{-}5}$ at 40 mK. $R_{0\text{-}25,1\text{-}5}$ is zero for all values of the magnetic field with the exception of a peak at the coercive field H_C, where the QAHE is lost over a narrow field range upon magnetization reversal. Similarly, $R_{0\text{-}25,6\text{-}5}$ shows a square hysteresis loop with a transition between $+h/e^2$ and $-h/e^2$ at the coercive field $\pm H_c$. Figures 4.2(a-b) show the coercive field peaks in the longitudinal resistance $R_{0\text{-}25,1\text{-}x}$ with $x = \{5, 9, 11, 13, 17, 21\}$ measured between different contact pairs. The linear relation between the peak value of $R_{0\text{-}25,1\text{-}x}$ at H_c and the contact spacing L is indicative of 2D diffusive transport through the bulk of the sample when the magnetic exchange gap is closed at H_c.

Figure 4.2(c) shows the current-induced breakdown of the QAHE for the same contact pairs. The longitudinal voltage $V_{1\text{-}x}$ shows a broad plateau at 0 V up to ∼0.16 μA, above which a sharp increase signifies the breakdown of the dissipationless state. Note that this breakdown current density (∼1.6 nA/μm) is among the highest reported so far [50, 54, 83, 133].[4] The Hall voltage $V_{6\text{-}5}$ follows the expected linear behavior of the QAHE, $V_{6\text{-}5} \approx (h/e^2)I$, with only a small deviation at high current values. Hence, the breakdown in the transverse voltage V_y is much less pronounced than in the longitudinal voltage V_x, see Fig. 4.3(b) for a fair comparison. This is consistent with the earliest studies of

[3] In this thesis, the temperature at which an apparent long-range ferromagnetic order shows up in the QAH films, will be referred to as the 'Curie temperature' T_C. However, as discussed in section 2.2.2, this may actually be the 'superparamagnetic blocking temperature' instead. Nevertheless, since no scanning SQUID experiments were performed on any of our QAH films, the magnetic order (long-range FM or superparamagnetism) is not known.

[4] As shown later in Fig. 4.14, the critical current density in our samples can be further increased by electrostatic gating to ∼4.16 nA/μm.

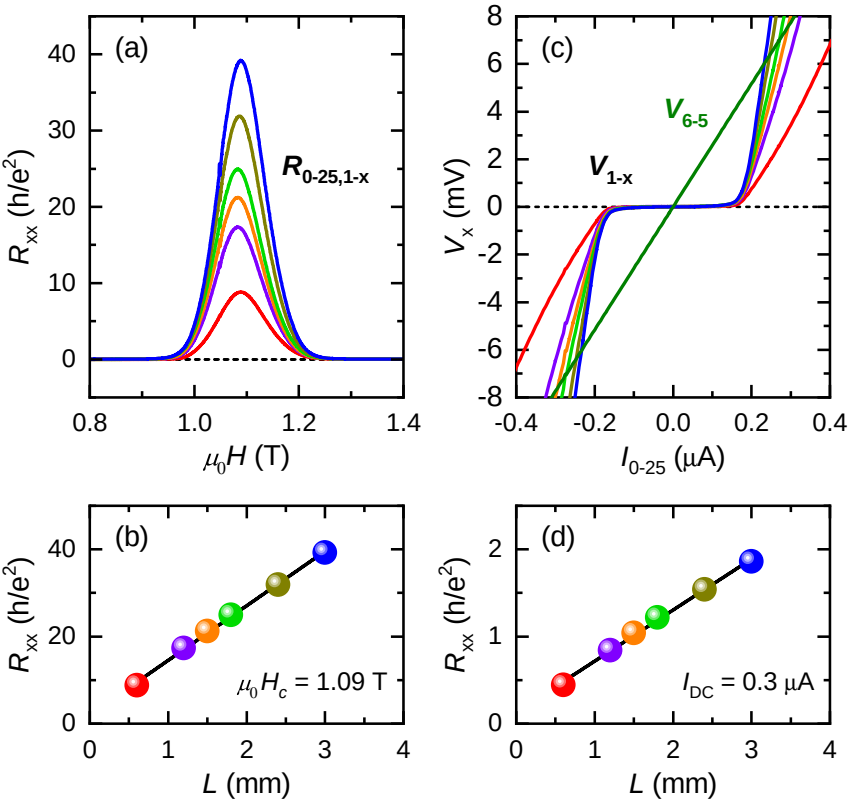

Figure 4.2: Length dependence of the longitudinal resistance of the QAHI, measured on the 26-terminal Hall-bar device B at 40 mK. (a) Longitudinal resistance $R_{0\text{-}25,1\text{-}x}$ near the coercive field $\mu_0 H_c = 1.09$ T, measured with respect to different contacts $x = \{5, 9, 11, 13, 17, 21\}$ with $I_{\mathrm{DC}} = 30$ nA. (b) The peak values of $R_{0\text{-}25,1\text{-}x}$ at the coercive field H_c as a function of the voltage-contact spacing L. (c) Plots of the longitudinal voltage $V_{1\text{-}x}$ vs $I_{0\text{-}25}$, measured at +2 T. The breakdown of the QAHE occurs at $\sim$0.16 μA. The transverse voltage $V_{6\text{-}5}$ is shown as well, for comparison. (d) The value of $V_{1\text{-}x}/I_{0\text{-}25}$ at 0.3 μA as a function of L.

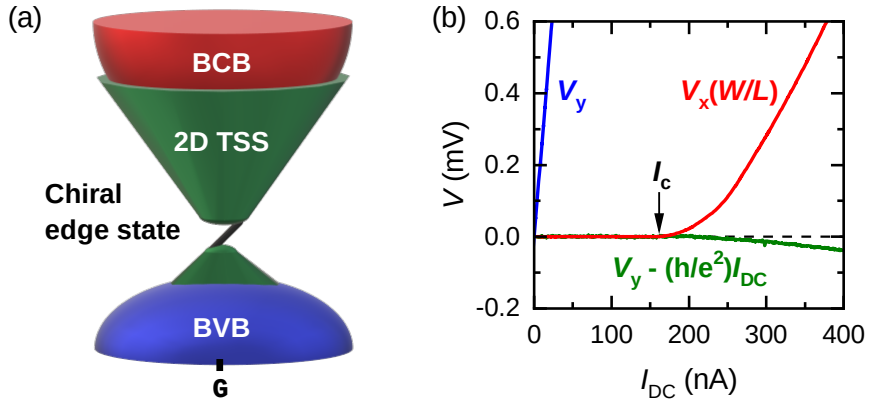

Figure 4.3: (a) Illustration of the energy spectrum: The bulk conduction band (BCB) and bulk valence band (BVB) are well separated. The 2D topological surface states (TSS) have an exchange gap at the Γ-point, but the gap closes at the sample's edges where the chiral edge state connects the upper and lower branches. (b) Current-induced breakdown in device A, measured at 10 mK in 0 T (after training the sample at +2 T to align all the magnetic domains). Above ∼160 nA, both the longitudinal voltage V_x and the transverse voltage V_y show deviations from the ideal QAHE. Notice that V_x was normalized by the Hall-bar width W and voltage-contact spacing L for a fair comparison.

the QAHE, where the transverse resistance was close to h/e^2, while having a sizable longitudinal resistance of several kΩ [30]. The procedure used in this thesis to extract the value of the critical current I_c is given in appendix C.

Figure 4.2(d) shows the longitudinal resistance value at $I_{DC} = 0.3$ μA as a function of L. A linear dependence on the contact spacing is found, similar to that in Fig. 4.2(b). This linear dependence seems to indicate that the dissipative state above breakdown is also governed by 2D diffusive transport through the bulk of the sample. Hence, for small probe currents the system behaves as an ideal QAHI in which the chiral edge states are the only transport channels [see Fig. 4.3(a)], whereas for large probe currents the 2D surface states also seem to carry a fraction of the current. It was suggested that the large transverse electric field gives rise to a small leakage current through the 2D bulk states across the width of the Hall-bar, leading to the breakdown of the QAHE [50, 83]. In the next section, it will be shown using the Landauer-Büttiker formalism [28] that such a leakage current crossing the width of the Hall-bar indeed affects the longitudinal resistance, while leaving the Hall resistance unchanged.

4.2 Landauer-Büttiker Description of Breakdown

In this section, the effect of the current-induced breakdown of the QAHE on the measured resistance is described using the Landauer-Büttiker formalism [28]. The simplistic model by no means describes the physics of the current-induced breakdown fully. However, as will be shown throughout the chapter, it does capture the key feature of the breakdown mechanism, namely, the loss of the edge current from the high-potential branch of the chiral edge state to the low-potential branch. Below, the effect of such a leakage current on the measured four-terminal and three-terminal resistances is addressed. Here, the Landauer-Büttiker treatment will be limited to a 6-terminal Hall-bar; several more complicated models for a 12-terminal Hall-bar are included in appendix D.

4.2.1 Four-terminal Measurement Geometry

Figure 4.4(a) shows a schematic of a 6-terminal Hall-bar device for an upward, out-of-plane magnetization ($M > 0$). The current flows from contact 1 to 4, and the chiral edge state runs counterclockwise along the sample edge. The high- and low-potential branches of the chiral edge state are separated by the width of the Hall-bar. To describe the fraction of the current leaking from the high- to the low-potential branch, the scattering probabilities α, β, γ are introduced, as depicted in Fig. 4.4. In the Landauer-Büttiker formalism [28], the current-voltage relation is given by

$$I_i = \frac{e^2}{h} \sum_j (T_{ji} V_i - T_{ij} V_j), \tag{4.1}$$

where V_i is the voltage on the ith contact, I_i is the current flowing through the ith contact into the sample, and T_{ji} is the transmission probability from the ith to the jth contact. Consider the edge channel running from contact 6 to 5; there is a $T_{56} = (1 - \beta)$ probability of reaching contact 5 and a $T_{26} = \beta$ probability of scattering to contact 2. Similarly, the other nonzero transmission coefficients can be found to be:

$$\begin{aligned} T_{11} &= T_{62} = \alpha, & T_{12} &= T_{61} = (1 - \alpha), \\ T_{26} &= T_{53} = \beta, & T_{23} &= T_{56} = (1 - \beta), \\ T_{35} &= T_{44} = \gamma, & T_{34} &= T_{45} = (1 - \gamma). \end{aligned} \tag{4.2}$$

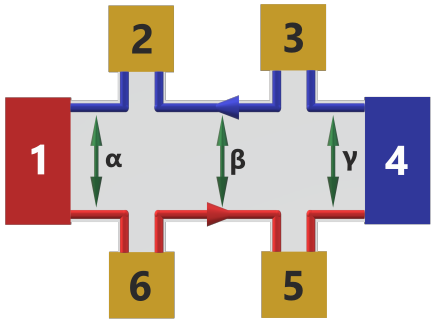

Figure 4.4: Schematic of the edge transport in a 6-terminal Hall-bar device for $M > 0$, with the 'leakage' between opposing edges parametrized by the scattering probabilities α, β, and γ. Contact 1 acts as the source, while contact 4 is the drain. The high- and low-potential branches of the chiral edge state are represented by the red and blue arrows, respectively.

Using $V_4 = 0$, $I_1 = -I_4 = I$ and $I_2 = I_3 = I_5 = I_6 = 0$, Eq. 4.1 gives a set of equations which can be solved for I and V_i. The four-terminal longitudinal and transverse resistances then become:

$$R_{xx} = \frac{V_2 - V_3}{I} = \frac{V_6 - V_5}{I} = \frac{\beta}{1-\beta}\frac{h}{e^2}, \tag{4.3}$$

$$R_{yx} = \frac{V_6 - V_2}{I} = \frac{V_5 - V_3}{I} = \frac{h}{e^2}, \tag{4.4}$$

where R_{xx} only depends on β, the scattering probability between the voltage contacts, as expected. Notice that R_{yx} remains quantized in our simple model.[5] This is clearly not the case for a real device where R_{yx} starts to deviate from h/e^2 with increasing temperature or probe current. However, despite the simplicity of the model, it shows that R_{xx} is more strongly affected by breakdown than R_{yx}, in agreement with the measured I-V characteristic shown in Fig. 4.3(b).

[5]Some authors choose to include an additional scattering probability δ in the Landauer-Büttiker model, which directly shorts the transverse contact pairs [49, 50], i.e. contact 2 to 6 and 3 to 5 in Fig. 4.4. This solves the issue of R_{yx} remaining quantized in a broken-down QAHI ($\alpha, \beta, \gamma, \delta \neq 0$). However, with an increasing amount of scattering probabilities describing the 2D leakage paths, it is probably more instructive to move to a finite-element or tight-binding model on a 2D grid to better describe the breakdown process.

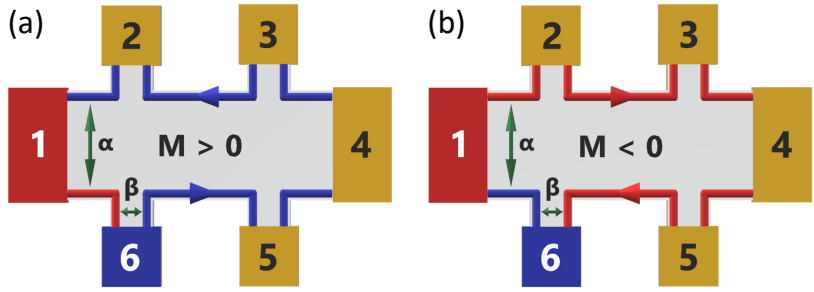

Figure 4.5: (a-b) Schematics of the edge transport in a 6-terminal Hall-bar device for $M > 0$ (a) and $M < 0$ (b), with the 'leakage' between opposing edges for a wide and narrow contacts parametrized by the scattering probabilities α and β, respectively. Contact 1 acts as the source, while contact 6 is the drain. The high- and low-potential branches of the chiral edge state are represented by the red and blue arrows, respectively.

4.2.2 Three-terminal Measurement Geometry

Figure 4.5 shows a schematic of a 6-terminal Hall-bar device for $M > 0$ and $M < 0$. The current flows from contact 1 to 6. Contacts 3, 4 and 5 are spatially separated from the current contacts in this nonlocal configuration. To describe the breakdown in the current contacts, the scattering probabilities α and β between the high- and low-potential branches near contacts 1 and 6, respectively, are introduced. The nonzero transmission coefficients for $M > 0$ then become:

$$\begin{aligned} &T_{11} = \alpha, && T_{12} = (1-\alpha), && T_{51} = \beta(1-\alpha), \\ &T_{66} = \beta, && T_{56} = (1-\beta), && T_{62} = \alpha(1-\beta), \\ &T_{23} = T_{34} = T_{45} = 1, && T_{52} = \alpha\beta, && T_{61} = (1-\alpha)(1-\beta). \end{aligned} \tag{4.5}$$

The transmission coefficients for $M < 0$ are related via $T_{ij}(M < 0) = T_{ji}(M > 0)$. Using $V_6 = 0$, $I_1 = -I_6 = I$ and $I_2 = I_3 = I_4 = I_5 = 0$, Eq. 4.1 can be solved for I and V_i. The three-terminal resistance $R_{1\text{-}6,5\text{-}6}$ then becomes:

$$R_{1\text{-}6,5\text{-}6} = \frac{V_5 - V_6}{I} = \begin{cases} \frac{\beta}{1-\beta}\frac{h}{e^2} & \text{for } M > 0, \\ \frac{1}{1-\beta}\frac{h}{e^2} & \text{for } M < 0, \end{cases} \tag{4.6}$$

where $R_{1\text{-}6,5\text{-}6}$ only depends on β, the breakdown in the small contact arm, as one would expect.

Moreover, taking the difference between both magnetization directions yields:

$$R_{1\text{-}6,5\text{-}6}(M<0) - R_{1\text{-}6,5\text{-}6}(M>0) = \frac{h}{e^2}. \tag{4.7}$$

Hence, the breakdown near the source/drain contact will result in a constant offset of the hysteresis loop in the magnetic-field dependence of the three-terminal resistance. Note that all nonlocal resistances are equal, i.e. $R_{1\text{-}6,2\text{-}6} = R_{1\text{-}6,3\text{-}6} = R_{1\text{-}6,4\text{-}6} = R_{1\text{-}6,5\text{-}6}$, as there are no leakage channels in the nonlocal region (see appendix D for the inclusion of nonlocal leakage paths). Lastly, if the three-terminal resistance is measured with respect to contact 1, an expression similar to Eq. 4.6 is found, which only depends on α instead of β.

4.3 Nonlocal Transport & Breakdown

To clearly disentangle dissipative bulk current paths from the chiral edge channel, the transport properties of the QAHE were studied in a nonlocal measurement geometry. In the measurement shown in Figs. 4.6(b-d), the current flowed from contact 1 to 14. From the point of view of local/nonlocal transport, contacts 0 to 14 belong to the 'local' transport region, while contacts 15 to 25 are in the 'nonlocal' region. The four-terminal resistance $R_{1\text{-}14,6\text{-}10}$ and $R_{1\text{-}14,6\text{-}5}$ correspond to the longitudinal and transverse resistance, respectively. As can be seen from Figs. 4.6(b-d), the sample shows an ideal QAHE for a probe current of 10 nA. The nonlocal resistance $R_{1\text{-}14,17\text{-}21}$ shows a near perfect zero resistance throughout the magnetic-field sweep. This indicates either a near-perfect nonlocal (and dissipationless) edge transport or the absence of current flow in the nonlocal region. If the latter is the case, the potential of contact 25 would always be equal to the drain potential of contact 14, and hence $R_{1\text{-}14,0\text{-}25}$ would be zero for $M < 0$. However, the observed $R_{1\text{-}14,0\text{-}25}$ is quantized to $-h/e^2$ for $M < 0$, meaning that the potential of contact 25 is equal to the source potential of contact 1. This proves that the nonlocal edge transport is realized.

Having demonstrated an ideal QAHE and nonlocal transport, the breakdown of the QAHE with increasing probe current will be addressed next. Figure 4.7 shows the voltages appearing at three different contact pairs as a function of the DC probe current $I_{1\text{-}14}$ for the same configuration as shown in Fig. 4.6(a). While the breakdown is clearly observed in the local transport region, dissipationless edge transport is maintained in the nonlocal region: As shown in Fig. 4.7, $V_{17\text{-}21}$ remains zero beyond $\sim$0.16 μA up to the maximum current employed (0.4 μA), to within the accuracy of our DC measurement ($\sim$1 μV). This is in agreement with our simple Landauer-Büttiker model shown in Fig. 4.5, and points to the

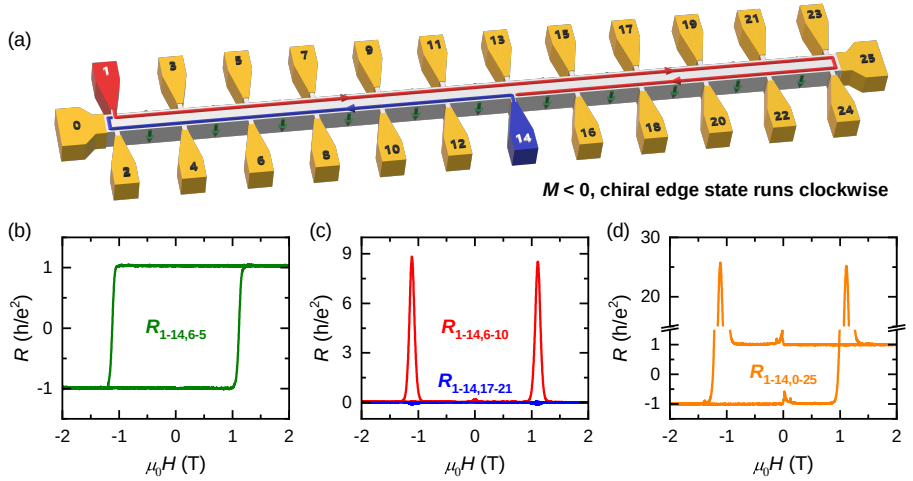

Figure 4.6: Local and nonlocal transport measured below the breakdown current in device A. (a) Schematic picture of the 26-terminal Hall-bar device with a width of 100 μm. The red (blue) line shows the high (low) potential portion of the chiral edge state for a downward, out-of-plane magnetization ($M < 0$) when current flows from contact 1 to 14. (b-d) Magnetic-field dependence of the resistance measured between contacts 6-5 (b), 6-10 and 17-21 (c), and 0-25 (d), showing the QAHE in the local and nonlocal regions at 15 mK, measured with a DC current of 10 nA. The small peaks near $\mu_0 H \approx 0$ T are heating artifacts in the dilution refrigerator, resulting from a temporary increase of the sample temperature when inverting the magnetic-field orientation of the SC magnet.

large transverse electric field as the driving force for breakdown, as was also suggested in Refs. [50, 83]. Such a large electric field is absent in the nonlocal region where the edge potential is constant (see appendix E for additional data); as a result there is no loss of edge current and no dissipation in the nonlocal region (see appendix D for a detailed Landauer-Büttiker treatment).

A possible trivial explanation for the apparent absence of breakdown in the nonlocal region would be that once breakdown occurs in the local transport region, most or all of the current reaches the drain (contact 14) through dissipative channels rather than the chiral edge state. To address this question, Fig. 4.8(b) shows the three-terminal rms-voltage $V_{\rm rms}$ as a function of the AC rms-current $I_{\rm rms,1\text{-}12}$, which flows from contact 1 to 12. For an upward, out-of-plane magnetization ($M > 0$), the chiral edge state runs counterclockwise along the sample edge, as shown in Fig. 4.8(a). Hence, $V_{5\text{-}12}$ and $V_{6\text{-}12}$ correspond to the low- and high-potential branches of the chiral edge state, respectively. Their

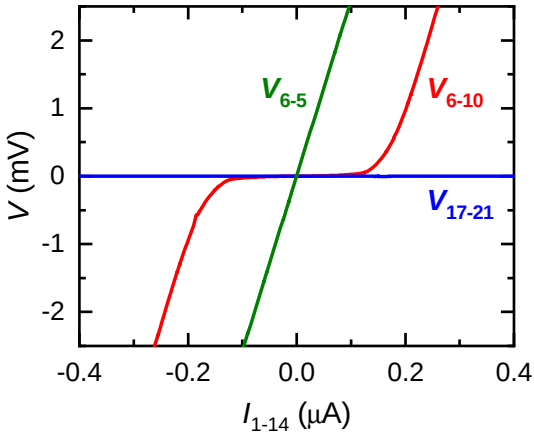

Figure 4.7: Four-terminal current-voltage characteristics in the local and nonlocal transport regions for the same configuration as shown in Fig. 4.6(a), measured at 15 mK in +2 T. The breakdown of the QAHE occurs only in the local transport region ($V_{6\text{-}10}$) at ∼0.16 μA, whereas dissipationless charge transport persists in the nonlocal region ($V_{17\text{-}21}$).

difference approximately follows the relation $\sim (h/e^2)I_{\mathrm{rms,1\text{-}12}}$. It is important to note here that Fig. 4.8(b) was measured using the AC lock-in technique, hence V_{rms} is integrated over the AC probe current up to the peak-current amplitude $I_{\mathrm{peak,1\text{-}12}} = \sqrt{2}I_{\mathrm{rms,1\text{-}12}}$. As a result, the features of Fig. 4.8(b) are slightly smoothened as compared to a DC I-V characteristic.

At $I_{\mathrm{rms,1\text{-}12}} \approx 60$ nA, a dent can be seen in the curves for $V_{5\text{-}12}$ and $V_{6\text{-}12}$ in Fig. 4.8(b). This corresponds to the breakdown of the QAHE in the 'local' 100-μm-wide section of the Hall-bar; namely, the peak-amplitude of the probe current $I_{\mathrm{peak,1\text{-}12}} \approx 85$ nA becomes equal to the breakdown current I_{c}. Moreover, $V_{5\text{-}12}$ and $V_{6\text{-}12}$ are not zero below $I_{\mathrm{rms,1\text{-}12}} \approx 60$ nA due to a second resistance contribution stemming from the breakdown of the QAHE in the 20-μm-wide drain contact 12 [see Fig. 3.9(b) for schematics]. The voltage $V_{19\text{-}12}$ is nonlocal and corresponds to the low-potential branch of the chiral edge state for $M > 0$; as a result, its value is entirely determined by this second resistance contribution stemming from the breakdown in the drain (contact 12). In other words, $V_{5\text{-}12}$ is equal to $V_{19\text{-}12}$ up to ∼60 nA where the Hall-bar (with the exception of the source and drain regions) is in the zero-resistance state. Above ∼60 nA, $V_{5\text{-}12}$ (and $V_{6\text{-}12}$) acquire a larger slope due to the breakdown in the local region of the Hall-bar, while the nonlocal voltage $V_{19\text{-}12}$ does not show an abrupt change in slope.

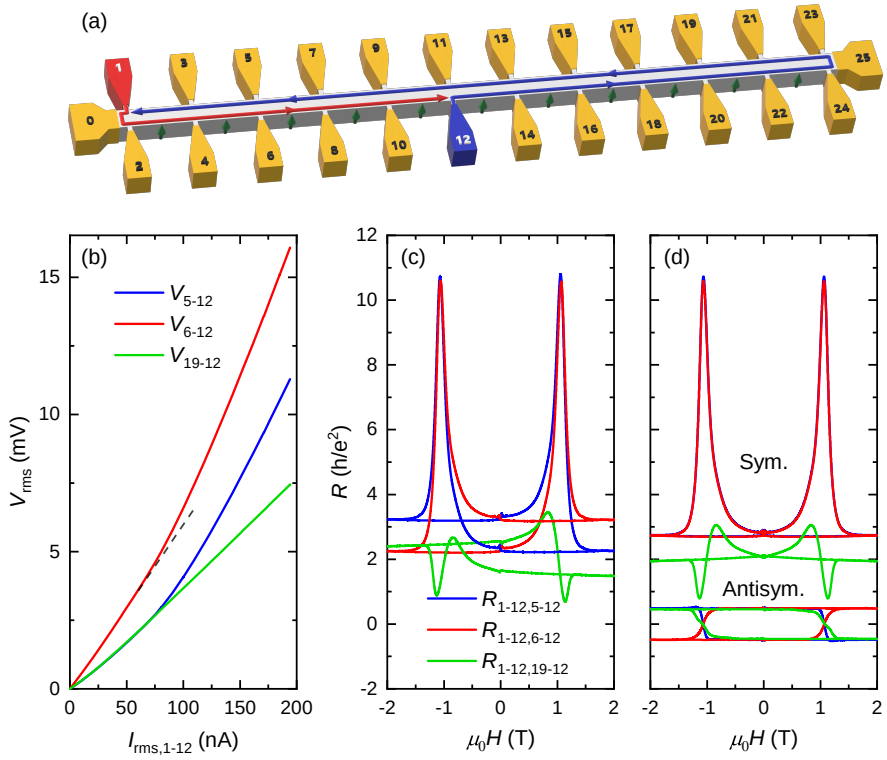

Figure 4.8: Local and nonlocal transport measured above the breakdown current in the 26-terminal Hall-bar device C. (a) Schematic of the high (red) and low (blue) potential portions of the chiral edge state for $M > 0$; arrow heads signify the direction of the current flow. The geometry is the same as in Figs. 4.6 and 4.7 with the slight difference that contact 12 is grounded instead of contact 14, and that M is reversed. (b) Three-terminal rms-voltages $V_{5\text{-}12}$, $V_{6\text{-}12}$, and $V_{19\text{-}12}$ vs the AC rms-current $I_{\mathrm{rms},1\text{-}12}$ measured at 20 mK in +2 T with respect to the 20-μm-wide contact 12. (c) Magnetic-field dependencies of the three-terminal resistances $R_{1\text{-}12,5\text{-}12}$ (blue), $R_{1\text{-}12,6\text{-}12}$ (red), and $R_{1\text{-}12,19\text{-}12}$ (green) measured at 20 mK with an AC rms-current of 200 nA. (d) Symmetric and antisymmetric components of $R_{1\text{-}12,5\text{-}12}$, $R_{1\text{-}12,6\text{-}12}$, and $R_{1\text{-}12,19\text{-}12}$.

Figure 4.8(c) shows the magnetic-field dependence of the corresponding three-terminal resistances $R_{1\text{-}12,5\text{-}12}$, $R_{1\text{-}12,6\text{-}12}$, and $R_{1\text{-}12,19\text{-}12}$. In the ideal case (i.e. $\beta = 0$ in Eq. 4.6), a zero to h/e^2 transition upon magnetization reversal is expected for $R_{1\text{-}12,5\text{-}12}$, $R_{1\text{-}12,6\text{-}12}$, and $R_{1\text{-}12,19\text{-}12}$. Since the three-terminal resistances are measured with an AC rms-current of 200 nA, which is well above breakdown, $R_{1\text{-}12,5\text{-}12}$ and $R_{1\text{-}12,6\text{-}12}$ acquire a large longitudinal resistance contribution from the broken-down QAH state in the local region of the Hall-bar. Additionally, $R_{1\text{-}12,5\text{-}12}$, $R_{1\text{-}12,6\text{-}12}$ and $R_{1\text{-}12,19\text{-}12}$ also pick up a second resistance contribution stemming from the breakdown of the QAHE in the 20-μm-wide drain contact 12, as discussed above.

Figure 4.8(d) shows the symmetric and antisymmetric components of $R_{1\text{-}12,5\text{-}12}$, $R_{1\text{-}12,6\text{-}12}$, and $R_{1\text{-}12,19\text{-}12}$. The symmetric components of $R_{1\text{-}12,5\text{-}12}$ and $R_{1\text{-}12,6\text{-}12}$ are equal to the resistance contribution from the broken-down QAHI state, while their antisymmetric component shows a square hysteresis loop with the resistance value equal to $\sim 0.48h/e^2$. This corresponds to the expected zero to h/e^2 transition upon magnetization reversal for this configuration. The deviation of $\sim$4% from h/e^2 is a consequence of the broken-down QAH state in the local Hall-bar region. Notice that the antisymmetric component of $R_{1\text{-}12,19\text{-}12}$ overlaps with the hysteresis loop of $R_{1\text{-}12,5\text{-}12}$ and $R_{1\text{-}12,6\text{-}12}$. Hence, no loss of the edge potential occurs in the nonlocal region. The observed magnetic-field dependence of $R_{1\text{-}12,19\text{-}12}$ speaks against the trivial explanation mentioned above, proving the presence of the QAH edge current in the nonlocal region even above the current-induced breakdown of the QAHE. Based on the transport data measured below and above breakdown (Figs. 4.7 and 4.8, respectively) it can be concluded that the breakdown of the QAHE, to be understood as the loss of the dissipationless edge transport, solely occurs in the local transport region of the Hall-bar device.

4.4 Spurious Contributions to the Three-terminal Resistance

In the previous section, it was already shown that breakdown plays a strong role near the source and drain contacts, where the high- and low-potential branches of the chiral edge state come together. However, the measurement shown in Fig. 4.8 is rather complicated. Hence, it is instructive to briefly address the breakdown in narrow contacts, and show that it can lead to a large spurious contribution to the measured three-terminal resistance.

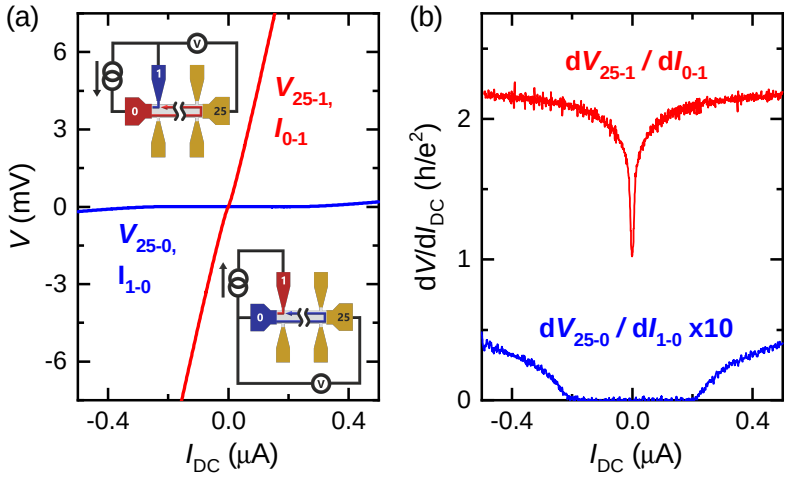

Figure 4.9: Breakdown of the QAHE in narrow contacts. (a) The three-terminal current-voltage characteristic of device B for contact 0 (100 μm, blue) and contact 1 (20 μm, red) with contact 25 as reference, measured at 40 mK in +2 T ($M > 0$). Insets show the measurement configurations. (b) Corresponding differential resistance for contacts 0 and 1. The curve for $dV_{25\text{-}0}/dI_{1\text{-}0}$ is magnified by a factor of 10 for clarity.

In the 26-terminal Hall-bar devices used in this thesis, contacts 1 to 24 are made via a 20-μm-wide section of the magnetic TI film, while contacts 0 and 25 are made along the full width (100 μm) of the device [see Fig. 3.9(b) for schematics]. To elucidate the adverse effect of a narrow contact on the breakdown, the three-terminal measurement geometry is used involving contacts 0, 1, and 25. Figure 4.9 shows the three-terminal I-V characteristics and corresponding differential resistance for two configurations with $M > 0$. The voltage $V_{25\text{-}0}$ was measured with contact 0 as the drain ($I_{1\text{-}0}$). Since the edge current flows counterclockwise for $M > 0$, contact 25 was at the drain potential in this measurement. Indeed, the differential resistance $dV_{25\text{-}0}/dI_{1\text{-}0}$ is approximately zero with an upturn at $\sim$0.16 μA due to the breakdown of the QAHE. Hence, there is no additional resistance associated with contact 0.

On the other hand, $V_{25\text{-}1}$ was measured with contact 1 as the drain ($I_{0\text{-}1}$). Now contact 25 is at the source potential, and hence $dV_{25\text{-}1}/dI_{0\text{-}1}$ should be equal to h/e^2. However, $dV_{25\text{-}1}/dI_{0\text{-}1}$ immediately deviates from h/e^2 for any value of the current I_{DC} [see the red curve in Fig. 4.9(b)]. As demonstrated in section 4.2 using the Landauer-Büttiker formalism [28], this can be explained by the large electric field appearing in the narrow contact arm, causing an

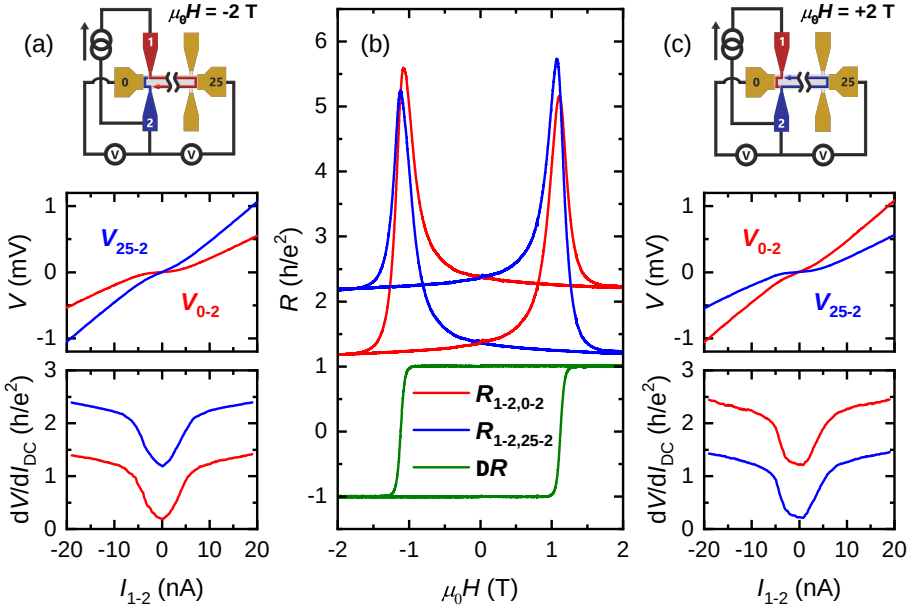

Figure 4.10: The three-terminal resistance of the 20-μm-wide contact 2 of the 26-terminal Hall-bar device B measured at 40 mK. (a) Schematic of the high (red) and low (blue) potential branch of the chiral edge state at $\mu_0 H = -2$ T with the measurement-circuit configuration (top), corresponding I-V characteristics (middle), and the corresponding differential resistances (bottom). (b) Magnetic-field dependencies of the three-terminal resistances $R_{1\text{-}2,0\text{-}2}$ and $R_{1\text{-}2,25\text{-}2}$, measured with $I_{\mathrm{DC}} = 30$ nA. $\Delta R \equiv R_{25\text{-}2} - R_{0\text{-}2}$ reconstructs the four-terminal transverse resistance. (c) Schematic of the chiral edge state potential at $\mu_0 H = +2$ T with the measurement-circuit configuration (top), corresponding I-V characteristics (middle), and the corresponding differential resistances (bottom).

immediate breakdown and enhancing the three-terminal resistance (see Eq. 4.6). This demonstrates the necessity to avoid a three-terminal configuration with a narrow contact to minimize the breakdown effect. For example, in a recent study using a ∼200-nm-wide Nb electrode on top of a QAHI film, the breakdown of the QAHE was the dominant contribution to the measured conductance [84], making it difficult to detect the Andreev reflection at the Nb/QAHI interface.

To gain further insight into the effect of the current-induced breakdown near the source/drain contacts, the magnetic-field dependence of the three-terminal resistance of the 20-μm-wide contact 2 is shown in Fig. 4.10. The resistances $R_{1\text{-}2,0\text{-}2}$ and $R_{1\text{-}2,25\text{-}2}$ are measured with contact 2 as the drain. For an upward, out-of-plane magnetization ($M > 0$), $R_{1\text{-}2,0\text{-}2}$ represents the high-potential branch of the chiral edge state, while $R_{1\text{-}2,25\text{-}2}$ represents the low-potential branch. In the absence of breakdown, the hysteresis loop of $R_{1\text{-}2,0\text{-}2}$ ($R_{1\text{-}2,25\text{-}2}$) should go from zero ($h/e^2$) at $M < 0$ to h/e^2 (zero) at $M > 0$, see Eqs. 4.6–4.7. For the 20-μm-wide contact 2, however, the hysteresis loop is offset by about ∼31 kΩ. When the difference $\Delta R = R_{1\text{-}2,0\text{-}2} - R_{1\text{-}2,25\text{-}2}$ is taken, both the resistance peaks at the coercive field and the offset due to breakdown disappear [green curves in Fig. 4.10(b)]. The ΔR curves show an ideal hysteresis loop from $+h/e^2$ to $-h/e^2$, as expected for a four-terminal Hall measurement of the QAHE below breakdown. This demonstrates that the breakdown affecting the three-terminal measurement is confined to the region with the shortest separation between the high- and low-potential branches of the chiral edge state, i.e. at the source/drain contacts.

4.5 Width Dependence of the Critical Current

To investigate the scaling of the critical current I_c on the edge state separation W, four types of 6-terminal Hall-bar devices F, G, H, I were fabricated on the same V-doped $(Bi_xSb_{1-x})_2Te_3$-InP wafer (see table 3.1 for details) with their Hall-bar (contact) widths equal to 100 μm (30 μm), 150 μm (40 μm), 200 μm (50 μm), and 250 μm (60 μm), respectively. Figures 4.11(a-b) show representative three- and four-terminal I-V characteristics for devices F2, G2, H, and I. By employing both the three-terminal and four-terminal geometries, the dependence of breakdown on the edge state separation could be probed over a range of 30 to 250 μm. One can see an approximately linear dependence of I_c on W in Fig. 4.11(c), which corroborates the assumption that the transverse electric field governs the breakdown process.

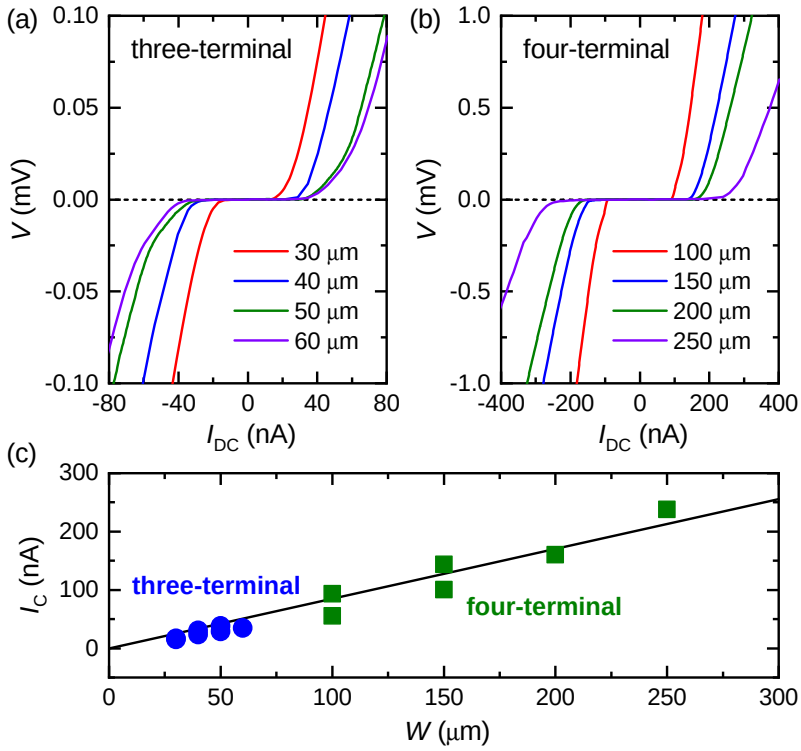

Figure 4.11: Current-voltage characteristics showing the current-induced breakdown of the QAHE at 25 mK in 0 T (after training at +2 T), measured for various widths of the sample in the three-terminal (a) and four-terminal (b) geometries. The specified widths in panels (a) and (b) correspond to the contact and Hall-bar widths, respectively, of devices F2, G2, H, and I (cf. table 3.1). The devices were fabricated on the same wafer. (c) Corresponding width dependence of the critical current I_c. The black solid line is a linear fit through both data sets, yielding a slope of $\sim$0.85 nA/μm.

Namely, breakdown occurs at a particular value of the nominal critical current density

$$j_{\mathrm{c}} \equiv \frac{I_{\mathrm{c}}}{W} \sim \frac{e^2}{h} E_{yx}, \tag{4.8}$$

independent of the device dimensions, as one can infer from Figs. 4.2(c-d) and 4.11(c). The procedure used in this thesis to extract the value of the critical current I_{c} is given in appendix C.

4.6 Temperature Dependence of Breakdown

Now we turn to the temperature dependence of the breakdown effect. The 6-terminal devices D and E were measured in the regular four-terminal Hall-bar geometry. Figure 4.12(a) shows a 2D mapping of the longitudinal voltage V_x as functions of temperature T and probe current I_{DC}; the plots of V_x vs I_{DC} at selected temperatures are shown in Fig. 4.12(b). A well-extended zero-voltage plateau is seen up to ∼100 mK, while a linear I-V relation is slowly restored at higher temperatures. The temperature dependence of the current density j_{c}, which tends to saturate towards lower T, is plotted in Fig. 4.12(c).

Figure 4.12(d) shows the longitudinal and transverse sheet conductance, σ_{xx} and σ_{xy}, calculated using the relations:

$$\sigma_{xx} = \frac{\rho_{xx}}{\rho_{xx}^2 + \rho_{yx}^2}, \quad \sigma_{xy} = \frac{\rho_{yx}}{\rho_{xx}^2 + \rho_{yx}^2}, \tag{4.9}$$

where $\rho_{xx} = R_{xx}(W/L)$ and $\rho_{yx} = R_{yx}$ are the longitudinal and transverse sheet resistance, respectively. The longitudinal conductance σ_{xx} is fitted well by

$$\sigma_{xx} = \sigma_0 e^{-T_0/T}, \tag{4.10}$$

at high temperature, showing that the thermal activation of charge carriers determines the conductance above ∼100 mK with a small activation energy of $k_{\mathrm{B}}T_0 \approx 40$ μeV (i.e. $T_0 \approx 0.5$ K). This value is comparable to the values ∼17–121 μeV found in previous transport studies [17, 31, 50, 83, 137, 159]. It is worthwhile to note that this activation energy is much smaller than the exchange gap of ∼14–28 meV observed in scanning tunneling spectroscopy [37, 101], hinting at the role of disorder.

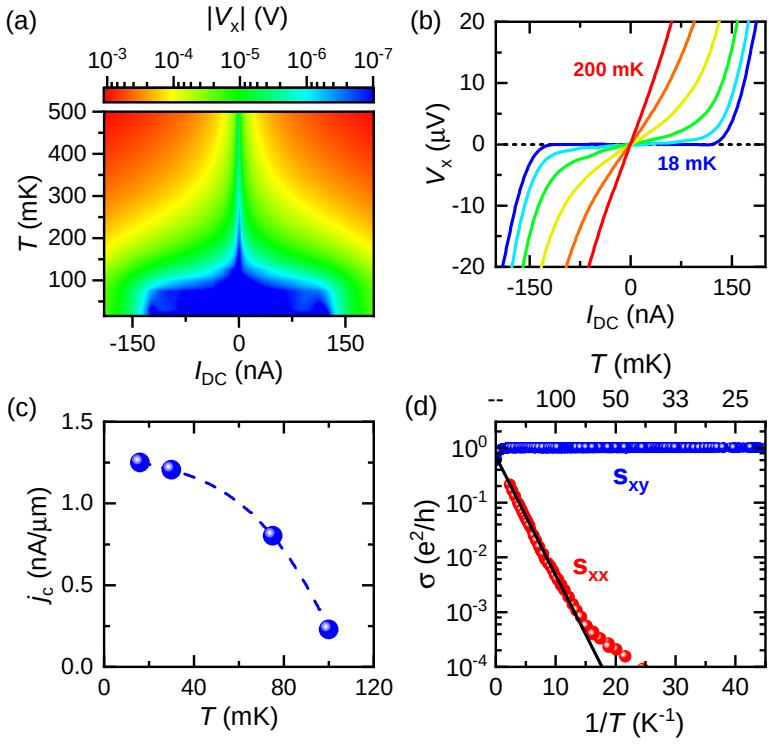

Figure 4.12: Temperature dependence of the QAHE in 0 T after training at +2 T. (a) 2D color mapping of the longitudinal voltage $|V_x|$ as functions of T and I_{DC} for the 100-μm-wide device E. (b) V_x vs I_{DC} at 18, 100, 125, 150, 175, and 200 mK, showing the evolution of the current-induced breakdown curve. (c) Plot of the critical current density j_{c} as a function of T; the dashed line is a guide to the eye. (d) Arrhenius plot of the longitudinal conductance σ_{xx} and transverse conductance σ_{xy} of device D, measured with an AC rms-current of 10 nA. The black solid line is a fit of Eq. 4.10 to the linear regime of σ_{xx}, yielding $T_0 \approx 0.5$ K.

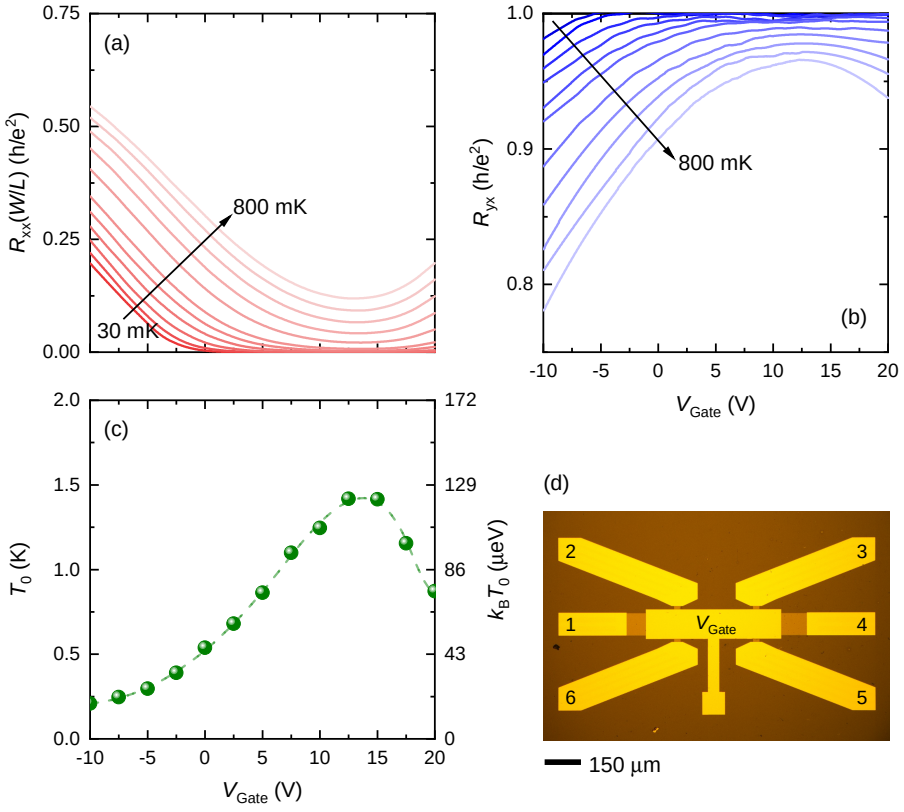

Figure 4.13: (a-b) The gate-voltage dependence of $R_{xx} = R_{1\text{-}4,2\text{-}3}$ (a) and $R_{yx} = R_{1\text{-}4,6\text{-}2}$ (b) at different temperatures $T = 30$, 100, 150, 200, 250, 300, 400, 500, 600, 700, and 800 mK for device F1, measured with $I_{DC} = 10$ nA in 0 T (after training at +2 T). R_{xx} is normalized by the Hall-bar width $W = 100$ μm and voltage-contact spacing $L = 350$ μm for a fair comparison. (c) Gate-voltage dependence of the activation temperature T_0, extracted by fitting Eq. 4.10, with $\rho_{xx} = dV_x/dI_{DC}(W/L)$ and $\rho_{yx} = dV_y/dI_{DC}$ obtained from the differential resistance measurement with an AC excitation of $I_{rms} = 1$ nA. (d) Picture of the 6-terminal Hall-bar device F1 with top-gate electrode. The device was measured in the regular four-terminal Hall-bar geometry with the current flowing from contact 1 to 4.

4.7 Gating Dependence of the QAHE

Until now the breakdown of the QAHE has been studied at zero gate voltage. However, due to fluctuations in the experimental conditions as-grown QAH films do not have the Fermi level located exactly in the middle of the exchange gap [Fig. 4.3(a)]. Hence, electrostatic gating will help to improve the breakdown current I_c of QAH films, and allow the investigation of I_c as the Fermi level is swept across the exchange gap. Figure 4.13 shows the V_{Gate}-dependence of R_{xx} and R_{yx} at different temperatures for the 100-μm-wide Hall-bar device F1 with top-gate. A well-pronounced zero-resistance (quantized) plateau for R_{xx} (R_{yx}) is seen over a large gate-voltage range up to ∼150 mK, after which R_{xx} and R_{yx} start to deviated from the ideal QAHE. Using Eq. 4.10, the activation temperature T_0 can be extracted as a function of V_{Gate}, see Fig. 4.13(c). As expected, T_0 reaches a maximum in the middle of the zero-resistance plateau, corresponding to the Fermi level being on average in the middle of the exchange gap. Note that the sample quality (at $V_{\mathrm{Gate}} = 0$ V) of device F1 is comparable to device D shown in Fig. 4.12, i.e. $k_{\mathrm{B}}T_0 \approx 45$ μeV. This activation energy increases to ∼120 μeV in the middle of the plateau, but is still significantly smaller than the expected size of the exchange gap of ∼14–28 meV [37, 101].

Next, the same experiment is shown in Figs. 4.14(a-b), but now the V_{Gate}-dependence of R_{xx} and corresponding differential resistance dV_x/dI_{DC} were recorded for different values of the current I_{DC} on the 150-μm-wide Hall-bar device G1. A zero-resistance plateau is maintained up to 600 nA, after which breakdown occurs at the charge-neutrality-point ($V_{\mathrm{CNP}} = +14$ V) at $I_c \approx 625$ nA (i.e. $j_{\mathrm{c}} \approx 4.16$ nA/μm), see the I-V characteristics at different V_{Gate} in Fig. 4.14(c). Moreover, notice the small difference in the resistance values between the R_{xx} and dV_x/dI_{DC} curves at the same value of I_{DC}, which is the consequence of the nonlinear I-V relation. The V_{Gate}-dependence of the critical current density j_{c}, which shows a peak at the CNP, is plotted in Fig. 4.14(d).

Lastly, it is important to comment on the gating efficiency. The activation energy at the CNP is about ∼120 μeV, and the zero-resistance plateau spans about ∼38 V (assuming the size of the plateau is symmetric around $V_{\mathrm{CNP}} = +14$ V). This means the gating efficiency corresponds to only a few μeV/V. This is surprisingly low, if one compares it to the gating efficiency of the $(Bi_xSb_{1-x})_2Te_3$ nanowires (with a rectangular cross-section of thickness ∼16 nm and width ∼200 nm) reported by Legg *et al.* [103], which have a nearly identical gate stack (40-nm Al_2O_3 dielectric covered with a 5/40 nm Pt/Au electrode), and were fabricated in the same clean room. Legg *et al.* could tune the Fermi level through the 2D surface Dirac cone, effectively moving from the 3D valence band to the 3D conduction band (∼300 meV), using only a gate voltage range of

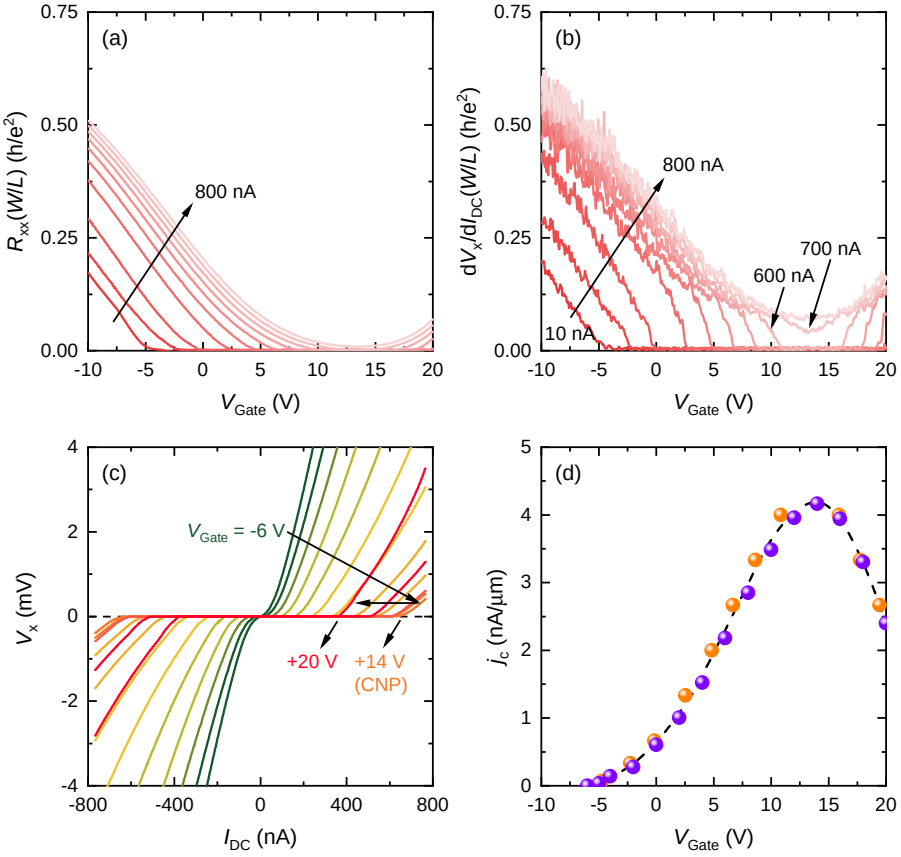

Figure 4.14: (a-b) The gate-voltage dependence of $R_{xx} = R_{1\text{-}4,6\text{-}5}$ (a) and the corresponding differential resistance dV_x/dI_{DC} (b) at different DC current values $I_{\mathrm{DC}} = 10$, 50, 100, 200, 300, 400, 500, 600, 700, and 800 nA for device G1, measured at 30 mK in 0 T (after training at +2 T). The dV_x/dI_{DC} curves were measured using an AC excitation of $I_{\mathrm{rms}} = 1$ nA. Both R_{xx} and dV_x/dI_{DC} are normalized by the Hall-bar width $W = 150$ μm and voltage-contact spacing $L = 350$ μm. (c) Four-terminal current-voltage characteristics, measured in steps of 2 V between $V_{\mathrm{Gate}} = -6$ and +20 V. At the CNP ($V_{\mathrm{CNP}} = +14$ V), the breakdown of the QAHE occurs at ∼625 nA. (d) Plot of the current density j_c as a function of V_{Gate}; the orange data points were extracted from (b), and the purple data points from (c). The dashed line is a guide to the eye.

about ∼15 V. Moreover, resistance oscillations close to the CNP with a period of about ∼0.3–0.5 V were identified as subband crossings in the quantum-confined TI nanowire [103]. Note that the corresponding subband spacing is on the order of a few meV. Hence, the gating efficiency of the $(Bi_xSb_{1-x})_2Te_3$ nanowires, as compared to the V-doped $(Bi_xSb_{1-x})_2Te_3$ QAH films, is several orders of magnitude higher. Hence, the Fermi level of the QAH films seems to be pinned in the exchange gap, hinting at a huge (but localized) density of states in the gap. Quantum-capacitance measurements are ideally suited to give further insight here, as it allows for the direct measurement of the density of states and Fermi-level position as a function of the gate voltage without a priori knowledge of the band structure. Such studies were already performed on 2D- and 3D-TIs [39, 71, 72, 96, 194], and are scheduled on our QAH films in collaboration with Prof. Bocquillon in the near future.

4.8 Magnetic-field Dependence of Breakdown

In chapter 1, it was shown that the critical current for the breakdown of the QHE follows an universal $B^{3/2}$-dependence on the applied magnetic-field B (see Fig. 1.4). For the QAHE, the magnetic-field dependence is very different as shown in Fig. 4.15. The applied magnetic field decreases the current needed to break the QAHE, as evidenced by the reduction of the zero-resistance plateau as a function of both the gate voltage and DC current, see Figs. 4.15(a-b). This is contrary to the magneto-transport data of the first realization of the QAHE, where the transverse resistance was quantized to h/e^2, but the longitudinal resistance was several kΩ [30]. In this study, increasing the magnetic-field above 10 T lead to the suppression of the dissipative states in the sample, and a significant reduction of the longitudinal resistance [30]. However, it seems if the zero-resistance state is already realized in the absence of a magnetic field, then applying/increasing the magnetic field actually decreases the critical current density j_c, as shown in Fig. 4.15(c). The data points follow an approximate linear dependence at the CNP, with j_c decreasing by ∼0.5 nA/μm per Tesla.

Recall the low-energy effective Hamiltonian for the QAHE (Eq. 2.16) discussed in chapter 2. In this model the spin-splitting increases by applying a magnetic-field in addition to the exchange field, and the result is a more stable QAH phase. Orbital effects, however, were not considered. Liu *et al.* calculated that the 3D bulk gap of (nonmagnetic) Bi_2Se_3 decreases by a significant amount of ∼160 meV at 5 T due to the formation of Landau levels [113], which might decrease the overall insulating state of the system. Moreover, Böttcher *et al.* calculated a critical orbital field at which the zeroth Landau level of the 2D surface states crosses the Fermi level, and causes a quantum-phase transition

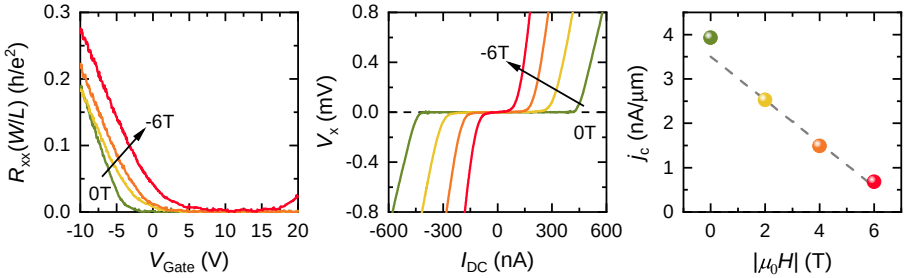

Figure 4.15: Magnetic-field dependence of breakdown, measured at 40 mK. (a) The gate voltage dependence of $R_{xx} = R_{1\text{-}4,6\text{-}5}$ at different values of the magnetic-field $\mu_0 H_c = 0$ T (trained at -2 T), -2 T, -4 T, and -6 T for device F1, measured with $I_{DC} = 10$ nA. R_{xx} is normalized by the Hall-bar width $W = 100$ μm and voltage-contact spacing $L = 350$ μm. (b) The corresponding four-terminal current-voltage characteristics, measured at $V_{CNP} = +13$ V. (d) Plot of the current density j_c at the CNP as a function of the applied magnetic-field. The grey dashed line is a linear fit through the data points, yielding a slope of $\sim$0.5 nA/(Tμm).

from the QAH phase to a trivial insulator [21, 22].[6] Nevertheless, the bulk mobility in our QAH films is only a few hundred cm^2/(Vs), and orbital effects are not expected. Hence, the peculiar magnetic-field dependence of the critical current [Fig. 4.15(c)] is not easily explained by considering orbital and Zeeman contributions to the band structure, and for now remains an open question.

4.9 Absence of Additional Quasi-helical Edge States

Before discussing the different breakdown mechanisms proposed for the QAHE, it is prudent to first comment on the possibility of additional quasi-helical edge states, as predicted by Wang *et al.* [187]. These quasi-helical edge states can be thought of as the remnants of the 2D topological surface states on the side surfaces of a 3D magnetic TI when reducing the thickness to form the quasi-2D QAHI films, see Fig. 4.16. Wang *et al.* predicted an exponential length dependence of the edge potential in case these quasi-helical edge states

[6] The models in Refs. [21, 22] assume an infinite coercive field for the QAHI, which makes their main claim of 'the violation of the Onsager relation' a trivial statement (cf. Fig. 4 in the supplementary material of Ref. [22]). Nevertheless, the calculation of the critical orbital field might have been experimentally relevant, were it not for the low bulk mobility of our QAH films.

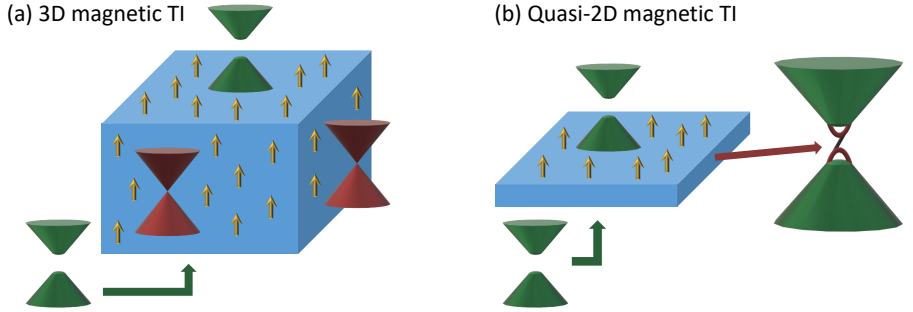

Figure 4.16: Illustration of quasi-helical edge states in a QAHI. (a) A 3D magnetic TI, with the magnetic impurities (yellow arrows) randomly distributed throughout the bulk. The magnetization M is pointing upward. For the top and bottom surfaces, M is out-of-plane breaking TRS and opening an exchange gap in the 2D Dirac cone of the top and bottom surface states (green cones). For the side surfaces, M is in-plane and the 2D Dirac cone of the side surface states remains gapless (red cones). The QAHE cannot be observed, since the side surfaces offer parallel metallic conduction channels to the chiral QAH edge state. (b) A quasi-2D magnetic TI, where the Dirac surface states on the side surfaces are transformed into gapped 'quasi-helical' 1D edge modes due to the confinement effect with decreasing sample thickness. The chiral QAH edge state is shown by the black line crossing the exchange gap; the quasi-helical 1D edge states (red parabola) form a minigap on the side surfaces.

are coexisting with the chiral edge state of the QAHE [187]. The model is reproduced in appendix D (see Eqs. D.14-D.15) for the nonlocal configuration shown in Fig. 4.6(a), and indeed leads to a nonzero and position-dependent edge potential in the nonlocal region of the Hall-bar.

Nevertheless, as seen in Fig. 4.7, no sign of dissipation was observed in the nonlocal region (see appendix E for additional data). Moreover, when the I-V characteristics were recorded for different voltage contact spacings L [see Figs. 4.2(c-d)], a clear linear dependence of R_{xx} on L was observed above breakdown. This too does not fit the expected length dependence of Eqs. D.14-D.15. The absence of a nonlocal position-dependent edge potential, together with the linear relation of R_{xx} on L, point to 2D diffusive transport as the origin of dissipation and speak against the presence of additional dissipative edge states as was proposed in Refs. [31, 94, 187].

4.10 The QAH Breakdown Mechanism

In this section, different breakdown mechanisms for the QAHE will be discussed. Fox *et al.* attributed the breakdown to bootstrap electron heating (BSEH) [50, 90]. However, it will be argued that the heating effect in QAHI films is too small. The percolation of the chiral edge state via magnetic domains and Landau-Zener tunneling between 2D charge puddles will be dismissed as well, as possible breakdown mechanisms. Rather, it will be argued that electric-field-driven percolation of 2D charge puddles in the gapped surface states of the compensated QAH films is the most likely cause of the current-induced breakdown.

4.10.1 Bootstrap Electron Heating

First, let us discuss the role of electron heating in the breakdown process. It is obvious that an abrupt increase in the longitudinal resistance will lead to heating, and that the resulting increase in the electron temperature would accelerate the breakdown process. However, the assumption that electron heating itself lies at the origin of the breakdown of the QAHE is doubtful. In the BSEH model [90], which was discussed in chapter 1 for the integer QHE, the breakdown is attributed to runaway electron heating and described by the balance equation:

$$\rho_{xx}(T_{el})j^2 = \frac{\epsilon(T_{el}) - \epsilon(T_L)}{\tau}, \tag{4.11}$$

with j the current density, $\epsilon(T)$ the energy of the system at temperature T, T_{el} and T_L the electron and lattice temperature, respectively, and τ the relaxation time of the heated electrons [90]. Upon increasing the current, the energy gained by electrons, $\rho_{xx}(T_{el})j^2$, causes Eq. (4.11) to become unstable and a new equilibrium is found at a higher T_{el}. The model is in good agreement with the experimentally observed critical current values of the QHE [90, 127]. Moreover, it is quite generic and independent of the microscopic details of the samples. Hence, the BSEH model can be easily employed to describe the breakdown of the QAHE as well [50].

However, by comparing the critical current density j_c at which breakdown occurs for both the QHE (∼1–10 A/m [2, 9, 73, 141]) and the QAHE (∼1–4 mA/m), it is clear that the heating effect differs by several orders of magnitude. Even if one considers the much smaller excitation energy of the QAHE (∼40–120 μeV in our samples) compared to the QHE ($\hbar\omega_c \approx 10$ meV at 10 T, with ω_c the cyclotron frequency), runaway electron heating seems unlikely. Moreover, if one compares the shape of the breakdown curve of the QHE [Fig. 1.3] to that of the QAHE

[Fig. 1.5(b)], the large vertical jump in the longitudinal resistance at j_c in the QHE case, attributed to the jump in T_{el}, is absent in the QAHE breakdown curves. Hence, while electron heating would accelerate the breakdown of the QAHE, it does not seem to be its origin.

4.10.2 Percolation of the Edge State via Magnetic Domains

In chapter 2, the magnetic disorder in Cr/V-doped $(Bi_xSb_{1-x})_2Te_3$ thin films was discussed, and a scanning SQUID image (Fig. 2.13) of the out-of-plane magnetic field above the surface of a magnetic TI thin film was shown [98]. Rather than a long-range ferromagnetic order, Fig. 2.13 is indicative of a superparamagnetic phase with magnetic domains of a few tens of nm in size [98, 99]. Moreover, Lachman *et al.* reported that even if the sample demonstrates full quantization of the transverse resistance, still a significant fraction of up to 5% of the magnetic domains can be found with the opposite magnetization direction [98].

Figure 4.17 shows a schematic picture of a QAH film with a sizable hybridization gap m_0 (see Eqs. 2.15–2.16) and magnetic disorder (i.e. spatial fluctuations in the size of $|gM|$). In the schematic, the sample consists of isolated magnetic domains/islands with $|gM| > |m_0|$ and Chern number $\mathcal{C} = \pm 1$ in a trivial insulating background with $|gM| < |m_0|$ and $\mathcal{C} = 0$ (see Eq. 2.20). Each magnetic domain constitutes a tiny QAHI with its own chiral 'edge' state, while the macroscopic QAH phase is established via the percolation of these chiral states across the sample. Such a network model was initially proposed by Wang *et al.* to describe the critical behavior of the QAH-plateau transitions near the coercive field (see Fig. 2.12), where magnetic disorder is large [188]. However, in light of the reports of superparamagnetism in Cr-doped $(Bi_xSb_{1-x})_2Te_3$ thin films [98, 99], such a percolation picture with strong magnetic disorder might not only be appropriate for the description of the QAH-plateau transitions near the coercive field [82, 95], but may govern the entire magnetic field range [53]. In this case, the tunneling between the chiral edge states of the small QAHI islands causes a finite leakage current across the width of the sample, resulting in the breakdown of the zero-resistance state.

Let us examine whether such a network model fits the current-induced breakdown of the QAHE in our V-doped $(Bi_xSb_{1-x})_2Te_3$ thin films. In section 4.8, it was shown that the application of a magnetic field decreases the critical current density for breakdown (see Fig. 4.15). This finding is incompatible with the scenario shown in Fig. 4.17. Namely, with increasing magnetic field the fraction of the magnetic domains with the opposite magnetization direction would decrease, reducing the overall magnetic disorder. Moreover, the applied magnetic field would align the spins in the regions of the film with a low

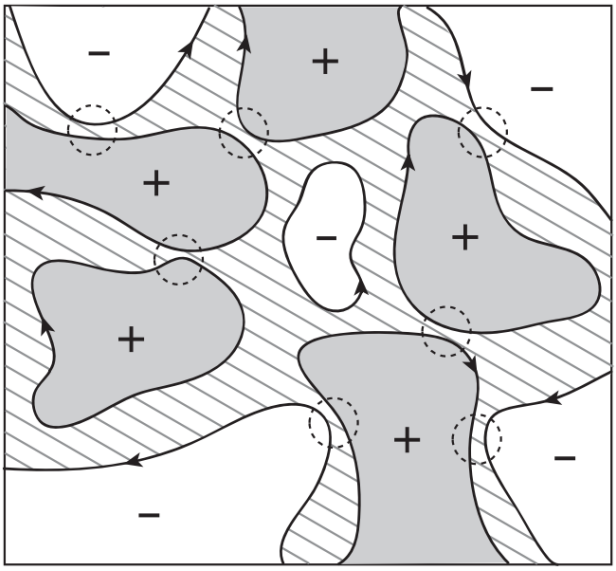

Figure 4.17: Percolation of the chiral edge state at the coercive field, or in the superparamagnetic phase. The magnetic domains with a downward (upward) magnetization direction with $|gM| > |m_0|$ (see Eq. 2.20) are denoted by the symbol + (−) and cover the gray (white) colored regions. The shaded area denotes the region where $|gM| < |m_0|$. The arrows represent the chiral 'edge' states circling the individual magnetic domains, and the dashed circles enclose the tunneling points between the chiral states causing a percolation path across the sample. Reprinted figure with permission from Ref. [188]. © Copyright (2014) by the American Physical Society.

V-concentration, which make up the paramagnetic (and trivial insulating) background of the superparamagnetic phase (shaded area in Fig. 4.17), possibly causing a toplogical phase transition to the QAH phase if $|gM| > |m_0|$ is satisfied. Hence, the 'correctly-aligned' QAHI islands (the magnetic domains) are expected to grow with increasing magnetic field, leading to a more robust macroscopic QAHI. Lastly, it is important to note that the hybridization gap m_0 in our V-doped $(Bi_xSb_{1-x})_2Te_3$ thin films is small due to the relatively large film thickness of ∼8 nm. Hence, the condition $|gM| < |m_0|$ would lead to a trivial insulator with a very small band gap, and the shaded area in Fig. 4.17 would most likely be metallic, rather than insulating as proposed be Wang *et al.* [188]. In the former scenario, the macroscipic QAHE would not be observed as the transport in the thin film would be fully dominated by the trivial metallic background.

In summary, the observation of superparamagnetism in thin films of Cr/V-doped $(Bi_xSb_{1-x})_2Te_3$ [53, 98, 99] suggests that the magnetic disorder is large, and the size of the local exchange gap fluctuates strongly across the sample's surface. Nevertheless, the observation of an ideal QAHE with a well-pronounced zero-resistance state in our thick V-doped $(Bi_xSb_{1-x})_2Te_3$ thin films indicates that the magnetic disorder (away from the coercive field) is not large enough to cause a significant fraction of the sample to undergo a topological phase transition to a trivial insulator. Hence, the network model shown in Fig. 4.17 is not applicable for the description of the current-induced breakdown of the QAHE. However, local reductions in the exchange gap size due to magnetic disorder may lead to the formation of metallic puddles in the sample, which may play an important role as will be discussed in detail in the next section.

4.10.3 Electric-field-driven Percolation of 2D Charge Puddles

To understand the origin of the breakdown, as well as the strongly reduced activation energy, it is useful to consider the role of charge puddles appearing in compensated TI materials [20, 25, 86]. As discussed in chapter 2, it is well established that the puddle formation in 3D compensated TIs is an unavoidable consequence of the long-range nature of the Coulomb interaction [35, 167, 169]. While the 3D bulk puddles are strongly suppressed near the surface due to the screening by the metallic surface states [19, 168], 2D surface puddles are predicted to show up in compensated TI thin films [69]. In this regard, $(Bi_xSb_{1-x})_2Te_3$ is a solid-solution of n-type Bi_2Te_3 and p-type Sb_2Te_3, achieving a charge compensation that results in a vanishing 2D surface carrier concentration at low temperature [92, 213]. In the QAHI films, the tendency to form 2D puddles would be strong, because the averaged chemical potential is tuned into the gap opened at the Dirac point [Fig. 4.3(a)]. In such a case, little surface carriers are available to screen the Coulomb potential and the screening can only occur nonlinearly through the formation of 2D electron and hole puddles [169], as illustrated in Fig. 4.18(a). In addition, the large dielectric constant of TI films slows down the decay of the Coulomb potential in space and greatly enhances the puddle formation [69]. Indeed, signatures of puddle formation have been observed in the resistivity of ultra-thin films of $(Bi_xSb_{1-x})_2Te_3$ [130].

In light of the likely existence of 2D puddles in compensated TI thin films, we propose that the breakdown occurs via the formation of metallic percolation paths connecting these 2D puddles across the width of the sample. The QAHI films can be thought of as an insulating background containing isolated metallic puddles, as shown in Fig. 4.18(c). In analogy to Ref. [176] for the QHE, we propose that at high enough source potential, the insulating regions separating

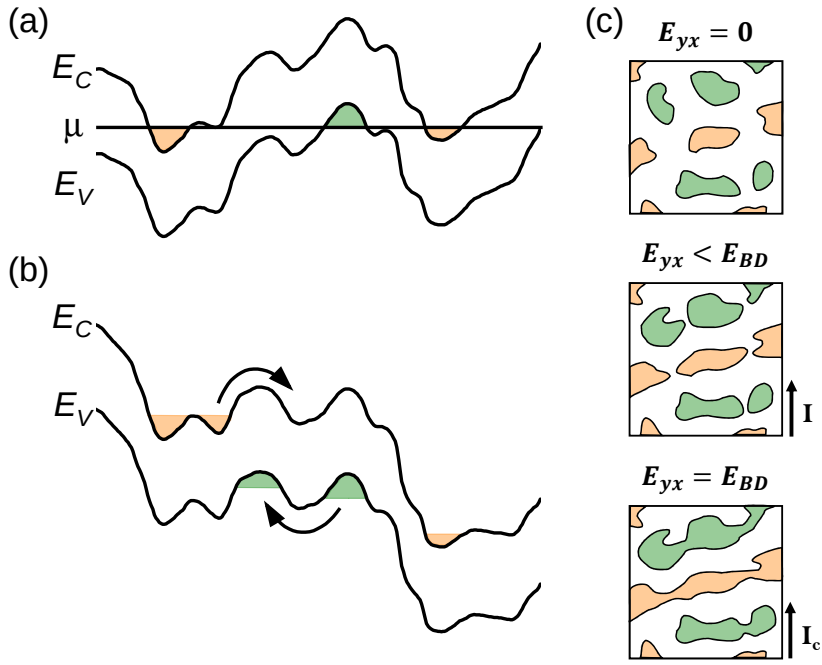

Figure 4.18: Illustration of puddles in compensated QAHI films and their response to an electric field. (a) The spatial variation of the energy spectrum of the gapped 2D surface state. The meandering lines represent the 2D conduction and valence band edges, E_C and E_V, respectively, in the presence of Coulomb disorder. When the Fermi level μ crosses the band edges, electron and hole puddles (shaded regions) are created. (b) The situation close to the breakdown of the QAHE. The arrows depict thermally activated or hopping transport. (c) The growth of the charge puddles with increasing electric field E_{yx} until breakdown occurs at $E_{yx} = E_{\mathrm{BD}}$, based on Ref. [176]. The critical current I_{c} is reached when the source potential produces the electric field E_{BD} between the two opposing edge states causing a metallic short to form across the width of the sample. The shaded regions correspond to electron and hole puddles in an insulating background (white region).

two adjacent electron or hole puddles break down due to the high transverse electric field created across the width of the sample. Since the local potential is constant within the metallic puddles, the electric field is confined to the insulating regions. As the puddles grow with increasing source potential, the local electric field in-between the puddles increases rapidly, facilitating further puddle growth in a non-linear manner, see Fig. 4.18(b-c). At the critical value of the source potential (corresponding to the critical current I_c), the growth becomes unstable and leads to an avalanche process [176], so that the metallic paths percolate from one edge of the sample to the other and causes an abrupt onset of dissipation.

The puddle breakdown mechanism proposed here also sheds new light on the very low temperature required to observe the QAHE, which is much lower than that expected from the Curie temperature T_C (∼15–20 K) or the spectroscopically-resolved exchange gap (∼14–28 meV) [37, 101]. In the presence of charge puddles, electrons are not excited across the 2D exchange gap; rather, electrons and holes are thermally excited from the puddles to the percolation levels [169]. As demonstrated already for 3D bulk puddles in compensated TIs, this reduces the activation energy for thermally-activated transport [35, 167, 169]. Moreover, at low temperature the electrons and holes may hop or tunnel directly between puddles, possibly giving rise to a crossover from activated transport to variable-range-hopping (VRH) behavior [169], as was observed in some transport studies on QAHI films [50, 83]. The puddle scenario is also consistent with the bulk dissipation observed in a Corbino geometry [49, 158].

4.10.4 Zener Tunneling between 2D Charge Puddles

Lastly, Landau-Zener tunneling between neighboring electron-hole puddles is discussed as a possible breakdown mechanism. Estimates of the tunneling probability for such a process in ultrathin TI films possessing a hybridization gap in the 2D surface state spectrum were made in Refs. [69, 130]. Assuming a defect density of $N_{\mathrm{def}} \approx 10^{19}$ cm^{-3}, an insulating state in our QAHI films is expected to be realized for a gap $\Delta >$ 10–60 meV at the Dirac point. This is exactly the range of exchange gap sizes found for magnetically-doped $(Bi_xSb_{1-x})_2Te_3$ thin films [37, 101]. Note that in the presence of charge puddles, the application of an electric field is not required to induce Zener tunneling, because the disorder potential provides the required local electric field and band bending. In other words, in the presence of puddles, Zener tunneling would provide a finite bulk short even at infinitesimally small currents. As a result, no sudden onset of Zener tunneling at some critical current is expected.

It is prudent to mention that an estimate based on Refs. [69, 130] would predict a sizable Zener tunneling in our films. However, a near-dissipationless QAHI state has been experimentally observed, at least for low probe currents, with a longitudinal sheet resistance as low as 1–2 mΩ [50, 133]. This speaks against any major role of Zener tunneling in compensated QAHIs. Nevertheless, Zener tunneling might be relevant to the small, non-vanishing resistance in the pre-breakdown regime.

4.11 Summary

It was demonstrated that the breakdown of the QAHE occurs in the region with the shortest separation between the high- and low-potential branches of the chiral edge state, while it is absent in nonlocal transport regions. This indicates that the transverse electric field is responsible for the breakdown and gives a guiding principle for minimizing the breakdown effect. Moreover, it was argued that the charge puddles play a key role in the breakdown mechanism for the QAHE and govern the diffusive transport through the 2D bulk states.

This chapter (w/o sections 4.7, 4.8, and 4.10.2) was published as:

Lippertz, G., Bliesener, A., Uday, A., Pereira, L. M. C., Taskin, A. A., and Ando, Y. Current-induced breakdown of the quantum anomalous Hall effect. *Phys. Rev. B 106* (Jul 2022), 045419.

Author contributions: Y.A. and A.A.T. conceived and supervised the project. G.L., A.B., A.U., and A.A.T. grew the QAH thin films. G.L. and L.M.C.P. analyzed the thin films. G.L. and A.U. fabricated the Hall-bar devices. G.L., A.B., A.U., and A.A.T. performed the experiments. G.L. performed the (Landauer-Büttiker) analysis of the data with the help of all authors. G.L. and Y.A. wrote the manuscript with input from all authors.

Chapter 5

Nonreciprocal Charge Transport

> *If you have a lemon, make a lemonade.*
>
> Dale Carnegie

In the previous chapter, the current-induced breakdown of the QAHE was studied in a negative light, as something to be avoided for QAHIs to be implemented as a novel resistance standard or as a platform to generate Majorana fermions. However, the interplay between the 1D and 2D electronic states for current densities above breakdown can lead to interesting nonreciprocal (diode-like) contributions to the edge potentials in a QAHI. In this chapter, the nonreciprocity in the edge potential will be investigated for high and low excitation currents, and their potential different origins will be discussed.

5.1 Nonreciprocity in the Edge Potential

Nonreciprocal charge transport, or rectification in plain language, is the phenomenon by which the resistance R has a different amplitude, depending on whether the current flows in the 'forward' or 'reverse' direction, i.e. $R(+I) \neq R(-I)$. The most common example is a semiconductor-diode, consisting of a

pn-junction. When a material or heterostructure lacks inversion symmetry, and time-reversal symmetry (TRS) is additionally broken by applying a magnetic field, an effect known as the 'magnetochiral anisotropy' (MCA) can occur [156, 174]. The MCA takes the form of a second-order correction to Ohm's law [156], such that:

$$V = R_0 I(1 + \beta H^2 + \gamma H I), \tag{5.1}$$

where V is the applied voltage, R_0 the Ohmic resistance term, I the current, β describes the normal magneto-resistance, H the magnitude of the magnetic field, and γ the rectification coefficient. Such nonreciprocal charge transport has been reported in various quantum materials, see table G.1 in the appendix. Moreover, its superconducting (SC) counterpart, known as the 'SC diode effect', has become an exciting new research topic in recent years as well [11, 102, 174].

Yasuda *et al.* were the first to demonstrate nonreciprocal charge transport in Cr-modulation-doped $(Bi_xSb_{1-x})_2Te_3$ thin films[1] at high temperatures and for excitation currents well above the breakdown of the QAHE [201]. The *I*-*V* characteristic was shown to obey:

$$V_{L/R} = R_0 I(1 + \tilde{\gamma} c_{L/R} n_{p/n} \hat{M} I), \tag{5.2}$$

where $V_{L/R}$ is the voltage drop measured along the left/right edge, I the excitation current, R_0 the Ohmic resistance term, $\tilde{\gamma}$ the rectification coefficient, $c_{L/R}$ the measured sample edge ($c_L = +1$ and $c_R = -1$ for the left and right edge, respectively), $n_{p/n}$ the 2D charge-carrier type ($n_p = +1$ and $n_n = -1$ for a *p*- and *n*-type 2D bulk, respectively), and $\hat{M}$ the magnetization direction ($\hat{M} = +1$ and $\hat{M} = -1$ for an upward and downward out-of-plane magnetization).[2]

Notice that γ in Eq. 5.1 for the MCA of a nonmagnetic material in an applied magnetic field has the units $A^{-1}T^{-1}$. On the contrary, $\tilde{\gamma}$ for a QAHI has the unit A^{-1}, as it is the remanent magnetization which determines the amplitude of the nonreciprocal response. Hence, no linear dependence on the applied magnetic field is expected for a QAHI, unlike for the family of materials showing MCA. Moreover, an intriguing distinction can be made for the broken-down QAH state with respect to other material systems displaying nonreciprocal charge transport (see tables G.1 and G.2 in the appendix). In a QAHI it is the chiral edge state itself that breaks the inversion symmetry [201], whereas the QAH system as a whole preserves inversion symmetry, i.e. $V_L + V_R = 0$.

[1] In modulation-doped magnetic TI thin films, the Cr/V dopants are located in a delta-layer close to the top and bottom surfaces of the film and stabilize the QAH phase, while the bulk of the thin film consists of undoped $(Bi_xSb_{1-x})_2Te_3$ [125].

[2] Equation 5.2 was already discussed in chapter 3 (section 3.4.2) in the context of the second-harmonic measurement.

For large current amplitudes in the broken-down QAH state ($I \gg I_c$), the current flows through both the 2D bulk and 1D edge states, see Fig. 5.1(a). Moreover, the high-potential branch of the chiral edge state is losing current to the 2D state, while a fraction of the current flowing through the 2D state scatters into the low-potential branch of the chiral edge state. In the simple Landauer-Büttiker model presented in chapter 4 (section 4.2), the current lost from the high-potential branch was assumed to be equal to the current gained in the low-potential branch. However, with a significant fraction of the current flowing from the source to the drain through the 2D bulk, the 2D states can act as a source or sink of current. Hence, the potential difference along the left and right edge of the sample no longer need to be equal ($V_L \neq V_R$), giving rise to the nonreciprocity in the longitudinal voltage described by Eq. 5.2. To explain this difference in 'leakage' rates between the left and right edges, Yasuda *et al.* argued that asymmetric skew scattering between the chiral 1D edge and gapped 2D surface states can lead to differing rates for edge-to-surface ($W_{\mathrm{E}\to\mathrm{S}}$) and surface-to-edge ($W_{\mathrm{S}\to\mathrm{E}}$) scattering processes [201], see Fig. 5.1(a).

While Yasuda *et al.* studied the nonreciprocal charge transport in the broken-down QAH state at elevated temperatures (0.5–40 K) and in the high-current limit (1–100 μA) [201], the question remains how the nonreciprocity evolves as the QAHI recovers the zero-resistance state (i.e. no 2D surface conduction) at low excitation current ($\lesssim$ 200 nA) and temperatures ($\lesssim$ 100 mK). In this chapter, the nonreciprocal charge transport will be first studied in the high-current limit, and the data will be compared to Eq. 5.2. Next, the nonreciprocal response will be studied for current values near the breakdown transition, and it will be shown that Eq. 5.2 no longer holds.

5.2 The Nonreciprocal Response at High Current

There are two methods to measure the nonreciprocal response. The most straightforward approach is to measure the 'total' longitudinal voltage/resistance using standard DC techniques. This has the advantage that it shows the 'full picture', but the method is generally limited by the requirement of a very high current as the Ohmic term R_0 otherwise completely dominates the signal. The second approach is to measure the second Fourier component (or 'second harmonic'), using standard AC lock-in techniques. The second-harmonic signal has the advantage that it filters out the inversion-symmetry breaking contribution to the measured voltage/resistance (see section 3.4.2 for details). First the DC results will be briefly shown, before addressing the detailed AC data sets.

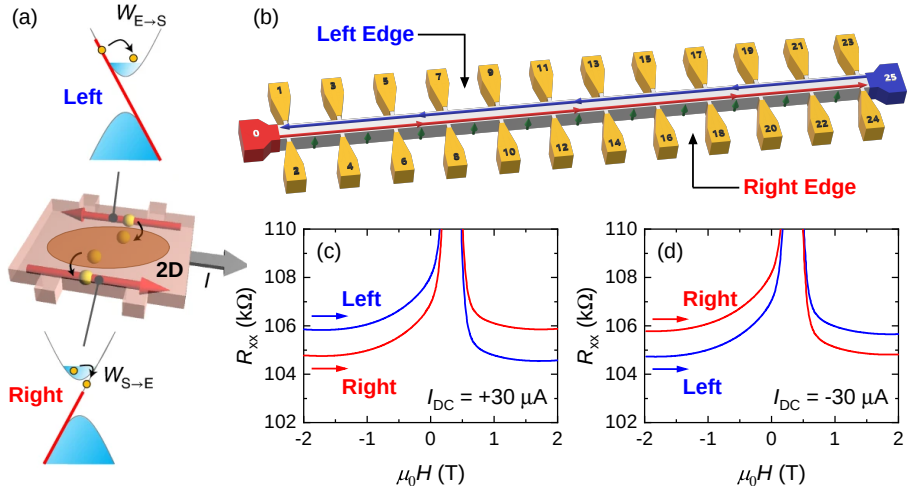

Figure 5.1: Nonreciprocal charge transport of the chiral edge states in the high-current limit. (a) Illustration of the interplay between the 1D chiral edge state and the gapped 2D surface states (for $n_n = -1$ and $\hat{M} = +1$). The energy spectrum is shown for the left and right edge of the Hall-bar device. The yellow spheres represent electrons. The chemical potentials of the edge states differ from that in the surface state, since the scattering rate between the edge and surface states is much smaller than that within the surface state [201]. This image is taken from Ref. [201], and reproduced with permission from SNCSC. (b) Schematic picture of the 26-terminal Hall-bar device C. The red (blue) line shows the high-(low-)potential branch of the chiral edge state for a upward, out-of-plane magnetization ($\hat{M} = +1$). The current flows from contact 0 to 25; the left/right edge is defined looking along the conventional current direction. (c-d) Magnetic-field dependence of the DC longitudinal resistance measured between contact pairs 5-9 ('Left') and 6-10 ('Right') at 3.5 K with $I_{DC} = +30$ μA (c) and $I_{DC} = -30$ μA (d). The coercive-field peaks reach $\sim$155 kΩ, and are not fully shown in the graphs.

5.2.1 The Nonreciprocal Response in DC Transport

The 26-terminal Hall-bar device C was measured in the regular four-terminal Hall-bar configuration with the current flowing from contact 0 to 25, see Fig. 5.1(b). Rather than distinguishing between the high/low-potential branches of the chiral edge state, it will instead be more convenient for the description of the nonreciprocal charge transport to differentiate between the right/left edges of the Hall-bar. Note that the choice of the contact labeling in the 26-terminal devices makes it easy to recognize the even and odd contact pairs as belonging to the right and left edges, respectively.

To investigate whether Eq. 5.2 also holds for uniformly V-doped $(Bi_xSb_{1-x})_2Te_3$ thin films, a DC current well above the critical current for breakdown ($I_c \approx$ 85 nA, see table 3.1) is applied to the sample. Figures 5.1(c-d) show the DC longitudinal resistance for the right and left edge of the device as the applied magnetic field is increased from -2 T to $+2$ T for a current of $I_{DC} = +30$ μA and -30 μA. The sample is highly resistive, far from the ideal QAH state. Notice the splitting of the curves for R_{xx} for the right and left edge; this is the nonreciprocal charge transport of the QAH edge states. The inversion between the amplitude of R_{xx} for the right and left edge at the coercive field, as well as with the change of current direction is in agreement with Eq. 5.2 and signifies the importance of the chirality of the 1D edge state for the observed nonreciprocity. The 2D charge carriers in this QAH thin film (device C) are n-type (see Fig. 3.6 in chapter 3). Hence, the polarity ($\mathcal{P} \equiv c_{L/R} n_{p/n} \hat{M}$) of the observed nonreciprocal response is fully consistent with Eq. 5.2, e.g. R_{xx} of the right edge ($c_R = -1$) > left edge ($c_L = +1$) for an n-type 2D surface state ($n_n = -1$) at $+2$ T ($\hat{M} = +1$) for $+30$ μA.

Figures 5.2(a-b) show the longitudinal voltage V_x for the right and left edge as a function of I_{DC}. The nonreciprocity in V_x is very small and is only clearly visible when inspecting the insets showing the splitting of V_x near ± 30 μA between the opposite magnetization directions ($\hat{M} = \pm 1$). The quadratic I-V relation can be made apparent by taking the difference $\Delta V_{\text{R-L}} \equiv V_{\text{Right}} - V_{\text{Left}}$ between the right and left edges, as shown in Fig. 5.2(c). In this case the dominant Ohmic term $R_0 I_{DC}$ is removed. The corresponding resistance difference $\Delta R_{\text{R-L}}$ [Fig. 5.2(d)] demonstrates a linear dependence on I_{DC} in the range ~5–30 μA. Fitting Eq. 5.2 to the I-V characteristics of Fig. 5.2 yields $R_0 \approx 112$ kΩ and $\tilde{\gamma} \approx 177$ A^{-1}. Similarly, by extracting $\Delta R_{xx}(I_{DC}) = R_{xx}(+I_{DC}) - R_{xx}(-I_{DC}) = 2\tilde{\gamma} R_0 I_{DC} \approx$ 1.07 kΩ (with $R_0 \approx 105$ kΩ) from Figs. 5.1(c-d) yields $\tilde{\gamma} \approx 169$ A^{-1}.

Calculating the current-direction-dependent resistance-ratio $\Delta R/R = 2\tilde{\gamma} I_{DC}$ at $I_{DC} = 30$ μA yields $\Delta R/R \approx 1\%$ for the uniformly V-doped $(Bi_xSb_{1-x})_2Te_3$ thin films at 3.5 K close to the CNP. This is about one order of magnitude

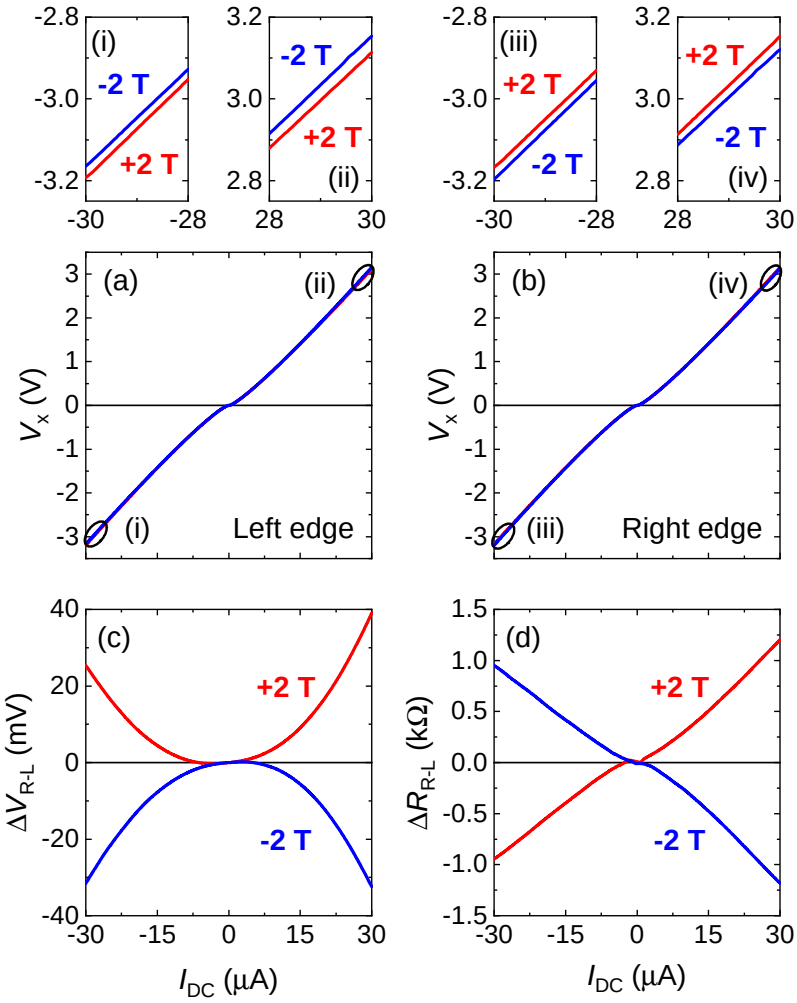

Figure 5.2: I-V characteristic for the 26-terminal Hall-bar device C at 3.5 K in ± 2 T, with the current flowing from contact 0 to 25 [see Fig. 5.1(b)]. The left and right edges correspond to contact pairs 5-9 (a) and 6-10 (b), respectively. The insets (i-iv) show the splitting of V_x near ± 30 μA between the opposite magnetization directions. (c) The I^2-dependence of the voltage difference between the right and left edge, $\Delta V_{\text{R-L}} \equiv V_{\text{Right}} - V_{\text{Left}}$. (d) The corresponding resistance difference $\Delta R_{\text{R-L}} = \Delta V_{\text{R-L}}/I_{\text{DC}}$.

smaller than the amplitudes reported by Yasuda *et al.* for Cr-modulation-doped $(Bi_xSb_{1-x})_2Te_3$ thin films [201], see column '$\Delta R/R/i$' in table G.2 of the appendix for a fair comparison.

5.2.2 The Nonreciprocal Response in AC Transport

For small values of the current (< 5 μA), the nonreciprocal signal could no longer be resolved with standard DC techniques. Hence, it was beneficial to switch the set-up to AC lock-in amplifiers and measure the second-harmonic response to an AC excitation $\sim I_0 \sin(\omega t)$. Using Eq. 5.2, the second-harmonic voltage and resistance then become:

$$V_x^{2\omega} = -\frac{1}{\sqrt{2}}(c_{L/R} n_{p/n} \hat{M}) \tilde{\gamma} R_0 I_{\mathrm{rms}}^2, \tag{5.3}$$

$$R_{xx}^{2\omega} = V_x^{2\omega} / I_{\mathrm{rms}}, \tag{5.4}$$

respectively, with $V_x^{2\omega} \equiv Y^{2\omega}$ and $I_{\mathrm{rms}} = I_0/\sqrt{2}$, see chapter 3 (section 3.4.2) for details. Notice that for the same polarity ($\mathcal{P} \equiv c_{L/R} n_{p/n} \hat{M}$), the nonreciprocal response picks up a minus sign for the AC voltage (Eq. 5.3) as compared to the DC measurement (Eq. 5.2). Moreover, while Eq. 5.3 gives the impression that the measured second-harmonic signal solely depends on the nonreciprocity in the edge potential of the QAHI, in reality the lock-in amplifiers will pick up sizable nonreciprocal contributions from unintentional rectification in the measurement circuit. As a result, it is customary to antisymmetrize the second-harmonic data in the magnetic field (Eq. 5.1), or in our case the magnetization (Eq. 5.2). Note that for a QAHI antisymmetrizing by taking the difference in potential between the left and right edges is also possible, since the QAHI as a whole preserves inversion symmetry.

Figure 5.3(a) shows the V_{Gate}-dependence of $R_{xx}^{2\omega}$ (antisymmetrized in $\hat{M}$) at different temperatures for Hall-bar device F1. The corresponding (first-harmonic) R_{yx} curves are shown in Fig. 5.3(b) for comparison. The CNP is located at $V_{\mathrm{Gate}} \approx 15$ V with $R_{yx} \approx 21.8$ kΩ at 2 K. Figure 5.3(a) shows that the amplitude of $R_{xx}^{2\omega}$ for the left and right edge vanishes near the CNP, and switches sign when the 2D state changes from n- to p-type, consistent with Eq. 5.3 ($n_{p/n} = \pm 1$). This dependence on the 2D charge-carrier type clearly indicates that 2D conduction is required to observe the nonreciprocal transport in a QAHI at high excitation currents. The same sign-inversion is seen when comparing the I-$V_x^{2\omega}$ characteristics at $V_{\mathrm{Gate}} = 0$ V (p-type) and $V_{\mathrm{Gate}} = 25$ V (n-type) shown in Figs. 5.3(c) and 5.3(d), respectively. Notice that $V_x^{2\omega}$ follows an approximate I^2-dependence as expected from Eq. 5.3. It is important to note here that since the I-$V_x^{2\omega}$ relations were measured by

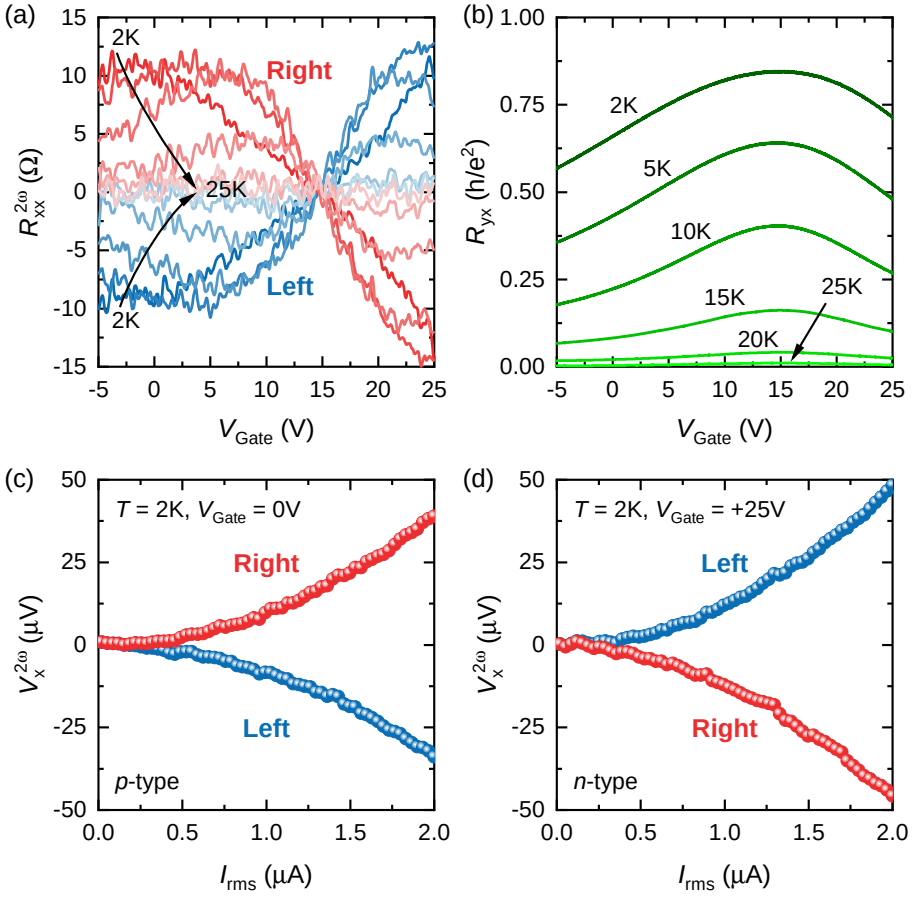

Figure 5.3: Gate-voltage, temperature, and rms-current dependencies of the nonreciprocal charge transport in the high-current limit for Hall-bar device F1. The current flows from contact 1 to 4; the left (right) edge corresponds to the contact pairs 2-3 (6-5), see Fig. 4.13 for a picture. (a) The V_{Gate}-dependence of $R_{xx}^{2\omega}$ for the left and right edges, measured with $I_{\mathrm{rms}} = 1$ μA at $T = 2$ K, 5 K, 10 K, 15 K, 20 K, and 25 K. (b) The corresponding (first harmonic) R_{yx}-curves. The CNP is located at $V_{\mathrm{Gate}} \approx 15$ V, with $R_{yx} \approx 21.8$ kΩ at 2 K. (c-d) $V_x^{2\omega}$ as a function of I_{rms} for the left and right edges at 2 K for $V_{\mathrm{Gate}} = 0$ V (c) and $V_{\mathrm{Gate}} = 25$ V (d). All data were measured in ±0.1 T (after training in ±2 T) to prevent demagnetization over time; the second-harmonic data were antisymmetrized in the magnetization and magnetic-field, i.e. $V_x^{2\omega} = [V_x^{2\omega}(+\hat{M}, +0.1\mathrm{T}) - V_x^{2\omega}(-\hat{M}, -0.1\mathrm{T})]/2$.

increasing the AC excitation current, $V_x^{2\omega}$ at a given I_{rms} is actually integrated from zero up to the peak-current amplitude $I_{\mathrm{peak}} = \sqrt{2} I_{\mathrm{rms}}$. As a result, the features of the curves in Figs. 5.3(c-d) are slightly smoothened as compared to a DC I-V characteristic [Fig. 5.2(c)]. For completeness, Fig. 5.4 shows the (antisymmetrized) magnetic-field dependencies of $R_{xx}^{2\omega}$ for the left and right edge for different gate voltages. A hysteresis loop is seen with $R_{xx}^{2\omega}$ changing sign when crossing the coercive field. The sign-inversions of $R_{xx}^{2\omega}$ between the left and right edges and with the 2D charge-carrier type are clearly seen as well.

Before discussing the temperature dependence, it is important to point out that the observed sign-inversion of $R_{xx}^{2\omega}$ with the 2D charge-carrier type ($n_{p/n}$) excludes leakage through the lock-in amplifiers as a possible trivial origin for the observed nonreciprocal behavior of the edge potential in a QAHI. Namely, the observed sign-inversions of $R_{xx}^{2\omega}$ between the left and right edge ($c_{L/R}$), for the opposite magnetization ($\hat{M}$) and current directions ($\pm I$), could also be explained by current leaking from the high-potential branch of the chiral edge state to ground through the leads of the lock-in amplifiers. Since the low-potential branch of the chiral edge state is at the ground potential, no leakage would take place on this edge. Hence, the leakage would only occur on one of the edges of the Hall-bar, resulting in a trivial nonreciprocal response. Since changing the magnetization or current directions swaps the high- and low-potential branches of the chiral edge state between the left and right edges of the Hall-bar, the trivial nonreciprocal response would change sign accordingly. However, Figs. 5.3(a) and 5.4 clearly demonstrate that the nonreciprocal response can be switched off by tuning the sample to the CNP. At the CNP, R_{yx} reaches a maximum [Fig. 5.3(b)] meaning the potential difference between the high-potential branch of the chiral edge state and the ground is maximum as well. As a consequence, the leakage current, and hence the *trivial* nonreciprocal response, would also be maximized at the CNP. This is exactly opposite to the V_{Gate}-dependence observed for $R_{xx}^{2\omega}$, which rules out the trivial origin for the nonreciprocal response.

Lastly, we turn to the temperature dependence of $R_{xx}^{2\omega}$ at high current ($I_{\mathrm{rms}} = 1\ \mu$A). Figure 5.3(a) already showed the gate-voltage dependencies for $R_{xx}^{2\omega}$ at different temperatures, whereas Fig. 5.5(a) shows the temperature dependence when the sample is heated from 2 K to 50 K at $V_{\mathrm{Gate}} = 0$ V. Figure 5.5(b) shows the temperature dependence of R_{xx} and R_{yx} for comparison; the dashed lines in (a) and (b) mark the Curie temperature $T_{\mathrm{C}} \approx 12$ K. In the absence of an applied magnetic field $R_{xx}^{2\omega}$ vanishes at T_{C}, as indicated by region 'I' in Fig. 5.5(a). This is consistent with the findings of Yasuda *et al.*, indicating that the 1D chiral edge state is a requisite for nonreciprocal charge transport [201]. Additional data in appendix F show the hysteresis loop of $R_{xx}^{2\omega}$ as a function of the magnetic field slowly closing upon reaching T_{C}, see Fig. F.6. However, in a

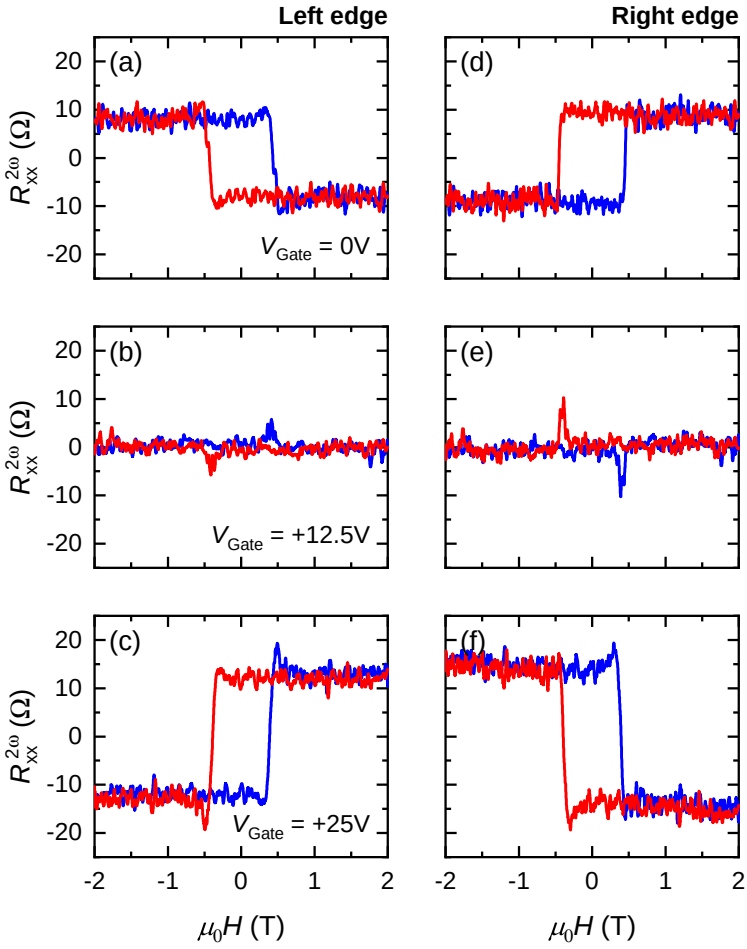

Figure 5.4: Magnetic-field and gate-voltage dependencies of the nonreciprocal charge transport in the high-current limit ($I_{\rm rms} = 1$ μA) for Hall-bar device F1 at 2 K. The current flows from contact 1 to 4; the left (right) edge corresponds to the contact pairs 2-3 (6-5), see Fig. 4.13 for a picture. (a-c) The magnetic-field dependence of $R_{xx}^{2\omega}$ for the left edge, measured at $V_{\rm Gate} = 0$ V (a), 12.5 V (b), and 25 V (c). (d-f) The corresponding magnetic-field dependence of $R_{xx}^{2\omega}$ for the right edge. The $R_{xx}^{2\omega}$ curves were antisymmetrized in the magnetization and magnetic-field, i.e. $R_{xx}^{2\omega} = [R_{xx}^{2\omega}(+\hat{M}, +\mu_0 H) - R_{xx}^{2\omega}(-\hat{M}, -\mu_0 H)]/2$.

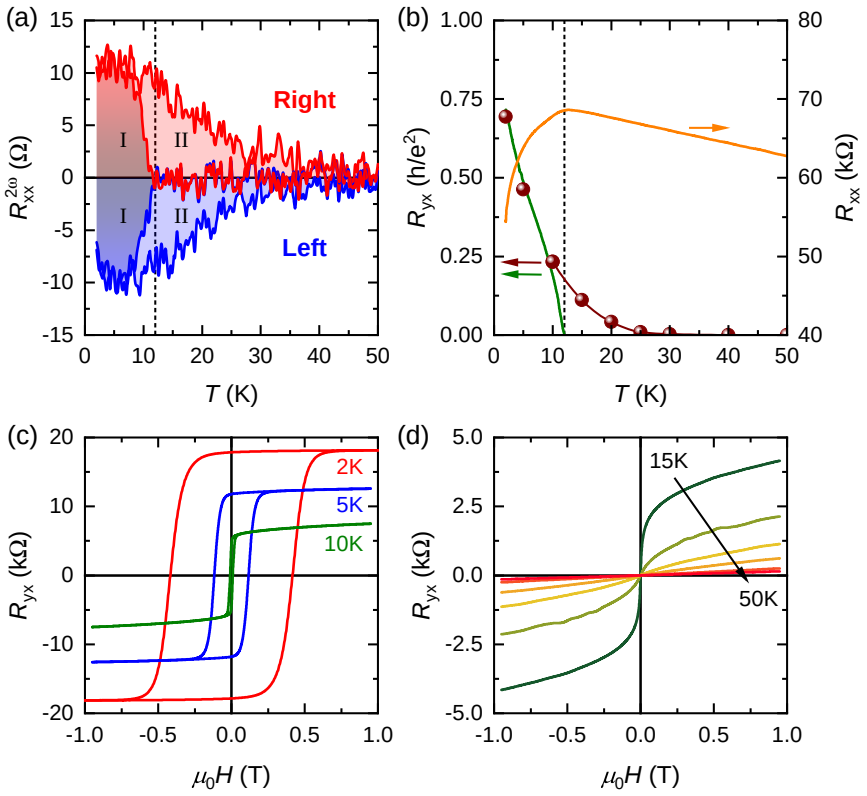

Figure 5.5: Temperature dependence of the nonreciprocal charge transport and anomalous Hall effect in the high-current limit for Hall-bar device F1 at $V_{\mathrm{Gate}} = 0$ V. The current flows from contact 1 to 4; the left (right) edge corresponds to the contact pairs 2-3 (6-5), see Fig. 4.13 for a picture. (a) Temperature dependencies of $R_{xx}^{2\omega}$ for the left and right edge from 2 K to 50 K, measured with $I_{\mathrm{rms}} = 1$ μA in 0 T (after training in ± 2 T) marked as 'I', and in ± 2 T marked as 'II'. The $R_{xx}^{2\omega}$ curves were antisymmetrized in the magnetization (and magnetic-field), i.e. $R_{xx}^{2\omega} = [R_{xx}^{2\omega}(+\hat{M}, +\mu_0 H) - R_{xx}^{2\omega}(-\hat{M}, -\mu_0 H)]/2$. (b) The corresponding temperature dependence for R_{yx} (green curve) and R_{xx} (orange curve) in 0 T. The red symbols show the field-induced AH effect, obtained from (c-d) after subtracting the linear ordinary Hall contribution. The dashed lines in (a) and (b) are a guide to the eye, and mark the Curie temperature $T_{\mathrm{C}} \approx 12$ K. (c-d) Magnetic-field dependence of R_{yx} at different temperatures below T_{C} (c): 2 K, 5 K, 10 K, and above T_{C} (d): 15 K, 20 K, 25 K, 30 K, 40 K, and 50 K.

magnetic-field strength of 2 T, $R_{xx}^{2\omega}$ remains nonzero up to about 30–40 K, as seen for region 'II' in Fig. 5.5(a). Figure 5.6 shows the magnetic-field dependence of $R_{xx}^{2\omega}$ for the left and right edge at different temperatures above T_C; the light and dark curves are the back and forward field-sweeps and show no hysteresis loop. The field-sweeps at 20 K, 25 K, and 30 K show a linear dependence on the applied-magnetic-field strength, consistent with Eq. 5.1 for an MCA. The shape of the field-sweep at 15 K corresponds to a crossover from the hysteresis loop below T_C (Fig. F.6) to the linear dependence above T_C (Fig. 5.6).

The temperature dependence of the nonreciprocal response matches the anomalous Hall (AH) amplitude above T_C when an out-of-plane magnetic field is applied to the sample. Below T_C, R_{yx} shows a hysteresis loop with the AH amplitude and the coercive field H_c decreasing with increasing temperature [Fig. 5.5(c)], and both quantities become zero at T_C. However, by applying a magnetic field an AH amplitude is induced in the thin film above T_C (alongside with the ordinary Hall effect), see Fig. 5.5(d). By subtracting the linear contribution from the ordinary Hall effect, the field-induced AH amplitude can be plotted as a function of temperature, see the red data points in Fig. 5.5(b). The field-induced AH amplitude follows the same temperature dependence as $R_{xx}^{2\omega}$ above T_C, vanishing at ∼30 K. This indicates that the so-called 'intrinsic' (Berry-phase) contribution to R_{yx} determines the (Q)AH effect both below and above T_C [128], with the observation of nonreciprocal transport giving direct evidence of edge-state physics [201] even when R_{yx} is far below the quantized value of h/e^2. Nevertheless, when comparing $R_{xx}^{2\omega}$ to R_{xx} in Fig. 5.5, the second-harmonic resistance is small ($\tilde{\gamma} \approx 226$ A^{-1} at 2 K), see table G.2 of the appendix for details.

5.3 The Nonreciprocal Response near Breakdown

In the previous section, the nonreciprocal response was always very small when compared to the longitudinal resistance. However, since V_x vanishes for low values of the excitation current in a QAHI, one might expect the ratio $V_x^{2\omega}/V_x^{1\omega}$ to become relatively large near the current-induced breakdown transition. All the data in the remainder of the chapter were measured using the AC lock-in technique (first & second harmonic), since DC measurements could not resolve the nonreciprocal charge transport for excitation currents below ∼5 μA.

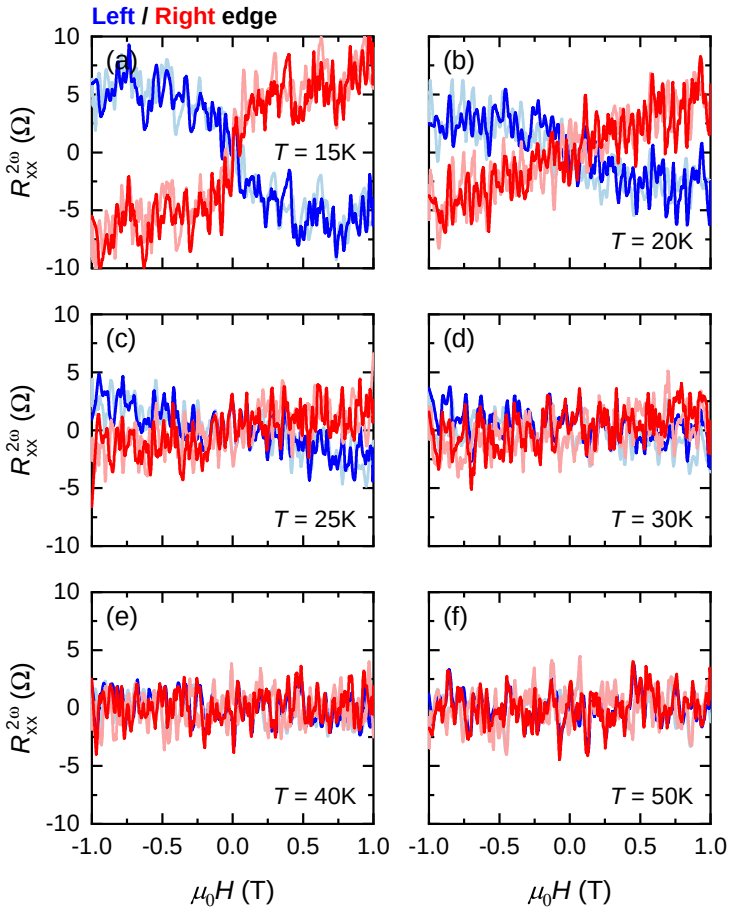

Figure 5.6: Magnetic-field dependence of the nonreciprocal charge transport at $V_{\mathrm{Gate}} = 0$ V at different temperatures above T_{C}: (a) 15 K, (b) 20 K, (c) 25 K, (d) 30 K, (e) 40 K, and (f) 50 K. A current of $I_{\mathrm{rms}} = 1$ μA flowed through Hall-bar device F1 (see Fig. 4.13 for a picture) from contact 1 to 4. The left (right) edge corresponds to the contact pairs 2-3 (6-5), and is shown in blue (red). The light and dark curves are the back and forward field-sweeps, and show no hysteresis loop. The $R_{xx}^{2\omega}$ curves were antisymmetrized in the magnetization and magnetic-field, i.e. $R_{xx}^{2\omega} = [R_{xx}^{2\omega}(+\hat{M}, +\mu_0 H) - R_{xx}^{2\omega}(-\hat{M}, -\mu_0 H)]/2$.

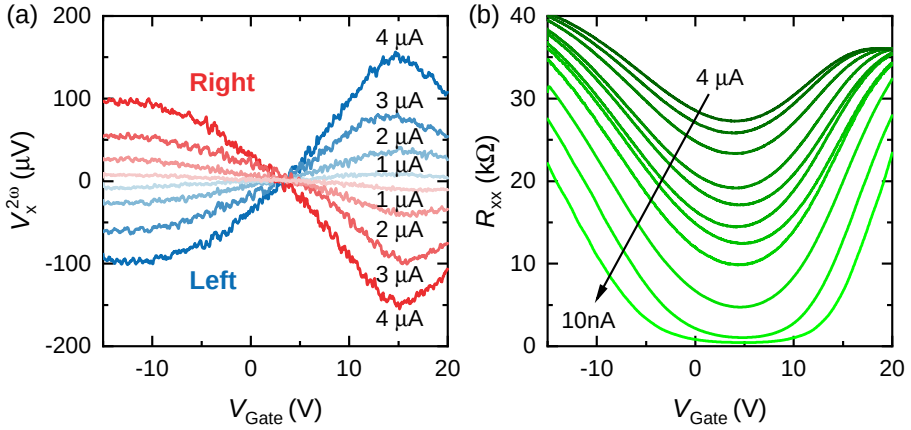

Figure 5.7: Gate-voltage dependence of the second-harmonic voltage and the longitudinal resistance, measured with different excitation currents for Hall-bar device J at 60 mK. The current flows from contact 1 to 4; the left (right) edge corresponds to the contact pairs 2-3 (6-5). (a) Gate-voltage dependence of $V_x^{2\omega}$ for the left and right edges, measured in ±2 T using different excitation currents $I_{\rm rms}$ = 1 μA, 2 μA, 3 μA, and 4 μA. The $V_x^{2\omega}$ curves were antisymmetrized in the magnetization and magnetic-field, i.e. $V_x^{2\omega} = [V_x^{2\omega}(+\hat{M}, +2\mathrm{T}) - V_x^{2\omega}(-\hat{M}, -2\mathrm{T})]/2$. (b) The longitudinal resistance R_{xx} as a function of $V_{\rm Gate}$, measured in +2 T using different excitation currents $I_{\rm rms}$ = 10 nA, 50 nA, 100 nA, 250 nA, 375 nA, 500 nA, 750 nA, 1 μA, 2 μA, 3 μA, and 4 μA.

5.3.1 Gate-voltage and Excitation-current Dependencies

Figures 5.7(a) and 5.8 show $V_x^{2\omega}$ as a function of $V_{\rm Gate}$, measured at 60 mK with different excitation currents $I_{\rm rms}$ from 4 μA down to 10 nA for Hall-bar device J. Figure 5.7(b) shows the corresponding curves of R_{xx} for comparison. For high excitation currents the CNP is at $V_{\rm Gate} \approx 4$ V and $V_x^{2\omega}$ is consistent with Eq. 5.3, inverting its sign when the 2D charge carriers change from p- to n-type. However, for $I_{\rm rms}$ = 750 nA [Fig. 5.8(a)] the crossing point between $V_x^{2\omega}$(Right) and $V_x^{2\omega}$(Left) no longer corresponds to the CNP, but has moved towards lower gate voltages ($V_{\rm Gate} \approx 1$ V). This trend continues with decreasing $I_{\rm rms}$, with $V_x^{2\omega}$(Left) becoming larger than $V_x^{2\omega}$(Right) across the full $V_{\rm Gate}$-range at $I_{\rm rms}$ = 100 nA, see Fig. 5.8(e). At $I_{\rm rms}$ = 10 nA, the sample recovers the zero-resistance state for a certain $V_{\rm Gate}$-range [Fig. 5.7(b)], and $V_x^{2\omega}$ becomes zero near CNP [Fig. 5.8(g)].

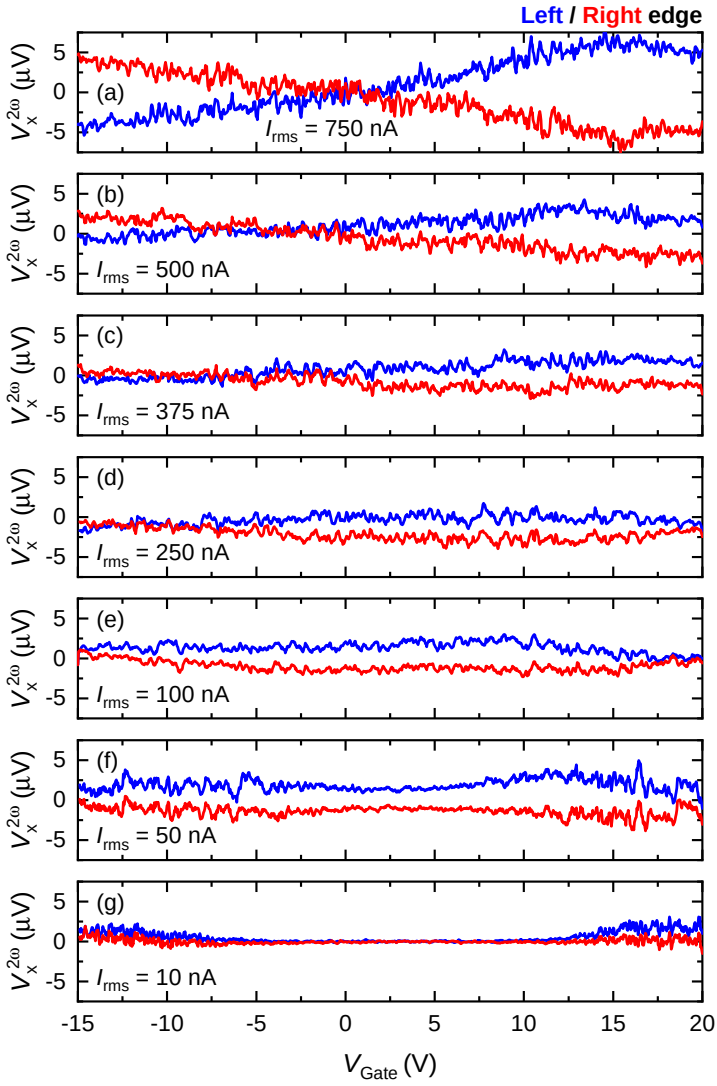

Figure 5.8: Gate-voltage dependence of the second-harmonic voltage at 60 mK, measured with different excitation currents $I_{\rm rms}$ = 750 nA (a), 500 nA (b), 375 nA (c), 250 nA (d), 100 nA (e), 50 nA (f) and 10 nA (g) for Hall-bar device J at 60 mK. The current flows from contact 1 to 4; the left (right) edge shown in blue (red) corresponds to the contact pairs 2-3 (6-5). The $V_x^{2\omega}$ curves were measured in ±2 T, and were antisymmetrized in the magnetization and magnetic-field, i.e. $V_x^{2\omega} = [V_x^{2\omega}(+\hat{M}, +2\mathrm{T}) - V_x^{2\omega}(-\hat{M}, -2\mathrm{T})]/2$.

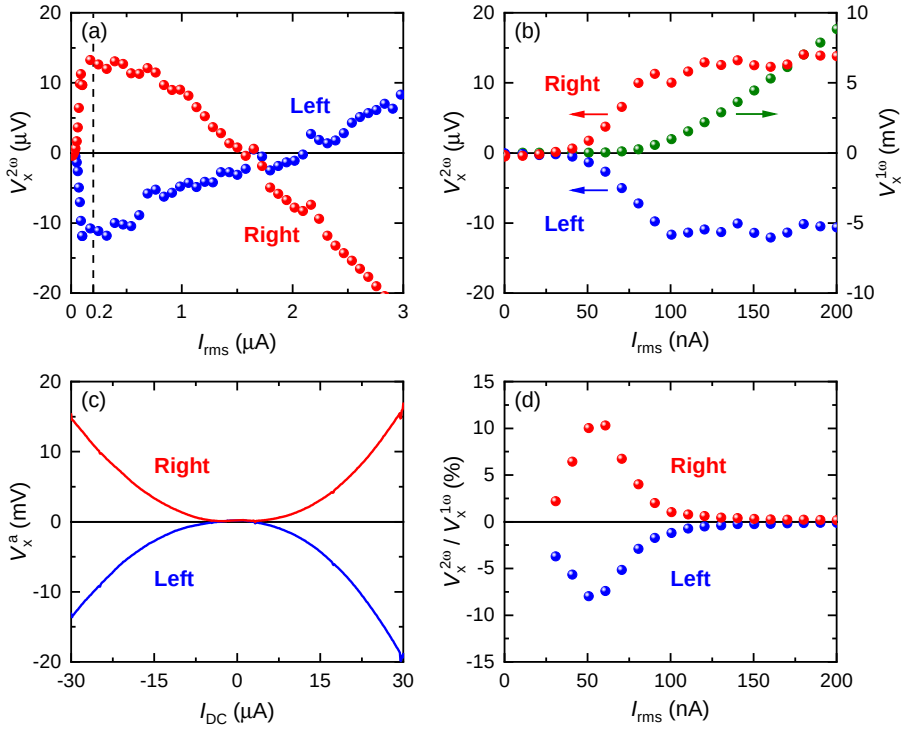

Figure 5.9: Current dependence of the nonreciprocal charge transport near breakdown for the 26-terminal Hall-bar device C, with the current flowing from contact 0 to 25, see Fig. 5.1(b) for a schematic of the device. (a) The second-harmonic voltage $V_x^{2\omega}$, measured between contact pairs 5-19 (Left) and 6-20 (Right) at 10 mK in 0 T after training in ±2 T. The $V_x^{2\omega}$ curves were antisymmetrized in the magnetization, i.e. $V_x^{2\omega} = [V_x^{2\omega}(+\hat{M}, 0\mathrm{T}) - V_x^{2\omega}(-\hat{M}, 0\mathrm{T})]/2$. The dashed line marks $I_{\mathrm{rms}} = 0.2$ μA. (b) Zoom of (a) up to 200 nA, showing $V_x^{1\omega}$ (in mV) and $V_x^{2\omega}$ (in μV). The current-induced breakdown of the QAHE occurs at $I_{\mathrm{rms}} \approx 60$ nA, i.e. at a peak-current value of $I_0 \approx 85$ nA. (c) The DC voltage V_x^{a} at 3.5 K, measured between contact pairs 5-9 (Left) and 6-10 (Right) in ±2 T. The data were taken from Fig. 5.2, and antisymmetrized in the magnetization and magnetic-field, i.e. $V_x^{\mathrm{a}} = [V_x(+\hat{M}, +2\mathrm{T}) - V_x(-\hat{M}, -2\mathrm{T})]/2$. (d) The ratio $V_x^{2\omega}/V_x^{1\omega}$, reaching a maximum of ∼10% at $I_{\mathrm{rms}} \approx 60$ nA.

For excitation currents below $I_{\mathrm{rms}} = 100$ nA, $V_x^{2\omega}$ no longer changes sign when sweeping the chemical potential across the CNP, and the nonreciprocal charge transport seems to no longer depend on the 2D charge-carrier type ($n_{p/n}$). This behavior was reproduced in several devices on different wafers, see Fig. F.10 in the appendix for similar measurements on device K. However, for the 6-terminal Hall-bar devices J and K the amplitude of $V_x^{2\omega}$ is low, since the separation between the voltage contacts is small. To confirm whether the nonreciprocal response indeed becomes independent of $n_{p/n}$, it is beneficial to return to the 26-terminal Hall-bar device C shown in Fig. 5.1 as the amplitude of $V_x^{2\omega}$ will be larger for large contact-pair separations. The disadvantage with this device is the lack of a top-gate.[3] Figures 5.9(a-b) show $V_x^{2\omega}$(Right), $V_x^{2\omega}$(Left) and $V_x^{1\omega}$ as a function of the excitation current I_{rms} for device C. Notice that $V_x^{2\omega}$ inverts sign at $I_{\mathrm{rms}} \approx 1.65$ μA. This is consistent with the sign-inversion with decreasing excitation current, observed in Figs. 5.8 and F.10 for any p-type gate voltage. The QAH film of device C, however, is n-type (see Fig. 3.6 in chapter 3). Hence, the sign-inversion of $V_x^{2\omega}$ with decreasing I_{rms} can occur on either the n- or p-type side of the CNP, meaning that the polarity of the nonreciprocal response at low excitation currents is sample dependent.

In addition, the quadratic I-V relation is lost for small excitation currents near the breakdown of the QAHE; only at much higher current values is the I^2-dependence recovered. This can be clearly seen by comparing Figs. 5.9(a) and 5.9(c) for the AC and DC measurements on device C, respectively. Remember that $V_x^{2\omega}$ picks up a minus sign (Eq. 5.3) as compared to the (antisymmetrized) DC voltage V_x^{a}. Hence, after the sign-inversion at $I_{\mathrm{rms}} \approx 1.65$ μA, the polarities for $V_x^{2\omega}$ and V_x^{a} are consistent. Lastly, while $V_x^{1\omega}$ is generally about 3 orders of magnitude larger than $V_x^{2\omega}$ [Fig. 5.9(b)], the ratio $V_x^{2\omega}/V_x^{1\omega}$ becomes $\sim$10% at $I_{\mathrm{rms}} \approx 60$ nA near the breakdown transition [Fig. 5.9(d)]. This yields a conservative estimate for the current-direction-dependent resistance-ratio of $\Delta R/R \approx 20\%$, and $\Delta R/R/i \approx 3 \times 10^4$. These values are among the highest reported nonreciprocal responses when compared to the other material systems in the literature, see tables G.1 and G.2 in the appendix. Note that it is no longer possible to define a rectification coefficient $\tilde{\gamma}$ due to the highly nonlinear I-V relation near breakdown.

[3] The fabrication of a top-gate electrode on the 26-terminal Hall-bar devices was not possible, as its large area always gave rise to a sizable leakage current through the gate dielectric.

5.3.2 Temperature Dependence

Next, the temperature dependence of the nonreciprocal response will be investigated near breakdown. Figure 5.10(a) shows $V_x^{2\omega}$ for Hall-bar device K as a function of V_{Gate} at 60 mK for an excitation current of $I_{\mathrm{rms}} = 100$ nA. The sample is in the zero-resistance state between $V_{\mathrm{Gate}} \approx 2$ V and 19 V, where $V_x^{2\omega}$(Left) and $V_x^{2\omega}$(Right) coincide. The nonzero $V_x^{2\omega}$-values in this V_{Gate}-range can be attributed to slight drifts in the experimental conditions, as well as hysteresis in the gate electrode when sweeping V_{Gate}, which give rise to the slight distortion after antisymmetrization. Notice that for $I_{\mathrm{rms}} = 100$ nA the nonreciprocal response in device K is seemingly independent of the 2D charge-carrier type ($n_{p/n}$), since $V_x^{2\omega}$(Left) $> V_x^{2\omega}$(Right) for all values of V_{Gate}. Figures 5.10(a-f) show the evolution of $V_x^{2\omega}$ measured at $I_{\mathrm{rms}} = 100$ nA for increasing temperatures up to 1 K; the amplitude of $V_x^{2\omega}$ decreases sharply with temperature and becomes zero before 500 mK.

Figures 5.11(a-f) show $V_x^{2\omega}$ as a function of V_{Gate} at the same temperatures, but for an excitation current of $I_{\mathrm{rms}} = 2$ μA. For this higher current amplitude, the nonreciprocal response in device K *does* depend on $n_{p/n}$, as evidenced by the sign-inversion of $V_x^{2\omega}$ across the CNP. Notice that the curves for $V_x^{2\omega}$ in Figs. 5.11(a-f) are nearly identical. Hence, the nonreciprocal response does not show a strong temperature dependence at high excitation currents, and $V_x^{2\omega}$ only decreases sharply when approaching the Curie temperature of the thin film in zero-applied magnetic field, as was shown in Fig. 5.5(a).

The strong temperature dependence of $V_x^{2\omega}$ at low excitation currents is reproduced for the 26-terminal Hall-bar device C, see Fig. F.3 in the appendix. The fact that the nonreciprocal response at low excitation currents seems to become independent from the 2D charge-carrier type, together with the strongly differing temperature dependencies for low and high excitation currents, may indicate that a different nonreciprocal mechanism emerges and becomes dominant at low excitation currents near breakdown. A detailed discussion will be given below in section 5.4.

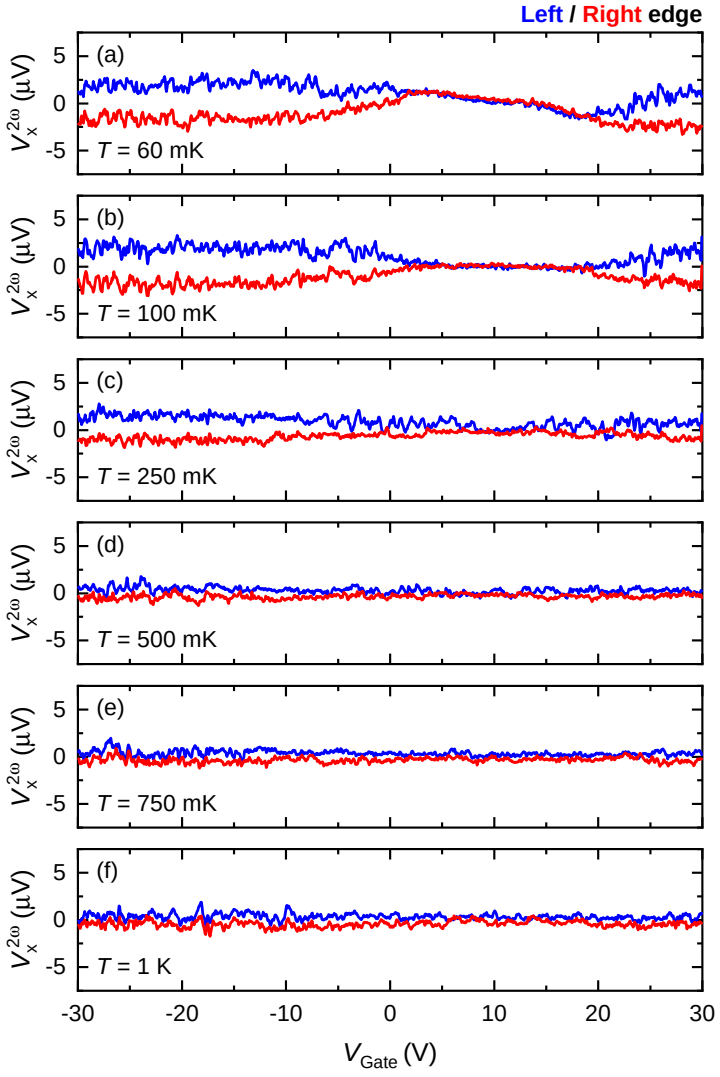

Figure 5.10: Gate-voltage dependence of the second-harmonic voltage, measured with $I_{\rm rms} = 100$ nA at different temperatures $T = 60$ mK (a), 100 mK (b), 250 mK (c), 500 mK (d), 750 mK (e), and 1 K (f) for Hall-bar device K. The current flows from contact 1 to 4; the left (right) edge corresponds to the contact pairs 2-3 (6-5) and are shown in blue (red). The $V_x^{2\omega}$ curves were measured in ± 2 T, and were antisymmetrized in the magnetization and magnetic-field, i.e. $V_x^{2\omega} = [V_x^{2\omega}(+\hat{M}, +2\mathrm{T}) - V_x^{2\omega}(-\hat{M}, -2\mathrm{T})]/2$.

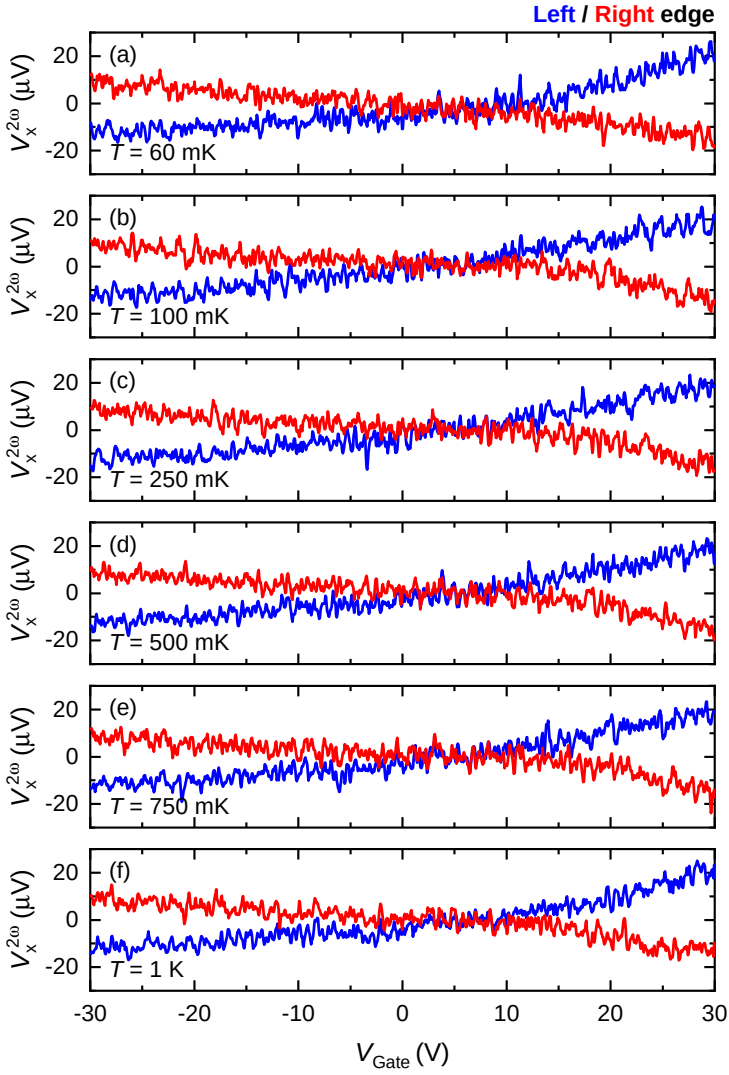

Figure 5.11: Gate-voltage dependence of the second-harmonic voltage, measured with $I_{\rm rms} = 2\ \mu$A at different temperatures $T = 60$ mK (a), 100 mK (b), 250 mK (c), 500 mK (d), 750 mK (e), and 1 K (f) for Hall-bar device K. The current flows from contact 1 to 4; the left (right) edge corresponds to the contact pairs 2-3 (6-5) and are shown in blue (red). The $V_x^{2\omega}$ curves were measured in ± 2 T, and were antisymmetrized in the magnetization and magnetic-field, i.e. $V_x^{2\omega} = [V_x^{2\omega}(+\hat{M}, +2\mathrm{T}) - V_x^{2\omega}(-\hat{M}, -2\mathrm{T})]/2$.

5.3.3 Reproducibility of the Nonreciprocal Amplitude at Low Excitation Currents

Thus far, it was shown that for devices J and K the sign-inversion at constant V_{Gate} occurs on the p-type side of the CNP when decreasing the excitation current (Figs. 5.8 and F.10, respectively), while for device C the sign-inversion takes place on the n-type side (Fig. 5.9). It is prudent to verify whether the amplitude and polarity of this '$n_{p/n}$-independent' nonreciprocal response dominant near breakdown is stable and reproduced along the full edge of a given Hall-bar device. To this end, the nonreciprocal response of device C was measured for excitation currents below the sign-inversion [$I_{\mathrm{rms}} < 1.65$ μA, see Fig. 5.9(a)], between different contact pairs with varying contact separations, see Figs. F.4 and F.5 in the appendix. The amplitude $|V_x^{2\omega}|$ extracted at $I_{\mathrm{rms}} = 200$ nA is shown in Fig. 5.12 as a function of the contact spacing L. Figures F.4, F.5, and 5.12 show that the amplitude of the nonreciprocal response scales linearly with the length as expected, and its polarity is maintained along the full length of the 26-terminal Hall-bar device C. Notice that the $|V_x^{2\omega}|$-amplitudes extracted from magnetic-field sweeps are slightly smaller than those obtained from I-V curves, as operating the magnet in the dilution refrigerator resulted in slight heating of the sample.

5.4 Discussion

Yasuda *et al.* proposed a mechanism for the nonreciprocal charge transport in which the 2D bulk channels act as a source/sink for the current, and hence the potential lost due to scattering from the high (source) potential 1D edge state to the 2D bulk differs from the potential gained due to scattering from the 2D bulk to the low (drain) potential 1D edge state [201], see Fig. 5.1(a). The I-V relation of the broken-down QAHI was shown to follow Eq. 5.2. However, their study was limited to relatively high temperatures (0.5–40 K) and currents (1–100 μA). In this chapter, the nonreciprocal response of a QAHI was investigated over a much larger temperature range. Equation 5.2 was shown to hold from the Curie temperature of the QAH thin films down to $\sim$10 mK for large excitation currents ($\gtrsim 1$ μA).

While the work in this thesis supports the results of Yasuda *et al.* for high excitation currents [201], the observed nonreciprocal response below $\sim$1 μA deviates significantly from Eq. 5.2. Firstly, the signature I^2-dependence is lost [Fig. 5.9]. Secondly, upon decreasing the excitation current the nonreciprocal response seemingly becomes independent of the 2D charge-carrier type (i.e. $n_{p/n}$ in Eq. 5.2), as evidenced by the crossing point of $V_x^{2\omega}$(Left) and $V_x^{2\omega}$(Right) in

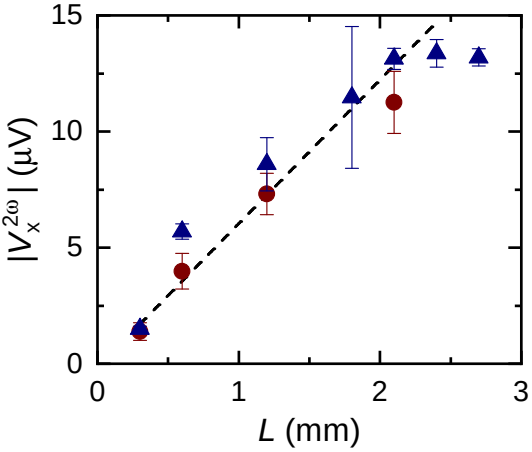

Figure 5.12: Length dependence of the second-harmonic voltage $|V_x^{2\omega}|$ for different contact pairs on the right and left edge of the 26-terminal Hall-bar device C, measured with $I_{\mathrm{rms}} = 200$ nA at 15 mK. The ▲ data points were extracted from the I-V curves shown in Fig. F.4, while the • data points were extracted from the magnetic-field sweeps shown in Fig. F.5. The large error bar for the ▲ data point at 1.8 mm originates from the dip in the curves near 200 nA in Fig. F.4(d), which is most likely an artifact originating from the antisymmetrization and a slight drift in the experimental conditions. The dashed line is a linear fit through both data sets, yielding a slope of ∼6.2 mV/m.

the V_{Gate}-dependence moving away from the CNP [Fig. 5.8]. Whether $V_x^{2\omega}$(Left) is larger or smaller than $V_x^{2\omega}$(Right) in the $n_{p/n}$-independent regime depends on an unknown parameter and seems to be sample dependent. Moreover, the amplitude of the $n_{p/n}$-independent nonreciprocal response at low currents is strongly suppressed with increasing temperature [Fig. 5.10], contrary to the nonreciprocal response at high currents which survives up to T_{C} [Fig. 5.5(a)].

As explained in chapters 2 and 4, the formation of charge puddles in the gapped 2D surface states of QAH thin films is expected due to the spatial fluctuations of the Coulomb potential as a result of the random distribution of donor and acceptor defects in compensated TIs (Fig. 4.18). When breakdown of the QAHE occurs, the large Hall electric field causes conduction to take place through the 2D bulk via the percolation of the 2D charge puddles (Fig. 4.18). If the contributions of the n- and p-type puddles to the nonreciprocal response are equal, than $V_x^{2\omega}$ is expected to vanish when the chemical potential lies in the exchange gap. However, in magnetic TIs it is not realistic to achieve perfect charge compensation, and the QAH thin films will always have a slight majority

of either n- or p-type puddles. The resulting unequal contribution of the n- and p-type puddles to the nonreciprocal charge transport then gives rise to a finite value for $V_x^{2\omega}$ when the chemical potential lies in the exchange gap.[4] Moreover, note that the gating efficiency is very low in our QAH thin films (only a few μeV/V), as explained in detail in chapter 4 (section 4.7). Hence, when inspecting the V_{Gate}-dependencies of $V_x^{2\omega}$ presented in this chapter, it is important to keep in mind that the Fermi level is pinned, and hence only moves a few tens of μeV with respect to its zero-gate-voltage position. This might explain why the values for $V_x^{2\omega}$(Left) and $V_x^{2\omega}$(Right) are independent of the gate voltage at low temperatures and excitation currents.

At high excitation currents and/or high temperatures, the Coulomb disorder profile no longer strongly influences the 2D conduction. At high excitation currents, for instance, the current is directly injected into the valence or conduction band of the gapped 2D surface states. Note that for a current of $\sim$1 μA the source-drain potential difference is $eV_{\text{S-D}} = \frac{h}{e} I_{\text{rms}} \approx 26$ meV, which matches the local exchange gap size of $\sim$14–28 meV measured in scanning tunneling spectroscopy experiments [37, 101]. Hence, for current values above $\gtrsim 1$ μA, the band bending due to $V_{\text{S-D}}$ is large enough for a current to flow through the 2D surface states without the need for electrons or holes to hop or tunnel between charge puddles. Instead of the chiral edge states interacting with the n- and p-type puddles (as is the case for low excitation currents), the nonreciprocal response originates from the chiral edge states interacting with the majority carriers of the 2D source-drain current. As a result, $V_x^{2\omega}$ depends on $n_{p/n}$ and undergoes a sign-inversion at the CNP.

For completeness, it is prudent to briefly comment on two other possible origins of the $n_{p/n}$-independent nonreciprocal response near breakdown. Firstly, the anomalous Nernst effect (ANE) can give rise to a second-harmonic response. Namely, the ANE induces a longitudinal voltage proportional to $j^2(M \times \nabla T)$ [6], when a transverse thermal gradient ∇T_y is present across the Hall-bar device. Nevertheless, since the $n_{p/n}$-independent nonreciprocal response is only observed near breakdown (i.e. for very small current densities), Joule heating is minimal. Hence, no sizable thermal gradient ∇T is realized. Secondly, Yasuda *et al.* demonstrated a large unidirectional magnetoresistance (UMR) in bilayers consisting of a magnetic Cr-doped $(Bi_xSb_{1-x})_2Te_3$ and undoped $(Bi_xSb_{1-x})_2Te_3$ layer [203]. However, this UMR does not fit the data presented in this chapter, because in order to observe the UMR an external magnetic field has to be applied to force an *in-plane* magnetization perpendicular to the direction of current flow.

[4] For devices J and K the n-type puddles are dominant, while for device C the p-type puddles seem to dominate.

5.5 Summary

The nonreciprocal response of a QAHI was investigated over a vast parameter space (T, H, V_{Gate}, I). For high excitation currents, the I-V relation is described well by Eq. 5.2. However, at ultra-low temperatures (< 100 mK) when the current amplitude is decreased to only slightly exceed the critical current for breakdown, the nonreciprocal charge transport seems to become independent of the 2D charge-carrier type ($n_{p/n}$), and the I^2-dependence is lost. The finite nonreciprocal response when the chemical potential lies inside the exchange gap, is most likely caused by an imperfect charge compensation in the QAHI thin films, which leads to a majority of either n- or p-type 2D charge puddles.

This chapter is in preparation to be published as:

Lippertz, G., Uday, A., Bliesener, A., Pereira, L. M. C., Taskin, A. A., and Ando, Y. Nonreciprocal charge transport on the edges of a quantum anomalous Hall insulator.

Author contributions: Y.A. and A.A.T. conceived and supervised the project. G.L., A.U., A.B., and A.A.T. grew the QAH thin films. G.L. and L.M.C.P. analyzed the thin films. G.L. and A.U. fabricated the Hall-bar devices. G.L., A.U., and A.A.T. performed the experiments. G.L. analyzed the data with the help of all authors. G.L. and Y.A. are preparing the manuscript with input from all authors.

Chapter 6

Conclusion

> *Nature's music is never over; her silences are pauses, not conclusions.*
>
> Mary Webb

In this thesis, the current-induced breakdown of the QAHE was addressed. When the current density flowing through a QAHI was increased, or the width of the transport region was constricted, an abrupt breakdown of the dissipationless state occurred. The sample resistance was found to scale linearly with the length of the transport channel, indicating that the dissipative state above breakdown was governed by 2D diffusive transport through the bulk of the sample. In addition, the critical current I_c was found to depend linearly on the separation between the chiral edge states, and breakdown was shown to be absent in nonlocal measurement geometries. This proved that the large Hall electric field was the driving force for the breakdown process. Since the gapped 2D surface states in the QAH thin films possessed charge puddles as a result of the Coulomb disorder, the electric field was confined to the small insulating regions in between the puddles. As the transverse electric field was increased by increasing the current or constricting the sample dimensions, the increased band bending caused the 2D charge puddles to grow. At the critical electric field the growth of the puddles became unstable and lead to an avalanche process. This caused a metallic percolation path to form from one edge of the sample to the other. This was the cause of the sudden onset of dissipation.

The interpretation of the breakdown process as the formation of a metallic short across the sample's width was further substantiated by a Landauer-Büttiker treatment of the measurement configurations used in the experiments. Other breakdown mechanisms, such as the bootstrap electron heating (BSEH) model and the percolation of the chiral edge state via magnetic domains, were also covered in this thesis. However, it was shown that both models were unable to explain the breakdown of the QAHE. Estimates for the Landau-Zener tunneling between 2D charge puddles were given, and it was argued that such tunneling events might explain the small but finite resistance in the pre-breakdown regime.

Next, the nonreciprocal charge transport was studied in the broken-down QAH-state. For large current amplitudes ($I \gg I_c$), the current flowed through both the 2D bulk and 1D edge states. Due to the large transverse electric field, the high-potential branch of the chiral edge state was losing current to the 2D state, while a fraction of the current flowing through the 2D state scattered into the low-potential branch of the chiral edge state. Since a significant fraction of the current was flowing from the source to the drain through the 2D bulk, the 2D states acted as a source or sink of current. Since the scattering rates between the chiral 1D edge and gapped 2D surface states were different for edge-to-surface and surface-to-edge processes [201], the potential differences along the left and right edge of the sample were not equal, which gave rise to the observed nonreciprocity in the longitudinal voltage. Hence, while the breakdown of the QAHE is generally a detrimental effect, it nevertheless can lead to interesting nonreciprocal (diode-like) features in transport experiments.

In this thesis, two distinct nonreciprocal regimes were identified: (i) At high excitation currents and/or temperatures, the nonreciprocal response followed the well-known quadratic current-voltage relation for nonreciprocal systems. Moreover, the amplitude of the nonreciprocal response showed a sign-inversion, when the out-of-plane magnetization direction was inverted, or the 2D charge carriers were tuned from n- to p-type. The nonreciprocal charge transport in this regime was not affected by the Coulomb disorder, as either the band bending due to the applied current or the thermal energy $k_B T$ were much larger than the activation energy for the percolation of the 2D charge puddles. (ii) At low excitation currents and temperatures, on the other hand, the signature I^2-dependence was lost, and the nonreciprocal response was found to be independent of the electrostatic gate potential. Near the breakdown transition disorder played a strong role. In this thesis, it was argued that the finite nonreciprocal response when the chemical potential lay inside the exchange gap, was most likely caused by an imperfect charge compensation in the QAHI thin films, which lead to a majority of either n- or p-type 2D charge puddles. This also explained why the polarity of the nonreciprocal response was sample-dependent near breakdown.

In this thesis, both the current-induced breakdown and the nonreciprocal transport at low currents and temperatures were attributed to puddle dynamics in the gapped 2D surface state of the QAHI. Theoretical work is needed to further clarify the important role Coulomb disorder plays in QAH systems, and to simulate the puddle formation for realistic experimental conditions. In addition, more experimental studies on the topic are needed to support and/or verify the universality of the claims made here. In particular, STM, optical conductivity, and quantum capacitance measurements could provide valuable insights into the formation of puddles (with decreasing temperature), the puddle size, their spatial distribution, as well as the localized density of states in the exchange gap. Moreover, while the thesis focused on uniformly V-doped $(Bi_xSb_{1-x})_2Te_3$ thin films, it would be of great interest to compare uniformly- and modulation-doped heterolayers, and perform similar studies on other QAH platforms, such as $MnBi_2Te_4$, twisted bilayer graphene, and $MoTe_2/WSe_2$ moiré heterobilayers.

The results presented in thesis advance the understanding of the current-induced breakdown of the QAHE, and offer guiding principles for its mitigation in future experiments and applications. Focusing on the latter, topological materials have long been proposed for low-power electronics. While the so-called 'topological protection' from backscattering of the spin-momentum-locked surface carriers in 3D-TIs should indeed suppress dissipation over length scales smaller than the inelastic mean-free-path, QAHIs do not suffer from this limitation. As shown in this thesis, near-dissipationless edge transport is readily available in QAHIs over macroscopic length scales, with only a quantized voltage drop of $(h/e^2)I$ at the source/drain electrodes. This quantization of the resistance is also of great interest for the field of metrology. Since the QAHE (contrary to the QHE) does not require the application of an external magnetic field, the QAHE and Josephson effect can be integrated into one low-temperature set-up, creating a quantum current generator which can act as a reference standard for the ohm, volt, and ampere within the international system of units (SI). Lastly, QAHIs when combined with s-wave superconductors may allow for the realization of so-called 'flying qubits', which if demonstrated would give an intriguing alternative to the currently envisioned route maps towards quantum computation. However, this thesis makes the case that these applications will only come to fruition with further improvements in: (i) the material quality, which should aim at the reduction of Coulomb and magnetic disorder. (ii) the design of the devices/experiments, which should aim at mitigating the breakdown of the QAHE, by spatially separating the high- and low-potential branches of the chiral edge states.

Chapter 7

Outlook

> *Any knowledge that doesn't lead to new questions dies out: it fails to maintain the temperature required for sustaining life.*
>
> Wislawa Szymborska

In this thesis, the focus lay on the dissipation mechanisms in QAH thin films at ultra-low temperatures in order to understand what determines the maximum current density the QAHI can sustain before breakdown occurs, and to propose strategies to improve it. Other research groups instead have focused on maximizing the temperature at which the transverse resistance is quantized. Figure 7.1 shows a timeline of the zero-field quantization temperature of the QAHE (T_{QAHE}) for different material systems. It is apparent that the majority of QAH systems realized in the past decade rely on magnetic doping or proximity coupled heterostructures of $(Bi_xSb_{1-x})_2Te_3$ ('BST' in Fig. 7.1) [115]. The QAHE was first realized in Cr-doped $(Bi_xSb_{1-x})_2Te_3$ at 30 mK in 2013 [30], and two years later in V-doped $(Bi_xSb_{1-x})_2Te_3$ at 120 mK [32]. Modulation-doping of the $(Bi_xSb_{1-x})_2Te_3$ thin films, where the Cr dopants were confined to a delta-layer below the top and bottom surface, pushed the upper quantization temperature up to 2 K [125], owing to its larger saturation magnetization. However, in these modulation-doped samples there seems to be a trade-off between the current density for breakdown at ultra-low temperatures and the upper quantization temperature. Namely, the very high Cr/V-concentration in the delta-layer yields the desired larger saturation magnetization at the cost of an increased defect density (in the delta-layer) and a deterioration

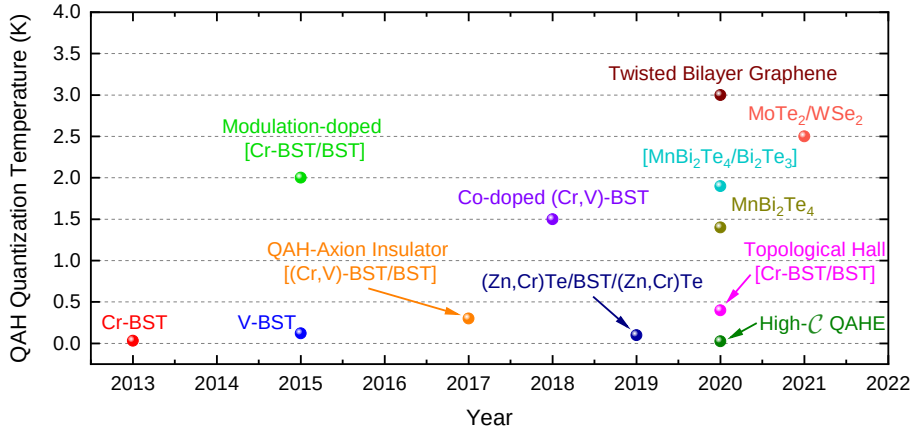

Figure 7.1: Timeline of the upper quantization temperature of the QAHE (T_{QAHE}) in different material systems, based on Ref. [115]. Here, $(\mathrm{Bi}_x\mathrm{Sb}_{1-x})_2\mathrm{Te}_3$ is abbreviated by 'BST'. The first realization of the QAHE was in Cr-doped $(\mathrm{Bi}_x\mathrm{Sb}_{1-x})_2\mathrm{Te}_3$ ('Cr-BST') thin films at 30 mK in 2013. The upper quantization temperature T_{QAHE}, however, rapidly increased to 2 K in modulation-doped heterostructures in 2015, and later to 3 K in twisted bilayer graphene in 2020. In parallel with the increase in T_{QAHE}, the novel material platforms also gave rise to new topological phenomena, such as the axion-insulator phase (2017), the topological/geometric Hall effect (2020), and higher-Chern-number ($\mathcal{C} > 1$) QAH superlattices (2020).

of the insulating state. Recent Cr-modulation-doped thin films displayed a critical current density of only $\sim$0.125 nA/μm at the CNP [132], compared to $\sim$4.16 nA/μm at the CNP in our uniformly V-doped $(\mathrm{Bi}_x\mathrm{Sb}_{1-x})_2\mathrm{Te}_3$ thin films [see Fig. 4.14(d)]. Interestingly, when Okazaki *et al.* decreased the Cr-concentration of the $\mathrm{Cr}_x(\mathrm{Bi}_y\mathrm{Sb}_{1-y})_{2-x}\mathrm{Te}_3$ delta-layer from $x = 0.36$ [132] to $x = 0.15$ [133], the critical current density increased from $\sim$0.125 nA/μm to $\sim$7.5 nA/μm, respectively. Hence, for Cr/V-modulation-doping concentrations similar to those found in uniformly Cr/V-doped QAH films, modulation doping actually results in lower defect densities and enhanced breakdown characteristics.

In 2017, the axion-insulator phase was realized in modulation-doped QAH thin films when the magnetization of the top and bottom surface were aligned out-of-plane and in the opposite direction to one-another [123, 124]. Axion insulators are an exciting new phase of quantum matter in their own right, and are predicted to exhibit the topological magnetoelectric effect [126, 144, 185, 192]. In 2018, the QAHE was observed in uniformly (Cr,V)-co-doped $(\mathrm{Bi}_x\mathrm{Sb}_{1-x})_2\mathrm{Te}_3$

thin films at 1.5 K [137], whereas in 2019 the first proximity-coupled QAH heterostructures at 100 mK were realized in (Zn,Cr)Te/$(Bi,Sb)_2Te_3$/(Zn,Cr)Te, in which (Zn,Cr)Te is a ferromagnetic insulator (FMI) [191]. Moreover, recent $Cr_2Si_2Te_6/(Bi,Sb)_2Te_3/Cr_2Si_2Te_6$ heterostructures showed an anomalous Hall resistance of $\sim 0.8h/e^2$ at 60 mK [120], and may soon become the second proximity-coupled QAH material platform. Although no values for the critical current density at ultra-low temperatures were reported for these material systems, proximity-coupling a TI to a FMI may circumvent the trade-off between the saturation magnetization and the critical current density, if a good epitaxial relationship can be found between the TI and FMI crystal structures, leading to QAH heterostructures with low defect densities.

In 2020, the QAHE was realized in several new material systems: twisted bilayer graphene up to 3 K [34, 142, 164, 175], flakes of the magnetic TI $MnBi_2Te_4$ at 1.4 K [42], and flakes containing superlattices of $MnBi_2Te_4/Bi_2Te_3$ at 1.9 K [41]. In the same year, a well-quantized QAHE with a tunable Chern number (up to $\mathcal{C} = 5$) was realized in superlattices consisting of alternating Cr-doped and undoped $(Bi_xSb_{1-x})_2Te_3$ layers ($T_{\mathrm{QAHE}} = 25$ mK) [215], and the topological/geometric Hall effect was observed in Cr-modulation-doped QAHE heterostructures ($T_{\mathrm{QAHE}} = 400$ mK) [76], possibly indicating the presence of magnetic Skyrmions [48, 64, 111, 183, 204]. In 2021, the QAHE was also realized in $MoTe_2/WSe_2$ moiré heterobilayers at 2.5 K [107].

The strong dissimilarity between the novel QAH material systems reported in recent years suggests this may only be the 'tip of the iceberg', with a multitude of material realizations waiting to be discovered, which instills hope of one day realizing robust topological phases at room temperature. In addition, moiré engineering has proven to be a powerful tool to create new band structures by combing and twisting existing VdW materials. Here, after the realization of the QAHE in twisted bilayer graphene and $MoTe_2/WSe_2$ moiré heterobilayers, the next big milestone would be the fractional quantum anomalous Hall effect (FQAHE), which has been theoretically predicted for both moiré systems [104, 116, 151]. Moreover, Yang *et al.* have recently predicted the QAHE for a twisted Sb_2 monolayer on top of a Sb_2Te_3 thin film [197], which would eliminate the need for magnetic dopants or proximity-coupled FMI layers in the $(Bi_xSb_{1-x})_2Te_3$ QAH platform altogether.

In the meantime, however, the current $(Bi_xSb_{1-x})_2Te_3$-based systems offer a rich playground for studying topological matter; in particular the modulation-doped heterostructures, which under the right conditions can display the QAHE [125], the axion-insulator phase [123, 124], the topological/geometric Hall effect [76, 204], as well as give rise to nonreciprocal charge transport [201, 202, 203] (as discussed in chapter 5). $MnBi_2Te_4$ is ideally suited to study the axion electrodynamics as well. Namely, the Mn atoms order

ferromagnetically within the $MnBi_2Te_4$ VdW layers of the crystal structure, but couple antiferromagnetically between the stacked VdW layers [105, 135, 136], leading to a QAHI (axion-insulator) phase for an odd (even) number of VdW layers [42, 110]. Moreover, $MnBi_2Te_4$ shows a rich magnetic phase diagram [8, 163], encouraging further research into the interplay between magnetism and band topology. Uniformly V/Cr-doped $(Bi_xSb_{1-x})_2Te_3$ thin films, on the other hand, remain relevant for ultra-low temperature experiments, such as the study of the superconducting proximity effect [84, 166], as well as the possible manipulation of chiral Majorana fermions in the future [1, 12, 13, 59].

Appendix A

Spinless Basis for the Bogoliubov-de Gennes Hamiltonian

The Bogoliubov-de Gennes (BdG) Hamiltonian for a QAHI proximitized by an s-wave superconductor (Eqs. 2.24–2.26) are reproduced here for convenience:

$$\mathcal{H}_{\mathrm{BdG}} = \frac{1}{2}\sum_k \Psi_k^\dagger H_{\mathrm{BdG}} \Psi_k, \tag{A.1}$$

$$H_{\mathrm{BdG}} = \begin{bmatrix} H_0(k) - \mu & \Delta_k \\ \Delta_k^\dagger & -H_0^*(-k) + \mu \end{bmatrix}, \tag{A.2}$$

$$\Delta_k = \begin{bmatrix} i\Delta_1\sigma_y & 0 \\ 0 & i\Delta_2\sigma_y \end{bmatrix}, \tag{A.3}$$

where $\Psi_k = [(c^t_{k\uparrow}, c^t_{k\downarrow}, c^b_{k\uparrow}, c^b_{k\downarrow}), (c^{t\dagger}_{-k\uparrow}, c^{t\dagger}_{-k\downarrow}, c^{b\dagger}_{-k\uparrow}, c^{b\dagger}_{-k\downarrow})]^T$. Here, μ denotes the chemical potential, while Δ_1 and Δ_2 are the pairing gap functions for the top and bottom surface state, respectively.

For the special case of $\Delta_1 = -\Delta_2 \equiv \Delta$ and $\mu = 0$, H_{BdG} (Eq. A.2) can be block-diagonalized using two consecutive basis transformations [189].

A.1 First Basis Transformation

The first basis transformation yields two models, $\breve{H}_1(k)$ and $\breve{H}_2(k)$, with opposite chirality:

$$\breve{H}_{\mathrm{BdG}} = \begin{bmatrix} \breve{H}_1(k) & 0 \\ 0 & \breve{H}_2(k) \end{bmatrix}, \tag{A.4}$$

where

$$\breve{H}_1(k) = \begin{bmatrix} m_k + gM & iv_F k_- & 0 & \Delta \\ -iv_F k_+ & -m_k - gM & -\Delta & 0 \\ 0 & -\Delta & -m_k - gM & -iv_F k_+ \\ \Delta & 0 & iv_F k_- & m_k + gM \end{bmatrix},$$

$$\breve{H}_2(k) = \begin{bmatrix} m_k - gM & -iv_F k_+ & 0 & -\Delta \\ iv_F k_- & -m_k + gM & \Delta & 0 \\ 0 & \Delta & -m_k + gM & iv_F k_- \\ -\Delta & 0 & -iv_F k_+ & m_k - gM \end{bmatrix},$$

with the new basis $(c^t_{k\uparrow} + c^b_{k\uparrow}, c^t_{k\downarrow} - c^b_{k\downarrow}, c^{t\dagger}_{-k\uparrow} + c^{b\dagger}_{-k\uparrow}, c^{t\dagger}_{-k\downarrow} - c^{b\dagger}_{-k\downarrow})^T/\sqrt{2}$ for $\breve{H}_1(k)$ and $(c^t_{k\downarrow} + c^b_{k\downarrow}, c^t_{k\uparrow} - c^b_{k\uparrow}, c^{t\dagger}_{-k\downarrow} + c^{b\dagger}_{-k\downarrow}, c^{t\dagger}_{-k\uparrow} - c^{b\dagger}_{-k\uparrow})^T/\sqrt{2}$ for $\breve{H}_2(k)$.

A.2 Second Basis Transformation

The second basis transformation further block-diagonalizes $\breve{H}_1(k)$ and $\breve{H}_2(k)$, yielding:

$$\tilde{H}_{\mathrm{BdG}} = \begin{bmatrix} \tilde{H}_1(k) & 0 \\ 0 & \tilde{H}_2(k) \end{bmatrix}, \tag{A.5}$$

where

$$\tilde{H}_1(k) = \begin{bmatrix} m_k + gM + \Delta & iv_F k_- & 0 & 0 \\ -iv_F k_+ & -m_k - gM - \Delta & 0 & 0 \\ 0 & 0 & -m_k - gM + \Delta & -iv_F k_+ \\ 0 & 0 & iv_F k_- & m_k + gM - \Delta \end{bmatrix},$$

$$\tilde{H}_2(k) = \begin{bmatrix} m_k - gM - \Delta & -iv_F k_+ & 0 & 0 \\ iv_F k_- & -m_k + gM + \Delta & 0 & 0 \\ 0 & 0 & -m_k + gM - \Delta & iv_F k_- \\ 0 & 0 & -iv_F k_+ & m_k - gM + \Delta \end{bmatrix}.$$

with the new *spinless* basis

$$\frac{1}{2}\begin{bmatrix} c^t_{k\uparrow} + c^b_{k\uparrow} + c^{t\dagger}_{-k\downarrow} - c^{b\dagger}_{-k\downarrow} \\ c^t_{k\downarrow} - c^b_{k\downarrow} + c^{t\dagger}_{-k\uparrow} + c^{b\dagger}_{-k\uparrow} \\ -c^t_{k\downarrow} + c^b_{k\downarrow} + c^{t\dagger}_{-k\uparrow} + c^{b\dagger}_{-k\uparrow} \\ -c^t_{k\uparrow} - c^b_{k\uparrow} + c^{t\dagger}_{-k\downarrow} - c^{b\dagger}_{-k\downarrow} \end{bmatrix} \text{ for } \tilde{H}_1(k),$$

$$\frac{1}{2}\begin{bmatrix} c^t_{k\downarrow} + c^b_{k\downarrow} + c^{t\dagger}_{-k\uparrow} - c^{b\dagger}_{-k\uparrow} \\ c^t_{k\uparrow} - c^b_{k\uparrow} + c^{t\dagger}_{-k\downarrow} + c^{b\dagger}_{-k\downarrow} \\ -c^t_{k\uparrow} + c^b_{k\uparrow} + c^{t\dagger}_{-k\downarrow} + c^{b\dagger}_{-k\downarrow} \\ -c^t_{k\downarrow} - c^b_{k\downarrow} + c^{t\dagger}_{-k\uparrow} - c^{b\dagger}_{-k\uparrow} \end{bmatrix} \text{ for } \tilde{H}_2(k).$$

Notice that $\tilde{H}_1(k)$ and $\tilde{H}_2(k)$ each describe two copies of a spinless $p_x \pm ip_y$ superconductor [51, 150, 189].

Appendix B

Why Long Multi-terminal Hall-bar Devices?

Chang *et al.* were the first to demonstrate clean nonlocal transport of the QAH edge states. The devices consisted of scratched, mm-size 6-terminal Hall-bar devices. While the current flowed through neighboring contacts, the magnetic-field dependence of the three-terminal resistances were recorded [31]. Here, similar nonlocal measurements are shown for a μm-size 6-terminal Hall-bar device.

Figure B.1 shows the four-terminal resistance of our μm-size 6-terminal Hall-bar device D. The transverse resistance $R_{1\text{-}3,6\text{-}2}$ and the longitudinal resistance $R_{1\text{-}3,6\text{-}5}$ show the quantized hysteresis loop and near-dissipationless state of the QAHE, respectively. Note that $R_{1\text{-}3,5\text{-}2} = R_{1\text{-}3,6\text{-}2} - R_{1\text{-}3,6\text{-}5}$, as expected. The resistance $R_{1\text{-}3,5\text{-}4}$ measures a nonlocal transport and should remain zero for any value of the magnetic field. However, small resistance peaks at the coercive field, corresponding to 2D diffusive transport, are clearly visible. As a result, when the Hall-bar dimension is reduced from mm- to μm-size, the simple 6-terminal device is no longer suitable for nonlocal transport measurements. For this reason, the Hall-bar in the main text was elongated and extra contacts were added to allow for length-dependent measurements.

Figure B.2 shows the three-terminal resistance measured in the same nonlocal geometry as in Refs. [31, 94]. The nonlocal resistances $R_{1\text{-}2,x\text{-}2}$ with $x = \{3, 4, 5, 6\}$ show the quantized hysteresis loop superimposed with resistance peaks at the coercive field. The additional component is due to the small V-doped $(Bi_xSb_{1-x})_2Te_3$ sections of the μm-size source/drain contacts, which

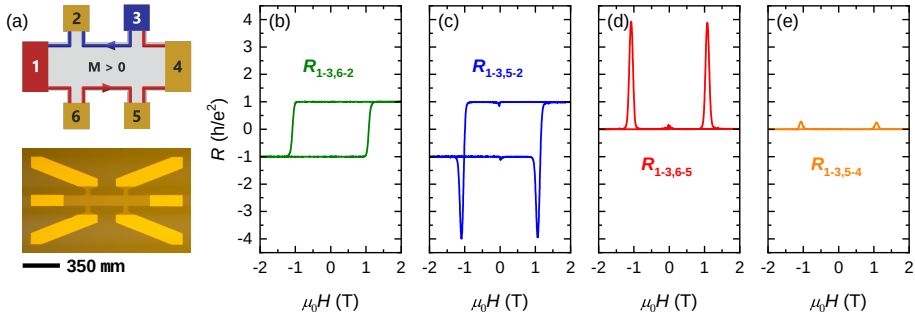

Figure B.1: (a) Schematic of the high (red) and low (blue) potential portions of the chiral edge state for $M > 0$ (top), and a picture of the 6-terminal Hall-bar device D having the width 100 μm and the contact separation 350 μm (bottom). (b-d) Magnetic-field dependencies of the 'local' resistances $R_{1\text{-}3,6\text{-}2}$, $R_{1\text{-}3,5\text{-}2}$ and $R_{1\text{-}3,6\text{-}5}$, measured at 30 mK with an AC probe current of 10 nA. (e) Magnetic-field dependence of the nonlocal resistance $R_{1\text{-}3,5\text{-}4}$.

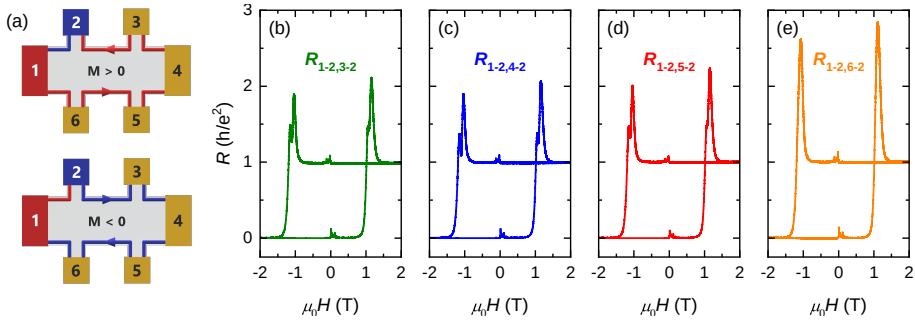

Figure B.2: (a) Schematics of the high (red) and low (blue) potential portions of the chiral edge state for $M > 0$ and $M < 0$. (b-e) Magnetic-field dependencies of the resistances $R_{1\text{-}2,x\text{-}2}$ with $x = \{3, 4, 5, 6\}$, measured at 30 mK with an AC probe current of 10 nA.

add a diffusive contribution to the 'nonlocal' three-terminal resistance. Note that for a probe current of 10 nA, no breakdown of the QAHE is observed near the 50 μm-wide drain contact 2 (i.e. $\beta = 0$ in Eq. 4.6). A detailed analysis of the breakdown of the QAHE, using the Landauer-Büttiker formalism [28], is given in chapter 4.

Appendix C

Procedure to Extract the Critical Current

In this appendix, the procedure that was used to extract the critical current for breakdown in this thesis will be explained.

In the first report of the breakdown of the QAHE by Kawamura *et al.*, the four-terminal current-voltage characteristics did not show a clear zero-voltage plateau [83]. The authors extracted a value for the critical current (denoted here by I_0) by extrapolating the approximately linear part of the I-V characteristics and defining the intercept with the I_{DC}-axis as I_0. This procedure is shown in Fig. C.1(a) for the I-V characteristic of device G1 at $V_{\mathrm{Gate}} = +2$ V [see Fig. 4.14(c) for the full data set]. The red curve, which fits the linear region at high probe currents, intersects the I_{DC}-axis at $I_0 \approx 276$ nA. Note that this definition of the critical current clearly yields values for I_0 that do not coincide with the abrupt onset of dissipation due to breakdown, and as a result this first procedure is not adopted in this work.

Instead of evaluating the critical current from the I-V characteristic, it is instructive to perform differential resistance measurements, see Fig. C.1(b). The curves for dV_x/dI_{DC} show a clear jump in the resistance when the breakdown of the QAHE occurs. The red curve shows a linear fit to this near vertical jump in dV_x/dI_{DC} at the breakdown point. The intercept with the I_{DC}-axis is taken as the critical current $I_{\mathrm{c}} \approx 151$ nA.[1] This second procedure is performed to obtain the I_{c}-values stated in this thesis.

[1] This I_{c}-value of 151 nA corresponds to the purple data point ($j_{\mathrm{c}} \approx 1$ nA/μm) at $V_{\mathrm{Gate}} = +2$ V in Fig. 4.14(d) for the 150-μm-wide Hall-bar device G1.

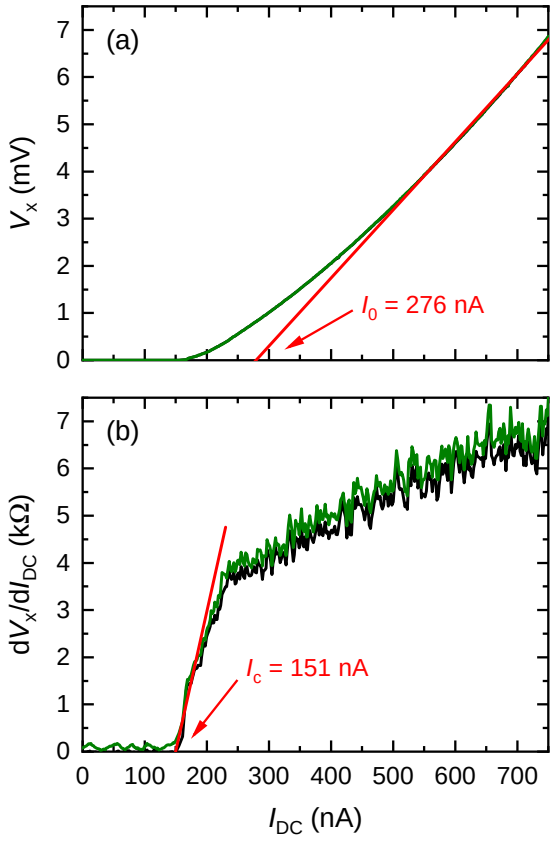

Figure C.1: Two procedures to extract a critical current value for breakdown. (a-b) The four-terminal current-voltage characteristic of $V_x = V_{2\text{-}3}(I_{1\text{-}4})$ [black curve] and $V_{6\text{-}5}(I_{1\text{-}4})$ [green curve] (a), and the corresponding I_{DC}-dependence of the differential resistance dV_x/dI_{DC} (b) for device G1, measured at 30 mK in 0 T (after training at +2 T) with $V_{\mathrm{Gate}} = +2$ V. The dV_x/dI_{DC} curves were measured using an AC excitation of $I_{\mathrm{rms}} = 1$ nA. In panel (a), the approximately linear part of the I-V characteristic is extrapolated [red curve] and the intercept with the I_{DC}-axis gives one measure for the critical current, denoted here by I_0. Clearly the value for $I_0 \approx 276$ nA does not coincide with the loss of the zero-resistance state. In panel (b), a clear jump in dV_x/dI_{DC} is observed when the zero-resistance state is lost. In this thesis, this jump in dV_x/dI_{DC} is fitted by a linear curve [red curve] and the intercept with the I_{DC}-axis is taken as the definition of the critical current I_{c}.

Appendix D

Landauer-Büttiker Treatment of Additional Leakage Paths

In chapter 4, it was shown that the current-induced breakdown of the QAHE, which is caused by a loss of edge current from the high-potential branch of the chiral edge state to the low-potential branch, can be described using a simple Landauer-Büttiker toy-model. Such a simplistic model by no means describes the physics of the current-induced breakdown accurately, but it can provide qualitative expressions for the observed resistances for currents exceeding the critical current for breakdown. While in chapter 4 the model was limited to simple four- and three-terminal geometries in a 6-terminal Hall-bar device, here the calculation is repeated for a 12-terminal Hall-bar device with the same nonlocal configuration as shown in Fig. 4.6. Moreover, four possible leakage paths in the nonlocal region will be addressed. The results further strengthen the claim that dissipationless charge transport persists in the nonlocal transport region of the Hall-bar, even for values of the current at which the QAHI state is broken down in the local region.

D.1 Nonlocal Leakage across the Hall-bar Width

First, we discuss the extension of the Landauer-Büttiker treatment to the nonlocal regime by considering the situation shown in Fig. D.1, which schematically models a 12-terminal Hall-bar device for $M < 0$ with the current flowing from contact 0 to 6. The scattering probabilities α, β, and γ describe the fraction of the current leaking between the opposite edge states in the local

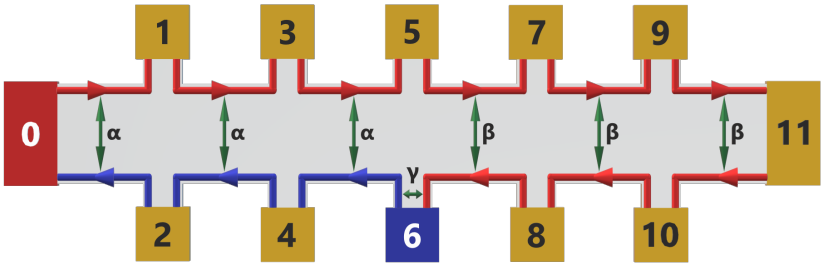

Figure D.1: Schematics of the edge transport in a 12-terminal Hall-bar device for $M < 0$, with the 'leakage' between opposing counter-propagating edges parametrized by the scattering probabilities α, β, and γ. The contact spacing between neighboring contacts are chosen to be equal, i.e. $L_{0\text{-}1} = L_{1\text{-}3} = L_{3\text{-}5} = L_{5\text{-}7} = L_{7\text{-}9} = L_{9\text{-}11}$.

region, nonlocal region, and in the current contact 6, respectively. Note that the spacing between neighboring contacts are chosen to be equal for simplicity, since α, β, and γ are length dependent. The Landauer-Büttiker formula [28] to describe the current-voltage relation was already shown in chapter 4 (as Eq. 4.1), but is reproduced here for convenience:

$$I_i = \frac{e^2}{h} \sum_j (T_{ji} V_i - T_{ij} V_j) \,, \tag{D.1}$$

where V_i is the voltage on the ith contact, I_i is the current flowing through the ith contact into the sample, and T_{ji} is the transmission probability from the ith to the jth contact. The full set of transmission coefficients T_{ji} are best expressed as a matrix (see Eq. D.5); which is shown on the next page.

Using $V_6 = 0$, $I_0 = -I_6 = I$ and $I_i = 0$ for all other contacts, Eq. D.1 can be solved for I and V_i, which allows us to calculate the longitudinal (R_{xx}), transverse (R_{yx}), and nonlocal (R^{NL}) resistances as follows:

$$R_{xx} = R_{0\text{-}6,1\text{-}3} = R_{0\text{-}6,2\text{-}4} = R_{0\text{-}6,3\text{-}5} = \frac{\alpha}{1-\alpha} \frac{h}{e^2} \,, \tag{D.2}$$

$$R_{yx} = R_{0\text{-}6,2\text{-}1} = R_{0\text{-}6,4\text{-}3} = -\frac{h}{e^2} \,, \tag{D.3}$$

$$R^{\mathrm{NL}} = R_{0\text{-}6,5\text{-}7} = R_{0\text{-}6,5\text{-}8} = \cdots = 0 \,. \tag{D.4}$$

$$
T_{ji} = \left[\begin{array}{cccccccccccccccc}
\alpha & 0 & 1-\alpha & 0 & 0 & 0 & 0 & 0 & 0 & 0 & 0 & 0 & 0 & 0 & 0 & 0 \\
1-\alpha & 0 & \alpha & 0 & 0 & 0 & 0 & 0 & 0 & 0 & 0 & 0 & 0 & 0 & 0 & 0 \\
0 & \alpha & 0 & 0 & 1-\alpha & 0 & 0 & 0 & 0 & 0 & 0 & 0 & 0 & 0 & 0 & 0 \\
0 & 1-\alpha & 0 & 0 & \alpha & 0 & 0 & 0 & 0 & 0 & 0 & 0 & 0 & 0 & 0 & 0 \\
0 & 0 & 0 & \alpha & 0 & (1-\alpha)\beta\gamma & (1-\alpha)(1-\gamma) & 0 & \beta & 0 & 0 & 0 & 1-\beta & 0 & 0 & 0 \\
0 & 0 & 0 & 1-\alpha & 0 & \alpha\beta\gamma & \alpha(1-\gamma) & 0 & 1-\beta & 0 & 0 & \beta & 0 & 0 & 1-\beta & 0 \\
0 & 0 & 0 & 0 & 0 & \beta(1-\gamma) & \gamma & 0 & 0 & (1-\beta)(1-\gamma) & 0 & 0 & 0 & 0 & 0 & \beta \\
0 & 0 & 0 & 0 & 0 & 1-\beta & 0 & 0 & 0 & \beta & 0 & 0 & 0 & 0 & 0 & 0 \\
0 & 0 & 0 & 0 & 0 & 0 & 0 & \beta & 0 & 0 & (1-\alpha)(1-\beta)\gamma & 0 & 0 & 0 & 0 & 0 \\
0 & 0 & 0 & 0 & 0 & 0 & 0 & 1-\beta & 0 & 0 & \alpha(1-\beta)\gamma & 0 & 0 & 0 & 0 & 0 \\
0 & 0 & 0 & 0 & 0 & 0 & 0 & 0 & 0 & 0 & (1-\beta)(1-\gamma) & 0 & 0 & 0 & 0 & 0 \\
0 & 0 & 0 & 0 & 0 & 0 & 0 & 0 & 0 & 0 & \beta & 0 & 0 & 0 & 0 & 0 \\
0 & 0 & 0 & 0 & 0 & 0 & 0 & 0 & 0 & 0 & 0 & 0 & 1-\beta & 0 & 0 & 0 \\
0 & 0 & 0 & 0 & 0 & 0 & 0 & 0 & 0 & 0 & 0 & 0 & 0 & \beta & 0 & 0 \\
0 & 0 & 0 & 0 & 0 & 0 & 0 & 0 & 0 & 0 & 0 & 0 & 0 & 0 & 1-\beta & 1-\beta \\
0 & 0 & 0 & 0 & 0 & 0 & 0 & 0 & 0 & 0 & 0 & 0 & 1-\beta & 0 & 0 & \beta
\end{array}\right] \tag{D.5}
$$

Note that R^{NL} is the resistance between any pair of contacts in the nonlocal region (contacts 5, 7, 8, 9, 10, 11) for the current flowing from contact 0 to 6. The results for R_{xx} and R_{yx} are the same as those for the simple four-terminal geometry discussed in chapter 4, cf. Eqs. 4.3–4.4. The result $R^{\mathrm{NL}} = 0$ means that additional resistive channels in the middle of the nonlocal region (represented by β) do not carry any non-equilibrium current, as they are short-circuited by the dissipationless chiral edge channel.

Similarly, the three-terminal resistances can be obtained from the solution of the Landauer-Büttiker formula for the case of Fig. D.1:

$$R_{0\text{-}6,0\text{-}1} = \frac{\alpha}{1-\alpha}\frac{h}{e^2}\,, \qquad R_{0\text{-}6,0\text{-}2} = \frac{1}{1-\alpha}\frac{h}{e^2}\,, \tag{D.6}$$

$$R_{0\text{-}6,4\text{-}6} = \frac{\alpha - 2\alpha\gamma + \gamma}{(1-\alpha)(1-\gamma)}\frac{h}{e^2}\,, \qquad R_{0\text{-}6,8\text{-}6} = \frac{1}{1-\gamma}\frac{h}{e^2}\,. \tag{D.7}$$

Note that the resistances shown in Figs. 4.9 and 4.10 correspond to the case of $\gamma \gg \alpha$.

D.2 Forced Nonlocal Leakage across the Hall-bar Width

To gain a deeper understanding of the possible role of coexisting dissipative channels in the nonlocal region, it is useful to consider a slightly modified network model shown in Fig. D.2, where β is now chosen to be nonreciprocal. In this case, a fraction β of the current in the top edge is forced to 'leak' into the bottom edge. The nonzero transmission coefficients for contact 8, 10 and 11 now become

$$T_{4,8} = (1-\alpha)\gamma, \quad T_{5,8} = \alpha\gamma, \quad T_{6,8} = \gamma, \quad T_{8,10} = T_{10,11} = 1, \tag{D.8}$$

resulting in a position-dependent edge potential in the nonlocal region:

$$V_7 = V_8 = (1-\beta)V_5, \tag{D.9}$$

$$V_9 = V_{10} = (1-\beta)^2 V_5, \tag{D.10}$$

$$V_{11} = (1-\beta)^3 V_5, \tag{D.11}$$

which decreases towards contact 11. Namely, as β increases, the nonlocal voltage contacts are slowly 'cut out' from the circuit, becoming essentially floating contacts. Hence, if some non-equilibrium currents were flowing between

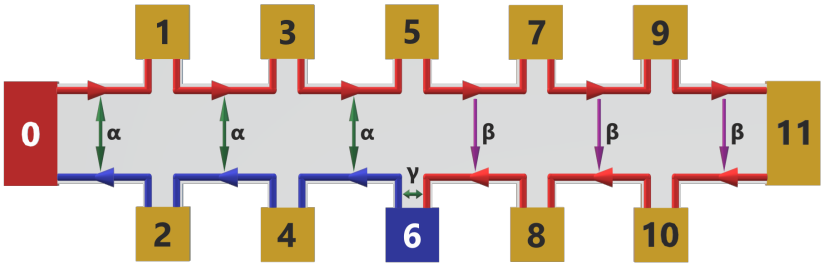

Figure D.2: Schematics of the edge transport in a 12-terminal Hall-bar device for $M < 0$, with the 'leakage' between opposing counter-propagating edges parametrized by the scattering probabilities α, β, and γ, where β is chosen to be nonreciprocal. The contact spacing between neighboring contacts are chosen to be equal, i.e. $L_{0\text{-}1} = L_{1\text{-}3} = L_{3\text{-}5} = L_{5\text{-}7} = L_{7\text{-}9} = L_{9\text{-}11}$.

the opposite edge states in the nonlocal region, the measured nonlocal voltages would be non-zero. This is clearly not the case, as can be seen in Figs. 4.7, E.1, and E.3, where the nonlocal edge potential remains zero. It is interesting to note that one could imagine a scenario as presented in Fig. D.2 to become relevant for very small edge channel separations where the opposite edge states start to hybridize. Such hybridization in very narrow voltage contacts, for example, would lead to a reduction of the measured voltage by $\sim (1 - \beta)$, even though there is no large local electric field present. The smallest contacts in this work (see table 3.1) had a width of 20 μm with no sign of hybridization, meaning that the edge states were always well separated in the experiments.

D.3 Nonlocal Leakage to the Drain Contact

Next, let us consider resistive channels in the nonlocal region, which leak to the drain contact (instead of leaking across the Hall-bar width), as shown in Fig. D.3. Notice that the contact numbering is modified, which will allow more concise expressions for the edge potential. One can imagine the leakage in the nonlocal region to take place through the 2D state. Moreover, there is an electric field present in this scenario to drive the breakdown, consistent with our percolation model (see section 4.10.3). In this case, β should in principle become smaller as the voltage probes are farther from the drain contact, but for simplicity, let us take the scattering probability β to be uniform throughout

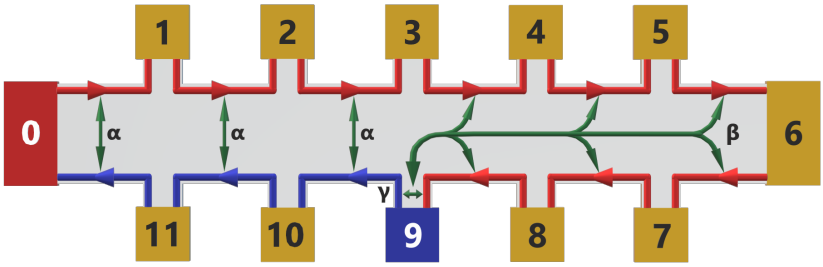

Figure D.3: Schematics of the edge transport in a 12-terminal Hall-bar device for $M < 0$, with the current flowing from contact 0 to 9. Notice that the contact numbering now runs clockwise around the Hall-bar device. The contact spacing between neighboring contacts are still chosen to be equal, i.e. $L_{0\text{-}1} = L_{1\text{-}2} = L_{2\text{-}3} = L_{3\text{-}4} = L_{4\text{-}5} = L_{5\text{-}6}$. The 'leakage' between opposing counter-propagating edges is parametrized by the scattering probabilities α and γ. Additionally, the scattering probability β describes the leakage of the edge state in the nonlocal region of the Hall-bar to the drain contact 9. The leakage of the edge state in the local region of the Hall-bar to the drain contact 9 is not considered as it is negligible compared to the leakage path described by α.

the nonlocal region. The transmission coefficients now become:

$$\begin{aligned}
&T_{0,0} = T_{1,11} = T_{2,10} = T_{10,2} = T_{11,1} = \alpha, && T_{3,8} = \alpha(1-\beta)\gamma, \\
&T_{0,11} = T_{1,0} = T_{2,1} = T_{3,2} = T_{11,10} = 1-\alpha, && T_{9,8} = 1-(1-\beta)\gamma, \\
&T_{9,3} = T_{9,4} = T_{9,5} = T_{9,6} = T_{9,7} = \beta, && T_{9,8} = (1-\alpha)(1-\beta)\gamma, \\
&T_{4,3} = T_{5,4} = T_{6,5} = T_{7,6} = T_{8,7} = 1-\beta,
\end{aligned} \tag{D.12}$$

where all $T_{j,9}$ were omitted since they drop out of Eq. D.1, because $V_9 = 0$. The resulting edge potential in the nonlocal region, given by

$$V_i = (1-\beta)^{i-3} V_3, \qquad i = 4,5,6,7,8 \tag{D.13}$$

is nonzero and position-dependent, again in disagreement with our experimental observations.

D.4 Dissipation through Additional Quasi-helical Edge States

Lastly, let us consider the presence of additional quasi-helical edge states as proposed in Ref. [187] and employed in Refs. [31, 94] to explain their non-ideal nonlocal measurements in 6-terminal Hall-bar devices. Note that these 'quasi-helical' edge states are thought of as the remnants of the 2D topological surface states on the side surfaces of a 3D magnetic TI when reducing the thickness to form the quasi-2D QAHI films, see Fig. 4.16 for an illustration.

Figure D.4 shows the same schematic of the 12-terminal Hall-bar device for $M < 0$ with the current flowing from contact 1 to 9. This time, however, the current is not only carried by the chiral edge state of the QAHI, but also by two counter-propagating quasi-helical edge states (shown in purple and green in Fig. D.4). In accordance with Ref. [187], let us assume perfect transmission through the chiral edge channel, i.e. $T_{i+1,i} = 1$, while for the quasi-helical states we assume $T_{i+1,i} = \alpha$ and $T_{i,i+1} = \beta$. Unlike the case of the helical edge states in the quantum spin Hall effect (QSHE) where $\alpha = \beta = 1$, these 'quasi-helical' states are not protected from backscattering ($\alpha, \beta < 1$). The total transmission coefficients then become $T_{i+1,i} = 1 + \alpha$ and $T_{i,i+1} = \beta$.

The voltages appearing in the Hall-bar for $M < 0$ can be expressed concisely by using $r \equiv \beta/(1 + \alpha)$ as

$$V_i = \frac{1 - r^{9-i}}{1 - r^9} V_0 \qquad (\text{for } 0 \leqslant i \leqslant 8), \tag{D.14}$$

$$V_i = \frac{1 - r^{9-i}}{1 - r^{-3}} V_0 \qquad (\text{for } i = 10, 11), \tag{D.15}$$

which is in agreement with the expressions derived by Wang *et al.* in Ref. [187] for a 6-terminal Hall-bar device. Note that when moving clockwise along the edge of the Hall-bar, the voltage decreases from contact 0 to 9 on the red-colored edge, whereas the voltage increases from contact 9 to 0 on the blue-colored edge. Moreover, there is no distinction in this model between local and nonlocal transport. Since our QAHI films are rather thick (∼8 nm), the presence of additional (dissipative) edge states certainly seems possible. Nevertheless, as explained in chapter 4 (section 4.9), we did not observe any signatures of quasi-helical edge states in our transport experiments.

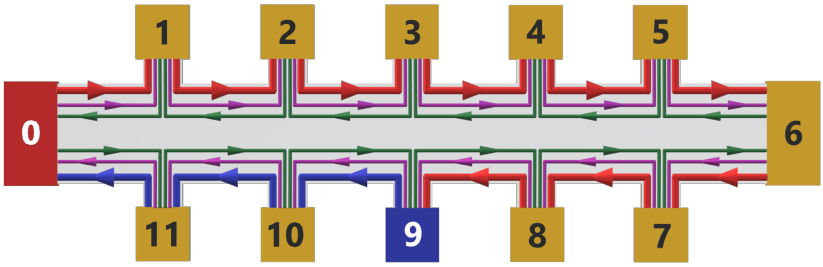

Figure D.4: Schematics of the edge transport in a 12-terminal Hall-bar device for $M < 0$, with the current flowing from contact 0 to 9. Notice that the contact numbering now runs clockwise around the Hall-bar device. The contact spacing between neighboring contacts are still chosen to be equal, i.e. $L_{0\text{-}1} = L_{1\text{-}2} = L_{2\text{-}3} = L_{3\text{-}4} = L_{4\text{-}5} = L_{5\text{-}6}$. The high and low potential branches of the QAH edge state are shown in red and blue, respectively. Two counter-propagating 'quasi-helical' edge states are added in this model, they are shown in purple and green.

D.5 Summary

If in the nonlocal region resistive channels in the 2D bulk are allowed to carry some leakage current to the drain contact, or additional, dissipative quasi-helical edge states are included in the model, a position-dependent expression for the edge potential in the nonlocal region is obtained. However, experimentally we found a linear length dependence for the breakdown in the local region of the Hall-bar [see Figs. 4.2(c-d)], while the nonlocal voltages always remained zero, as can be seen in Figs. 4.7, E.1, and E.3. This clearly indicates that no edge current is lost in the nonlocal region through such leakage paths and the dissipationless edge transport is maintained in the nonlocal region. This is consistent with the statement that the transverse electric field governs the breakdown process.

Appendix E

Additional Nonlocal Transport Data

In this appendix, the transport data are shown for three additional nonlocal configurations for the 26-terminal Hall-bar device:

Figure E.1 shows the '90°-rotated' Hall-bar configuration, with the current flowing from contact 5 to 6. The transverse resistance $R_{5\text{-}6,0\text{-}25}$ is quantized, demonstrating that the chiral edge state runs along the edge of the sample. Figure E.1(c) shows the resistances $R_{5\text{-}6,a\text{-}b}$ with a-b being the contact pairs $\{1\text{-}2, 9\text{-}10, 13\text{-}14, 17\text{-}18, 21\text{-}22, 17\text{-}21\}$. $R_{5\text{-}6,a\text{-}b}$ remains essentially zero for any value of the magnetic field, showing near-dissipationless nonlocal edge transport. Moreover, $R_{5\text{-}6,a\text{-}b}$ shows no exponential length dependence as proposed for additional quasi-helical edge states that are not protected from backscattering [187], see Eqs. D.14–D.15. It should be noted, however, that the large nonlocal device geometry used here might not be best suited to study these proposed dissipative edge states, as their observation might be limited by the phase coherent length L_ϕ and the proposed features in Ref. [187] would be strongly suppressed for our large probe separations of 300 μm.

Figure E.2 shows the 'left-edge' Hall-bar configuration, with the current flowing from contacts 1 to 9. The transverse resistance $R_{1\text{-}9,6\text{-}5}$ is quantized at 40 and 500 mK. The resistances $R_{1\text{-}9,5\text{-}x}$, with the voltage contact x being $\{13, 14, 17, 18, 21, 22, 25\}$, demonstrate a quantized hysteresis loop at 40 mK as well, but acquire an additional offset at 500 mK due to a nonzero longitudinal resistance at this elevated temperature. Notice that the hysteresis loops of $R_{1\text{-}9,6\text{-}5}$ and $R_{1\text{-}9,5\text{-}x}$ are opposite, since the polarity of the voltage contacts is

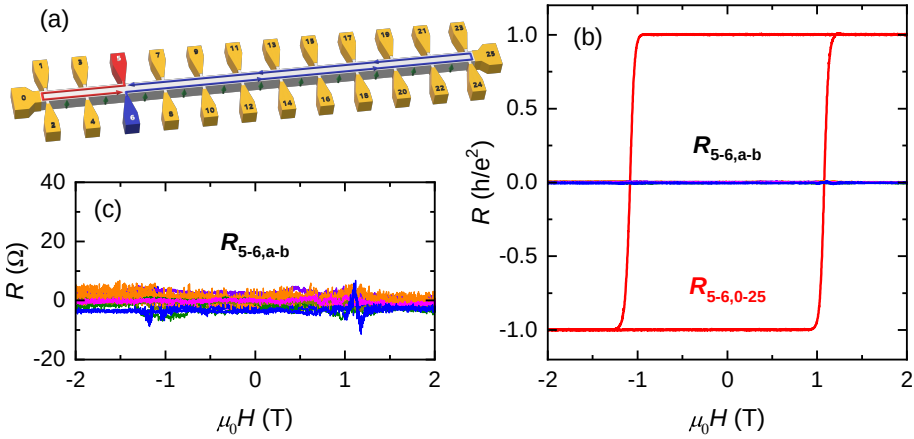

Figure E.1: '90°-rotated' configuration for the 26-terminal Hall-bar device A, measured at 30 mK with $I_{\mathrm{DC}} = 80$ nA. (a) Schematic of the potential distribution in the chiral edge state for $M > 0$. (b) Magnetic-field dependencies of $R_{5\text{-}6,a\text{-}b}$ with $a\text{-}b = \{1\text{-}2, 9\text{-}10, 13\text{-}14, 17\text{-}18, 21\text{-}22, 17\text{-}21\}$ and the transverse resistance $R_{5\text{-}6,0\text{-}25}$. (c) Magnified plot of $R_{5\text{-}6,a\text{-}b}$ vs H.

switched. Both the offset and the peaks at the coercive field originate from 2D diffusive transport between contacts 1 and 9. $R_{1\text{-}9,5\text{-}x}$ remains the same for all voltage contact x of $\{13, 14, 17, 18, 21, 22, 25\}$, and hence there is no length dependence in the nonlocal region. Moreover, the reported 'nonlocal hysteresis loop' (and its temperature dependence) assigned to the existence of additional quasi-helical edge states in Refs. [31, 94] was not observed.

Figure E.3 shows the 'middle-edge' Hall-bar configuration, with the current flowing from contact 9 to 13. The current dependence of $V_{1\text{-}5}$ and $V_{17\text{-}21}$, measured nonlocally, shows no sign of breakdown. The voltage $V_{1\text{-}21}$, on the other hand, includes both $V_{1\text{-}5}$ and $V_{17\text{-}21}$ as well as the small local region in-between. This $V_{1\text{-}21}$ shows the breakdown of the QAHE at $\sim$0.16 μA, demonstrating again that the breakdown only occurs in the local transport region.

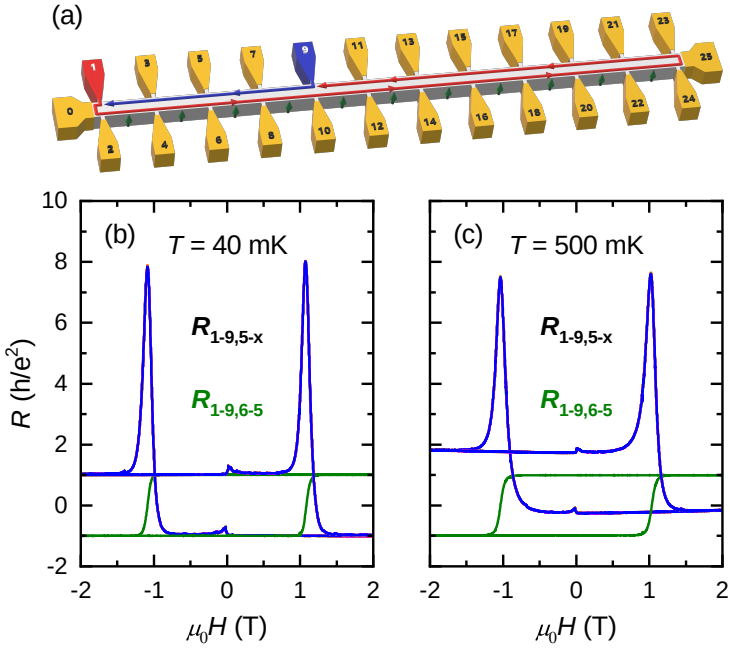

Figure E.2: 'Left-edge' configuration for the 26-terminal Hall-bar device A, measured with $I_{\mathrm{DC}} = 80$ nA. (a) Schematic of the potential distribution in the chiral edge state for $M > 0$. (b-c) Magnetic-field dependencies of $R_{1\text{-}9,5\text{-}x}$ with $x = \{13, 14, 17, 18, 21, 22, 25\}$ and the transverse resistance $R_{1\text{-}9,6\text{-}5}$ measured at 40 mK (b) and at 500 mK (c).

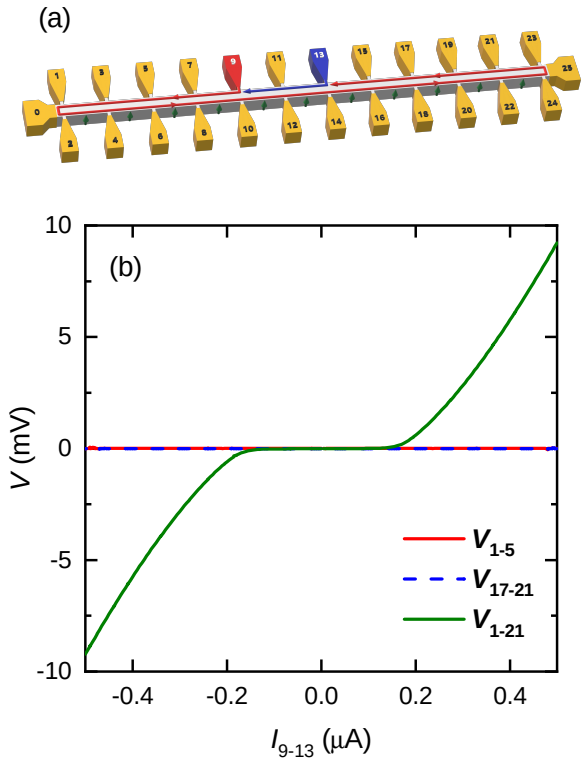

Figure E.3: 'Middle-edge' configuration for the 26-terminal Hall-bar device B, measured at 40 mK in +2 T. (a) Schematic of the potential distribution in the chiral edge state for $M > 0$. (b) I-V characteristics for $V_{1\text{-}5}$, $V_{17\text{-}21}$, and $V_{1\text{-}21}$ with $I_{9\text{-}13}$. The voltages $V_{1\text{-}5}$ and $V_{17\text{-}21}$ are nonlocal, while $V_{1\text{-}21}$ includes the 'local' contribution from the portion between contacts 9 and 13. The breakdown of the QAHE occurs at $\sim$0.16 μA.

Appendix F

Additional Nonreciprocal Transport Data

The nonreciprocal charge transport was studied using four Hall-bar devices (C, F1, J, and K). The most important results were discussed in chapter 5. In this appendix, additional data are provided for the devices, such that each device possesses a complete data on its own.

F.1 26-terminal Hall-bar Device C

The nonreciprocal charge transport in device C was measured using AC and DC techniques. The DC data were discussed in chapter 5 (Figs. 5.1 and 5.2); below additional AC data are provided for device C.

F.1.1 Excitation-current Dependence

The excitation-current dependence of the second-harmonic voltage $V_x^{2\omega}$, antisymmetrized in the magnetization and magnetic field, was already shown in Fig. 5.9 of chapter 5. Figure F.1 shows the same data, but presented as the second-harmonic voltage difference $\Delta V_{\text{R-L}}^{2\omega} = V_x^{2\omega}(\text{Right}) - V_x^{2\omega}(\text{Left})$ between the right and left contact pairs. Note that the large $V_x^{2\omega}/V_x^{1\omega}$ ratio $\sim$10% near breakdown is reproduced, regardless of the method of antisymmetrization.

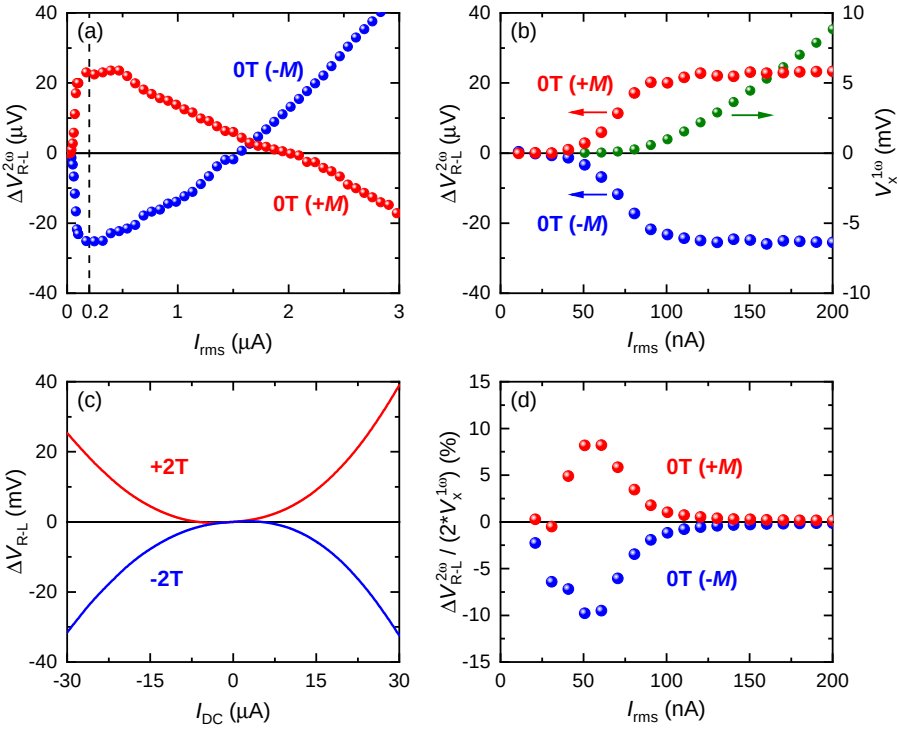

Figure F.1: Current dependence of the nonreciprocal charge transport near breakdown for the 26-terminal Hall-bar device C, with the current flowing from contact 0 to 25, see Fig. 5.1(b) for a schematic of the device. (a) The second-harmonic voltage difference $\Delta V^{2\omega}_{\text{R-L}} = V^{2\omega}_x(\text{Right}) - V^{2\omega}_x(\text{Left})$ between the right (6-20) and left (5-19) contact pairs at 10 mK, shown for zero field after training in ± 2 T. The dashed line marks $I_{\text{rms}} = 0.2$ μA. (b) Zoom of (a) up to 200 nA, showing V^{ω}_x (in mV) and $\Delta V^{2\omega}_{\text{R-L}}$ (in μV). The current-induced breakdown of the QAHE occurs at $I_{\text{rms}} \approx 60$ nA, i.e. at a peak-current value of $I_0 \approx 85$ nA. (c) The DC voltage difference $\Delta V_{\text{R-L}}$ between the right (6-10) and left (5-9) contact pairs at 3.5 K in ± 2 T. The data set is reproduced from Fig. 5.2(c). (d) The ratio $\Delta V^{2\omega}_{\text{R-L}}/(2{*}V^{\omega}_x)$, reaching $\sim$10% at $I_{\text{rms}} \approx 50$–60 nA.

F.1.2 Magnetic-field Dependence

Figure F.2 shows the magnetic-field dependence of $V_x^{2\omega}$ for the left and right edge for different current values near the breakdown of the QAHE. As the current is increased past the critical value for breakdown, a hysteresis loop opens up in $V_x^{2\omega}$. The sign-inversion of the nonreciprocal response is observed between the left and right edge, as well as when the magnetization is reversed when crossing the coercive field.

A double peak feature is observed at the coercive field for 20, 70 nA, and 2.5 μA. These peaks are consistent with the closing of the exchange gap in the 2D surface state as the net magnetization passes through zero at the coercive field. Namely, as the size of the exchange gap reduces, the insulating QAH state is lost, leading to a finite amplitude of $V_x^{2\omega}$. However, when the exchange gap closes entirely, the chiral 1D edge states is lost and $V_x^{2\omega}$ becomes zero at the coercive field. As the exchange gap reopens and a 1D edge state of opposite chirality is formed, $V_x^{2\omega}$ displays a second inverted peak, which disappears again when the exchange gap is large enough to form the insulating QAH state.

Lastly, as explained in chapter 5, $V_x^{2\omega}$ undergoes a sign-inversion at $I_{\mathrm{rms}} \approx 1.65$ μA (see Fig. 5.9 or F.1). This sign-inversion is also observed when comparing Figs. F.2(c,g) for $I_{\mathrm{rms}} = 200$ nA with Figs. F.2(d,h) for $I_{\mathrm{rms}} = 2.5$ μA, respectively.

F.1.3 Temperature Dependence

Figure F.3(a) shows the temperature dependence of the nonreciprocal response near breakdown, measured at $I_{\mathrm{rms}} = 200$ nA below the sign-inversion at $I_{\mathrm{rms}} \approx 1.65$ μA. The data points were extracted from magnetic-field sweeps. Contrary to the temperature dependence of the nonreciprocal response at high-current values (see Figs. 5.5 and 5.11), the amplitude of $V_x^{2\omega}$ at $I_{\mathrm{rms}} = 200$ nA vanishes quickly with increasing temperature. Figure F.3(b) shows the temperature dependence of R_{xx} and R_{yx} for comparison, measured with $I_{\mathrm{rms}} = 200$ nA.

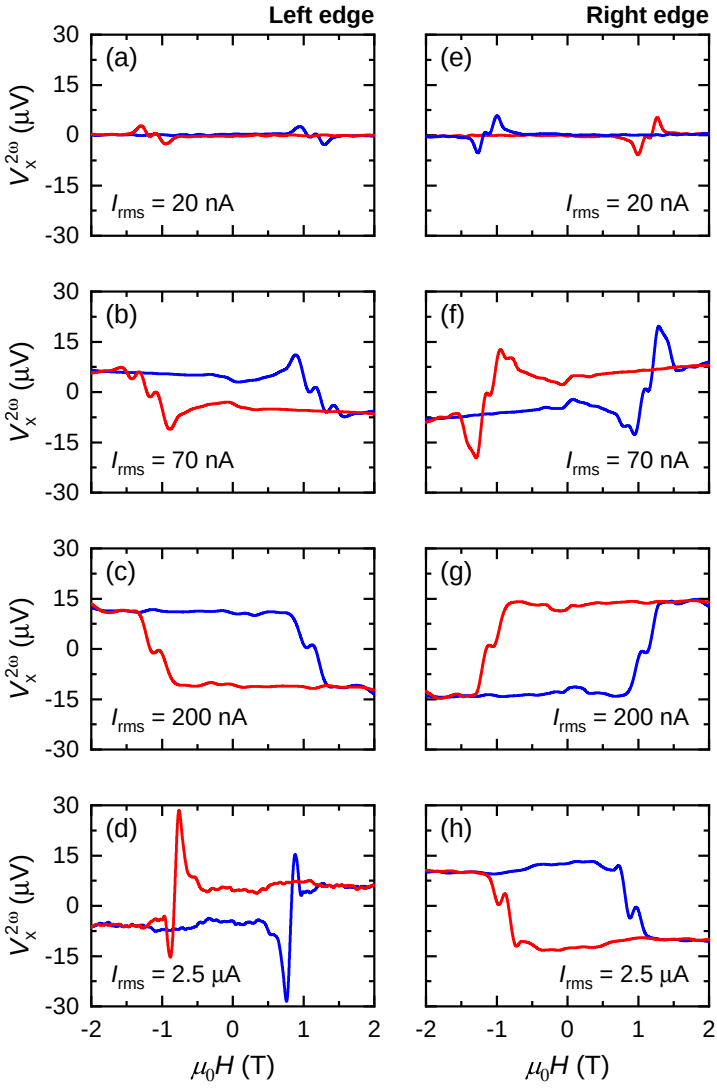

Figure F.2: Magnetic-field dependence of the nonreciprocal charge transport for different excitation currents near breakdown at 15 mK. In the 26-terminal Hall-bar device C the current flowed from contact 0 to 25, see Fig. 5.1(b) for a schematic of the device. (a-d) The magnetic-field dependence of $V_x^{2\omega}$ for the contact pair 5-19 (left edge), measured with $I_{\mathrm{rms}} = 20$ nA (a), 70 nA (b), and 200 nA (c), and 2.5 μA (d). (e-h) The corresponding magnetic-field dependence of $V_x^{2\omega}$ for the contact pair 6-20 (right edge). The $V_x^{2\omega}$ curves were antisymmetrized in the magnetization and magnetic-field, i.e. $V_x^{2\omega} = [V_x^{2\omega}(+\hat{M}, +\mu_0 H) - V_x^{2\omega}(-\hat{M}, -\mu_0 H)]/2$.

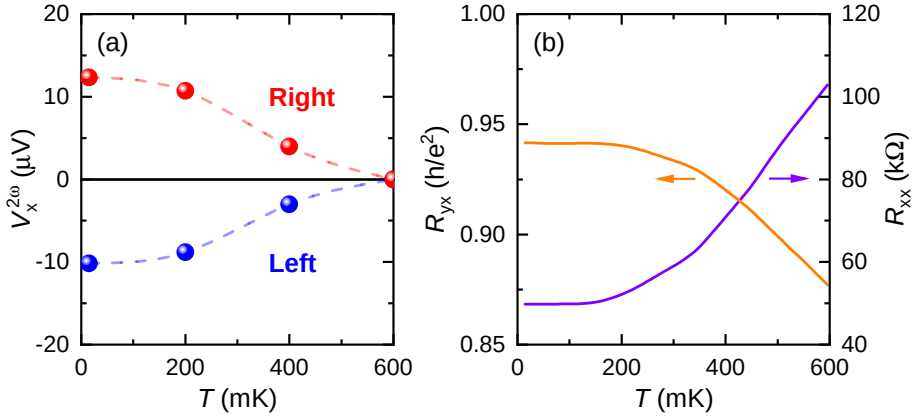

Figure F.3: Temperature dependence of the nonreciprocal charge transport in the low-current limit ($I_{\mathrm{rms}} = 200$ nA) for the 26-terminal Hall-bar device C, with the current flowing from contact 0 to 25, see Fig. 5.1(b) for a schematic of the device. (a) The temperature dependence of the second-harmonic voltage $V_x^{2\omega}$, measured between contact pairs 5-19 (Left) and 6-20 (Right) in 0 T after training in ±2 T. The $V_x^{2\omega}$ curves were antisymmetrized in the magnetization, i.e. $V_x^{2\omega} = [V_x^{2\omega}(+\hat{M}, 0\mathrm{T}) - V_x^{2\omega}(-\hat{M}, 0\mathrm{T})]/2$. The dashed line is a guide to the eye. (b) The temperature dependence of the longitudinal and transverse resistance, R_{xx} and R_{yx} respectively, shown for comparison and measured with $I_{\mathrm{rms}} = 200$ nA in +2 T.

F.1.4 Length Dependence

In chapter 5, Fig. 5.12 shows the length dependence of $|V_x^{2\omega}|$ measured using different contact pairs. The data points were extracted from I-V curves and magnetic-field sweeps. Figures F.4 and F.5 show representative $V_x^{2\omega}$ curves used to construct Fig. 5.12. The $|V_x^{2\omega}|$ amplitudes extracted from the magnetic-field sweeps tend to be slightly smaller than those obtained from the I-$V^{2\omega}$ characteristics as sweeping the magnet in the dilution refrigerator resulted in slight heating of the sample. As can be seen from Figs. F.4 and F.5, the nonreciprocal response is reproduced for all measured contact pairs, and the same polarity is maintained along the full length of the 26-terminal Hall-bar device C.

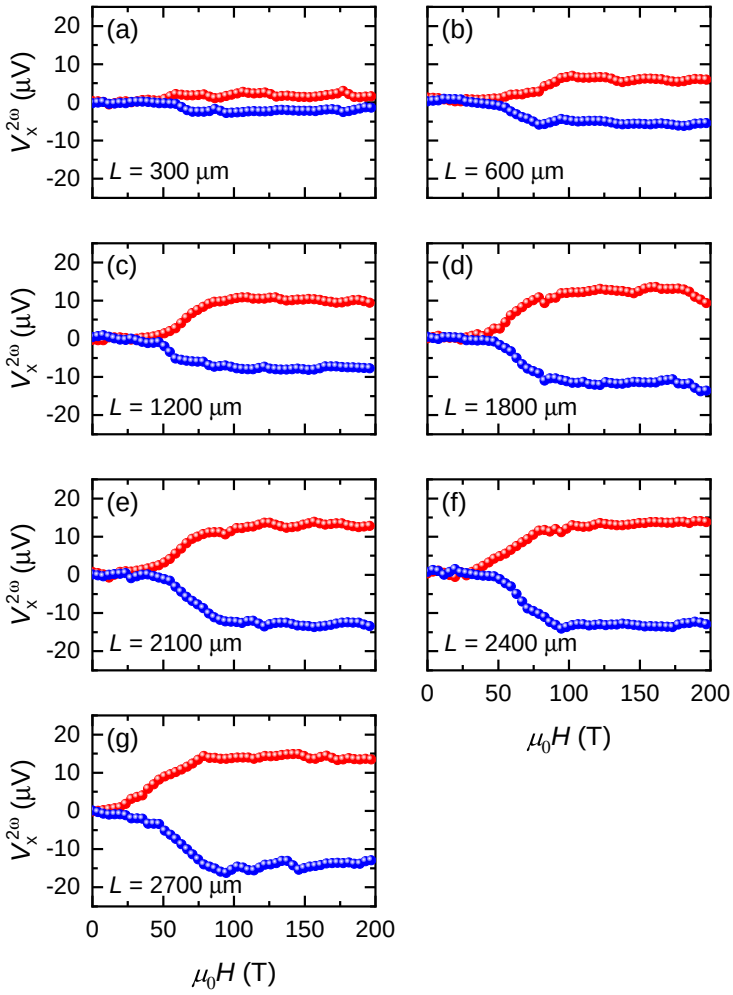

Figure F.4: I-$V_x^{2\omega}$ characteristics for different contact pairs of the 26-terminal Hall-bar device C, measured at 15 mK in ±2 T. An approximate linear length dependence is observed for $V_x^{2\omega}$. The $V_x^{2\omega}$ curves were antisymmetrized in the magnetization and magnetic field, i.e. $V_x^{2\omega} = [V_x^{2\omega}(+\hat{M}, +2\mathrm{T}) - V_x^{2\omega}(-\hat{M}, -2\mathrm{T})]/2$.

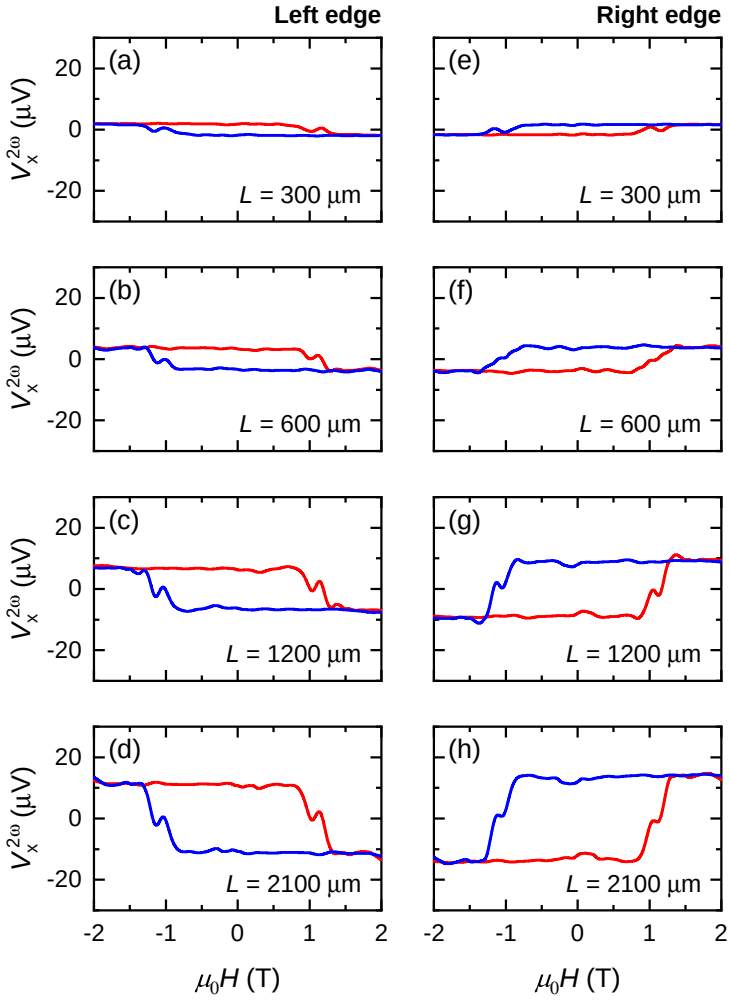

Figure F.5: Magnetic-field dependence for different contact pairs of the 26-terminal Hall-bar device C, measured at 15 mK with $I_{\mathrm{rms}} = 200$ nA. An approximate linear length dependence is observed for $V_x^{2\omega}$. The $V_x^{2\omega}$ curves were antisymmetrized in the magnetization and magnetic field, i.e. $V_x^{2\omega} = [V_x^{2\omega}(+\hat{M}, +\mu_0 H) - V_x^{2\omega}(-\hat{M}, -\mu_0 H)]/2$.

F.2 6-terminal Hall-bar Device F1

The nonreciprocal response in device F1 was measured between 2 K and 50 K in the high-current limit, see chapter 5 (section 5.2.2). Figure 5.5(a) shows the temperature dependence of $R_{xx}^{2\omega}$ from 2 K to 50 K at $V_{\mathrm{Gate}} = 0$ V. Figure F.6 shows the corresponding magnetic-field sweeps for $R_{xx}^{2\omega}$ at different temperatures up to $\sim T_{\mathrm{C}}$. The hysteresis loop in $R_{xx}^{2\omega}$ becomes smaller with increasing temperature, with $R_{xx}^{2\omega}$ vanishing at the Curie temperature $T_{\mathrm{C}} \approx 12$ K in zero magnetic field.

F.3 6-terminal Hall-bar Device J

The gate-voltage dependence of the nonreciprocal response in device J, measured at 60 mK for different excitation currents, was shown in Figs. 5.7 and 5.8 of chapter 5. Figures F.7(a) and F.7(b) show the corresponding I-$V_x^{2\omega}$ characteristics on the p-type ($V_{\mathrm{Gate}} = -10$ V) and n-type ($V_{\mathrm{Gate}} = +15.5$ V) side of the CNP, respectively. Simularly, Figs. F.8(a) and F.8(b) show the magnetic-field dependence of $V_x^{2\omega}$ on the p-type ($V_{\mathrm{Gate}} = -15$ V) and n-type ($V_{\mathrm{Gate}} = +20$ V) side of the CNP, respectively.

F.4 6-terminal Hall-bar Device K

The gate-voltage dependencies of the nonreciprocal response in device K, measured at different temperatures with $I_{\mathrm{rms}} = 100$ nA and $I_{\mathrm{rms}} = 2$ μA, were shown in Figs. 5.10 and 5.11 of chapter 5, respectively. Figure F.9(a) shows the longitudinal and transverse resistance at $I_{\mathrm{rms}} = 2$ μA for comparison. The CNP is located at $V_{\mathrm{Gate}} \approx +10$ V, while the crossing point between the curves for $V_x^{2\omega}$(Right) and $V_x^{2\omega}$(Left) occurs at $V_{\mathrm{Gate}} \approx +6$ V. Hence, at $I_{\mathrm{rms}} = 2$ μA the crossing point of $V_x^{2\omega}$ has already moved away from the CNP. This shift with decreasing excitation current continues till $I_{\mathrm{rms}} = 100$ nA, after which the curves for $V_x^{2\omega}$(Right) and $V_x^{2\omega}$(Left) no longer cross and $V_x^{2\omega}$(Right) $> V_x^{2\omega}$(Left), see Fig. F.10. Moreover, notice that for $I_{\mathrm{rms}} = 100$ nA [Fig. F.10(f)], $V_x^{2\omega}$(Right) and $V_x^{2\omega}$(Left) coincide near the CNP ($V_{\mathrm{Gate}} \approx +10$ V), where the QAH film recovers the zero-resistance state below breakdown. Lastly, Figs. F.9(c) and F.9(s) show the corresponding I-$V_x^{2\omega}$ characteristics on the p-type ($V_{\mathrm{Gate}} = -30$ V) and n-type ($V_{\mathrm{Gate}} = +30$ V) side of the CNP, respectively.

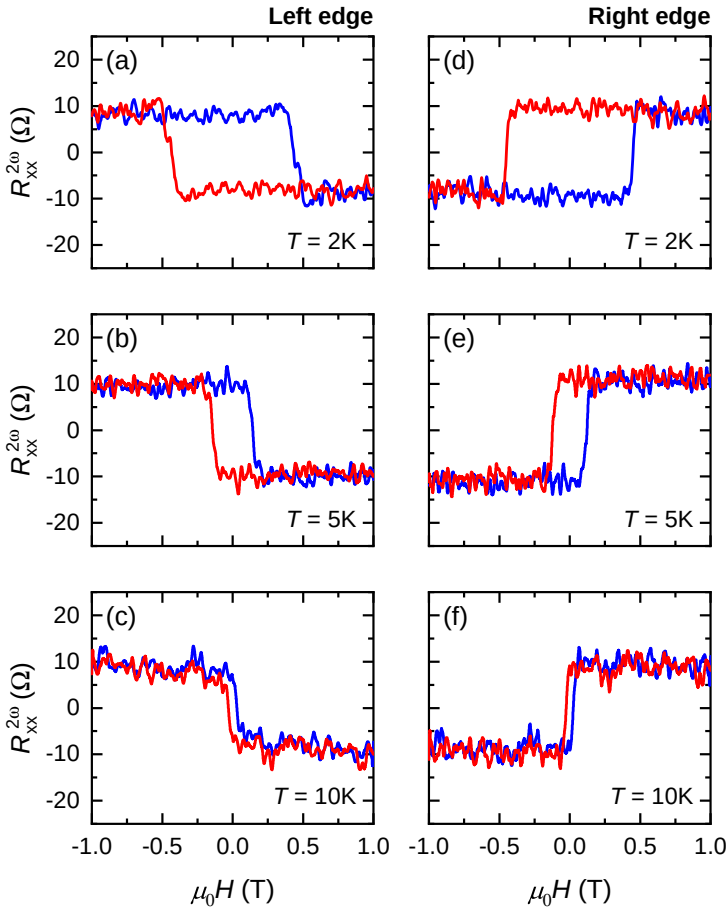

Figure F.6: Magnetic-field dependence of the nonreciprocal charge transport at different temperatures up to $T_C \approx 12$ K: (a,d) 2 K, (b,e) 5 K, and (c,f) 10 K. A current of $I_{\mathrm{rms}} = 1$ μA flowed through Hall-bar device F1 from contact 1 to 4, see Fig. 4.13 for a picture. The left edge (a-c) and right edge (d-f) correspond to the contact pairs 2-3 and 6-5, respectively. The 2D charge carriers are p-type, since $V_{\mathrm{Gate}} = 0$ V. The $R_{xx}^{2\omega}$ curves were antisymmetrized in the magnetization and magnetic-field, i.e. $R_{xx}^{2\omega} = [R_{xx}^{2\omega}(+\hat{M}, +\mu_0 H) - R_{xx}^{2\omega}(-\hat{M}, -\mu_0 H)]/2$.

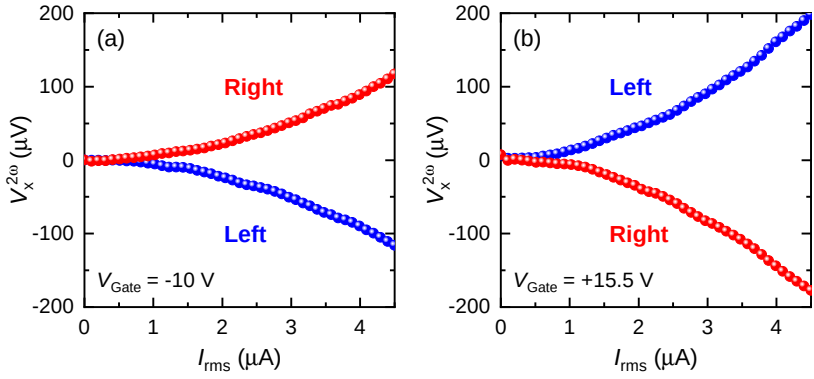

Figure F.7: Current dependence of the nonreciprocal charge transport at 65 mK in ±2 T for Hall-bar device J at different gate voltages: (a) $V_{\mathrm{Gate}} = -10$ V and (b) $V_{\mathrm{Gate}} = +15.5$ V. The current flows from contact 1 to 4; the left (right) edge corresponds to the contact pairs 2-3 (6-5) and are shown in blue (red). The $V_x^{2\omega}$ curves were antisymmetrized in the magnetization and magnetic-field, i.e. $V_x^{2\omega} = [V_x^{2\omega}(+\hat{M}, +2\mathrm{T}) - V_x^{2\omega}(-\hat{M}, -2\mathrm{T})]/2$.

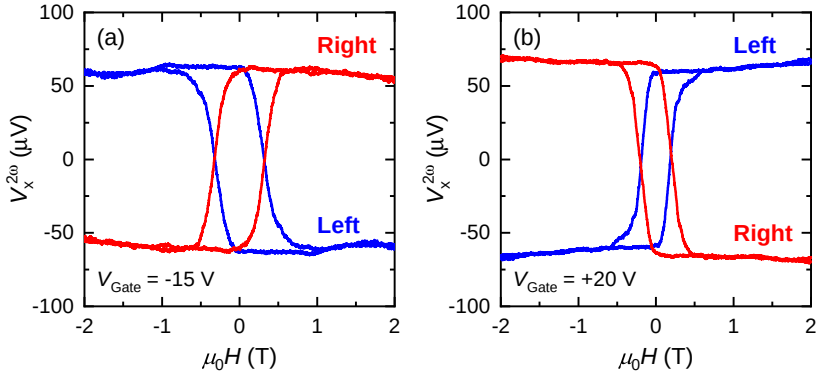

Figure F.8: Magnetic-field dependence of the nonreciprocal charge transport at 65 mK with $I_{\mathrm{rms}} = 3$ μA for Hall-bar device J at different gate voltages: (a) $V_{\mathrm{Gate}} = -15$ V and (b) $V_{\mathrm{Gate}} = +20$ V. The current flows from contact 1 to 4; the left (right) edge corresponds to the contact pairs 2-3 (6-5) and are shown in blue (red). The $V_x^{2\omega}$ curves were antisymmetrized in the magnetization and magnetic-field, i.e. $V_x^{2\omega} = [V_x^{2\omega}(+\hat{M}, +\mu_0 H) - V_x^{2\omega}(-\hat{M}, -\mu_0 H)]/2$.

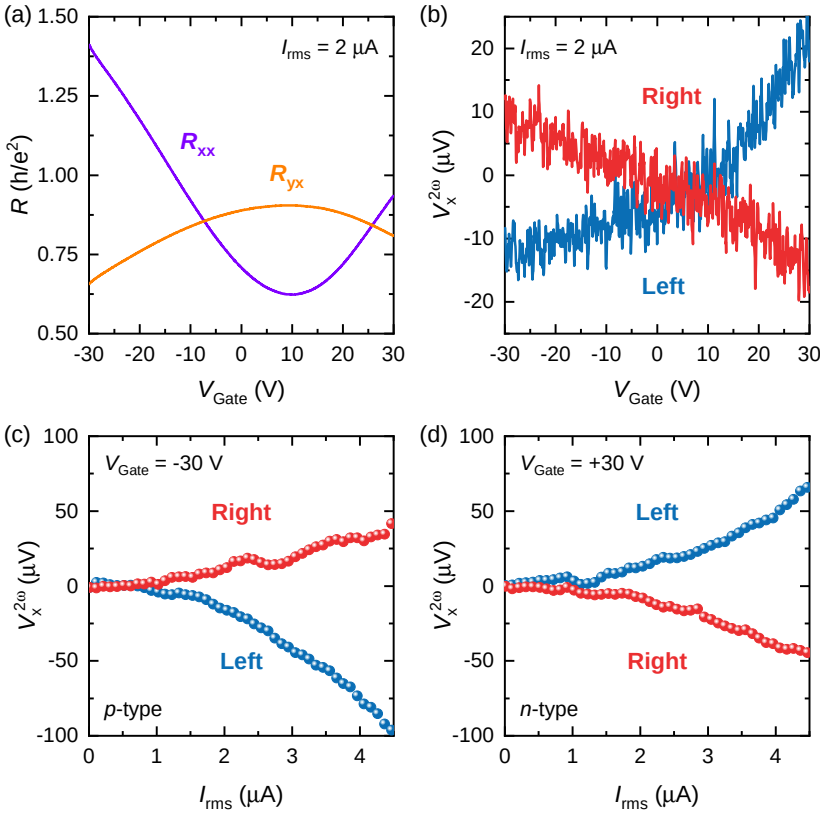

Figure F.9: Gate-voltage and current dependencies of the nonreciprocal charge transport at 60 mK for Hall-bar device K. The current flows from contact 1 to 4; the left (right) edge corresponds to the contact pairs 2-3 (6-5). (a) Gate-voltage dependence of the longitudinal and transverse resistance, R_{xx} and R_{yx}, respectively. (b) Gate-voltage dependence of the second-harmonic voltage $V_x^{2\omega}$ at $I_{\rm rms} = 2\ \mu$A. (c-d) Excitation-current dependence of $V_x^{2\omega}$ at $V_{\rm Gate} = -30$ V (c) and $V_{\rm Gate} = +30$ V (d). The $V_x^{2\omega}$ curves were measured in ± 2 T, and were antisymmetrized in the magnetization and magnetic-field, i.e. $V_x^{2\omega} = [V_x^{2\omega}(+\hat{M}, +2\text{T}) - V_x^{2\omega}(-\hat{M}, -2\text{T})]/2$.

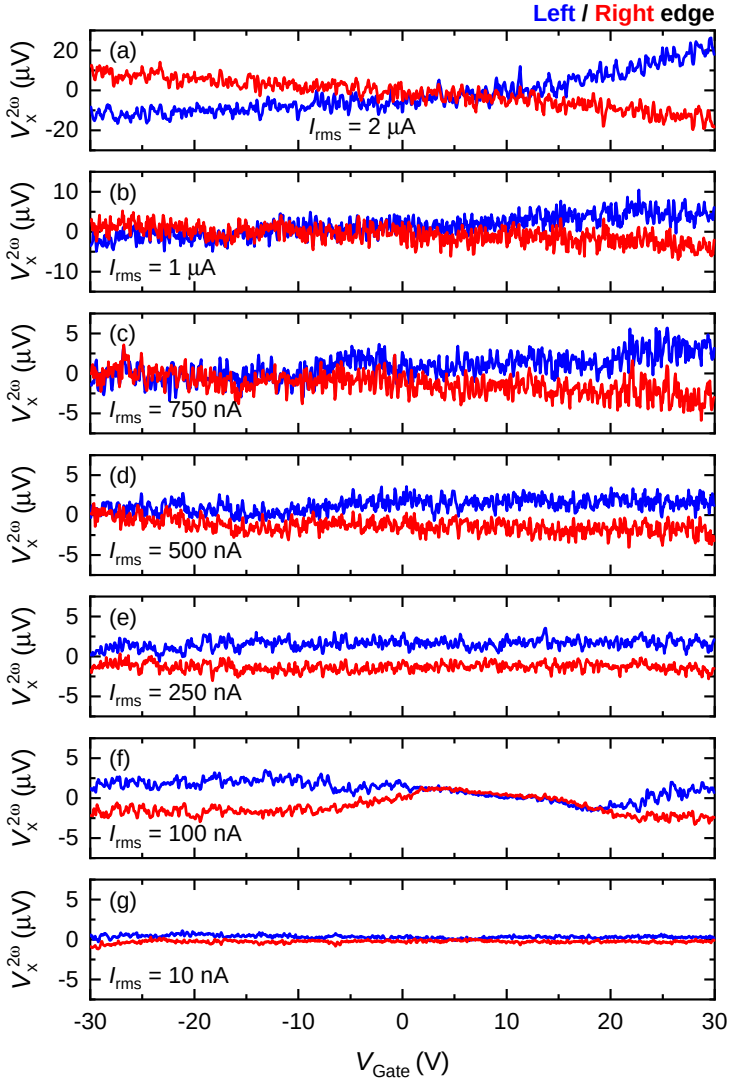

Figure F.10: Gate-voltage dependence of the second-harmonic voltage, measured with different excitation currents $I_{\mathrm{rms}} = 750$ nA (a), 500 nA (b), 375 nA (c), 250 nA (d), 100 nA (e), 50 nA (f) and 10 nA (g) for Hall-bar device K at 55 mK. The current flows from contact 1 to 4; the left (right) edge corresponds to the contact pairs 2-3 (6-5) and are shown in blue (red). The $V_x^{2\omega}$ curves were measured in ±2 T, and were antisymmetrized in the magnetization and magnetic-field, i.e. $V_x^{2\omega} = [V_x^{2\omega}(+\hat{M}, +2\mathrm{T}) - V_x^{2\omega}(-\hat{M}, -2\mathrm{T})]/2$.

Appendix G

Comparison of Nonreciprocal Response to Other Material Systems

Here, the amplitude of the nonreciprocal response of the V-doped $(Bi_xSb_{1-x})_2Te_3$ thin films studied in chapter 5 is compared with other material platforms. Table G.1 lists the materials for which a large magnetochiral anisotropy (MCA) has been reported, whereas table G.2 gives an overview of magnetic materials/heterostructures displaying sizable nonreciprocal charge transport. For the MCA, the different material platforms are benchmarked by comparing their γ-values (or $\gamma' = \gamma A$, with A the cross-sectional area), see Eq. 5.1. However, since for magnetic systems time-reversal symmetry (TRS) is spontaneously broken (rather than by the application of a magnetic field), their nonreciprocal responses are not classified as 'MCA'. Moreover, the amplitude of the nonreciprocity does not scale linearly with the magnetic-field strength, which means that the rectification coefficient γ in units of $A^{-1}T^{-1}$ is not well-defined.

When comparing the 'raw' rectification $\Delta R/R$ (expressed in %) in tables G.2 and G.2, it is clear that the nonreciprocal response of QAHIs outperforms most material platforms by a large margin. One might argue that such a comparison is not justified, since $\Delta R/R$ scales linearly with the current density i (and applied magnetic field H in the MCA). Nevertheless, for any possible implementation of these rectification phenomena, the performance would depend on the maximum achievable $\Delta R/R$ for the largest possible i (and H) the material system or application can sustain.

	Material	T [K]	$\mu_0 H$ [T]	ΔR [Ω]	R_0 [Ω]	$\Delta R/R$ [%]	i [A/m^2]	$\Delta R/R/i$ [10^{-10} m^2/A]	I [A]	Area [m^2]	γ [A^{-1}T^{-1}]	γ' [m^{2}A^{-1}T^{-1}]	MCA type	Ref.
Normal conductors	$(Bi,Sb)_2Te_3$ nanowire	0.08	0.035	14	12250	0.114	3×10^{7}	0.38	1×10^{-7}	3.3×10^{-15}	327000	1.1×10^{-9}	Vector-product	[103]
	n-type Si FET	300	2	0.8	620	0.13	1×10^{10}	1.3×10^{-3}	1×10^{-3}	1×10^{-13}	0.1	1×10^{-14}	Vector-product	[157]
	[DM-EDT-TTF]$_2$ClO$_4$	300	3.2	0.59	3000	0.020	2×10^{5}	9.9	1×10^{-3}	5×10^{-9}	0.01	5×10^{-11}	Inner-product	[143]
	Carbon nanotube	2.5	14	23	10000	0.23	3.5×10^{10}	6.6×10^{-4}	3.5×10^{-7}	1×10^{-17}	230	2.3×10^{-15}	Inner-product	[97]
	$SrTiO_3$	7	0.18	0.45	50	0.9	8.3×10^{8}	0.1	5×10^{-4}	6×10^{-13}	20	1.2×10^{-11}	Vector-product	[61]
	BiTeBr	2	9	0.036	1000	0.0037	1.3×10^{9}	2.8×10^{-4}	1.3×10^{-4}	1×10^{-13}	1	3×10^{-12}	Vector-product	[70]
	WTe_2	300	14	0.027	180	0.015	7.1×10^{9}	2.1×10^{-4}	1.2×10^{-3}	1.7×10^{-13}	0.22	3.7×10^{-14}	Vector-product	[60]
	Ge(111)	15	1	120	29000	0.41	1.7×10^{5}	0.41	1×10^{-5}	6×10^{-11}	0.7	4.2×10^{-11}	Vector-product	[56]
	Bi_2Se_3	60	9	0.11	1800	0.0063	1.4×10^{9}	4.6×10^{-4}	5.6×10^{-3}	4×10^{-13}	0.0006	2.4×10^{-16}	Vector-product	[62]
	t-Te	300	1.5	-	-	0.01	1.3×10^{4}	77	6.5×10^{-3}	5×10^{-7}	0.00073	3.6×10^{-9}	Inner-product	[155]
	$ZrTe_5$	3	0.02	0.014	29.6	0.047	8.3×10^{4}	57	2×10^{-4}	2.4×10^{-9}	195	4.7×10^{-7}	Vector-product	[190]
Superconductors	MoS_2	2	0.7	1.8	32	5.7	1.1×10^{9}	0.51	1.7×10^{-5}	1.6×10^{-14}	3800	5.9×10^{-11}	Vector-product	[184]
	WS_2 nanotube	4	2	0.57	40	1.4	4.5×10^{6}	31	3.5×10^{-8}	7.9×10^{-15}	10000	7.9×10^{-10}	Inner-product	[148]
	Bi2Te3/FeTe	6.9	0.5	0.0057	0.36	1.6	6.7×10^{7}	2.4	2×10^{-4}	3×10^{-12}	0.00065	2×10^{-14}	Vector-product	[205]
	InAs 2DEG	1.45	0.09	400	45000	0.89	-	-	2.8×10^{-8}	-	4.15×10^{6}	-	Vector-product	[11]

Table G.1: Overview of the MCA in different material systems with large amplitudes of the nonreciprocal response (γ or γ'). The table was adapted from Ref. [103].

	Material	T [K]	$\mu_0 H$ [T]	ΔR [Ω]	R_0 [Ω]	$\Delta R/R$ [%]	i [A/m^2]	$\Delta R/R/i$ [10^{-10} m^2/A]	I [A]	Area [m^2]	Ref.
Magnet/ SC	YIG/MoGe	4	7.3	0.073	0.86	8.5	5.7×10^{4}	14900	0.00004	-	[117]
Magnet	Pt/Co	300	2	0.2	290	0.069	4.9×10^{11}	1.4×10^{-4}	0.0213	4.3×10^{-14}	[7]
	Ta/Co	300	0.2	0.014	574	0.0025	1.0×10^{11}	2.5×10^{-5}	0.0085	8.5×10^{-14}	[6]
	Pt/Py	300	0.015	0.04	40	0.1	1.1×10^{12}	9.1×10^{-5}	0.0033	3.0×10^{-15}	[108]
	Pt/Co	300	0.2	0.0031	170	0.0018	1.0×10^{11}	1.8×10^{-5}	0.003	3.0×10^{-14}	[208]
	Co_2MnSi/Pt	300	0.075	0.05	33000	0.00015	1.7×10^{11}	8.9×10^{-7}	0.41	2.4×10^{-11}	[109]
	GaMnAs	130	0.002	2.2	1720	0.13	7.5×10^{9}	0.0017	0.00015	2.0×10^{-14}	[134]
	MnSi	35	0.4	0.00011	1	0.011	1.0×10^{9}	0.0011	0.0025	2.5×10^{-12}	[209]
	$(Bi,Sb)_2Te_3$/ CoFeB	150	0.02	0.0085	730	0.0012	6.7×10^{9}	1.7×10^{-4}	0.0020	3.0×10^{-13}	[118]
	$(Bi,Sb)_2Te_3$/ $Cr_x(Bi,Sb)_{2-x}Te_3$	2	0.7	35	14000	0.25	6.3×10^{6}	3.97	5.0×10^{-7}	8.0×10^{-14}	[203]
	$(Bi,Sb)_2Te_3$/ $Cr_x(Bi,Sb)_{2-x}Te_3$	1.9	1	51	14000	0.23	2.5×10^{6}	15	6×10^{-7}	2.4×10^{-13}	[47]
	$CrNb_3S_6$	<200	2	$\mathcal{O}(10^{-6})$	-	-	1.1×10^{9}	-	0.0045	4.1×10^{-12}	[5]
QAHI	$V_x(Bi,Sb)_{2-x}Te_3$	0.01	0	-	-	∼20	7.5×10^{4}	$\sim3\times10^{4}$	6.0×10^{-8}	8.0×10^{-13}	This work
	$V_x(Bi,Sb)_{2-x}Te_3$	2	0	25	5.4×10^{4}	0.045	1.3×10^{6}	3.5	1×10^{-6}	8.0×10^{-13}	This work
	$V_x(Bi,Sb)_{2-x}Te_3$	3.5	-	1.1×10^{3}	1.1×10^{5}	1.0	3.8×10^{7}	2.7	3.0×10^{-5}	8.0×10^{-13}	This work
	$Cr_x(Bi,Sb)_{2-x}Te_3$	0.5	0.1	190	16000	1.1	3.8×10^{6}	31	3×10^{-6}	8.0×10^{-13}	[201]
	$Cr_x(Bi,Sb)_{2-x}Te_3$	2	0.1	4100	16000	26	1.3×10^{8}	21	0.0001	8.0×10^{-13}	[201]

Table G.2: Overview of the nonreciprocal response in different magnetic systems. Here, the non-reciprocal responses are determined by the spontaneous magnetization, and the magnetic field H is mentioned for completeness. As a result, the γ-value is not a well-defined parameter to characterize the nonreciprocal response. The reader is instead advised to compare the values of $\Delta R/R$ or $\Delta R/R/i$. Note that for the nonreciprocal response of $V_x(Bi,Sb)_{2-x}Te_3$ at 60 nA stating values for ΔR and R_0 is not appropriate due to the strongly nonlinear I-V relation. The table was adapted from Ref. [103].

Erklärung zur Dissertation

Hiermit versichere ich an Eides statt, dass ich die vorliegende Dissertation selbstständig und ohne die Benutzung anderer als der angegebenen Hilfsmittel und Literatur angefertigt habe. Alle Stellen, die wörtlich oder sinngemäß aus veröffentlichten und nicht veröffentlichten Werken dem Wortlaut oder dem Sinn nach entnommen wurden, sind als solche kenntlich gemacht. Ich versichere an Eides statt, dass diese Dissertation noch keiner anderen Fakultät oder Universität zur Prüfung vorgelegen hat; dass sie - abgesehen von unten angegebenen Teilpublikationen und eingebundenen Artikeln und Manuskripten - noch nicht veröffentlicht worden ist sowie, dass ich eine Veröffentlichung der Dissertation vor Abschluss der Promotion nicht ohne Genehmigung des Promotionsausschusses vornehmen werde. Die Bestimmungen dieser Ordnung sind mir bekannt. Darüber hinaus erkläre ich hiermit, dass ich die Ordnung zur Sicherung guter wissenschaftlicher Praxis und zum Umgang mit wissenschaftlichem Fehlverhalten der Universität zu Köln gelesen und sie bei der Durchführung der Dissertation zugrundeliegenden Arbeiten und der schriftlich verfassten Dissertation beachtet habe und verpflichte mich hiermit, die dort genannten Vorgaben bei allen wissenschaftlichen Tätigkeiten zu beachten und umzusetzen. Ich versichere, dass die eingereichte elektronische Fassung der eingereichten Druckfassung vollständig entspricht.

Teilpublikationen:

Lippertz, G., Bliesener, A., Uday, A., Pereira, L. M. C., Taskin, A. A., and Ando, Y. Current-induced breakdown of the quantum anomalous Hall effect. *Phys. Rev. B 106* (Jul 2022), 045419.

Gertjan Lippertz, 12 May 2023

Bibliography

[1] Adagideli, I., Hassler, F., A., G., Pacholski, M., and Beenakker, C. W. J. Time-resolved electrical detection of chiral edge vortex braiding. *SciPost Phys. 8* (Jan 2020), 13.

[2] Alexander-Webber, J. A., Baker, A. M. R., Janssen, T. J. B. M., Tzalenchuk, A., Lara-Avila, S., Kubatkin, S., Yakimova, R., Piot, B. A., Maude, D. K., and Nicholas, R. J. Phase space for the breakdown of the quantum Hall effect in epitaxial graphene. *Phys. Rev. Lett. 111* (Aug 2013), 096601.

[3] Ando, Y. Topological insulator materials. *J. Phys. Soc. Japan 82*, 10 (Sep 2013), 102001.

[4] Annett, J. F. *Superconductivity, Superfluids and Condensates*, 1 ed. Oxford Master Series in Condensed Matter Physics. Oxford University Press, Jun 2004.

[5] Aoki, R., Kousaka, Y., and Togawa, Y. Anomalous nonreciprocal electrical transport on chiral magnetic order. *Phys. Rev. Lett. 122* (Feb 2019), 057206.

[6] Avci, C. O., Garello, K., Ghosh, A., Gabureac, M., Alvarado, S. F., and Gambardella, P. Unidirectional spin Hall magnetoresistance in ferromagnet/normal metal bilayers. *Nat. Phys. 11*, 7 (Jun 2015), 570–575.

[7] Avci, C. O., Mendil, J., Beach, G. S. D., and Gambardella, P. Origins of the unidirectional spin Hall magnetoresistance in metallic bilayers. *Phys. Rev. Lett. 121* (Aug 2018), 087207.

[8] Bac, S.-K., Koller, K., Lux, F., Wang, J., Riney, L., Borisiak, K., Powers, W., Zhukovskyi, M., Orlova, T., Dobrowolska, M., Furdyna, J. K., Dilley, N. R., Rokhinson, L. P., Mokrousov,

Y., McQueeney, R. J., Heinonen, O., Liu, X., and Assaf, B. A. Topological response of the anomalous Hall effect in $MnBi_2Te_4$ due to magnetic canting. *npj Quantum Mater. 7* (Apr 2022), 46.

[9] Baker, A. M. R., Alexander-Webber, J. A., Altebaeumer, T., and Nicholas, R. J. Energy relaxation for hot Dirac fermions in graphene and breakdown of the quantum Hall effect. *Phys. Rev. B 85* (Mar 2012), 115403.

[10] Batey, G., and Teleberg, G. Principles of Dilution Refrigeration. Tech. rep., Oxford Instruments, Sept 2015. Technology Guide.

[11] Baumgartner, C., Fuchs, L., Costa, A., Reinhardt, S., Gronin, S., Gardner, G. C., Lindemann, T., Manfra, M. J., Faria Junior, P. E., Kochan, D., Fabian, J., Paradiso, N., and Strunk, C. Supercurrent rectification and magnetochiral effects in symmetric Josephson junctions. *Nat. Nanotechnol. 17* (2022), 39–44.

[12] Beenakker, C. Angels & Demons: Majorana & Dirac fermions in a quantum Hall edge channel. Journal Club for Condensed Matter Physics, Sep 2017.

[13] Beenakker, C. W. J., Baireuther, P., Herasymenko, Y., Adagideli, I., Wang, L., and Akhmerov, A. R. Deterministic creation and braiding of chiral edge vortices. *Phys. Rev. Lett. 122* (Apr 2019), 146803.

[14] Bernevig, B. A., and Hughes, T. L. *Topological Insulators and Topological Superconductors*. Princeton University Press, 2013.

[15] Bernevig, B. A., Hughes, T. L., and Zhang, S.-C. Quantum spin Hall effect and topological phase transition in HgTe quantum wells. *Science 314*, 5806 (Dec 2006), 1757–1761.

[16] Bernevig, B. A., and Zhang, S.-C. Quantum spin Hall effect. *Phys. Rev. Lett. 96* (Mar 2006), 106802.

[17] Bestwick, A. J., Fox, E. J., Kou, X., Pan, L., Wang, K. L., and Goldhaber-Gordon, D. Precise quantization of the anomalous Hall effect near zero magnetic field. *Phys. Rev. Lett. 114* (May 2015), 187201.

[18] Bliesener, A. *Molecular Beam Epitaxy Growth of Topological Materials*. PhD thesis, Universität zu Köln, Mar 2021.

[19] Bömerich, T., Lux, J., Feng, Q. T., and Rosch, A. Length scale of puddle formation in compensation-doped semiconductors and topological insulators. *Phys. Rev. B 96* (Aug 2017), 075204.

[20] Borgwardt, N., Lux, J., Vergara, I., Wang, Z., Taskin, A. A., Segawa, K., van Loosdrecht, P. H. M., Ando, Y., Rosch, A., and Grüninger, M. Self-organized charge puddles in a three-dimensional topological material. *Phys. Rev. B 93* (Jun 2016), 245149.

[21] Böttcher, J., Tutschku, C., and Hankiewicz, E. M. Fate of quantum anomalous Hall effect in the presence of external magnetic fields and particle-hole asymmetry. *Phys. Rev. B 101* (May 2020), 195433.

[22] Böttcher, J., Tutschku, C., Molenkamp, L. W., and Hankiewicz, E. M. Survival of the quantum anomalous Hall effect in orbital magnetic fields as a consequence of the parity anomaly. *Phys. Rev. Lett. 123* (Nov 2019), 226602.

[23] Bradlyn, B., Elcoro, L., Cano, J., Vergniory, M. G., Wang, Z., Felser, C., Aroyo, M. I., and Bernevig, B. A. Topological quantum chemistry. *Nature 547* (Jul 2017), 298–305.

[24] Breunig, O., and Ando, Y. Opportunities in topological insulator devices. *Nat. Rev. Phys. 4* (Mar 2022), 184–193.

[25] Breunig, O., Wang, Z., Taskin, A., Lux, J., Rosch, A., and Ando, Y. Gigantic negative magnetoresistance in the bulk of a disordered topological insulator. *Nat. Commun. 8* (May 2017), 15545.

[26] Brun-Picard, J., Djordjevic, S., Leprat, D., Schopfer, F., and Poirier, W. Practical quantum realization of the ampere from the elementary charge. *Phys. Rev. X 6* (Dec 2016), 041051.

[27] Budewitz, A., Bendias, K., Leubner, P., Khouri, T., Shamim, S., Wiedmann, S., Buhmann, H., and Molenkamp, L. W. Quantum anomalous Hall effect in Mn doped HgTe quantum wells. *arXiv e-prints: 1706.05789* (Sep 2017).

[28] Büttiker, M. Absence of backscattering in the quantum Hall effect in multiprobe conductors. *Phys. Rev. B 38* (Nov 1988), 9375–9389.

[29] Cava, R. J., Ji, H., Fuccillo, M. K., Gibson, Q. D., and Hor, Y. S. Crystal structure and chemistry of topological insulators. *J. Mater. Chem. C 1* (Mar 2013), 3176–3189.

[30] Chang, C.-Z., Zhang, J., Feng, X., Shen, J., Zhang, Z., Guo, M., Li, K., Ou, Y., Wei, P., Wang, L.-L., Ji, Z.-Q., Feng, Y., Ji, S., Chen, X., Jia, J., Dai, X., Fang, Z., Zhang, S.-C., He, K., Wang, Y., Lu, L., Ma, X.-C., and Xue, Q.-K. Experimental observation of the quantum anomalous Hall effect in a magnetic topological insulator. *Science 340*, 6129 (Apr 2013), 167–170.

[31] Chang, C.-Z., Zhao, W., Kim, D. Y., Wei, P., Jain, J. K., Liu, C., Chan, M. H. W., and Moodera, J. S. Zero-field dissipationless chiral edge transport and the nature of dissipation in the quantum anomalous Hall state. *Phys. Rev. Lett. 115* (Jul 2015), 057206.

[32] Chang, C.-Z., Zhao, W., Kim, D. Y., Zhang, H., Assaf, B. A., Heiman, D., Zhang, S.-C., Liu, C., Chan, M. H. W., and Moodera, J. S. High-precision realization of robust quantum anomalous Hall state in a hard ferromagnetic topological insulator. *Nat. Mater. 14* (Mar 2015), 473–477.

[33] Chaubet, C., and Geniet, F. Nonequilibrium occupation of Landau levels and universal critical field in the quantum-Hall-effect breakdown. *Phys. Rev. B 58* (Nov 1998), 13015–13027.

[34] Chen, G., Sharpe, A. L., Fox, E. J., Zhang, Y.-H., Wang, S., Jiang, L., Lyu, B., Li, H., Watanabe, K., Taniguchi, T., Shi, Z., Senthil, T., Goldhaber-Gordon, D., Zhang, Y., and Wang, F. Tunable correlated Chern insulator and ferromagnetism in a moiré superlattice. *Nature 579* (Mar 2020), 56–61.

[35] Chen, T., and Shklovskii, B. I. Anomalously small resistivity and thermopower of strongly compensated semiconductors and topological insulators. *Phys. Rev. B 87* (Apr 2013), 165119.

[36] Chen, Y. L., Chu, J.-H., Analytis, J. G., Liu, Z. K., Igarashi, K., Kuo, H.-H., Qi, X. L., Mo, S. K., Moore, R. G., Lu, D. H., Hashimoto, M., Sasagawa, T., Zhang, S. C., Fisher, I. R., Hussain, Z., and Shen, Z. X. Massive Dirac fermion on the surface of a magnetically doped topological insulator. *Science 329*, 5992 (Aug 2010), 659–662.

[37] Chong, Y. X., Liu, X., Sharma, R., Kostin, A., Gu, G., Fujita, K., Davis, J. C. S., and Sprau, P. O. Severe Dirac mass gap suppression in Sb_2Te_3-based quantum anomalous Hall materials. *Nano Lett. 20*, 11 (Sep 2020), 8001–8007.

[38] Dai, X., Hughes, T. L., Qi, X.-L., Fang, Z., and Zhang, S.-C. Helical edge and surface states in HgTe quantum wells and bulk insulators. *Phys. Rev. B 77* (Mar 2008), 125319.

[39] Dartiailh, M. C., Hartinger, S., Gourmelon, A., Bendias, K., Bartolomei, H., Kamata, H., Berroir, J.-M., Fève, G., Plaçais, B., Lunczer, L., Schlereth, R., Buhmann, H., Molenkamp, L. W., and Bocquillon, E. Dynamical separation of bulk and edge transport

in HgTe-based 2D topological insulators. *Phys. Rev. Lett. 124* (Feb 2020), 076802.

[40] Delahaye, F., and Jeckelmann, B. Revised technical guidelines for reliable dc measurements of the quantized Hall resistance. *Metrologia 40*, 5 (Sep 2003), 217–223.

[41] Deng, H., Chen, Z., Wołoś, A., Konczykowski, M., Sobczak, K., Sitnicka, J., Fedorchenko, I. V., Borysiuk, J., Heider, T., Pluciński, L., Park, K., Georgescu, A. B., Cano, J., and Krusin-Elbaum, L. High-temperature quantum anomalous Hall regime in a $MnBi_2Te_4/Bi_2Te_3$ superlattice. *Nat. Phys. 17* (Aug 2021), 36–42.

[42] Deng, Y., Yu, Y., Shi, M. Z., Guo, Z., Xu, Z., Wang, J., Chen, X. H., and Zhang, Y. Quantum anomalous Hall effect in intrinsic magnetic topological insulator $MnBi_2Te_4$. *Science 367*, 6480 (Feb 2020), 895–900.

[43] des Poids et Mesures, B. I. The International System of Units (SI). *SI Brochure 9* (2019).

[44] Dmitriev, I. A., Mirlin, A. D., Polyakov, D. G., and Zudov, M. A. Nonequilibrium phenomena in high Landau levels. *Rev. Mod. Phys. 84* (Nov 2012), 1709–1763.

[45] Eaves, L., and Sheard, F. W. Size-dependent quantised breakdown of the dissipationless quantum Hall effect in narrow channels. *Semicond. Sci. Technol. 1* (Sep 1986), 346–349.

[46] Eber, G., von Klitzing, K., Ploog, K., and Weinmann, G. Two-dimensional magneto-quantum transport on GaAs-$Al_xGa_{1-x}As$ heterostructures under non-ohmic conditions. *J. Phys. C: Solid State Phys. 16*, 28 (Oct 1983), 5441–5448.

[47] Fan, Y., Shao, Q., Pan, L., Che, X., He, Q., Yin, G., Zheng, C., Yu, G., Nie, T., Masir, M. R., MacDonald, A. H., and Wang, K. L. Unidirectional magneto-resistance in modulation-doped magnetic topological insulators. *Nano Lett. 19*, 2 (Jan 2019), 692–698.

[48] Fijalkowski, K. M., Hartl, M., Winnerlein, M., Mandal, P., Schreyeck, S., Brunner, K., Gould, C., and Molenkamp, L. W. Coexistence of surface and bulk ferromagnetism mimics Skyrmion Hall effect in a topological insulator. *Phys. Rev. X 10* (Jan 2020), 011012.

[49] Fijalkowski, K. M., Liu, N., Mandal, P., Schreyeck, S., Brunner, K., Gould, C., and Molenkamp, L. W. Quantum anomalous Hall

edge channels survive up to the Curie temperature. *Nat. Commun. 12* (Sep 2021), 5599.

[50] Fox, E. J., Rosen, I. T., Yang, Y., Jones, G. R., Elmquist, R. E., Kou, X., Pan, L., Wang, K. L., and Goldhaber-Gordon, D. Part-per-million quantization and current-induced breakdown of the quantum anomalous Hall effect. *Phys. Rev. B 98* (Aug 2018), 075145.

[51] Fu, L., and Kane, C. L. Superconducting proximity effect and Majorana fermions at the surface of a topological insulator. *Phys. Rev. Lett. 100* (Mar 2008), 096407.

[52] Ginley, T. P., Wang, Y., and Law, S. Topological insulator film growth by molecular beam epitaxy: A review. *Crystals 6* (Nov 2016).

[53] Grauer, S., Schreyeck, S., Winnerlein, M., Brunner, K., Gould, C., and Molenkamp, L. W. Coincidence of superparamagnetism and perfect quantization in the quantum anomalous Hall state. *Phys. Rev. B 92* (Nov 2015), 201304.

[54] Götz, M., Fijalkowski, K. M., Pesel, E., Hartl, M., Schreyeck, S., Winnerlein, M., Grauer, S., Scherer, H., Brunner, K., Gould, C., Ahlers, F. J., and Molenkamp, L. W. Precision measurement of the quantized anomalous Hall resistance at zero magnetic field. *Appl. Phys. Lett. 112*, 7 (Feb 2018), 072102.

[55] Guignard, J., Leprat, D., Glattli, D. C., Schopfer, F., and Poirier, W. Quantum Hall effect in exfoliated graphene affected by charged impurities: Metrological measurements. *Phys. Rev. B 85* (Apr 2012), 165420.

[56] Guillet, T., Zucchetti, C., Barbedienne, Q., Marty, A., Isella, G., Cagnon, L., Vergnaud, C., Jaffrès, H., Reyren, N., George, J.-M., Fert, A., and Jamet, M. Observation of large unidirectional Rashba magnetoresistance in Ge(111). *Phys. Rev. Lett. 124* (Jan 2020), 027201.

[57] Hall, E. H. On a new action of the magnet on electric currents. *Am. J. Math. 2* (Sep 1879), 287–292.

[58] Hall, E. H. On the new action of magnetism on a permanent electric current. *Am. J. Sci. 20*, 3 (Dec 1880), 161–186.

[59] Hassler, F., Grabsch, A., Pacholski, M. J., Oriekhov, D. O., Ovdat, O., Adagideli, I., and Beenakker, C. W. J. Half-integer charge injection by a Josephson junction without excess noise. *Phys. Rev. B 102* (Jul 2020), 045431.

[60] He, P., Hsu, C.-H., Shi, S., Cai, K., Wang, J., Wang, Q., Eda, G., Lin, H., Pereira, V. M., and Yang, H. Nonlinear magnetotransport shaped by Fermi surface topology and convexity. *Nat. Commun. 10*, 1 (Mar 2019), 1290.

[61] He, P., Walker, S. M., Zhang, S. S.-L., Bruno, F. Y., Bahramy, M. S., Lee, J. M., Ramaswamy, R., Cai, K., Heinonen, O., Vignale, G., Baumberger, F., and Yang, H. Observation of out-of-plane spin texture in a $SrTiO_3(111)$ two-dimensional electron gas. *Phys. Rev. Lett. 120* (Jun 2018), 266802.

[62] He, P., Zhang, S. S. L., Zhu, D., Liu, Y., Wang, Y., Yu, J., Vignale, G., and Yang, H. Bilinear magnetoelectric resistance as a probe of three-dimensional spin texture in topological surface states. *Nat. Phys. 14*, 5 (Feb 2018), 495–499.

[63] He, Q. L., Pan, L., Stern, A. L., Burks, E. C., Che, X., Yin, G., Wang, J., Lian, B., Zhou, Q., Choi, E. S., Murata, K., Kou, X., Chen, Z., Nie, T., Shao, Q., Fan, Y., Zhang, S.-C., Liu, K., Xia, J., and Wang, K. L. Chiral Majorana fermion modes in a quantum anomalous Hall insulator-superconductor structure. *Science 357*, 6348 (Jul 2017), 294–299. Retracted (Nov 2022).

[64] He, Q. L., Yin, G., Grutter, A. J., Pan, L., Che, X., Yu, G., Gilbert, D. A., Disseler, S. M., Liu, Y., Shafer, P., Zhang, B., Wu, Y., Kirby, B. J., Arenholz, E., Lake, R. K., Han, X., and Wang, K. L. Exchange-biasing topological charges by antiferromagnetism. *Nat. Commun. 9* (Jul 2018), 2767.

[65] Herman, M. A., and Sitter, H. *Molecular Beam Epitaxy, Fundamentals and Current Status*, 2nd, rev. and updated ed. Springer Series in Materials Science 7. Springer Berlin, Heidelberg, May 1996.

[66] Hsieh, D., Qian, D., Wray, L., Xia, Y., Hor, Y. S., Cava, R. J., and Hasan, M. Z. A topological Dirac insulator in a quantum spin Hall phase. *Nature 452* (Apr 2008), 970–974.

[67] Hsieh, D., Xia, Y., Wray, L., Qian, D., Pal, A., Dil, J. H., Osterwalder, J., Meier, F., Bihlmayer, G., Kane, C. L., Hor, Y. S., Cava, R. J., and Hasan, M. Z. Observation of unconventional quantum spin textures in topological insulators. *Science 323*, 5916 (Feb 2009), 919–922.

[68] Huang, Y., Setiawan, F., and Sau, J. D. Disorder-induced half-integer quantized conductance plateau in quantum anomalous Hall insulator-superconductor structures. *Phys. Rev. B 97* (Mar 2018), 100501.

[69] Huang, Y., and Shklovskii, B. I. Disorder effects in topological insulator thin films. *Phys. Rev. B 103* (Apr 2021), 165409.

[70] Ideue, T., Hamamoto, K., Koshikawa, S., Ezawa, M., Shimizu, S., Kaneko, Y., Tokura, Y., Nagaosa, N., and Iwasa, Y. Bulk rectification effect in a polar semiconductor. *Nat. Phys. 13*, 6 (Mar 2017), 578–583.

[71] Inhofer, A., Duffy, J., Boukhicha, M., Bocquillon, E., Palomo, J., Watanabe, K., Taniguchi, T., Estève, I., Berroir, J. M., Fève, G., Plaçais, B., and Assaf, B. A. rf Quantum capacitance of the topological insulator Bi_2Se_3 in the bulk depleted regime for field-effect transistors. *Phys. Rev. Appl. 9* (Feb 2018), 024022.

[72] Inhofer, A., Tchoumakov, S., Assaf, B. A., Fève, G., Berroir, J. M., Jouffrey, V., Carpentier, D., Goerbig, M. O., Plaçais, B., Bendias, K., Mahler, D. M., Bocquillon, E., Schlereth, R., Brüne, C., Buhmann, H., and Molenkamp, L. W. Observation of Volkov-Pankratov states in topological HgTe heterojunctions using high-frequency compressibility. *Phys. Rev. B 96* (Nov 2017), 195104.

[73] Jeckelmann, B., and Jeanneret, B. The quantum Hall effect as an electrical resistance standard. *Rep. Prog. Phys. 64*, 12 (Nov 2001), 1603–1655.

[74] Jeckelmann, B., Rufenacht, A., Jeanneret, B., Overney, F., Pierz, K., von Campenhausen, A., and Hein, G. Optimization of QHE-devices for metrological applications. *IEEE Trans. Instrum. Meas. 50*, 2 (Apr 2001), 218–222.

[75] Ji, W., and Wen, X.-G. $\frac{1}{2}(e^2/h)$ conductance plateau without 1D chiral Majorana fermions. *Phys. Rev. Lett. 120* (Mar 2018), 107002.

[76] Jiang, J., Xiao, D., Wang, F., Shin, J.-H., Andreoli, D., Zhang, J., Xiao, R., Zhao, Y.-F., Kayyalha, M., Zhang, L., Wang, K., Zang, J., Liu, C., Samarth, N., Chan, M. H. W., and Chang, C.-Z. Concurrence of quantum anomalous Hall and topological Hall effects in magnetic topological insulator sandwich heterostructures. *Nat. Mater. 19* (Feb 2020), 732–737.

[77] Jin, H., Im, J., and Freeman, A. J. Topological and magnetic phase transitions in Bi_2Se_3 thin films with magnetic impurities. *Phys. Rev. B 84* (Oct 2011), 134408.

[78] Jozwiak, C., Sobota, J. A., Gotlieb, K., Kemper, A. F., Rotundu, C. R., Birgeneau, R. J., Hussain, Z., Lee, D.-H., Shen, Z.-X., and

Lanzara, A. Spin-polarized surface resonances accompanying topological surface state formation. *Nat. Commun. 7* (Oct 2016), 13143.

[79] Kacman, P. Spin interactions in diluted magnetic semiconductors and magnetic semiconductor structures. *Semicond. Sci. Technol. 16*, 4 (Mar 2001), R25–R39.

[80] Kane, C. L., and Mele, E. J. Quantum spin Hall effect in graphene. *Phys. Rev. Lett. 95* (Nov 2005), 226801.

[81] Kawaji, S. Breakdown of the integer quantum Hall effect at high currents in GaAs/AlGaAs heterostructures. *Semicond. Sci. Technol. 11*, 11S (Nov 1996), 1546–1551.

[82] Kawamura, M., Mogi, M., Yoshimi, R., Tsukazaki, A., Kozuka, Y., Takahashi, K. S., Kawasaki, M., and Tokura, Y. Topological quantum phase transition in magnetic topological insulator upon magnetization rotation. *Phys. Rev. B 98* (Oct 2018), 140404.

[83] Kawamura, M., Yoshimi, R., Tsukazaki, A., Takahashi, K. S., Kawasaki, M., and Tokura, Y. Current-driven instability of the quantum anomalous Hall effect in ferromagnetic topological insulators. *Phys. Rev. Lett. 119* (Jul 2017), 016803.

[84] Kayyalha, M., Xiao, D., Zhang, R., Shin, J., Jiang, J., Wang, F., Zhao, Y.-F., Xiao, R., Zhang, L., Fijalkowski, K. M., Mandal, P., Winnerlein, M., Gould, C., Li, Q., Molenkamp, L. W., Chan, M. H. W., Samarth, N., and Chang, C.-Z. Absence of evidence for chiral Majorana modes in quantum anomalous Hall-superconductor devices. *Science 367*, 6473 (Jan 2020), 64–67.

[85] Kitaev, A. Y. Fault-tolerant quantum computation by anyons. *Ann. Phys. 303*, 1 (Jan 2003), 2–30.

[86] Knispel, T., Jolie, W., Borgwardt, N., Lux, J., Wang, Z., Ando, Y., Rosch, A., Michely, T., and Grüninger, M. Charge puddles in the bulk and on the surface of the topological insulator $BiSbTeSe_2$ studied by scanning tunneling microscopy and optical spectroscopy. *Phys. Rev. B 96* (Nov 2017), 195135.

[87] Koma, A. Van der Waals epitaxy – a new epitaxial growth method for a highly lattice-mismatched system. *Thin Solid Films 216*, 1 (Aug 1992), 72–76.

[88] Koma, A. Van der Waals epitaxy for highly lattice-mismatched systems. *J. Cryst. Growth 201–202* (May 1999), 236–241.

[89] Koma, A., Sunouchi, K., and Miyajima, T. Fabrication and characterization of heterostructures with subnanometer thickness. *Microelectron. Eng. 2*, 1 (Oct 1984), 129–136.

[90] Komiyama, S., and Kawaguchi, Y. Heat instability of quantum Hall conductors. *Phys. Rev. B 61* (Jan 2000), 2014–2027.

[91] Komiyama, S., Takamasu, T., Hiyamizu, S., and Sasa, S. Breakdown of the quantum Hall effect due to electron heating. *Solid State Commun. 54*, 6 (May 1985), 479–484.

[92] Kong, D., Chen, Y., Cha, J. J., Zhang, Q., Analytis, J. G., Lai, K., Liu, Z., Hong, S. S., Koski, K. J., Mo, S.-K., Hussain, Z., Fisher, I. R., Shen, Z.-X., and Cui, Y. Ambipolar field effect in the ternary topological insulator $(Bi_xSb_{1-x})_2Te_3$ by composition tuning. *Nat. Nanotechnol. 6* (Oct 2011), 705–709.

[93] König, M., Wiedmann, S., Brüne, C., Roth, A., Buhmann, H., Molenkamp, L. W., Qi, X.-L., and Zhang, S.-C. Quantum spin Hall insulator state in HgTe quantum wells. *Science 318*, 5851 (Nov 2007), 766–770.

[94] Kou, X., Guo, S.-T., Fan, Y., Pan, L., Lang, M., Jiang, Y., Shao, Q., Nie, T., Murata, K., Tang, J., Wang, Y., He, L., Lee, T.-K., Lee, W.-L., and Wang, K. L. Scale-invariant quantum anomalous Hall effect in magnetic topological insulators beyond the two-dimensional limit. *Phys. Rev. Lett. 113* (Sep 2014), 137201.

[95] Kou, X., Pan, L., Wang, J., Fan, Y., Choi, E. S., Lee, W.-L., Nie, T., Murata, K., Shao, Q., Zhang, S.-C., and Wang, K. L. Metal-to-insulator switching in quantum anomalous Hall states. *Nat. Commun. 6* (Oct 2015), 8474.

[96] Kozlov, D. A., Bauer, D., Ziegler, J., Fischer, R., Savchenko, M. L., Kvon, Z. D., Mikhailov, N. N., Dvoretsky, S. A., and Weiss, D. Probing quantum capacitance in a 3D topological insulator. *Phys. Rev. Lett. 116* (Apr 2016), 166802.

[97] Krstić, V., Roth, S., Burghard, M., Kern, K., and Rikken, G. L. J. A. Magneto-chiral anisotropy in charge transport through single-walled carbon nanotubes. *J. Chem. Phys. 117*, 24 (Dec 2002), 11315–11319.

[98] Lachman, E. O., Mogi, M., Sarkar, J., Uri, A., Bagani, K., Anahory, Y., Myasoedov, Y., Huber, M. E., Tsukazaki, A., Kawasaki, M., Yoshinori, T., and Zeldov, E. Observation of superparamagnetism in coexistence with quantum anomalous Hall $C = \pm 1$ and $C = 0$ Chern states. *npj Quantum Mater. 2* (Dec 2017), 70.

[99] Lachman, E. O., Young, A. F., Richardella, A., Cuppens, J., Naren, H. R., Anahory, Y., Meltzer, A. Y., Kandala, A., Kempinger, S., Myasoedov, Y., Huber, M. E., Samarth, N., and Zeldov, E. Visualization of superparamagnetic dynamics in magnetic topological insulators. *Sci. Adv. 1*, 10 (Nov 2015), e1500740.

[100] Lanius, M., Kampmeier, J., Weyrich, C., Kölling, S., Schall, M., Schüffelgen, P., Neumann, E., Luysberg, M., Mussler, G., Koenraad, P. M., Schäpers, T., and Grützmacher, D. P-N junctions in ultrathin topological insulator Sb_2Te_3/Bi_2Te_3 heterostructures grown by molecular beam epitaxy. *Cryst. Growth Des. 16*, 4 (Mar 2016).

[101] Lee, I., Kim, C. K., Lee, J., Billinge, S. J. L., Zhong, R., Schneeloch, J. A., Liu, T., Valla, T., Tranquada, J. M., Gu, G., and Davis, J. C. S. Imaging Dirac-mass disorder from magnetic dopant atoms in the ferromagnetic topological insulator $Cr_x(Bi_{0.1}Sb_{0.9})_{2-x}Te_3$. *Proc. Natl. Acad. Sci. U.S.A. 112*, 5 (Feb 2015), 1316–1321.

[102] Legg, H. F., Loss, D., and Klinovaja, J. Superconducting diode effect due to magnetochiral anisotropy in topological insulators and Rashba nanowires. *Phys. Rev. B 106* (Sep 2022), 104501.

[103] Legg, H. F., Rössler, M., Münning, F., Fan, D., Breunig, O., Bliesener, A., Lippertz, G., Uday, A., Taskin, A. A., Loss, D., Klinovaja, J., and Ando, Y. Giant magnetochiral anisotropy from quantum-confined surface states of topological insulator nanowires. *Nat. Nanotechnol. 17* (May 2022), 696–700.

[104] Li, H., Kumar, U., Sun, K., and Lin, S.-Z. Spontaneous fractional Chern insulators in transition metal dichalcogenide moiré superlattices. *Phys. Rev. Res. 3* (Sep 2021), L032070.

[105] Li, J., Li, Y., Du, S., Wang, Z., Gu, B.-L., Zhang, S.-C., He, K., Duan, W., and Xu, Y. Intrinsic magnetic topological insulators in van der Waals layered $MnBi_2Te_4$-family materials. *Sci. Adv. 5*, 6 (Jun 2019), eaaw5685.

[106] Li, M., Chang, C.-Z., Wu, L., Tao, J., Zhao, W., Chan, M. H. W., Moodera, J. S., Li, J., and Zhu, Y. Experimental verification of the Van Vleck nature of long-range ferromagnetic order in the vanadium-doped three-dimensional topological insulator Sb_2Te_3. *Phys. Rev. Lett. 114* (Apr 2015), 146802.

[107] Li, T., Jiang, S., Shen, B., Zhang, Y., Li, L., Tao, Z., Devakul, T., Watanabe, K., Taniguchi, T., Fu, L., Shan, J., and Mak, K. F.

Quantum anomalous Hall effect from intertwined moiré bands. *Nature 600* (Dec 2021), 641–646.

[108] Li, T., Kim, S., Lee, S.-J., Lee, S.-W., Koyama, T., Chiba, D., Moriyama, T., Lee, K.-J., Kim, K.-J., and Ono, T. Origin of threshold current density for asymmetric magnetoresistance in Pt/Py bilayers. *Appl. Phys. Express 10* (Jun 2017), 073001–073001.

[109] Lidig, C., Cramer, J., Weisshoff, L., Thomas, T., Kessler, T., Kläui, M., and Jourdan, M. Unidirectional spin Hall magnetoresistance as a tool for probing the interfacial spin polarization of Co_2MnSi. *Phys. Rev. Appl. 11* (Apr 2019), 044039.

[110] Liu, C., Wang, Y., Li, H., Wu, Y., Li, Y., Jiaheng Li, He, K., Xu, Y., Zhang, J., and Wang, Y. Robust axion insulator and Chern insulator phases in a two-dimensional antiferromagnetic topological insulator. *Nat. Mater. 19* (Jan 2020), 522–527.

[111] Liu, C., Zang, Y., Ruan, W., Gong, Y., He, K., Ma, X., Xue, Q.-K., and Wang, Y. Dimensional crossover-induced topological Hall effect in a magnetic topological insulator. *Phys. Rev. Lett. 119* (Oct 2017), 176809.

[112] Liu, C.-X., Qi, X.-L., Dai, X., Fang, Z., and Zhang, S.-C. Quantum anomalous Hall effect in $Hg_{1-y}Mn_yTe$ quantum wells. *Phys. Rev. Lett. 101* (Oct 2008), 146802.

[113] Liu, C.-X., Qi, X.-L., Zhang, H., Dai, X., Fang, Z., and Zhang, S.-C. Model Hamiltonian for topological insulators. *Phys. Rev. B 82* (Jul 2010), 045122.

[114] Liu, C.-X., Zhang, H., Yan, B., Qi, X.-L., Frauenheim, T., Dai, X., Fang, Z., and Zhang, S.-C. Oscillatory crossover from two-dimensional to three-dimensional topological insulators. *Phys. Rev. B 81* (Jan 2010), 041307.

[115] Liu, J., and Hesjedal, T. Magnetic topological insulator heterostructures: A review. *Adv. Mater.* (Oct 2021), 2102427.

[116] Liu, Z., Abouelkomsan, A., and Bergholtz, E. J. Gate-tunable fractional Chern insulators in twisted double bilayer graphene. *Phys. Rev. Lett. 126* (Jan 2021), 026801.

[117] Lustikova, J., Shiomi, Y., Yokoi, N., Kabeya, N., Kimura, N., Ienaga, K., Kaneko, S., Okuma, S., Takahashi, S., and Saitoh, E. Vortex rectenna powered by environmental fluctuations. *Nat. Commun. 9*, 1 (Nov 2018), 4922.

[118] Lv, Y., Kally, J., Zhang, D., Lee, J. S., Jamali, M., Samarth, N., and Wang, J.-P. Unidirectional spin-Hall and Rashba-Edelstein magnetoresistance in topological insulator-ferromagnet layer heterostructures. *Nat. Commun. 9*, 1 (Jan 2018), 111.

[119] Majorana, E. Teoria simmetrica dell'elettrone e del positrone. *Nuovo Cim. 14* (1937), 171–184.

[120] Masataka, M. Magnetic proximity induced quantum anomalous Hall effect. In *Quantized Phenomena of Transport and Magneto-Optics in Magnetic Topological Insulator Heterostructures*, Springer Theses. Springer Nature Singapore, May 2022, pp. 39–65.

[121] MicroChemicals. *Composition and Properties of AZ® and TI Photoresists*. Basics of Microstructuring.

[122] Min, H., Hill, J. E., Sinitsyn, N. A., Sahu, B. R., Kleinman, L., and MacDonald, A. H. Intrinsic and Rashba spin-orbit interactions in graphene sheets. *Phys. Rev. B 74* (Oct 2006), 165310.

[123] Mogi, M., Kawamura, M., Tsukazaki, A., Yoshimi, R., Takahashi, K. S., Kawasaki, M., and Tokura, Y. Tailoring tricolor structure of magnetic topological insulator for robust axion insulator. *Sci. Adv. 3*, 10 (Oct 2017), eaao1669.

[124] Mogi, M., Kawamura, M., Yoshimi, R., Tsukazaki, A., Kozuka, Y., Shirakawa, N., Takahashi, K. S., Kawasaki, M., and Tokura, Y. A magnetic heterostructure of topological insulators as a candidate for an axion insulator. *Nat. Mater. 16* (Feb 2017), 516–521.

[125] Mogi, M., Yoshimi, R., Tsukazaki, A., Yasuda, K., Kozuka, Y., Takahashi, K. S., Kawasaki, M., and Tokura, Y. Magnetic modulation doping in topological insulators toward higher-temperature quantum anomalous Hall effect. *Appl. Phys. Lett. 107*, 18 (Nov 2015), 182401.

[126] Morimoto, T., Furusaki, A., and Nagaosa, N. Topological magnetoelectric effects in thin films of topological insulators. *Phys. Rev. B 92* (Aug 2015), 085113.

[127] Nachtwei, G. Breakdown of the quantum Hall effect. *Physica E Low Dimens. Syst. Nanostruct. 4* (Apr 1999), 79–101.

[128] Nagaosa, N., Sinova, J., Onoda, S., MacDonald, A. H., and Ong, N. P. Anomalous Hall effect. *Rev. Mod. Phys. 82* (May 2010), 1539–1592.

[129] Nagata, S., Galazka, R. R., Mullin, D. P., Akbarzadeh, H., Khattak, G. D., Furdyna, J. K., and Keesom, P. H. Magnetic susceptibility, specific heat, and the spin-glass transition in $Hg_{1-x}Mn_xTe$. *Phys. Rev. B 22* (Oct 1980), 3331–3343.

[130] Nandi, D., Skinner, B., Lee, G. H., Huang, K.-F., Shain, K., Chang, C.-Z., Ou, Y., Lee, S.-P., Ward, J., Moodera, J. S., Kim, P., Halperin, B. I., and Yacoby, A. Signatures of long-range-correlated disorder in the magnetotransport of ultrathin topological insulators. *Phys. Rev. B 98* (Dec 2018), 214203.

[131] Nishide, A., Taskin, A. A., Takeichi, Y., Okuda, T., Kakizaki, A., Hirahara, T., Nakatsuji, K., Komori, F., Ando, Y., and Matsuda, I. Direct mapping of the spin-filtered surface bands of a three-dimensional quantum spin Hall insulator. *Phys. Rev. B 81* (Jan 2010), 041309.

[132] Okazaki, Y., Oe, T., Kawamura, M., Yoshimi, R., Nakamura, S., Takada, S., Mogi, M., Takahashi, K. S., Tsukazaki, A., Kawasaki, M., Tokura, Y., and Kaneko, N.-H. Precise resistance measurement of quantum anomalous Hall effect in magnetic heterostructure film of topological insulator. *Appl. Phys. Lett. 116*, 14 (Apr 2020), 143101.

[133] Okazaki, Y., Oe, T., Kawamura, M., Yoshimi, R., Nakamura, S., Takada, S., Mogi, M., Takahashi, K. S., Tsukazaki, A., Kawasaki, M., Tokura, Y., and Kaneko, N.-H. Quantum anomalous Hall effect with a permanent magnet defines a quantum resistance standard. *Nat. Phys. 18* (Dec 2021), 25–29.

[134] Olejník, K., Novák, V., Wunderlich, J., and Jungwirth, T. Electrical detection of magnetization reversal without auxiliary magnets. *Phys. Rev. B 91* (May 2015), 180402.

[135] Otrokov, M. M., Klimovskikh, I. I., Bentmann, H., Estyunin, D., Zeugner, A., Aliev, Z. S., Gass, S., Wolter, A. U. B., Koroleva, A. V., Shikin, A. M., Blanco-Rey, M., Hoffmann, M., Rusinov, I. P., Vyazovskaya, A. Y., Eremeev, S. V., Koroteev, Y. M., Kuznetsov, V. M., Freyse, F., Sánchez-Barriga, J., Amiraslanov, I. R., Babanly, M. B., Mamedov, N. T., Abdullayev, N. A., Zverev, V. N., Alfonsov, A., Kataev, V., Büchner, B., Schwier, E. F., Kumar, S., Kimura, A., Petaccia, L., Di Santo, G., Vidal, R. C., Schatz, S., Kiss ner, K., Ünzelmann, M., Min, C. H., Moser, S., Peixoto, T. R. F., Reinert, F., Ernst, A., Echenique, P. M., Isaeva, A., and

Chulkov, E. V. Prediction and observation of an antiferromagnetic topological insulator. *Nature 576* (Dec 2019), 416–422.

[136] Otrokov, M. M., Rusinov, I. P., Blanco-Rey, M., Hoffmann, M., Vyazovskaya, A. Y., Eremeev, S. V., Ernst, A., Echenique, P. M., Arnau, A., and Chulkov, E. V. Unique thickness-dependent properties of the van der Waals interlayer antiferromagnet $MnBi_2Te_4$ films. *Phys. Rev. Lett. 122* (Mar 2019), 107202.

[137] Ou, Y., Liu, C., Jiang, G., Feng, Y., Zhao, D., Wu, W., Wang, X.-X., Li, W., Song, C., Wang, L.-L., Wang, W., Wu, W., Wang, Y., He, K., Ma, X.-C., and Xue, Q.-K. Enhancing the quantum anomalous Hall effect by magnetic codoping in a topological insulator. *Adv. Mater. 30*, 1 (Nov 2018), 1703062.

[138] Park, J., Soh, Y.-A., Aeppli, G., Bland, S. R., Zhu, X.-G., Chen, X., Xue, Q.-K., and Grey, F. Crystal structure and epitaxy of Bi_2Te_3 films grown on Si. *Appl. Phys. Lett. 101*, 22 (Nov 2012), 221910.

[139] Park, J., Soh, Y.-A., Aeppli, G., Feng, X., Ou, Y., He, K., and Xue, Q.-K. Crystallinity of tellurium capping and epitaxy of ferromagnetic topological insulator films on $SrTiO_3$. *Sci. Rep. 5*, 11595 (Jun 2015).

[140] Pobell, F. *Matter and Methods at Low Temperatures*, 2 ed. Springer Berlin, Heidelberg, Nov 1995.

[141] Poirier, W., and Schopfer, F. Resistance metrology based on the quantum Hall effect. *Eur. Phys. J.: Spec. Top. 172* (Jun 2009), 207–245.

[142] Polshyn, H., Zhu, J., Kumar, M. A., Zhang, Y., Yang, F., Tschirhart, C. L., Serlin, M., Watanabe, K., Taniguchi, T., MacDonald, A. H., and Young, A. F. Electrical switching of magnetic order in an orbital Chern insulator. *Nature 588* (Nov 2020), 66–70.

[143] Pop, F., Auban-Senzier, P., Canadell, E., Rikken, G. L. J. A., and Avarvari, N. Electrical magnetochiral anisotropy in a bulk chiral molecular conductor. *Nat. Commun. 5* (May 2014), 3757.

[144] Qi, X.-L., Hughes, T. L., and Zhang, S.-C. Topological field theory of time-reversal invariant insulators. *Phys. Rev. B 78*, 19 (Nov 2008), 195424.

[145] Qi, X.-L., Hughes, T. L., and Zhang, S.-C. Chiral topological superconductor from the quantum Hall state. *Phys. Rev. B 82* (Nov 2010), 184516.

[146] Qi, X.-L., Wu, Y.-S., and Zhang, S.-C. Topological quantization of the spin Hall effect in two-dimensional paramagnetic semiconductors. *Phys. Rev. B 74* (Aug 2006), 085308.

[147] Qi, X.-L., and Zhang, S.-C. Topological insulators and superconductors. *Rev. Mod. Phys. 83* (Oct 2011), 1057–1110.

[148] Qin, F., Shi, W., Ideue, T., Yoshida, M., Zak, A., Tenne, R., Kikitsu, T., Inoue, D., Hashizume, D., and Iwasa, Y. Superconductivity in a chiral nanotube. *Nat. Commun. 8*, 1 (Feb 2017), 14465.

[149] Rasic, D., and Narayan, J. Epitaxial growth of thin films. In *Crystal Growth*, V. Glebovsky, Ed. IntechOpen, Sep 2019, ch. 5.

[150] Read, N., and Green, D. Paired states of fermions in two dimensions with breaking of parity and time-reversal symmetries and the fractional quantum Hall effect. *Phys. Rev. B 61* (Apr 2000), 10267–10297.

[151] Reddy, A. P., Alsallom, F. F., Zhang, Y., Devakul, T., and Fu, L. Fractional quantum anomalous Hall states in twisted bilayer $MoTe_2$ and WSe_2. *arXiv e-prints: 2304.12261* (Apr 2023).

[152] Ren, Z., Taskin, A. A., Sasaki, S., Segawa, K., and Ando, Y. Optimizing $Bi_{2-x}Sb_xTe_{3-y}Se_y$ solid solutions to approach the intrinsic topological insulator regime. *Phys. Rev. B 84* (Oct 2011), 165311.

[153] Richardella, A., Kandala, A., Lee, J. S., and Samarth, N. Characterizing the structure of topological insulator thin films. *APL Mater. 3*, 8 (Jul 2015), 083303.

[154] Richardson, C. L., Devine-Stoneman, J. M., Divitini, G., Vickers, M. E., Chang, C.-Z., Amado, M., Moodera, J. S., and Robinson, J. W. A. Structural properties of thin-film ferromagnetic topological insulators. *Sci. Rep. 7* (Sep 2017), 12061.

[155] Rikken, G. L. J. A., and Avarvari, N. Strong electrical magnetochiral anisotropy in tellurium. *Phys. Rev. B 99* (Jun 2019), 245153.

[156] Rikken, G. L. J. A., Fölling, J., and Wyder, P. Electrical magnetochiral anisotropy. *Phys. Rev. Lett. 87* (Nov 2001), 236602.

[157] Rikken, G. L. J. A., and Wyder, P. Magnetoelectric anisotropy in diffusive transport. *Phys. Rev. Lett. 94* (Jan 2005), 016601.

[158] Rodenbach, L. K., Rosen, I. T., Fox, E. J., Zhang, P., Pan, L., Wang, K. L., Kastner, M. A., and Goldhaber-Gordon, D. Bulk dissipation in the quantum anomalous Hall effect. *APL Mater. 9*, 8 (Aug 2021), 081116.

[159] Rosen, I. T., Fox, E. J., Kou, X., Pan, L., Wang, K. L., and Goldhaber-Gordon, D. Chiral transport along magnetic domain walls in the quantum anomalous Hall effect. *npj Quantum Mater. 2* (Dec 2017), 69.

[160] Roushan, P., Seo, J., Parker, C. V., Hor, Y. S., Hsieh, D., Qian, D., Richardella, A., Hasan, M. Z., Cava, R. J., and Yazdani, A. Topological surface states protected from backscattering by chiral spin texture. *Nature 460* (Aug 2009), 1106–1109.

[161] Salehi, M., Yao, X., and Oh, S. From classical to quantum regime of topological surface states via defect engineering. *SciPost Phys. Lect. Notes* (Jul 2022), 58.

[162] Sarma, S. D., Freedman, M., and Nayak, C. Majorana zero modes and topological quantum computation. *npj Quantum Inf. 1* (Oct 2015), 15001.

[163] Sass, P. M., Kim, J., Vanderbilt, D., Yan, J., and Wu, W. Robust *A*-type order and spin-flop transition on the surface of the antiferromagnetic topological insulator $MnBi_2Te_4$. *Phys. Rev. Lett. 125* (Jul 2020), 037201.

[164] Serlin, M., Tschirhart, C. L., Polshyn, H., Zhang, Y., Zhu, J., Watanabe, K., Taniguchi, T., Balents, L., and Young, A. F. Intrinsic quantized anomalous Hall effect in a moiré heterostructure. *Science 367*, 6480 (Feb 2020), 900–903.

[165] Shamim, S., Beugeling, W., Böttcher, J., Shekhar, P., Budewitz, A., Leubner, P., Lunczer, L., Hankiewicz, E. M., Buhmann, H., and Molenkamp, L. W. Emergent quantum Hall effects below 50 mT in a two-dimensional topological insulator. *Sci. Adv. 6*, 26 (Jun 2020), eaba4625.

[166] Shen, J., Lyu, J., Gao, J. Z., Xie, Y.-M., Chen, C.-Z., Cho, C.-w., Atanov, O., Chen, Z., Liu, K., Hu, Y. J., Yip, K. Y., Goh, S. K., He, Q. L., Pan, L., Wang, K. L., Law, K. T., and Lortz, R. Spectroscopic fingerprint of chiral Majorana modes at the edge of a quantum anomalous Hall insulator/superconductor heterostructure. *Proc. Natl. Acad. Sci. U.S.A. 117*, 1 (Dec 2020), 238–242.

[167] Skinner, B., Chen, T., and Shklovskii, B. I. Why is the bulk resistivity of topological insulators so small? *Phys. Rev. Lett. 109* (Oct 2012), 176801.

[168] Skinner, B., and Shklovskii, B. I. Theory of the random potential and conductivity at the surface of a topological insulator. *Phys. Rev. B 87* (Feb 2013), 075454.

[169] Skinner, B., T. Chen, T., and Shklovskii, B. I. Effects of bulk charged impurities on the bulk and surface transport in three-dimensional topological insulators. *J. Exp. Theor. Phys. 117* (Oct 2013), 579–592.

[170] Śliwa, C., Autieri, C., Majewski, J. A., and Dietl, T. Superexchange dominates in magnetic topological insulators. *Phys. Rev. B 104* (Dec 2021), L220404.

[171] Stanford Research Systems. *MODEL SR830 DSP Lock-In Amplifier*, 2.5 ed., Oct 2011.

[172] Taskin, A. A., and Ando, Y. Quantum oscillations in a topological insulator $Bi_{1-x}Sb_x$. *Phys. Rev. B 80* (Aug 2009), 085303.

[173] Tcakaev, A., Zabolotnyy, V. B., Green, R. J., Peixoto, T. R. F., Stier, F., Dettbarn, M., Schreyeck, S., Winnerlein, M., Vidal, R. C., Schatz, S., Vasili, H. B., Valvidares, M., Brunner, K., Gould, C., Bentmann, H., Reinert, F., Molenkamp, L. W., and Hinkov, V. Comparing magnetic ground-state properties of the V- and Cr-doped topological insulator $(Bi,Sb)_2Te_3$. *Phys. Rev. B 101* (Jan 2020), 045127.

[174] Tokura, Y., and Nagaosa, N. Nonreciprocal responses from non-centrosymmetric quantum materials. *Nat. Commun. 9* (Sep 2018), 3740.

[175] Tschirhart, C. L., Serlin, M., Polshyn, H., Shragai, A., Xia, Z., Zhu, J., Zhang, Y., Watanabe, K., Taniguchi, T., Huber, M. E., and Young, A. F. Imaging orbital ferromagnetism in a moiré Chern insulator. *Science 372*, 6548 (Jun 2021), 1323–1327.

[176] Tsemekhman, V., Tsemekhman, K., Wexler, C., Han, J. H., and Thouless, D. J. Theory of the breakdown of the quantum Hall effect. *Phys. Rev. B 55* (Apr 1997), R10201–R10204.

[177] Vergniory, M. G., Elcoro, L., Felser, C., Regnault, N., Bernevig, B. A., and Wang, Z. A complete catalogue of high-quality topological materials. *Nature 566* (Feb 2019), 480–485.

[178] Vergniory, M. G., Otrokov, M. M., Thonig, D., Hoffmann, M., Maznichenko, I. V., Geilhufe, M., Zubizarreta, X., Ostanin, S., Marmodoro, A., Henk, J., Hergert, W., Mertig, I., Chulkov, E. V., and Ernst, A. Exchange interaction and its tuning in magnetic binary chalcogenides. *Phys. Rev. B 89* (Apr 2014), 165202.

[179] Vergniory, M. G., Wieder, B. J., Elcoro, L., Parkin, S. S. P., Felser, C., Bernevig, B. A., and Regnault, N. All topological bands of all nonmagnetic stoichiometric materials. *Science 376*, 6595 (May 2022), eabg9094.

[180] von Klitzing, K. Quantum Hall effect: Discovery and application. *Annu. Rev. Condens. Matter Phys. 8*, 1 (Mar 2017), 13–30.

[181] von Klitzing, K., Chakraborty, T., Kim, P., Madhavan, V., Dai, X., McIver, J., Tokura, Y., Savary, L., Smirnova, D., Rey, A. M., Felser, C., Gooth, J., and Qi, X. 40 years of the quantum Hall effect. *Nat. Rev. Phys. 2* (Jul 2020), 397–401.

[182] von Klitzing, K., Dorda, G., and Pepper, M. New method for high-accuracy determination of the fine-structure constant based on quantized Hall resistance. *Phys. Rev. Lett. 45* (Aug 1980), 494–497.

[183] Wakatsuki, R., Ezawa, M., and Nagaosa, N. Domain wall of a ferromagnet on a three-dimensional topological insulator. *Sci. Rep. 5* (Sep 2015), 13638.

[184] Wakatsuki, R., Saito, Y., Hoshino, S., Itahashi, Y. M., Ideue, T., Ezawa, M., Iwasa, Y., and Nagaosa, N. Nonreciprocal charge transport in noncentrosymmetric superconductors. *Sci. Adv. 3*, 4 (Apr 2017), e1602390.

[185] Wang, J., Lian, B., Qi, X.-L., and Zhang, S.-C. Quantized topological magnetoelectric effect of the zero-plateau quantum anomalous Hall state. *Phys. Rev. B 92* (Aug 2015), 081107.

[186] Wang, J., Lian, B., Zhang, H., Xu, Y., and Zhang, S.-C. Quantum Anomalous Hall Effect with Higher Plateaus. *Phys. Rev. Lett. 111* (Sep 2013), 136801.

[187] Wang, J., Lian, B., Zhang, H., and Zhang, S.-C. Anomalous edge transport in the quantum anomalous Hall state. *Phys. Rev. Lett. 111* (Aug 2013), 086803.

[188] Wang, J., Lian, B., and Zhang, S.-C. Universal scaling of the quantum anomalous Hall plateau transition. *Phys. Rev. B 89* (Feb 2014), 085106.

[189] Wang, J., Zhou, Q., Lian, B., and Zhang, S.-C. Chiral topological superconductor and half-integer conductance plateau from quantum anomalous Hall plateau transition. *Phys. Rev. B 92* (Aug 2015), 064520.

[190] Wang, Y., Legg, H. F., Bömerich, T., Park, J., Biesenkamp, S., Taskin, A. A., Braden, M., Rosch, A., and Ando, Y. Gigantic magnetochiral anisotropy in the topological semimetal $ZrTe_5$. *Phys. Rev. Lett. 128* (Apr 2022), 176602.

[191] Watanabe, R., Yoshimi, R., Kawamura, M., Mogi, M., Tsukazaki, A., Yu, X. Z., Nakajima, K., Takahashi, K. S., Kawasaki, M., and Tokura, Y. Quantum anomalous Hall effect driven by magnetic proximity coupling in all-telluride based heterostructure. *Appl. Phys. Lett. 115*, 10 (Sep 2019), 102403.

[192] Wilczek, F. Two applications of axion electrodynamics. *Phys. Rev. Lett. 58* (May 1987), 1799–1802.

[193] Winnerlein, M., Schreyeck, S., Grauer, S., Rosenberger, S., Fijalkowski, K. M., Gould, C., Brunner, K., and Molenkamp, L. W. Epitaxy and structural properties of $(V,Bi,Sb)_2Te_3$ layers exhibiting the quantum anomalous Hall effect. *Phys. Rev. Mater. 1* (Jun 2017), 011201.

[194] Xu, S., Han, Y., Chen, X., Wu, Z., Wang, L., Han, T., Ye, W., Lu, H., Long, G., Wu, Y., Lin, J., Cai, Y., Ho, K. M., He, Y., and Wang, N. Van der Waals epitaxial growth of atomically thin Bi_2Se_3 and thickness-dependent topological phase transition. *Nano Lett. 15*, 4 (Mar 2015), 2645–2651.

[195] Yan, B., Stadtmüller, B., Haag, N., Jakobs, S., Seidel, J., Jungkenn, D., Mathias, S., Cinchetti, M., Aeschlimann, M., and Felser, C. Topological states on the gold surface. *Nat. Commun. 6* (Dec 2015), 10167.

[196] Yan, B., and Zhang, S.-C. Topological materials. *Rep. Prog. Phys. 75*, 9 (Aug 2012), 096501.

[197] Yang, K., Xu, Z., Feng, Y., Schindler, F., Xu, Y., Bi, Z., Bernevig, B. A., Tang, P., and Liu, C.-X. $\mathbb{Z}_2$-nontrivial moiré minibands and interaction-driven quantum anomalous Hall insulators in topological insulator based moiré heterostructures. *arXiv e-prints: 2304.09907* (Apr 2023).

[198] Yang, M., Couturaud, O., Desrat, W., Consejo, C., Kazazis, D., Yakimova, R., Syväjärvi, M., Goiran, M., Béard, J., Frings, P.,

Pierre, M., Cresti, A., Escoffier, W., and Jouault, B. Puddle-induced resistance oscillations in the breakdown of the graphene quantum Hall effect. *Phys. Rev. Lett. 117* (Dec 2016), 237702.

[199] Yang, W., Graef, H., Lu, X., Zhang, G., Taniguchi, T., Watanabe, K., Bachtold, A., Teo, E. H. T., Baudin, E., Bocquillon, E., Fève, G., Berroir, J.-M., Carpentier, D., Goerbig, M. O., and Plaçais, B. Landau velocity for collective quantum Hall breakdown in bilayer graphene. *Phys. Rev. Lett. 121* (Sep 2018), 136804.

[200] Yao, Y., Ye, F., Qi, X.-L., Zhang, S.-C., and Fang, Z. Spin-orbit gap of graphene: First-principles calculations. *Phys. Rev. B 75* (Jan 2007), 041401.

[201] Yasuda, K., Morimoto, T., Yoshimi, R., Mogi, M., Tsukazaki, A., Kawamura, M., Takahashi, K. S., Kawasaki, M., Nagaosa, N., and Tokura, Y. Large non-reciprocal charge transport mediated by quantum anomalous Hall edge states. *Nat. Nanotechnol. 15* (Jul 2020), 831–835.

[202] Yasuda, K., Tsukazaki, A., Yoshimi, R., Kondou, K., Takahashi, K. S., Otani, Y., Kawasaki, M., and Tokura, Y. Current-nonlinear Hall effect and spin-orbit torque magnetization switching in a magnetic topological insulator. *Phys. Rev. Lett. 119* (Sep 2017), 137204.

[203] Yasuda, K., Tsukazaki, A., Yoshimi, R., Takahashi, K. S., Kawasaki, M., and Tokura, Y. Large unidirectional magnetoresistance in a magnetic topological insulator. *Phys. Rev. Lett. 117* (Sep 2016), 127202.

[204] Yasuda, K., Wakatsuki, R., Morimoto, T., Yoshimi, R., Tsukazaki, A., Takahashi, K. S., Ezawa, M., Kawasaki, M., Nagaosa, N., and Tokura, Y. Geometric Hall effects in topological insulator heterostructures. *Nat. Phys. 12* (Feb 2016), 555–559.

[205] Yasuda, K., Yasuda, H., Liang, T., Yoshimi, R., Tsukazaki, A., Takahashi, K. S., Nagaosa, N., Kawasaki, M., and Tokura, Y. Nonreciprocal charge transport at topological insulator/superconductor interface. *Nat. Commun. 10*, 1 (Jun 2019), 2734.

[206] Ye, M., Li, W., Zhu, S., Takeda, Y., Saitoh, Y., Wang, J., Pan, H., Nurmamat, M., Sumida, K., Ji, F., Liu, Z., Yang, H., Liu, Z., Shen, D., Kimura, A., Qiao, S., and Xie, X. Carrier-mediated ferromagnetism in the magnetic topological insulator Cr-doped $(Sb,Bi)_2Te_3$. *Nat. Commun. 6* (Nov 2015), 8913.

[207] Ye, M., Xu, T., Li, G., Qiao, S., Takeda, Y., Saitoh, Y., Zhu, S.-Y., Nurmamat, M., Sumida, K., Ishida, Y., Shin, S., and Kimura, A. Negative Te spin polarization responsible for ferromagnetic order in the doped topological insulator $V_{0.04}(Sb_{1-x}Bi_x)_{1.96}Te_3$. *Phys. Rev. B 99* (Apr 2019), 144413.

[208] Yin, Y., Han, D.-S., de Jong, M. C. H., Lavrijsen, R., Duine, R. A., Swagten, H. J. M., and Koopmans, B. Thickness dependence of unidirectional spin-Hall magnetoresistance in metallic bilayers. *Appl. Phys. Lett. 111*, 23 (Dec 2017), 232405.

[209] Yokouchi, T., Kanazawa, N., Kikkawa, A., Morikawa, D., Shibata, K., Arima, T., Taguchi, Y., Kagawa, F., and Tokura, Y. Electrical magnetochiral effect induced by chiral spin fluctuations. *Nat. Commun. 8*, 1 (Oct 2017), 866.

[210] Yu, R., Zhang, W., Zhang, H.-J., Zhang, S.-C., Dai, X., and Fang, Z. Quantized anomalous Hall effect in magnetic topological insulators. *Science 329*, 5987 (Jul 2010), 61–64.

[211] Zhang, H., Liu, C.-X., Qi, X.-L., Dai, X., Fang, Z., and Zhang, S.-C. Topological insulators in Bi_2Se_3, Bi_2Te_3 and Sb_2Te_3 with a single Dirac cone on the surface. *Nat. Phys. 5* (May 2009), 438–442.

[212] Zhang, J., Chang, C.-Z., Tang, P., Zhang, Z., Feng, X., Li, K., Wang, L.-l., Chen, X., Liu, C., Duan, W., He, K., Xue, Q.-K., Ma, X., and Wang, Y. Topology-driven magnetic quantum phase transition in topological insulators. *Science 339*, 6127 (Mar 2013), 1582–1586.

[213] Zhang, J., Chang, C.-Z., Zhang, Z., Wen, J., Feng, X., Li, K., Liu, M., He, K., Wang, L., Chen, X., Xue, Q.-K., Ma, X., and Wang, Y. Band structure engineering in $(Bi_{1-x}Sb_x)_2Te_3$ ternary topological insulators. *Nat. Commun. 2* (Dec 2011), 574.

[214] Zhang, R.-X., Hsu, H.-C., and Liu, C.-X. Electrically tunable spin polarization of chiral edge modes in a quantum anomalous Hall insulator. *Phys. Rev. B 93* (Jun 2016), 235315.

[215] Zhao, Y.-F., Zhang, R., Mei, R., Zhou, L.-J., Yi, H., Zhang, Y.-Q., Yu, J., Xiao, R., Wang, K., Samarth, N., Chan, M. H. W., Liu, C.-X., and Chang, C.-Z. Tuning the Chern number in quantum anomalous Hall insulators. *Nature 588* (Dec 2020), 419–423.

List of Publications

1. Lippertz, G., Uday, A., Bliesener, A., Pereira, L. M. C., Taskin, A. A., and Ando, Y. Nonreciprocal charge transport on the edges of a quantum anomalous Hall insulator. *In preparation.*

2. Uday, A., Lippertz, G., Bhujel, B., Taskin, A. A., and Ando, Y. The trivial origin of the half-integer quantized conductance observed in superconductor – quantum anomalous Hall insulator heterostuctures. *In preparation.*

3. Brede, J., Bagchi, M., Greichgauer, A., Taskin, A. A., Uday, A., Bliesener, A., Lippertz, G., Yazdanpanah, R., Rüssmann, P., Blügel, S., and Ando, Y. Superconducting proximity effect in $(Bi_{1-x}Sb_x)_2Te_3$ thin films probed by STM. *In preparation.*

4. Brede, J., Bagchi, M., Greichgauer, A., Uday, A., Bliesener, A., Lippertz, G., Yazdanpanah, R., Taskin, A., and Ando, Y. Characterizing the chemical potential disorder in the topological insulator $(Bi_{1-x}Sb_x)_2Te_3$ thin films. *Phys. Rev. Mater.* (Accepted Oct 2024).

5. Röper, T., Thomas, H., Rosenbach, D., Uday, A., Lippertz, G., Denis, A., Morfin, P., Taskin, A. A., Ando, Y, and Bocquillon, E. Propagation, dissipation, and breakdown in quantum anomalous Hall edge states probed by microwave edge plasmons. *Phys. Rev. B 110* (Oct 2024), L161403.

6. Lippertz, G., Breunig, O., Fister, R., Uday, A., Bliesener, A., Brede, J., Taskin, A., and Ando, Y. Selective-area epitaxy of bulk-insulating $(Bi_xSb_{1-x})_2Te_3$ films and nanowires by molecular beam epitaxy. *ACS Appl. Mater. Interfaces 16*, 31 (Jul 2024), 41293–41299.

7. Uday, A., Lippertz, G., Moors, K., Legg, H. F., Bliesener, A., Pereira, L. M. C., Taskin, A. A., and Ando, Y. Induced superconducting correlations in a quantum anomalous Hall insulator. *Nat. Phys. 20* (Jul 2024), 1589–1595.

8. Rössler, M., Fan, D., Münning, F., Legg, H. F., Bliesener, A., Lippertz, G., Uday, A., Yazdanpanah, R., Feng, J., Taskin, A., and Ando, Y. Top-down fabrication of bulk-insulating topological insulator nanowires for quantum devices. *Nano Lett. 23*, 7 (Mar 2023), 2846–2853.

9. Thupakula, U., Laha, P., Lippertz, G., Schouteden, K., Netsou, A.-M., Seliverstov, A., Terryn, H., Pereira, L. M. C., and Van Haesendonck, C. Two-dimensional tellurium superstructures on Au(111) surfaces. *J. Chem. Phys. 157* (Oct 2022), 164703.

10. Lippertz, G., Bliesener, A., Uday, A., Pereira, L. M. C., Taskin, A. A., and Ando, Y. Current-induced breakdown of the quantum anomalous Hall effect. *Phys. Rev. B 106* (Jul 2022), 045419.

11. Legg, H. F., Rössler, M., Münning, F., Fan, D., Breunig, O., Bliesener, A., Lippertz, G., Uday, A., Taskin, A. A., Loss, D., Klinovaja, J., and Ando, Y. Giant magnetochiral anisotropy from quantum-confined surface states of topological insulator nanowires. *Nat. Nanotechnol. 17* (May 2022), 696–700.

12. Bai, M., Wei, X.-K., Feng, J., Luysberg, M., Bliesener, A., Lippertz, G., Uday, A., Taskin, A. A., Mayer, J., and Ando, Y. Proximity-induced superconductivity in $(Bi_{1-x}Sb_x)_2Te_3$ topological-insulator nanowires. *Commun. Mater. 3* (Apr 2022), 20.

13. Wahl, U., Correia, J. G., Costa, A. R. G., David-Bosne, E., Kappers, M. J., da Silva, M. R., Lippertz, G., Lima, T. A. L., Villarreal, R., Vantomme, A., and Pereira, L. M. C. Lattice location studies of the amphoteric nature of implanted Mg in GaN. *Adv. Electron. Mater. 7* (Jun 2021), 2100345.

14. Reinhoffer, C., Mukai, Y., Germanskiy, S., Bliesener, A., Lippertz, G., Uday, A., Taskin, A. A., Ando, Y., Wang, Z., and van Loosdrecht, P. H. M. Relaxation dynamics of the optically driven nonequilibrium states in the electron- and hole-doped topological-insulator materials $(Bi_{1-x}Sb_x)_2Te_3$. *Phys. Rev. Mater. 4* (Dec 2020), 124201.

15. Bai, M., Yang, F., Luysberg, M., Feng, J., Bliesener, A., Lippertz, G., Taskin, A. A., Mayer, J., and Ando, Y. Novel self-epitaxy for inducing superconductivity in the topological insulator $(Bi_{1-x}Sb_x)_2Te_3$. *Phys. Rev. Mater. 4* (Sep 2020), 094801.

16. Madarevic, I., Thupakula, U., Lippertz, G., Claessens, N., Lin, P.-C., Bana, H., Gonzalez, S., Di Santo, G., Petaccia, L., Nair, M. N., Pereira, L. M. C., Van Haesendonck, C., and Van Bael, M. J. Structural and electronic properties of the pure and stable elemental 3D topological Dirac semimetal α-Sn. *APL Mater. 8* (Mar 2020), 031114.

17. Augustyns, V., van Stiphout, K., Joly, V., Lima, T. A. L., Lippertz, G., Trekels, M., Menéndez, E., Kremer, F., Wahl, U., Costa, A. R. G., Correia, J. G., Banerjee, D., Gunnlaugsson, H. P., von Bardeleben, J., Vickridge, I., Van Bael, M. J., Hadermann, J., Araújo, J. P., Temst, K., Vantomme, A., and Pereira, L. M. C. Evidence of tetragonal distortion as the origin of the ferromagnetic ground state in γ-Fe nanoparticles. *Phys. Rev. B 96* (Nov 2017), 174410.

18. Wahl, U., Amorim, L. M., Augustyns, V., Costa, A., David-Bosne, E., Lima, T. A. L., Lippertz, G., Correia, J. G., da Silva, M. R., Kappers, M. J., Temst, K., Vantomme, A., and Pereira, L. M. C. Lattice location of Mg in GaN: A fresh look at doping limitations. *Phys. Rev. Lett. 118* (Mar 2017), 095501.

FACULTY OF SCIENCE
DEPARTMENT OF PHYSICS AND ASTRONOMY
QUANTUM SOLID STATE PHYSICS
Celestijnenlaan 200D box 2414
B-3001 Leuven

FACULTY OF MATHEMATICS AND NATURAL SCIENCE
DEPARTMENT OF PHYSICS, INSTITUTE OF PHYSICS II
TOPOLOGICAL MATTER LABORATORY COLOGNE
Zülpicher Straße 77
50937 Cologne
Germany